Production of cryogens using wind energy for use in deep mine cooling and ventilation

by

Saruna Kunwar

A thesis submitted in partial fulfilment
of the requirements for the degree of
Doctor of Philosophy (PhD)
in Natural Resources Engineering

The Faculty of Graduate Studies
Laurentian University
Sudbury, Ontario, Canada

THESIS DEFENCE COMMITTEE/COMITÉ DE SOUTENANCE DE THÈSE
Laurentian Université/Université Laurentienne
Faculty of Graduate Studies/Faculté des études supérieures

Title of Thesis Titre de la thèse	Production of cryogens using wind energy for use in deep mine cooling and ventilation
Name of Candidate Nom du candidat	Kunwar, Saruna
Degree Diplôme	Doctor of Philosophy
Department/Program Département/Programme	Natural Resources Engineering
Date of Defence Date de la soutenance	September 05, 2017

APPROVED/APPROUVÉ

Thesis Examiners/Examinateurs de thèse:

Dr. Dean Millar
(Supervisor/Directeur(trice) de thèse)

Dr. Meysar Zenalli
(Committee member/Membre du comité)

Dr. Ramesh Subramanian
(Committee member/Membre du comité)

Dr. Brent Lievers
(Committee member/Membre du comité)

Dr. Rupp Carriveau
(External Examiner/Examinateur externe)

Dr. Graeme Spiers
(Internal Examiner/Examinateur interne)

Approved for the Faculty of Graduate Studies
Approuvé pour la Faculté des études supérieures
Dr. David Lesbarrères
Monsieur David Lesbarrères
Dean, Faculty of Graduate Studies
Doyen, Faculté des études supérieures

ACCESSIBILITY CLAUSE AND PERMISSION TO USE

Abstract

This research work, named as 'CryoVent', was focused on determining the feasibility of using wind energy, to produce liquefied gases (cryogens) continuously in a safe approach that can be used for the cooling and ventilation of underground mines. The experimental work performed suggested that the continuous production of liquefied gases with variable input work is practical. The average specific power consumption for liquefaction of nitrogen in this work was 7.86 kWh/kg using the refrigeration produced by helium. This is ~20 times higher than that consumed by industrial scale gas liquefaction systems, but is practical for a small scale system. This specific power consumption could probably be lowered if the working fluid itself is liquefied.

Analysis on wind speed variability and wind speed data synthesis were also performed which suggested presence of multi-fractal nature in wind speed data that represent the temporal variation. A new method developed to generate high sampling frequency wind speed data from available low sampling frequency wind speed data can have contribution in all sectors when there is a need of higher sampling frequency time series data for simulation/study purposes.

The liquid nitrogen mass flow rate (kg/s) increased with increase in compressor motor frequency and also when operating at variable motor input frequency. However, the average compressor power consumption also increased compared to average power consumption during operation at standard motor frequency of 60 Hz. This was in a laboratory scale liquefaction system and needs to be tested in the large scale system experimentally. With 1 kg/s of liquefied nitrogen supplied, ~459 kW_r of cooling power is available to cool the deep mine air which is at 30-40^{0}C. A volumetric flow rate of 0.062 m^3/s of liquefied air can provide a cooling power equivalent to that provided by a volumetric flow rate of 4000 m^3/s of atmospheric air, which is the requirement of some of the biggest mines in the world.

The hydraulic wind turbine as proposed in this work can eliminate the system start-up issues following the calm period, which are typical concerns with the wind energy integrations. This research work has provided the required modeling and simulation results that are crucial in development of the full scale ‘CryoVent’.

Keywords: CryoVent, liquefied gases, gas liquefaction system, wind speed data synthesis, hydraulic wind turbine

Acknowledgements

This work would not have been completed without the continuous support and motivation from my supervisor Dr. Dean Millar. Therefore, I would like to take this time to thank Dr. Millar for providing me this great opportunity. The experiences I gathered from this work have in fact helped me achieve personal and professional advancement. This would never have been possible without his encouragement and positive approaches. I am always fascinated to learn how valuable and motivating his speeches and suggestions are. I would also like to thank my committee members for providing me with constructive feedbacks that definitely added more value to the final version of this thesis. I am very grateful to all of them.

My sincere gratitude also goes to CEMI, Canadian foundation for Innovation, MITACS and MIRARCO for the financial support for this research work. Without their financial support, I would never be able to pursue further.

My gratitude also extends to all the technicians and engineers from Cryomech Inc., USA who took their time to assemble and fabricate the laboratory equipment that met our requirement. They have been immensely helpful to me even after the delivery of the equipment. I would like to thank them for being so prompt in responding all my queries regarding the laboratory equipment and for supplying the missing parts on time.

Huge thanks are also extended to Dr. Ray Radebaugh, Dr. Seungwhan Baek and Dr. Peter Bradley at NIST, Colorado, USA for providing me great opportunity to work as an intern within the Cryogenics Division of National Institute of Standard & Technology. I am thankful for their cooperation, immense help and support during that period. I would like to thank Dr. Radebaugh for providing this opportunity which was a great learning platform. My sincere

appreciation goes to Dr. Baek, who expended his precious time for providing me required training on safe handling of cryogens at NIST facilities.

Next, I would like to thank my colleagues at MIRARCO, especially Alex Hutchison, Stephen Young and Chen Zhuo for helping during the laboratory equipment delivery and carrying around the equipment on campus. I would also like to thank Adam Walli, Ethan Armit and Gregory Lakanen from Laurentian University for their help while I was performing laboratory work. My gratitude also goes to Luc Beaudet from Chemistry Department for providing me with the extra Dewar storage vessels during experimentation.

My family and friends have supported me in every possible ways. I would not have been more motivated and encouraged without their love and support. I thank them all, especially my husband, my parents, and my brother, for everything. It would not have been easier for me to complete this work if you all were not there to care. Also, hearty gratitude to my special companions, my dogs for cheering me up all the time.

Thank you.

Saruna Kunwar

May 2017

Table of Contents

Abstract iii
Acknowledgements v
Table of Contents vii
List of Tables xii
List of Figures xiii
List of Appendix Figures xix
1 Introduction 1
1.1 Background 1
1.1.1 Integration of wind energy into energy systems 5
1.1.2 Integrated energy storage and generation 7
1.1.3 Availability and cost of wind energy 8
1.1.4 Illustrative case study: Large scale CryoVent production for mine cooling 9
1.2 Wind energy driven cryocooler concept 10
1.2.1 System components 11
1.2.2 Process flow diagram 11
1.3 Control systems 13
1.4 Applications 13
1.4.1 Application to cryogen production 13
1.4.2 Application to utility scale energy storage 14
1.4.3 Application to utility scale energy transportation 15
1.5 CryoVent concept initial steps towards cost estimation 16
1.6 Key research questions 18
1.7 Hypotheses of the thesis 20
1.7.1 Variability of cryogen production 20
1.7.2 Multifractal wind speed time series 20
1.8 Thesis objectives 21
1.9 Thesis outline 22
2 Overview of wind turbines 25
2.1 Introduction 25
2.2 Drag and lift on a blade element 28
2.3 Cp versus λ curve 31
2.4 Wind turbine power curve 33
2.5 Torque development from a wind turbine blade 35
2.6 Optimising wind energy capture with variable speed HAWT 37
2.7 Other HAWT components 38
2.7.1 Blading 39
2.7.2 Transmission systems 41
2.7.3 Generator 42
2.7.4 Power electronics 44
2.7.5 Pitch control system 46
2.7.6 Yaw control system 47
2.7.7 Rotational speed control system 48
2.8 Summary 49

3 Statistical analysis of wind climate 51
3.1 Factors affecting wind energy 51
3.1.1 Spatial factors 52
3.1.2 Temporal factors 56
3.2 Statistical measures 57
3.2.1 Mean wind speed 57
3.2.2 Standard deviation of wind speed 58
3.2.3 Turbulence intensity factor 58
3.2.4 Weibull distribution 59
3.2.5 Wind roses 60
3.2.6 Wind atlases (WAsP) 61
3.2.7 International Electro-technical Commission (IEC) wind classes for wind turbines 61
3.3 Source of wind speed data used in this thesis 62
3.4 Summary 64
4 Time series analysis of wind climate 65
4.1 Sampling frequency and sampling duration 69
4.1.1 Sampling frequency 69
4.1.2 Sampling duration 69
4.1.3 Windowing 70
4.2 Autocorrelation of wind speed time series 71
4.2.1 Lag 73
4.2.2 Correlation and Correlation coefficient 74
4.2.3 Auto-Regressive Moving Average (ARMA) and variants 75
4.3 Frequency domain analysis 78
4.3.1 Fast Fourier transform 78
4.3.2 Preparation of frequency array 79
4.3.3 Amplitude spectrum 79
4.3.4 Power spectrum 81
4.3.5 Phase spectrum 82
4.3.6 Modelling the power spectrum 83
4.3.7 Fractal dimension from power spectrum 84
4.3.8 Relation between average wind speed and magnitude spectrum 84
4.3.9 Relation between wind speed variability and power spectrum 85
4.4 Multifractal analysis 85
4.4.1 Higuchi algorithm 86
4.4.2 Modeling Higuchi plots 87
4.4.3 Domains of self similarity & calculation of domain fractal dimension 88
4.4.4 Comparison of the methods for determination of the fractal dimension 89
4.4.5 Options for computing fractal dimension 89
4.4.6 Characterisation of white and brown noise 90
4.4.7 Using Higuchi algorithm to compute the fractal dimension of the phase spectrum 91
4.4.8 Steps for generating high sampling frequency wind speed time series data preserving the variability in them 92
4.5 Summary 95
5 A review of gas refrigeration and liquefaction systems 97
5.1 Joule-Thomson effect 98

5.2 Reversed Brayton refrigeration Cycle....99
5.3 Ideal liquefaction systems....101
5.4 Simple Linde-Hampson cycle....102
5.5 Stirling cycle refrigeration....105
5.6 Gifford-McMahon cryocooler....108
5.7 Pulse tube cryocooler....110
5.8 Dewar vessels for cryogen storage....113
5.9 Thermodynamic performance comparison of some liquefaction systems....115
5.10 An analysis of the cryogenic air separation plant at Copper Cliff Smelter....117
5.11 Summary....119
6 A review of fluid power for wind turbines....121
6.1 Prior work....122
6.2 Hydrostatic transmission components....123
6.2.1 Hydraulic pumps and motors....123
6.2.2 Valves....125
6.3 Hydrostatic transmission wind turbine model....128
6.4 Dynamic simulation of a closed loop hydrostatic transmission....129
6.5 Reservoirs and accumulators....135
6.6 Control system....137
6.7 Dynamic simulation of an open loop hydrostatic transmission with short term energy storage....140
6.8 Summary....147
7 Dynamic simulation of a wind energy driven Gifford McMahon cryocooler....149
7.1 Introduction – overview of components and component options....150
7.2 Options for the hydrostatic transmission drive....151
7.2.1 Dynamic model of electric motor with constant rotation speed set point....151
7.2.2 Wind turbine rotor....151
7.3 Options for Helium compressor drive....151
7.3.1 Dynamical model of an electric motor with rotational speed varying between set point to set point....152
7.3.2 Open loop hydrostatic transmission....152
7.4 Thermo-mechanical dynamic process simulation of the GM cryocooler....153
7.5 Dynamical model for nitrogen liquefaction within a Dewar storage vessel....155
7.5.1 Geometry, configuration and materials....155
7.5.2 Delivery of nitrogen (air to drying system to nitrogen filtration)....158
7.5.3 Heat transfer by conduction....160
7.5.4 Heat transfer by radiation....161
7.5.5 External conditions assumed....162
7.5.6 Differential equation for heat transfer between gas and cold finger....163
7.5.7 Simulation of nitrogen condensation with defined cold finger temperatures....168
7.5.8 Simulation of nitrogen evaporation with defined cold finger temperatures....171
7.6 Simulations with integrated dynamical models....177
7.6.1 Simulations at steady speeds....177
7.6.2 Simulations at sinusoidal varying set points....180
7.6.3 Simulations at random set points....183
7.6.4 Simulations following wind speed data....188
7.7 Summary....195

8 Laboratory verification of liquid nitrogen production model 197
8.1 Experimental equipment 197
8.1.1 Process flow diagram for Cryomech Helium compressor unit with variable frequency drive electric motor 197
8.1.2 Heat exchanger and auxiliary systems 201
8.1.3 Cold head including rotary valve 204
8.1.4 Nitrogen generation, drying and purification system 205
8.1.5 Dewar flask 207
8.1.6 Mass balance 208
8.2 Development of the supervisory control and data acquisition system 209
8.2.1 Monitoring of lab environmental data 210
8.2.2 Cryomech Helium compressor data acquisition software 210
8.2.3 Development of the VFD interface in LabVIEW 211
8.2.4 Integration of the ultra low temperature sensor into LabVIEW HMI 216
8.2.5 Enhanced measurement resolution procedure for the Fairbanks UltraMax digital mass balance and integration to the LabVIEW HMI 217
8.3 Experimental program 218
8.3.1 60Hz testing 219
8.3.2 Prolonged tests at other driving frequencies 222
8.3.3 Sinusoidal varying motor driving frequency tests 229
8.3.4 Random variation of motor driving frequency 233
8.3.5 Wind speed time series scaled to motor driving frequency 239
8.4 Summary 242
9 Comparison of simulation and experimental results 244
9.1 Comparisons at different driving frequencies 244
9.2 Comparisons at sinusoidal varying frequencies 248
9.3 Comparisons at random varying frequencies 251
9.4 Comparisons for motor frequency corresponding to wind speeds 257
9.5 Summary 260
10 Extended simulations of a 5MW wind energy driven liquid nitrogen production system 263
10.1 Simulation with steady wind speeds 263
10.2 Simulation with actual wind speed time series from SWMTF 4Hz data 266
10.3 Simulation with 5MW rated wind rotor with Roskrow Barton 10 minute wind speed 268
10.4 Hydraulic accumulator volume calculations example 274
10.5 Summary 275
11 Conclusions, Contributions and Future Works 277
11.1 Conclusions 277
11.2 Contributions 281
11.3 Future works 282
References 285
Appendices 295
Appendix A. Conference paper 295
Appendix B. Script for Higuchi algorithm 305
Appendix C. Parameter list and script written by candidate for comparison of the hydraulic wind turbine model with that of Hamzehlouia et al. (2013) 306
Appendix D. Parameter list and script written by candidate for the GM cryocooler unit 309
Appendix E. Script for wind-driven GM cryocooler 313

Appendix F. Script for Chapter 10 simulation 318
Appendix G. Experimental results from 60 Hz operation 323
Appendix H. Experimental results from operating compressor at different frequencies 327
Appendix I. Experimental results from operating compressor at sinusoidal frequency input to compressor 329
Appendix J. Experimental results from operating compressor at random frequency input ..332
Appendix K. Experimental results when operating compressor with frequency scaled down from actual wind speed data 334
Appendix L. Laboratory equipment 338

List of Tables

Table 1: Relevance of reviewed materials in Chapter 2.....50
Table 2: Wind speed parameters for wind turbine classes according to IEC (as cited in Burton et al., 2001).....62
Table 3: Performance parameters of a simple Linde-Hampson cycle for various fluids: (T_1= 25^{o}C; P_1= 1 atm, P_2= 20 MPa) (Kanoglu et al., 2008).....116
Table 4: Specific power consumption for hydrogen liquefaction using different cycles (Krasae-in et al., 2010).....117
Table 5: List of parameters for closed loop hydrostatic transmission.....133
Table 6: Parameters used for simulation of the open loop hydrostatic transmission model (Hamzehlouia et al., 2013).....143
Table 7: Comparing obtained simulation results with those from Hamzehlouia et al. (2013)....148
Table 8: Parameters for wind turbine rotor and hydrostatic transmission.....150
Table 9: Parameters for GM cryocooler system 151
Table 10: Simulation results.....180
Table 11: Mass balance parameters 208
Table 12: Function codes supported by SJ700 series inverter and their functions (Hitachi, 2014) 213
Table 13: Modbus data format (Hitachi, 2014) 213
Table 14: List of monitored registers (Hitachi, 2014) 216
Table 15: Average compressor input power (kW) at different frequencies.....225
Table 16: Average liquid nitrogen mass flow rate (kg/s) at different frequencies 226
Table 17: Average cold head temperature (K) at different frequencies.....226
Table 18: List of average values for parameters at different frequencies.....227
Table 19: Range of statistic for simulated results 248
Table 20: Range of statistics for experimental results 248
Table 21: Results summary of the simulation.....268
Table 22: Parameters for wind turbine rotor and hydrostatic transmission.....269

List of Figures

Figure 1: Schematic of the 'CryoVent' concept showing use of the stored cryogen product for deep mine cooling 2
Figure 2: Installed costs for electricity generating technologies taken from NREL (2016) 8
Figure 3: Block diagram of the wind energy driven gas liquefaction system 10
Figure 4**:** Schematic of the CryoVent concept to produce cryogens 12
Figure 5: Schematic showing various energy generating systems using wind power with their respective costs and overall efficiencies. WT=Wind Turbine, CAES= Compressed Air Energy System (reproduced from Kunwar & Millar (2014)) 17
Figure 6: Thesis roadmap 24
Figure 7: 1 second average wind speed data SWMTF, Exeter, UK 25
Figure 8: Different types of wind turbines for wind energy conversion (Taylor, 2004) 27
Figure 9: Schematic for lift and drag on airfoil (Woodbank Communications Ltd, 2005) 29
Figure 10: Vector diagram showing a section through a moving horizontal axis wind turbine (HAWT) rotor blade (Taylor, 2004) 31
Figure 11: Chart showing the power coefficient and tip speed ratio for a two-bladed rotor (Magdi Ragheb & Ragheb, 2011) 33
Figure 12: A typical wind turbine power curve for a 600 kW wind turbine for pitch-controlled and stall-controlled system (Gasch & Twele, 2012) 34
Figure 13: 3D view of an HAWT rotor blade design (Taylor, 2004) 36
Figure 14: Wind turbine components inside the wind turbine nacelle. 1. Rotor blades, 2. Hub, 3. Main shaft, 4. Controller, 5. Gearbox, 6. Mechanical brake, 7. Generator, 8. Cooling system, 9. Anemometer, 10. Wind vane, 11. Yawing motor and yawing bearing (Jiang, 2010) 38
Figure 15: Multiple pole generator (Magdi Ragheb & Ragheb, 2011) Original source: Enercon GmbH (2016) 42
Figure 16: Squirrel cage and doubly fed induction generators for wind turbines (Djemai & Bouktir, 2008) 43
Figure 17: Sketch showing the wind turbine components connected to power system: 1. Rotor/blades, 2. Nacelle, 3.Tower, 4. Foundation, and 5. Transformer (Jiang, 2010) 45
Figure 18: A typical wind turbine power curve showing different control regions (K. E. Johnson et al., 2006) and (Rajabhandharaks, 2014) 49
Figure 19: A global wind map showing wind speeds over land and water (Vaisala, 2017) 52
Figure 20: Day and night time breeze conditions in sea and land and mountain and valley respectively (Douglas, 2006) 54
Figure 21: Relation between wind speed (m/s) and roughness above ground (m) 55
Figure 22: Wind power spectrum (Van der Hoven, 1956) 56
Figure 23: Example of wind rose (Pereira, 2015) (W_s = wind speed in (m/s)) 60
Figure 24: Roskrow Barton Wind farm (Wikimapia, 2016) 63
Figure 25: (a) Hourly averages, (b) Autocorrelation coefficients for hourly averages wind speed data at different lags. Data from Roskrow, Barton farm, UK for 3 days (72 hours) 72
Figure 26: Partial correlation coefficients for hourly averages wind speed data at different lags. Data from Roskrow, Barton farm, UK 73
Figure 27: Wind speed time series used for ARMA modelling 76
Figure 28: Measured and 1 step ahead predicted wind speed (m/s) using ARMA model 77
Figure 29: Measured and 5 step ahead predicted wind speed (m/s) using ARMA model 77

Figure 30: Measured 10 minute average wind speed data (m/s) used for data synthesis. Data from Roskrow Barton farm, UK 80
Figure 31: Magnitude spectrum for 10 minute average wind speed data from Roskrow, Barton farm, UK.....80
Figure 32: Power spectrum plot for 10 minute average wind speed data from Roskrow Barton farm, UK.....81
Figure 33: Phase spectrum presenting phase values at different frequency for 10 minute average wind speed data from Roskrow Barton farm, UK 83
Figure 34: A logarithmic plot of the phase spectrum for 10 minute average wind speed data from Roskrow Barton farm, UK 83
Figure 35: A typical Higuchi plot generated for wind speed time series data from a wind farm in Roskrow Barton, Cornwall, UK.....87
Figure 36: Higuchi plot showing cross-over indicating that the fractal dimensions for this set of wind speed data could be more than one slope (more than one value for fractal dimension) 88
Figure 37: Higuchi plot for phase spectrum of one year worth of wind speed data from Roskrow Barton wind farm, UK.....91
Figure 38: Pictorial representation of the novel method for generation of high sampling frequency wind speed time series data from available lower sampling frequency data. Synthesis of wind speed time series data using this method is in progress. 94
Figure 39: Isenthalpic expansion of a real gas (Barron, 1985).....99
Figure 40: a) A reverse Brayton refrigeration cycle, b) its T-s diagram (Dincer & Kanoglu, 2010) 101
Figure 41: Schematic (a) and T-s diagram (b) of an ideal liquefaction system for nitrogen (Venkatarathnam, 2010) 102
Figure 42: Schematic (a) and T-s diagram (b) of the Linde-Hampson liquefaction system for air 104
Figure 43: Schematic of a Striling cryocooler (Urieli, 2010) 106
Figure 44: Schematic of the Stirling cycle refrigerator (Van Sciver, 2012) 107
Figure 45: Schematic of the GM showing the process more visually 109
Figure 46: Schematic of five common cryocoolers (Radebaugh, 2009).....111
Figure 47: A cut-view of a typical cryogenic storage tank (Air products, 2017) 114
Figure 48: Cryogenic storage tank with required valves and gauges (Air Products and Chemicals, 2013).....115
Figure 49: Oxygen production requirements shown with costs and oxygen purity percentage: (a) plant investment for oxygen at 20 psig; (b) power requirements for oxygen at 20 psig; (c) power requirements for oxygen at pressures above 20 psig; and (d) operating costs. (MIT-maintenance, insurance, and taxes) taken from Queneau & Marcuson (1996).....118
Figure 50: Schematic showing working principle of fluid power transmission for wind turbine application (Diepeveen, 2013).....121
Figure 51: A typical radial piston pump/motor (Artemis Intelligent Power, 2016) 124
Figure 52: A check valve (Finotek, 2006) and its cut view (Design Aerospace LLC, 2013).....126
Figure 53: A pressure relief valve with its components (Finotek, 2006) 126
Figure 54: Schematic of closed loop hydrostatic transmission.....130
Figure 55: Variable pump speed (RPM) signals provided to the hydraulic pump with respect to time (sec) representing the changes in wind speed.....133
Figure 56: Corresponding hydraulic pump flow (m^3/s) as a result of change in pump speeds with respect to time (sec).....134

Figure 57: Motor flow (m^3/s) with respect to time (sec) 134
Figure 58: Hydraulic motor speed (RPM) with respect to time (sec) 135
Figure 59: A cut-view of a rectangular reservoir (Hydraulics & Pneumatics, 2012) 136
Figure 60: Bladder type hydraulic accumulator (J. Johnson, 2014) 137
Figure 61: Schematic of open loop hydrostatic transmission 141
Figure 62: Flow diagram for the high wind speed condition (Hamzehlouia et al., 2013) 142
Figure 63: Flow diagram for the low wind speed condition (Hamzehlouia et al., 2013) 142
Figure 64: Variable pump speed (RPM) signals provided to the hydraulic pump with respect to time (sec) representing the changes in wind speed 144
Figure 65: Pump flow rate (m^3/s) with respect to time 144
Figure 66: Hydraulic motor flow (m^3/s) with respect to time 145
Figure 67: Hydraulic motor speed (RPM) with time 145
Figure 68: State of charge (%) of the storage with respect to time (sec) 146
Figure 69: Cool down of the cold head when starting from room temperature (300K) 154
Figure 70: Cold head temperature (K) versus time taken (min) showing the simulated and experimental results 154
Figure 71: Schematic of Dewar vessel with installed safety features (PRV = Pressure Relief Valve) 156
Figure 72: A typical refrigerated air dryer (eCompressedair, 2017) 159
Figure 73: A hyper drain condensate which works on float valve mechanism 159
Figure 74: Dewar vessel configuration used for heat loss calculations 164
Figure 75: Dewar vessel configuration showing energy distribution for the nitrogen liquefaction process. Drawing adapted from Wang (2005) 164
Figure 76: The temperature entropy diagram for the GM refrigeration process (Barron, 1985) 166
Figure 77: Simulated cool down of the cold head when starting from room temperature of 300K 169
Figure 78: Simulated cold head temperature (K) when starting from liquid nitrogen boiling point 170
Figure 79: Cooling produced by the cold head 170
Figure 80: Liquid nitrogen mass flow rate (kg/s) with respect to time 171
Figure 81: Experimental cold head temperature rise (K) when the cryocooler system was shut down (compare with Figure 84) 173
Figure 82: Liquid nitrogen mass (kg) and gaseous nitrogen mass (kg) inside Dewar showing time taken to evaporate when Dewar was filled with ~8.75 Liters of liquid nitrogen 173
Figure 83: Liquid nitrogen mass (kg) and gaseous nitrogen mass (kg) inside Dewar showing time taken to evaporate when Dewar was filled with ~10.5 Liters of liquid nitrogen 174
Figure 84: Simulated cold head temperature rise (K) during system shut off (compare with Figure 81) 174
Figure 85: Liquid nitrogen mass (kg) and gaseous nitrogen mass (kg) inside Dewar showing time taken to evaporate when Dewar was filled with ~8.75 Liters of liquid nitrogen 175
Figure 86: Liquid nitrogen mass (kg) and gaseous nitrogen mass (kg) inside Dewar showing time taken to evaporate when Dewar was filled with ~10.5 Litres of liquid nitrogen 175
Figure 87: Schematic of the electric motor driven GM cryocooler system 178
Figure 88: Compressor power input required for different driving frequencies 178
Figure 89: Average liquid nitrogen mass flow rate at different frequencies with error bars 179
Figure 90: Cold head temperature (K) at different frequencies with error bars 179

Figure 91: Sinusoidal input of compressor driving frequency with frequency changing every minute....181
Figure 92: Compressor input power (W) with respect to time....181
Figure 93: Cold head temperature (K) with respect to time....182
Figure 94: Liquid nitrogen mass flow rate (kg/s) with respect to time....182
Figure 95: Random frequency set points (Hz) used for simulation....183
Figure 96: Compressor input power (W) with respect to time....184
Figure 97: Compressor input power (W) with respect to frequency (Hz)....184
Figure 98: Cold head temperature (K) with respect to time....185
Figure 99: Liquid nitrogen mass flow rate (kg/s) with respect to time....185
Figure 100: Frequency input (Hz) with respect to time (min)....186
Figure 101: Compressor input power (kW) with respect to time (min)....187
Figure 102: Compressor input power (W) with respect to frequency (Hz)....187
Figure 103: Liquid nitrogen mass flow rate (kg/s) with respect to frequency (Hz)....188
Figure 104: Wind speed (m/s) data used for scaling to compressor input frequency (Hz)....189
Figure 105: Input frequency (Hz) in proportion to wind speed of Figure 104 changing every minute....189
Figure 106: Compressor power input (W) to drive the cryocooler system....190
Figure 107: Compressor power input (W) with respect to frequency input (Hz)....190
Figure 108: Cold head temperature (K) with respect to time....191
Figure 109: Liquid nitrogen mass flow rate (kg/s) with respect to time....191
Figure 110: Liquid nitrogen mass flow rate (kg/s) with respect to frequency (Hz)....192
Figure 111: 1 second average wind speed (m/s) data....193
Figure 112: Proportional compressor driving frequency (Hz) with respect to time....193
Figure 113: Compressor input power (W) to drive the cryocooler system....194
Figure 114: Cold head temperature (K) with respect to time....194
Figure 115: Liquid nitrogen mass flow rate (kg/s) with respect to time....195
Figure 116: (a) Experimental setup schematic (Items shown within the dashed box are those required simply to provide a safe source of gas to liquefy for experimental purposes), and (b) laboratory setup....199
Figure 117: Process flow of helium refrigeration and oil injection cooling mechanism (Hitachi America Ltd., 2015)....200
Figure 118: Process flow diagram for the overall system showing helium gas lines and cooling water lines (courtesy: Cryomech Inc.)....202
Figure 119: Cooling water requirement for compressor CP830 (Cryomech, 2017)....203
Figure 120: Cold head assembly showing its component locations(Cryomech, 2014)....205
Figure 121: Set of filters in the nitrogen filter bank to remove water, oil, and carbon from the compressed air feed....206
Figure 122: Coalescing filter and water filter with the band of color-change medium....206
Figure 123: Membrane separator showing the separation process (Kopeliovich, 2017)....207
Figure 124: LNP10 liquid nitrogen generator system with air compressor, helium compressor, filter bank and Dewar vessel (Cryomech, 2017)....208
Figure 125: UltegraMax Flat top logging mass balance from Fairbanks Scales (Fairbanks Scales, 2017)....209
Figure 126: A block diagram showing the supervisory control and data acquisition system development....210
Figure 127: Cryomech Virtual panel for logging all the parameters(Cryomech, 2017)....211

Figure 128: LabVIEW block diagram error check code for inverter 214
Figure 129: LabVIEW block diagram for interfacing with inverter 215
Figure 130: LabVIEW block diagram for interfacing with the temperature monitor 217
Figure 131: LabVIEW block diagram for interfacing with the logging mass balance 218
Figure 132: Constant compressor input frequency of 60 (Hz) 221
Figure 133: Compressor input power (kW) at constant frequency of 60 Hz 221
Figure 134: Liquid nitrogen mass flow rate (kg/s) 222
Figure 135: Average compressor input power (kW) at different driving frequencies 224
Figure 136: Average liquid nitrogen mass flow rate (kg/s) at different driving frequencies 224
Figure 137: Average cold head temperature (K) at different driving frequencies 225
Figure 138: Motor driving frequency vs. liquid nitrogen mass flow rate (kg/s) 228
Figure 139: Compressor motor power performance vs. liquid nitrogen mass flow rate (kg/s) 228
Figure 140: Corresponding compressor input power (kW) with respect to time (sec) 231
Figure 141: Liquid nitrogen mass flow rate (kg/s) with respect to time 231
Figure 142: Cumulative liquid nitrogen collected in Dewar (kg) with respect to time 232
Figure 143: Cold head temperature (K) with respect to time 232
Figure 144: Power input to compressor (kW) 235
Figure 145: Cold head temperature (K) 235
Figure 146: Liquid nitrogen mass flow rate (kg/s) with respect to time 236
Figure 147: Cumulative liquid nitrogen mass flow rate (kg/s) with respect to time 236
Figure 148: Compressor input power (kW) 237
Figure 149: Liquid nitrogen mass flow rate (kg/s) 238
Figure 150: Compressor input power (kW) with respect to time (sec) 240
Figure 151: Liquid nitrogen mass flow rate (kg/s) with respect to time (sec) 240
Figure 152: Cumulative liquid nitrogen mass in Dewar (kg) 241
Figure 153: Cold head temperature (K) with respect to time (sec) 241
Figure 154: Average compressor input power (W) at different driving frequency (Hz) 245
Figure 155: Cold head temperature (K) at various driving frequencies (Hz) 246
Figure 156: Average liquid nitrogen mass flow rate (kg/s) at various driving frequencies (Hz) 247
Figure 157: Compressor input power (W) 249
Figure 158: Cold head temperature (K) 250
Figure 159: Liquid nitrogen mass flow rate (kg/s) 251
Figure 160: Compressor input power (W) 252
Figure 161: Cold head temperature (K) 253
Figure 162: Liquid nitrogen mass flow rate (kg/s) 254
Figure 163: Compressor input power (W) 255
Figure 164: Cold head temperature (K) 256
Figure 165: Liquid nitrogen mass flow rate (kg/s) 257
Figure 166: Compressor input power (W) 258
Figure 167: Cold head temperature (K) for simulated and experimental work 259
Figure 168: Liquid nitrogen mass flow rate (kg/s) 260
Figure 169: Dewar vessel showing thermal stratification, taken from (Partridge, 2010) 261
Figure 170: CryoVent schematic showing a wind energy driven GM cryocooler system for production of liquid nitrogen 264
Figure 171: Average available power in wind (W) at different wind speeds (m/s) 265
Figure 172: Average wind turbine power (W) and average hydraulic motor power (W) at different wind speeds (m/s) 265

Figure 173: Average liquid nitrogen mass flow rate (kg/s) at different wind speeds (m/s).....266
Figure 174: Series of 4Hz wind speeds (m/s) data from SWMTF used for simulation for a period of 10 minutes 267
Figure 175: Liquid nitrogen mass flow rate (kg/s) during simulation 267
Figure 176: High pressure fluid in accumulator (m^3) with respect to time 270
Figure 177: State of charge (%) of high pressure fluid in accumulator.....270
Figure 178: High pressure fluid in accumulator (m^3) with respect to time 271
Figure 179: High pressure fluid in accumulator (m^3) with respect to time 272
Figure 180: State of charge (%) of high pressure fluid in accumulator.....272
Figure 181: High pressure fluid in accumulator (m^3) with respect to time 273
Figure 182: State of charge (%) of high pressure fluid in accumulator.....273

List of Appendix Figures

Figure C.1: Simulink model for a hydraulic wind turbine 308
Figure D.1: Simulink model for GM cryocooler unit 312
Figure F.1: Simulink model for Chapter 10 simulation 322
Figure G.1: Motor current (A) with time 323
Figure G.2: Motor oil temperature (^{0}C) during 60 Hz operation.....323
Figure G.3: Helium gas low side pressure (kPaG) with respect to time 324
Figure G.4: Helium high side pressure (kPaG) with respect to time.....324
Figure G.5: Helium gas discharge temperature (^{0}C) during 60 Hz operation 325
Figure G.6: Cooling water inlet temperature (^{0}C) during 60 Hz operation 325
Figure G.7: Cooling water outlet temperature (^{0}C) during 60 Hz operation.....326
Figure G.8: Cold head temperature (K) during 60 Hz operation 326
Figure H.1: Average helium gas discharge temperature (^{0}C) 327
Figure H.2: Average helium gas low and high pressure (kPaG) 327
Figure H.3: Average motor oil temperature (^{0}C) 328
Figure H.4: Average cooling water inlet and outlet temperatures (^{0}C) 328
Figure I.1: Cold head temperature (K) for Sinusoidal frequency input to compressor motor 329
Figure I.2: Helium low and high pressure (kPaG) 329
Figure I.3: Helium gas discharge temperature (^{0}C).....330
Figure I.4: Cooling water inlet and outlet temperature (^{0}C) 330
Figure I.5: Compressor motor oil temperature (^{0}C).....331
Figure I.6: Compressor motor current (Amp) 331
Figure J.1: Helium low and high pressure (kPaG) 332
Figure J.2: Helium discharge temperature (^{0}C) and compressor motor oil temperature (^{0}C)....332
Figure J.3: Compressor motor current (Amp) 333
Figure K.1: Motor current (Amp).....334
Figure K.2: Motor oil temperature (^{0}C).....334
Figure K.3: Helium gas discharge temperature (^{0}C) 335
Figure K.4: Helium gas low pressure (kPaG) 335
Figure K.5: Helium gas discharge pressure (kPaG) 336
Figure K.6: Cooling water inlet temperature (^{0}C) 336
Figure K.7: Cooling water outlet temperature 337
Figure L.1: Air compressor for delivery of pressurized air to nitrogen generator 338
Figure L.2: Dewar vessel front and rear views with GM cold head on its top and the fittings ...338
Figure L.3: Front view of helium compressor panel showing Hitachi VFD and helium high and low pressure lines 339
Figure L.4: Helium compressor and Dewar vessel 339

1 Introduction

1.1 Background

The concept investigated in this thesis has been dubbed, ‘Cryovent’. It concerns the production of cryogens (gas/air with a boiling point at atmospheric pressure below -150^{o}C), (Kanoglu, Dincer, & Rosen, 2007) using wind energy to attain means of bulk cooling for industrial/commercial purposes. The work anticipates demand for alternative methods of cooling for deep mines, involving a cryogen supply chain. As with most renewable energy technologies, the proposed concept is capital intensive, but it aims to produce its product with close to nil marginal cost. The most important distinction between the CryoVent concept and competing wind energy concepts is that here, the intended product is not electricity, but a cryogen. An important advantage of this approach is that wind energy in the form of liquid air can be stored. It may also be liberated through reboiling using ambient heat to produce electricity on demand by direct contact mixing of the liquefied gas with mine ventilation air. The intended end use of the product is provision of cold. In the case of this application it is entirely unnecessary to convert energy in any form to or from electricity, simplifying integration considerably, and this idea is clearly depicted in Figure 1. The gas liquefaction system shown could be any of the cryogenic cycles that will be discussed in the chapters that follow. For illustration purposes, a Linde-Hampson gas liquefaction system is shown in Figure 1.

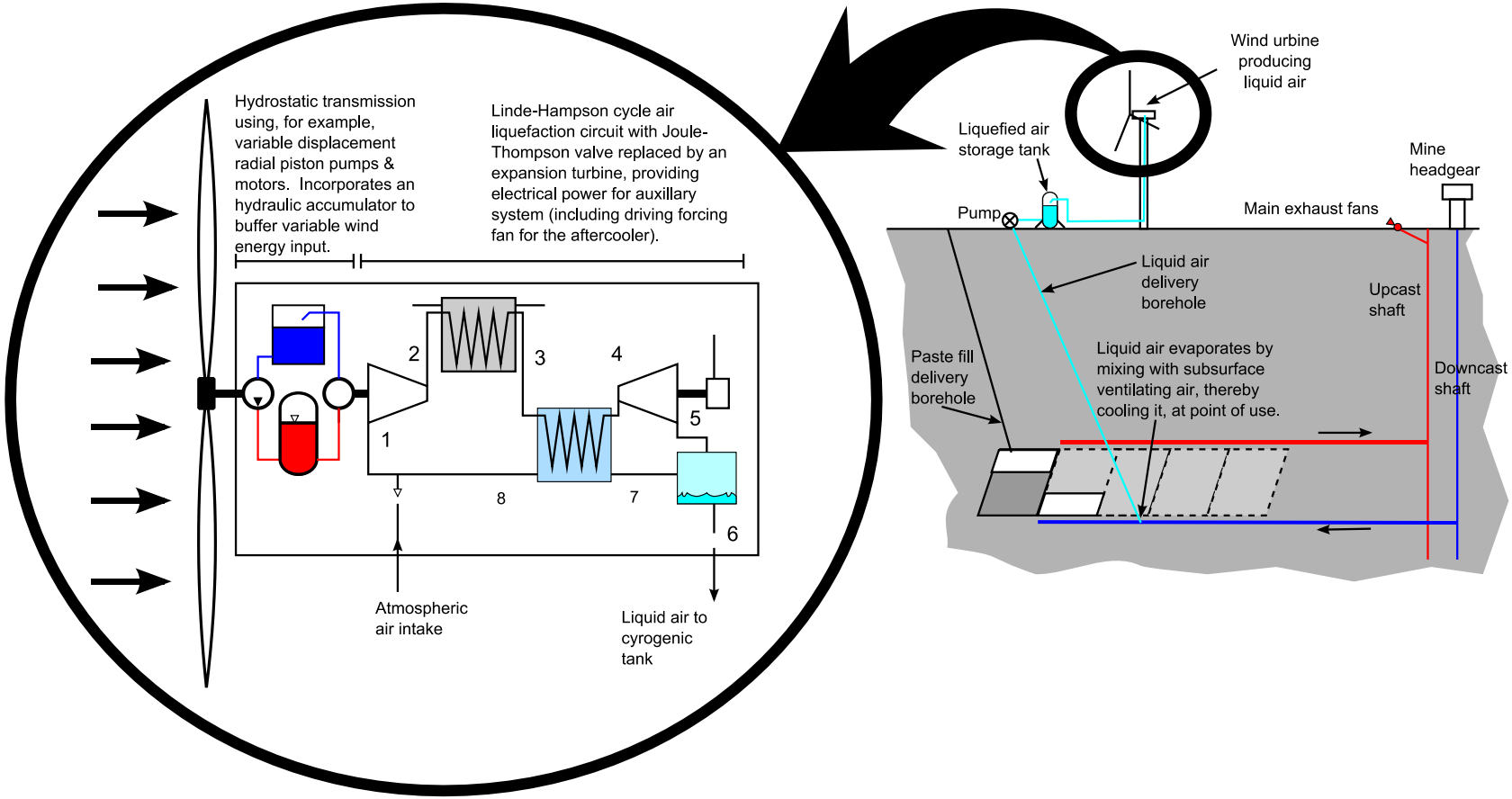

Figure 1: Schematic of the 'CryoVent' concept showing use of the stored cryogen product for deep mine cooling

Mine ventilation air is typically 30-40^{0}C in deep mines, and represents an abundant source of low grade heat to reboil cryogen thereby cooling the air. 1 kg of liquefied N_2 could provide 0.13 kWh of spot cooling in a mine heading or if supply is sustained at 1 kg/s then cooling power of 450 kW_r would result. If this cooling power had to be provided by conventional means, electrical power consumption of around 150 kW would be added to grid demand. Renewable production and on-demand consumption of the cryogen may thus be considered in terms of electric power and electricity consumption avoided.

Provision of cryogens offers advantages over conventional approaches to mine air refrigeration. Cryogens can be passed to the subsurface via a borehole (suitably lined) of a small diameter (as low as 0.1m), instead of passing additional mine air through a purposefully-excavated ventilation shaft that could be up to 5m in diameter. Capital costs associated with access openings to the subsurface would be significantly lowered. Liquefied air can be re-boiled at depth, simply through contact with the bulk ventilation air possibly in liquid-to-air plate-fin heat exchanger, thereby cooling the latter, which is not only desirable, but is the main objective.

The exhaustion of world class surface mineral ore bodies is driving the exploitation of deeper ore bodies using underground mining methods. Also, existing underground mines are extending workings deeper. Deeper mines mean hotter temperature since the temperature increases while descending underground from the surface. At specific depths, which vary from mine to mine depending on climate and geothermal regimes, the hotter working environment may become uncomfortable and unsafe (for workers). Furthermore, the rate at which the air temperature increases is greater with depth (Sheer, Burton, & Bluhm, 1984).

Thus at 3,000 metres depth, the temperature of air entering ore producing areas may be 20°C to 30°C higher than the surface air temperature, mostly due to adiabatic auto-compression

of air in the air shaft. The rate at which the temperature increases in the ground with greater depth is called the geothermal gradient and is due to geothermal flux and the radio-active decay of materials in the rocks underground. These factors, along with auto-compression of the air, which elevates temperatures by at most ~1°C/100 meters depth for adiabatic shafts, can cause air temperatures in work areas to reach 40°C at depths greater than 3,000 meters (McPherson, 2000). Heat from diesel equipment, virgin rock temperatures, and other sources contribute further to increasing the temperature of deep underground mines.

The current methods of cooling the air employ vapour compression refrigeration cycles, with large-scale cooling towers to eject condenser heat and bulk air cooling chambers (McPherson, 2000). The ratings of the largest plants used in mines that are 4000 meters deep can exceed 80MW_r (U.S. Patent No. 5251458, 1993). Refrigeration plants can also be installed in the sub-surface to simplify cooling distribution, but these operate with much lower coefficients of performance due to high condenser heat reject temperatures. The cumulative effect of these circumstances is a dramatic increase in energy consumption. This has motivated the investigation of an alternative means of providing cooling to deeper mines.

For Canadian mines, climatic variations and mining depths mean that load factors for refrigeration systems are currently around 25% but these load factors will approach unity with greater depths; cooling will need to be provided continuously. Capital costs of cooling plants (conventional or alternative) are currently the dominant factor but will become less important than the operating and energy input costs as load factors increase. Use of a renewable energy source to provide cooling as proposed with the concept herein will become increasingly attractive because the marginal energy input costs are close to zero from this source.

However renewable energy resources arise from geo-processes that are subject to natural variability and intermittency and so, the alternative cooling method must be able to store the coolth produced, while the renewable energy resource is 'active', for use at 'on-demand' times and rates. The locations where the renewable energy resources are most abundant may coincide with the locations of mineral deposits, but it must be assumed that, for the general case, they will not. Consequently, the alternative cooling method must allow for the transportation and distribution of the stored cooling from producing areas to consumer centres.

1.1.1 Integration of wind energy into energy systems

According to the Green Wind Energy Council, GWEC (2016), by end 2016, the total installed wind power was more than 82 GW in US, 11.9 GW in Canada, and 168 GW in China. Recently innovations in wind turbine design have concerned improvements in drive train layout, turbine blade design (including heating), and structural improvement to reduce the total mass and cost as well as improvements in the energy extraction efficiency and lifetime of the wind turbines. Due to its increasing technological maturity, and its cost effective nature, wind energy is already contributing significantly to the world energy market (Muyeen, 2012).

Wind power offers beneficial effects to power generation systems in that it reduces CO_2 and other emissions as it exploits one of the main renewable sources of energy and this has in some part driven this growth in adoption of wind energy. However developers of wind turbines have had to overcome some key technology challenges in order that wind turbines have gained the acceptance that they have. Chief amongst these are methods to reduce the impact of wind resource variability and intermittency.

Short term fluctuations in wind speed historically have translated to fluctuations in supply voltage, difficulties in synchronization of electricity produced with grid frequency and the

introduction of high frequency harmonics into the grid signal. Through various means, including improved control and the use of power electronics, such issues have now been overcome. Longer term fluctuations lead to questions related to security of power system operation. The predictability and high inter-temporal variations of wind power pose limitations that lead to problems which range from shorter term frequency deviations to longer term problems in balancing off electricity grid supply-demand systems. A series of new challenges and additional constraints arise for the operation of electricity grids with high degrees of penetration of wind turbines (Ibrahim, Ghandour, Dimitrova, Ilinca, & Perron, 2011). The integration of wind energy into electrical supply systems is therefore seen as challenging.

Electricity storage technology has had a significant role in permitting large contributions of wind derived electricity being admitted onto electrical supply grids. These have included compressed air energy storage systems (Safaei & Keith, 2014), pumped hydroelectric storage (Melikoglu, 2017), batteries (Hamzehlouia, Izadian, & Anwar, 2013), and high pressure hydraulic fluid energy storage (Diepeveen, 2013). These systems can store wind energy in the various forms and then convert these back to useful work and typically electricity. They integrate wind energy by storing it, and then coupling the stored energy resource to more conventional technologies to deliver the energy, acceptable to those charged with grid management.

Virtually all of these wind energy integration problems have their roots in a preoccupation of using wind energy to produce electricity. The problem can be relieved quickly, if an alternative mindset is adopted whereby wind energy is used to produce an alternative form of energy such as a cryogen.

1.1.2 Integrated energy storage and generation

Various attempts have been made to develop methods to overcome the challenges associated with the wind energy integration problems (Ibrahim et al., 2011). One such way showed that wind energy can be transformed into compressed air and stored in a tank (for a small-scale), in underground abandoned mines like paste-fills or in salt caverns (for large-scale purposes), and also in above ground pressure vessels (Safaei & Keith, 2014). The compressed air can then be used on demand but the underground storage or pressure vessel capacity can be affected by geological constraints and costly engineering and materials (Ameel et al., 2013). Electricity from wind energy can also be stored using batteries but this method remains expensive. The total installed cost for storing wind energy using Compressed Air Energy Storage (CAES) is around US \$125 kW^{-1} h^{-1} for an 8 hour storage duration and US \$450 kW^{-1} h^{-1} for lead acid battery for a 4 hour storage duration (Rastler, as cited in Shaw, Cai, & Liu, 2012).

A third way is through accumulating high pressure hydraulic fluid. The application of fluid power transmissions such as hydrostatic transmissions is gaining interest as a means to eliminate/minimize the effect of wind resource fluctuations and to minimize integration problems (Diepeveen, 2004). This technology, mature in its automotive applications, when applied to wind energy brings reliable components and eliminates the need for a frequency converter and reduces nacelle weight (Diepeveen, 2004). If the hydrostatic transmission is also open loop (unlike an automotive transmission) it could also serve as a temporary storage of wind energy; for short periods stored pressurized fluid could supply power to the load even during times of no/minimum wind. In the concept of the current concept, an additional benefit is that the hydraulic circuit can be used for control.

1.1.3 Availability and cost of wind energy

Installation and power generation costs can vary appreciably around the world depending on the regulatory regime, installation site, and local costs for materials and services, as is illustrated in Figure 2. According to the International Energy Agency (2013), capital cost reductions in land-based wind turbine developments will be 25% as the sector matures and scales to 2050. The corresponding estimate for offshore installation is 45%.

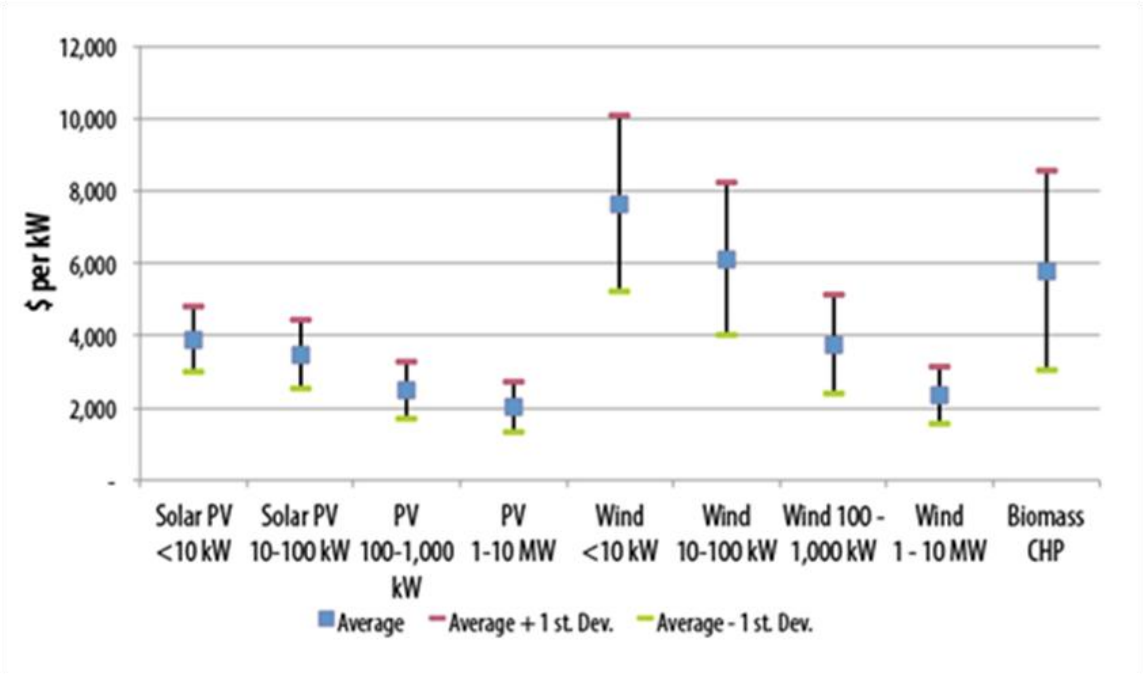

Figure 2: Installed costs for electricity generating technologies taken from NREL (2016)

The CryoVent project does not make use of the gearbox and generator in the wind turbine nacelle which contributes to the major costs of a wind turbine. However, these are replaced by the open loop hydrostatic transmission. As the capital costs for wind turbines will be lowered by 2050, the CryoVent project is intended to benefit from the development cost erosion from mainstream wind.

1.1.4 Illustrative case study: Large scale CryoVent production for mine cooling

To illustrate the potential scale of the problem and the credibility of the proposed concept, the following case is considered. The extension of a surface mine to subsurface operation in Rancagua, Chile is expected to start in the year 2017-early 2018 with expected copper ore production of ~130.000 tonnes per day and fresh air flow requirements of 4.62 tonnes per second for ventilation. This will be one of the largest scale underground mining operations in the world - ever. Three horizontal adits each of area 121 m^2 (11m x 11m) and 2,200 meters long will be required to admit the ventilation air for the mine and these alone are expected to have a total capital cost of ~US$214 million (Acuña & Soto, 2014).

Ventilation *and* cooling could be provided with alternate concepts involving air liquefaction. If adopted, for a volumetric air flow requirement of 4000 m^3/s for ventilation, assuming the air intake temperature of the mine cycle to be 25°C and the outlet temperature to be 30°C, the cooling power (for the mine) provided by this volumetric flow rate is 23,405kW. The same cooling power could be provided by liquid air with a mass flow rate of 196 tonnes/hour or a volumetric flow rate of 0.062 m^3/s, 5 orders of magnitude smaller than the atmospheric air volumetric flow rate.

Later on in this thesis, Vestas V52 wind turbines will be considered in a CryoVent context. It has a Vestas V52 wind turbine with a blade length of 52m, installed capacity of 850 kW (relatively small these days), and capacity factor of 0.25, would produce enough electrical power to produce 6205 tonnes/annum of liquid air. The number of V52s works out at around 276. Although this is a large number, it is not so large that it is in-credible. For the purposes of illustration only, V52s were supposed to produce electricity, used in a conventional industrial scale cryogenic plant. The scale of the required cryogenic plant is actually rather small, being

around 8 times smaller than the No. 4 LOX plant at Vale's Copper Cliff smelter, which is also referred to later in this thesis. CryoVent project can be cost effective and technically feasible if the variability and intermittency aspects of the wind energy are dealt with.

1.2 Wind energy driven cryocooler concept

This section articulates precisely what is meant by the CryoVent concept and it is provided so that the reader may develop an appreciation for the scope of work covered by this thesis. A wind energy driven cryocooler concept makes use of a variable speed horizontal axis wind turbine coupled to an open loop hydrostatic transmission system which powers a gas liquefaction system to produce cryogens as shown in Figure 3. The major component to store the liquefied gases is the Dewar vessel.

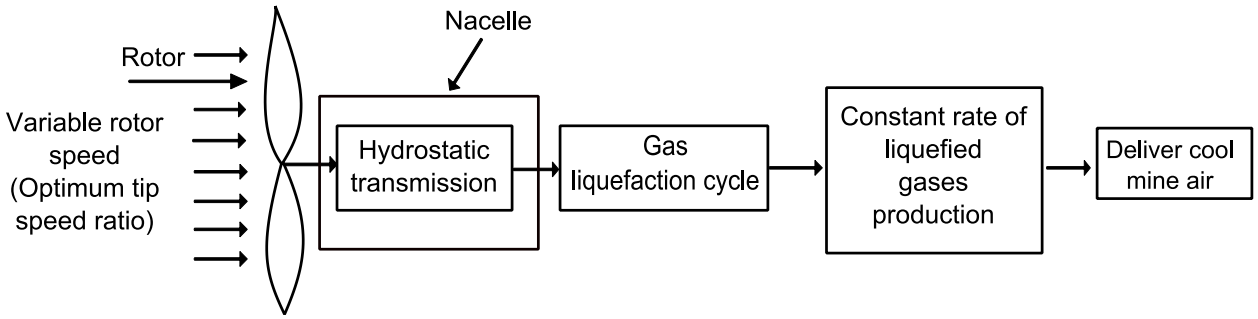

Figure 3: Block diagram of the wind energy driven gas liquefaction system

The gas liquefaction cycle to be adopted could be any of the cycles and this can either be placed in the wind turbine nacelle or on the ground. However, this work suggests placing the gas liquefaction system on the ground to lower the weight on nacelle. The CryoVent project could also adopt any scale of existing wind turbine technologies. CryoVent assumes that technology to reboil / evaporate cryogen in the sub-surface will be provided by others.

1.2.1 System components

The system components required to demonstrate the concept in this work are a wind turbine, a hydraulic pump, a hydraulic motor, check valve, pressure relief valve, hydraulic hoses, hydraulic accumulator and a cryocooler unit that includes a Dewar vessel. A Gifford McMahon (GM) cryocooler was selected because it was available in a format safe to use at laboratory scale, and its configuration is flexible. It is not particularly efficient in converting input work into stored cryogen, but is sufficiently efficient to produce significant (statistical sense) volumes of cryogen during experiments. This cryocooler can be configured to liquefy a variety of liquid gases. In this work where liquid nitrogen is used for safety reasons comprises of an air compressor with filtration system, a refrigeration compressor, flexible insulated hoses, a helium cryocooler system that produces the cold temperature, and an insulated storage unit for liquid gas collection and storage (the Dewar).

1.2.2 Process flow diagram

Figure 4 illustrates the process flow diagram for cryogen production, which is a wind energy driven cryocooler concept with a GM cryocooler. Given that most other cryogenic cycles involve the input of work to a compressor, the diagram readily generalizes. Also shown in Figure 4 is an open loop hydrostatic transmission that is expected to buffer the intermittency and variability of the rotational speed and torque developed by the wind turbine, if only in the short term. The hydrostatic transmission system is coupled to a helium compressor, which delivers helium to a so-called cold head (the GM cryocooler is explained in detail in Section 5.6) that gets very cold (-200^{o}C) as the gas expands according to the Joule-Thomson (JT) effect. Shown on the right side of the diagram, gaseous nitrogen then comes into contact with the outside of the cold head and condenses to liquid nitrogen. For the experimental purposes, however, an electric motor

with a variable frequency drive is used to drive the GM cryocooler unit. The full experimental set up used for carrying out experiments in the laboratory is presented in Section 8.1.1.

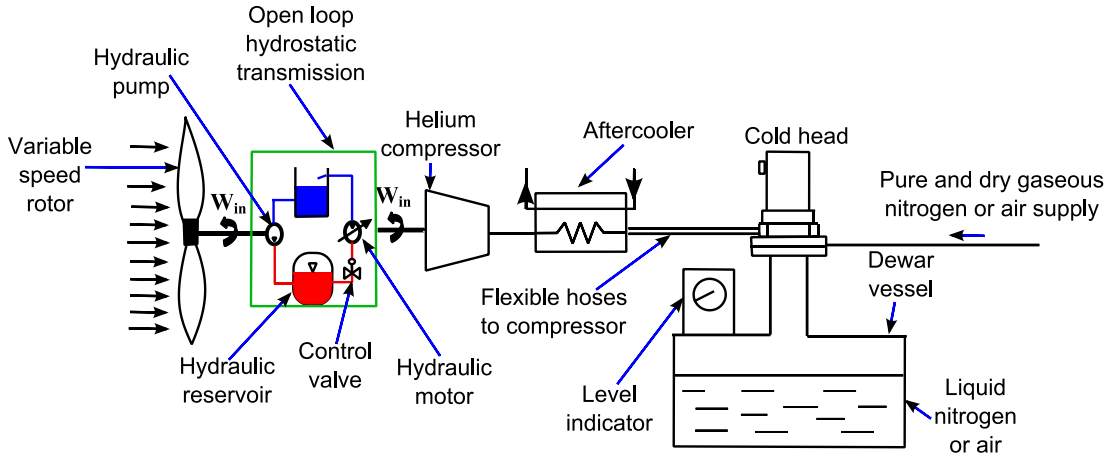

Figure 4: Schematic of the CryoVent concept to produce cryogens

The open-loop hydrostatic transmission system consists of a positive displacement hydraulic pump, a hydraulic motor and the required control valves, pipes, pressurized (accumulator) and non-pressurized reservoirs and fittings. The motor is driven by pressurized fluid drawn from the accumulator reservoir, which is replenished by the pump. For a system that accommodates variable work input, i.e. cannot rely on a constant input of power, an open-loop hydrostatic transmission system is used to store the pressurized fluid in the accumulator/reservoir, one measure to overcome some of the variability in input work (Esposito, 2009). The hydrostatic transmission can also be used to regulate the wind rotor speeds so that the rotor blade tip speed ratio is adjusted with varying wind speeds to maximise wind to rotor work efficiency. The fluid coupling of the wind rotor to the compressor is a form of torque converter equipped with energy storage. A torque converter is a fluid coupling that transfers torque from a prime mover to a load, in this case the load is the compressor of the cryogenic production circuit. The governing equations for both the open and closed loop hydrostatic transmission are presented later in Chapter 6.

1.3 Control systems

The control systems required for this concept are the wind turbine rotor speed control, pressure control of the hydrostatic transmission system, and the hydraulic motor speed control. The wind turbine rotor speed control is performed by controlling the hydraulic pump and/or hydraulic motor displacement. For the hydraulic motor speed control, a proportional integral derivative (PID) control is applied that controls the system pressure which in turn controls the speed of the hydraulic motor. The presence of the hydraulic accumulator in the system ensures that the system operates during a short periods of calm wind speed and so the system does not face problems restarting following calm periods. The energy stored in the hydraulic accumulator also helps in the smooth operation of the system and helps keeping the GM cryocooler running during low and no wind conditions. The check valve and the pressure relief valves in the hydrostatic transmission system regulate the flow and pressure in the system respectively. When the pressure and flow in the hydraulic system are regulated with respect to the wind conditions, the hydraulic motor speed is controlled. The control systems are explained in detail in Section 6.6.

1.4 Applications

1.4.1 Application to cryogen production

The use of wind energy to drive a hydrostatic transmission can have application in numerous sectors. An open loop hydrostatic transmission and the control system are required to buffer the transients in the wind energy conversion process, i.e to ensure the system operates smoothly during high and low winds. Such a system can then drive any other power equipment that can transfer power not only to the GM cyrocooler unit but also to a gas compression system, gas

liquefaction systems based on alternative cycles or any type of system that needs mechanical power to operate. In this work, the system is used for cryogen production. The amount of input energy required to produce 1 kg of liquid air is ~0.3 kWh (Castle, 2002), making it expensive if electricity has to be paid for. Although liquefying air is traditionally costly, the initial instalment costs of a Cryovent wind turbine would be offset with the major benefit of nil marginal cost of input work. In design of such systems, a key issue is how much cryogen is produced given the variable and intermittent work produced by the wind rotor.

1.4.2 Application to utility scale energy storage

Once the cryogens or liquefied gases are produced safely, these can be stored in low pressure insulated vessels that can maintain the low temperatures at which liquid nitrogen, liquid oxygen or other liquids exist. The insulation could take the form of a vacuum which acts as an excellent insulator because it does not allow the pressurized liquid to boil off when it comes in contact with the warm room temperature (Highview Power Storage, 2014). Liquefied air can store wind energy compactly. One kilogram of liquefied air at atmospheric pressure stores around 440 kJ of cooling (at ~ -200°C) that may be recovered through reboiling using the heat within ambient (mine ventilation) air (at ~30°C) and would otherwise have to be provided by a vapour compression refrigeration plant consuming electricity. One cubic meter of liquefied air effectively stores 400MJ (111 kWh) of cooling for the same conditions.

Vapour vent lines are required in the Dewar vessel to allow the vapour (that form as a result of heat in leak) to escape and prevent over pressurisation of the vessel. According to Huston (as cited in Amos, 1998), liquid nitrogen heat shields are also used in some tankers to cool the outer wall of the large scale Dewar vessel to further reduce boil-off during transportation (Huston, 1984). If the cryogens are produced offshore and need to be stored

onshore for later electricity generation, they can be delivered onshore with no extra cost other than the pumping costs. Cooling loss with cryogens stored in a Dewar vessel is principally by heat dissipation, which is ~1%/day (Y. Li, Chen, Zhang, Tan, & Ding, 2010). Dewar vessel schematics that are used for cryogens storage are presented later in thesis.

1.4.3 Application to utility scale energy transportation

An energy vector is not a source of energy but a means of transporting energy from one time or one place to another (Orecchini, 2006) and (Krajači et al., 2008). Cryogens become an energy vector like a fuel that can be used to transport energy from one place to another relatively easily. As cryogens can be used to store energy and as they can be transported in pipelines and tankers from one place to another, they can be considered energy vectors. This endows cryogens with additional economic value in comparison to some forms of energy such as electricity. Electricity itself must be consumed immediately when it has been produced and so is not in itself an energy vector. Essentially, this is the key integration problem with the wind generated electricity.

Cryogens can be transported in tank trucks, railcars, barges or sea-going vessels which have capacities of carrying several kilograms to millions of kilograms of liquefied gases safely (Amos, 1998). Another idea for transporting of liquefied gases could be through an insulated pipeline which would also include a super-conducting wire. The liquefied gas can act as a refrigerant for the superconductor and long distance transportation of electricity would be possible without having the high current losses of conventional power lines. The problem associated with this idea would only be the requirement of specialized insulation and losses from pumping and re-cooling the cryogens along the way (Oy; C. Timmerhaus & Flynn as cited in Amos, 1998). The costs for transporting cryogens would be the cost of tank trailer or railcar of

the pipelines. The important factors that impact the cost of transportation are the distance and the quantity of cryogens to be delivered. For higher production rates and short distances, pipeline delivery might be very inexpensive.

Therefore, CryoVent will facilitate cryogens becoming a new energy vector because wind energy could be transformed to cryogens, stored in Dewar vessels, be easily transported to the application areas, and then used on demand with a governed Rankine cycle plant which is very straightforward to integrate.

1.5 CryoVent concept initial steps towards cost estimation

The proposed Cryovent concept for delivering cool mine air is estimated to be ~18.27% efficient with total capital cost of ~$2700/kW. This thesis was not concerned about the efficiency of such a concept as the input energy required to drive the system is a renewable source, the cost of which is close to zero. The efficiencies and the cost calculations are shown in Figure 5. The annuitized cost for a 20 MW_r CryoVent system calculated assuming 15 years of life-time, and an interest rate of 10%, would be ~$7,900k/year with zero input energy costs. If the input energy is provided by an electric motor to drive the cryocooler compressor instead, this system would cost $6,958k/year with $2,499k/year input energy costs (Kunwar & Millar, 2014).

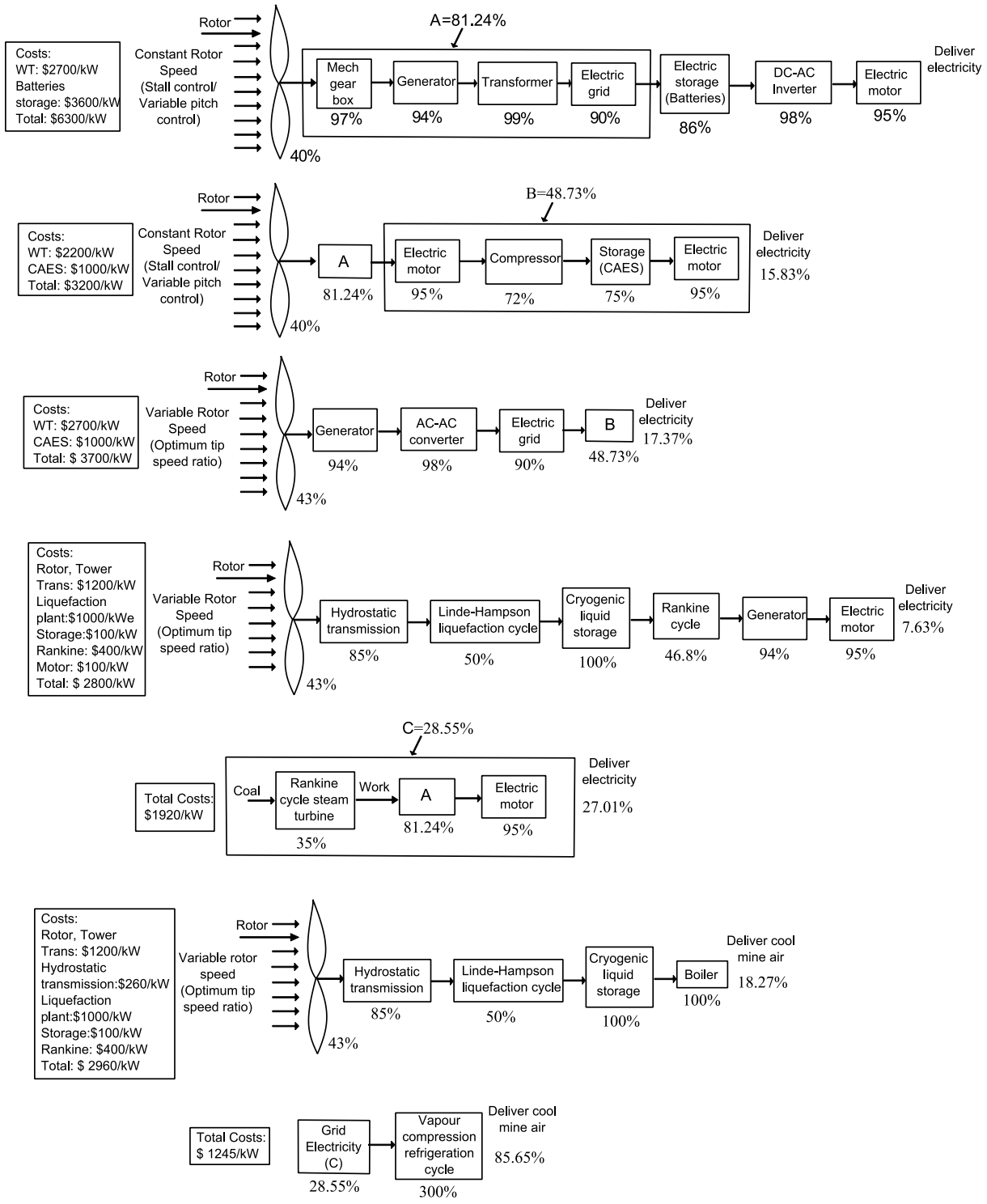

Figure 5: Schematic showing various energy generating systems using wind power with their respective costs and overall efficiencies. WT=Wind Turbine, CAES= Compressed Air Energy System (reproduced from Kunwar & Millar (2014)*)*

The conventional vapor compression refrigeration plant run by the electric grid would be ~85.8% efficient with ~$900/kW total capital cost providing the same amount of cooling as Cryovent but the annuitized cost for this system would be ~$6,963k/year with an annual input energy cost of ~$3,796k/year (Kunwar & Millar, 2014). The vapor compression refrigeration plant costs are calculated assuming 20$MW_{r,}$ with Coefficient of Performance (COP) of 3, interest rate of 10%, 15 years life time, and the installation cost of $65/MWh. The gas liquefaction system considered was a Linde Hampson gas liquefaction system. Detailed assumptions and references used for the cost and estimations are presented in a paper, which is also included in Appendix A for reader's convenience.

1.6 Key research questions

The proposed concept abbreviated 'Cryovent', will use wind energy to drive a gas liquefaction system for the production of cryogens without the intermediate production of electricity and focus on the cooling of deep underground mines but secure in the knowledge there are a multitude of additional uses and applications. The reason for this is that the form in which this energy is to be consumed is close to the form in which the energy is produced – coolth. McPherson, (2000) states that the term "coolth" is a decidedly unscientific but descriptive word sometimes used in association with chilled fluid distribution systems (McPherson, 2000). This definition and standpoint is adopted here for the cold that is produced by a CryoVent wind turbine and storage facility.

This CryoVent concept essentially involves the integration of well established technologies, so if wind energy, with its variable and intermittent characteristics, is to be the primary energy input, the key research question is not whether the well established wind rotor

system can or cannot be coupled to the well established gas liquefaction unit. The answer to this question is undoubtedly it can.

Instead the research question is:

> Can cryogens be produced continuously given that the input work is intermittent and variable?

Wind industry standard practice is to base wind resource assessment work on measured time series with sample intervals of 10 minutes to 1 hour which are probably adequate for techno-economic assessments. If the standard deviation of wind speed is logged simultaneously with the wind speed averages in such observations, they probably also provide a sufficient basis for the characterisation of turbulence intensity – which is important in selecting a wind turbine model of an appropriate International Electro-technical Commission (IEC) wind class. However, for the purposes of this work such data sources are inadequate to properly characterise the intermittency and variability that the wind to cryogen conversion concept aims to overcome. In order to develop models, and be able to apply them to make performance predictions at different production scales, and over very short term (order of seconds) time scales to very long time scales (inter-annual), techniques that characterise the temporal behavior of wind speeds have had to be investigated and improved.

The second key research question for this work therefore is:

> Whether or not the wind speed time series data be reliably synthesised for appropriate time scales for input to simulation work.

1.7 Hypotheses of the thesis

1.7.1 Variability of cryogen production

Cryogen production systems at all scales must remove substantial amounts of heat in the physical (metal) fabric of the facilities to get them cold, and this takes time. Once they are cold, insulation methods can generally keep the cold in for prolonged periods. There is thus appreciable thermal inertia in cryogenic production systems. A principal hypothesis of the thesis is thus that the thermal inertia should keep cryogen production relatively steady in the face of variable work input.

The thesis develops a model of cryogen production so that predictions of the performance, measured by cryogen production rate, can be made for systems of varying scale. The accuracy and reliability of such predictions will be tested by measurement of the cryogen production rate when the input work to a liquefaction system is deliberately varied and rendered intermittent. The CryoVent wind to cryogen concept uses a short-term mechanical energy storage system, the open-loop hydrostatic transmission, to minimize the potential influence of short term wind energy fluctuations and to enhance the stability of the rate of cryogen production.

1.7.2 Multifractal wind speed time series

Research investigations spanning fractal analysis, spectral analysis, geostatistical analysis have revealed complementarily as well as similarity in approaches to characterising wind speed variability and intermittency. A synthesis of these techniques has led to the development of novel methodology. Consequently the secondary hypothesis set out for this work is that the self-similarity behaviour, variography and frequency domain modelling of wind speed can reliably

produce wind speed time series taken as input to process simulations driven by wind energy. An algorithm to synthesise high frequency (1 Hz or less) wind speed time series data, using time series of hourly or 10 minute wind speed averages, while respecting seasonal and inter-annual wind speed trends will be presented in this thesis. The algorithm can be tested with wind speed time series data logged at various frequencies the highest of which is 4 Hz.

1.8 Thesis objectives

The major objectives of this research work are to:

1. develop a dynamic wind to cryogen simulation model for use in engineering analysis and design of CryoVent systems
2. develop procedure to characterise wind speed time series for simulations
3. perform practical experiments to investigate likely effect of wind variability on cryogen production rate
4. use experiments to verify the simulation model
5. determine if the variability and intermittency of the wind energy can be buffered with the help of a hydrostatic transmission
6. establish whether relatively continuous cryogen production using wind energy input work can be sustained in the face of defined levels of intermittency and variability
7. apply the simulation model to larger scale systems and real wind variability as input to techno-economic studies to appraise the impact of CryoVent wind to cryogen in various applications, but principally, deep mine cooling.

1.9 Thesis outline

The thesis is organised as follows. The introduction, background and purpose of carrying out this research have been presented in Chapter 1. This chapter also explained the reason behind introducing the fluid power technology to couple with the wind energy conversion system, the probable application of the work, and also a brief introduction of the proposed concept.

CryoVent relies on the incumbent paradigm of wind energy capture using 3 bladed horizontal axis wind turbines (HAWT) and so Chapter 2 reviews and summarises the state-of-the-art and latest developments in this technology for each component.

The statistical analysis of wind climate has been presented in Chapter 3. This chapter details in the factors affecting the wind energy that include spatial and temporal factors, and the common statistical measures used in wind speed measurement.

Chapter 4 presents the time series analysis of the wind climate. This chapter starts with the basic definitions of the terminologies that are normally used in the wind speed time series data analysis. The frequency domain analysis and multifractal analysis are reviewed and performed for reader's understanding. Some of the initial works necessary for the development of a new algorithm for the synthesis of wind speed time series is presented. High sampling frequency time series can then be synthesised using available low sampling frequency time series.

Chapter 5 presents a thorough literature review on the gas liquefaction systems including vapour compression refrigeration, gas liquefaction systems and some cryocoolers that can be used either in refrigeration systems or in liquefaction of gases.

The prior works reported by various authors on using fluid power technology for wind turbines are reviewed in Chapter 6. This chapter also details closed and open loop hydrostatic transmission systems and the system components, the control system involved, and dynamic modeling and simulation of both of the systems.

Chapter 7 presents the complete dynamic simulation of a wind energy driven Gifford McMahon (GM) cryocooler system. This chapter also illustrates in detail the geometry, numerical procedures and algorithms, and test scenarios considered for the simulation. The thermo-mechanical process for the Dewar storage vessel is also presented in this chapter. Results obtained from the simulations performed are presented.

The practical experimental verification of the predictions made in the simulations carried out in Chapter 7 is set out in Chapter 8. The details of the experimental work performed including the description of the gas liquefaction unit and its system components, development of the data acquisition system, tests carried out and the results obtained are also presented in this Chapter.

Chapter 9 presents a detailed statistical and time series analysis to compare the major results obtained from the simulation and experimental works. Chapter 10 contains the simulations performed for 5MW rated wind driven liquid nitrogen production system. The MATLAB/Simulink model is tested against different series of wind speed to determine expected system performance. The results obtained are presented in this Chapter. The MATLAB/Simulink script and model along with the detailed parameter lists for all the simulations are provided in the Appendices.

The principal conclusions, contributions, and future works are presented in Chapter 11. Chapter 12 contains references to all literature cited in the work. The thesis outline is also presented as thesis roadmap as shown in Figure 6.

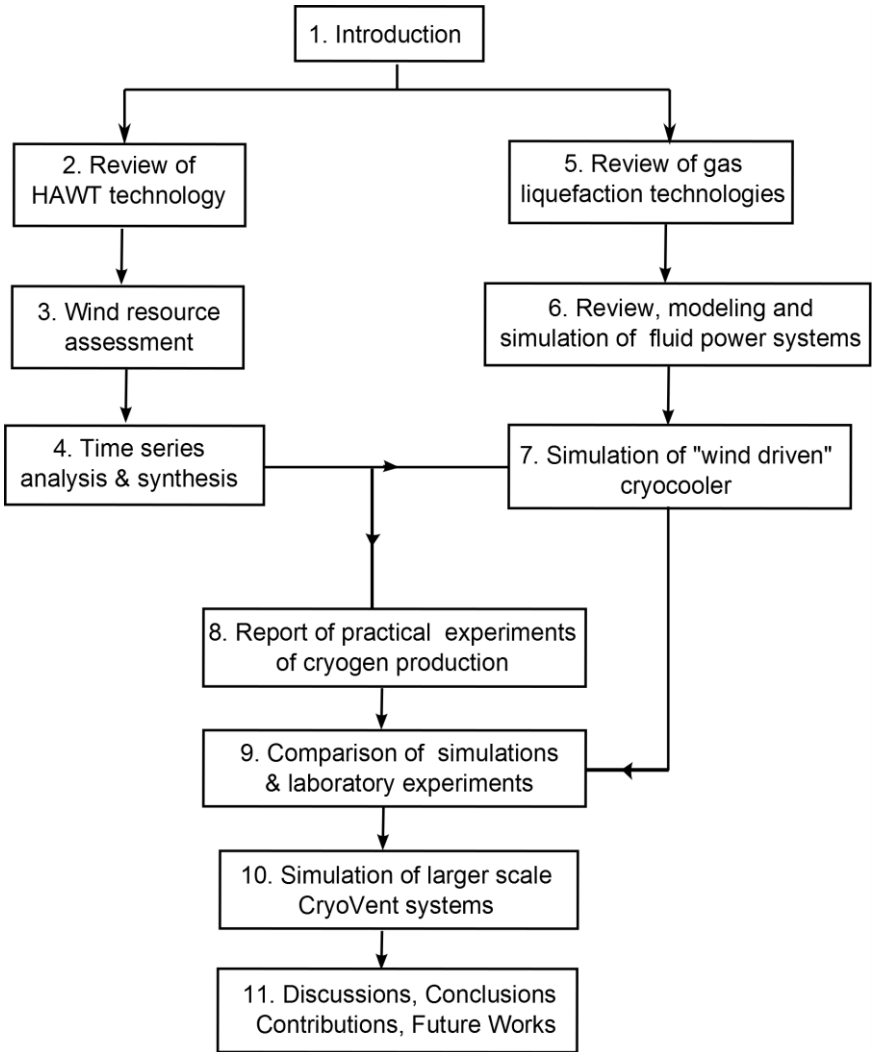

Figure 6: Thesis roadmap

2 Overview of wind turbines

2.1 Introduction

Wind energy is a potent source of renewable energy and it is now accepted as common place that wind turbines produce electrical energy economically and reliably. Wind power is becoming an alternative to fossil fuels and its use contributes to a reduction of green house gas (GHG) emissions in the atmosphere. Although it is an efficient and clean source of energy, harvesting its full potential actually remains an ongoing challenge in the renewable energy sector due to wind intermittency, variability and unpredictability. To illustrate the challenge, Figure 7 shows wind speed measured over 10 hour period, to produce a time series of 1 second averages showing wind speed variability. Studies are therefore being carried out to determine the best way to capture wind power and store it for future use.

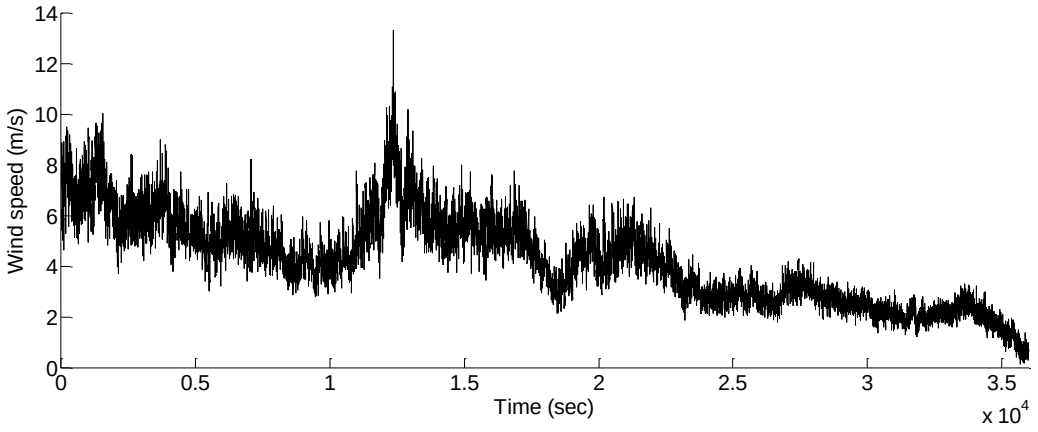

Figure 7: 1 second average wind speed data SWMTF, Exeter, UK

For millennia, wind energy was used specifically for milling grain, pumping water, and other mechanical applications such as grinding spices, dyes and paint stuffs and for making paper. More recently, interest in wind energy has undergone resurgence because the

technology has evolved to produce a pollution free means of generating electricity. Generation of electricity from the wind turbines started at the end of the 19th century. But the technology became mature enough only since the 1980s to enable large-scale industries to evolve, centered on the manufacture of large turbines for electricity production.

Wind turbines can broadly be classified into two groups, horizontal axis wind turbines, HAWT and vertical axis wind turbines, VAWT (Manwell, McGowan, & Rogers, 2010):. Over time, HAWTs have gained more interest, due to superior efficiency, reliability, access to resource so that they have become predominant. For electricity generation, 3 bladed systems prevail that do not suffer the extremes of loading that blades on 2 bladed turbine rotors experience when one of their blades passes in front of the wind turbine tower, despite having higher fundamental wind energy to rotor work efficiency. For some mechanical applications of wind turbines, for example water pumping it is the higher torque that is available from the wind rotor at low wind speeds that is more important and hence these turbines have large numbers of blades and high rotor solidity. While these units may be more suited to driving mechanical compressors, as required by CryoVent, the prominence of 3 bladed HAWT has led to significant erosion of their capital costs which is the dominant factor for consideration in this work. As HAWTs are so far ahead of other concepts commercially that it is the leading wind energy capture concept, that other paradigms will find it hard, if not impossible, to compete.

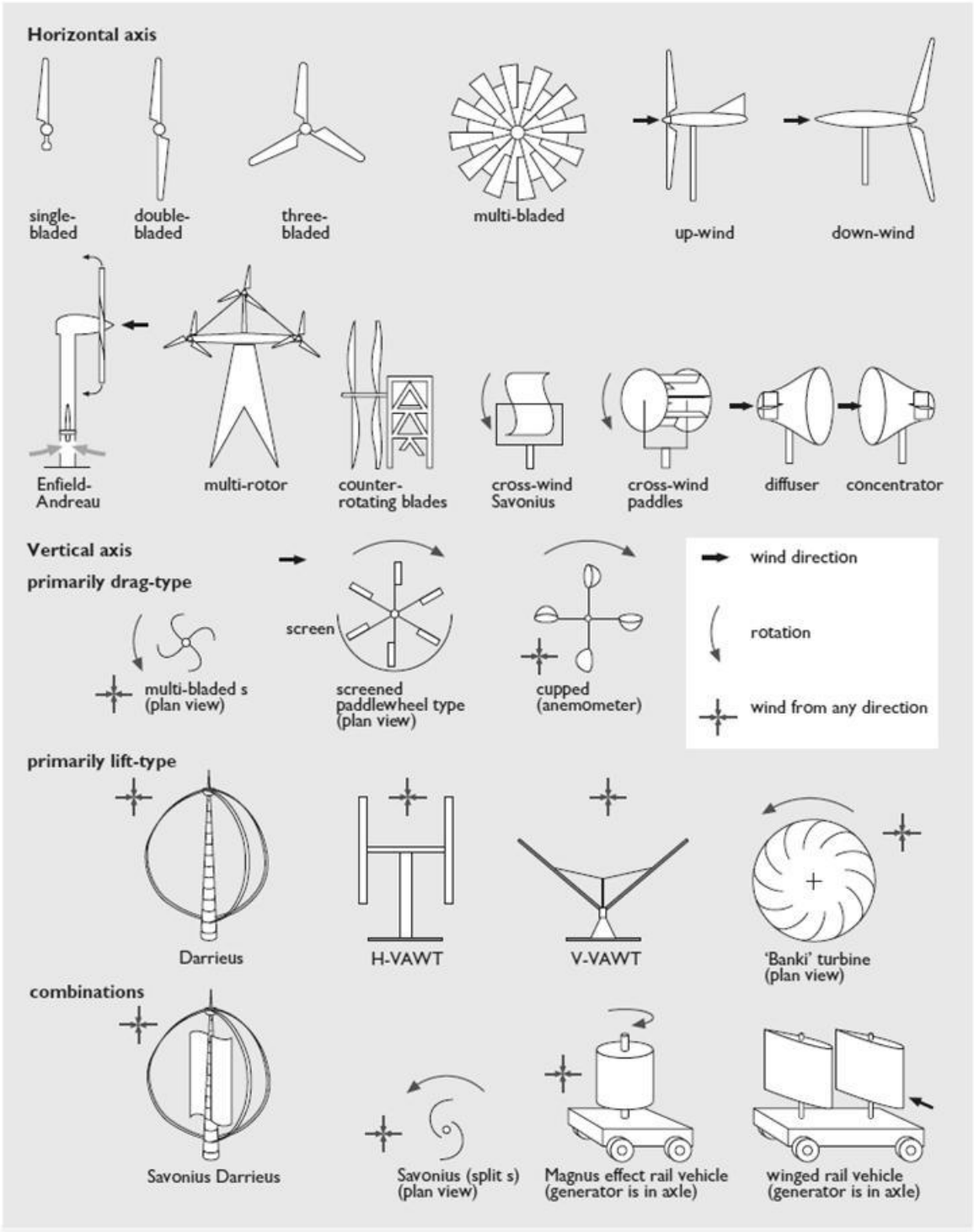

Figure 8: Different types of wind turbines for wind energy conversion (Taylor, 2004)

Figure 8 provides a summary of various wind turbine types and it also shows how they react to the wind direction. HAWTs could be single-bladed, double-bladed, or multi-bladed. These turbines can also be multi-rotor with more than one rotor in a single wind turbine system. Similarly the direction of rotor blades with wind blowing over them can be clockwise or anti-clockwise as is shown in

Figure 8. Different types of vertical axis wind turbines (VAWTs) are also presented in the same figure. However, only HAWTs are considered in this work.

2.2 Drag and lift on a blade element

A detailed diagram of the tip speed ratio, angular velocity and torque produced due to incident undisturbed wind energy is presented in Figure 10. The wind turbine blade is in motion and the direction from which the blade 'sees' the wind is the wind relative velocity W, which is the resultant of the tangential velocity u, at that position on the blade and the wind velocity, V_1 at the rotor. The wind velocity V_1 is the undisturbed velocity upstream of the wind, $V_{0,}$ reduced by a factor that slows down the wind due to the extracted power. The factor that is responsible for slowing down the wind is called the axial interference factor and is denoted by a.

ϕ is the relative wind angle that relative wind makes with the blade (at a particular point with local radius r along the blade) and is measured from the plane of rotation. Therefore the blade pitch angle β is the difference between the relative wind angle, ϕ and the angle of attack, α.

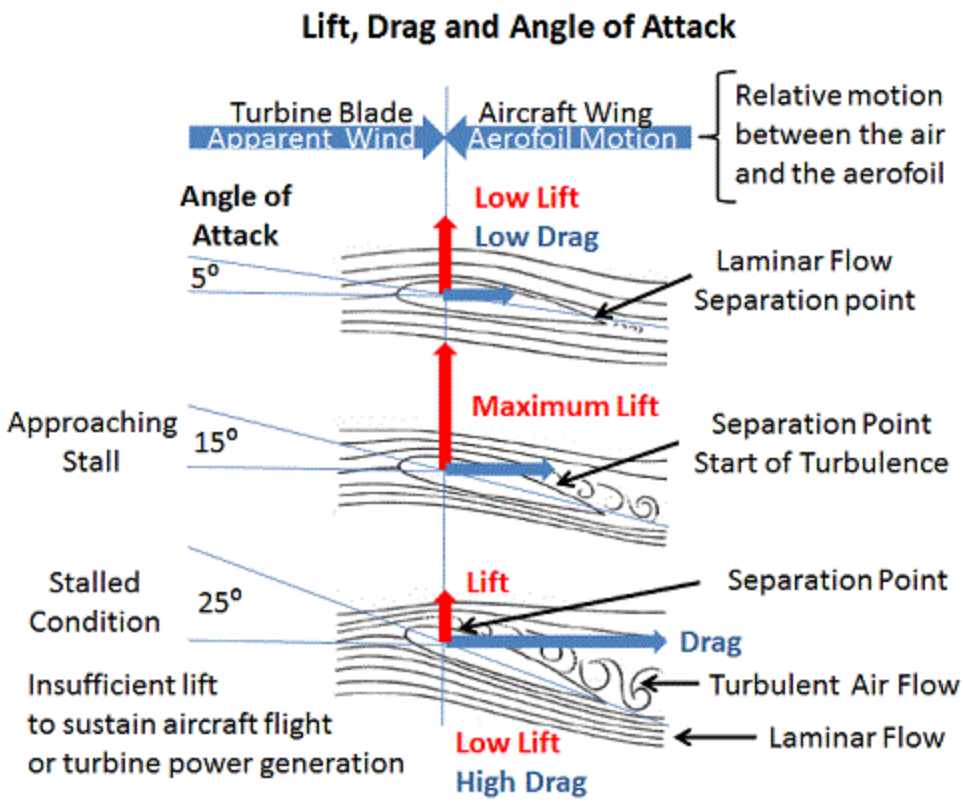

Figure 9: Schematic for lift and drag on airfoil (Woodbank Communications Ltd, 2005)

The lift and drag forces are dependent on some parameters, such as the shape of the blade, the surface area, the wind speed and the angle of attack. A detailed schematic of how lift and drag are created on an airfoil is depicted in Figure 9. The angle between the direction of the relative wind and the chord line of the blade is the angle of attack. The airflow over the aerofoil is smooth and laminar with some turbulence around the edge of the aerofoil when at very low angles of attack. This point where the laminar flow stops and turbulence starts is the separation point. The area of the aerofoil facing directly into the wind increases with increase in angle of attack. As a result, lift increases but the separation point of laminar flow of the air above the aerofoil also moves towards the leading edge. This increase in turbulent flow above the aerofoil results in increase in the drag. Generally maximum lift occurs at an angle of attack ~15 degrees

as shown in Figure 9. The turbulence increases above 15 degrees which causes the deterioration of the lift force and increases the drag at the same time that results in a stall (Woodbank Communications Ltd, 2005).

The lift force is the component which is perpendicular to the relative wind. The drag force is the component that is parallel to the direction of the air stream.

$$\beta = \phi - \alpha \tag{1}$$

The net driving force, in the plane of motion at radius, r,

$$F = L\sin\phi - D\cos\phi \tag{2}$$

where L is the lift force and D is the drag force (N).

Therefore, the torque is

$$T = (L\sin\phi - D\cos\phi) * r \tag{3}$$

The lift force L and the drag force D are given as (Taylor, 2004)

$$L = 0.5C_L\rho V^2 A_b \tag{4}$$

$$D = 0.5C_D\rho V^2 A_b \tag{5}$$

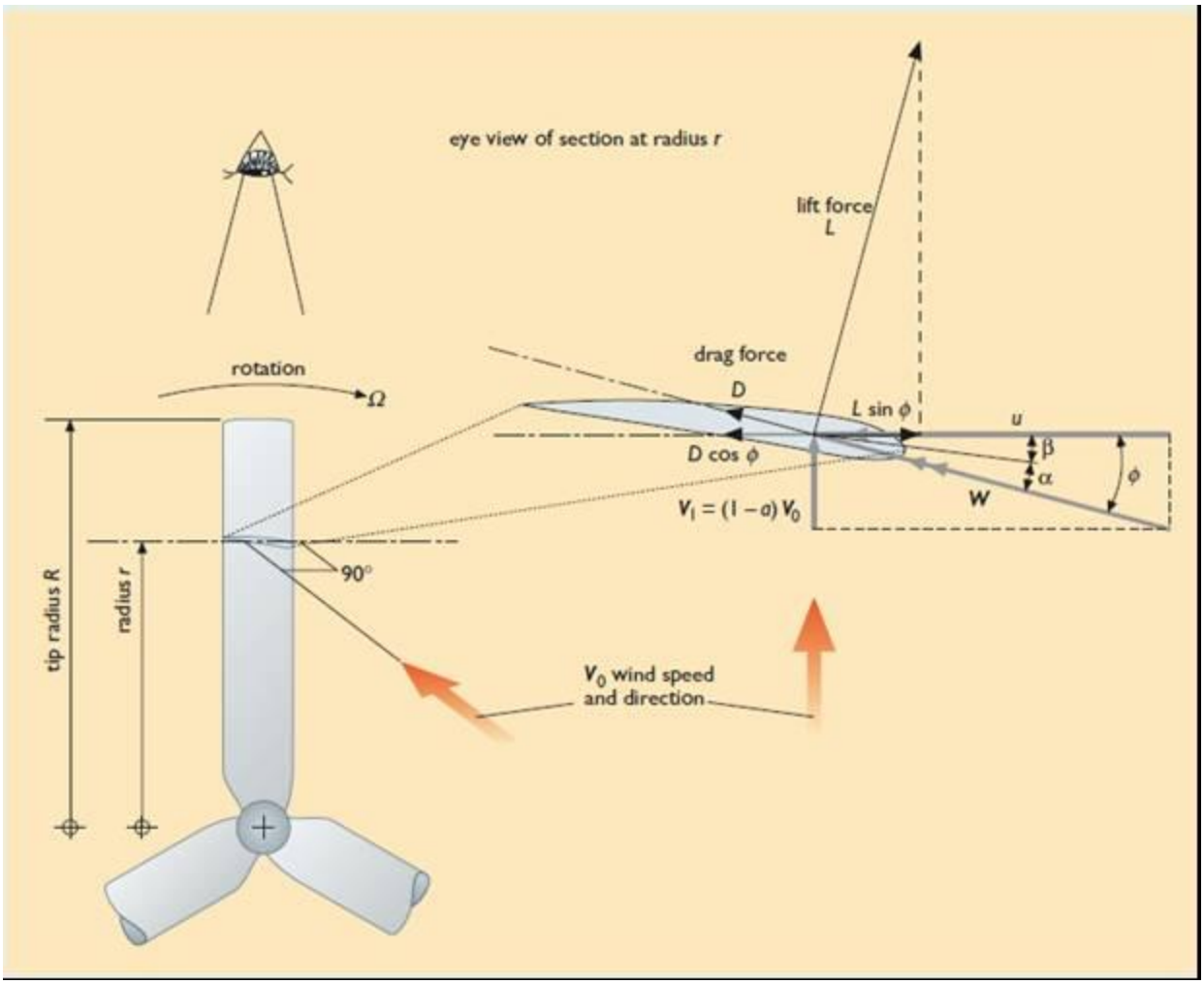

Figure 10: Vector diagram showing a section through a moving horizontal axis wind turbine (HAWT) rotor blade (Taylor, 2004)

2.3 Cp versus λ curve

The capacity factor Cp is the total annual energy produced by the renewable energy power plant over the amount of energy it would have produced, had the plant operated at its rated (maximum) capacity. This is not a measure of efficiency, but does depend on the specific geographical & wind resource, how the technology intersects with it, and operational factors such as maintenance and curtailment. Somewhat confusingly, in wind engineering, Cp can also

be used to denote the so-called 'power coefficient' of wind turbine rotor which is a measure of efficiency. In this section, it is this latter usage which applies.

The tip speed ratio is the ratio of the blade tip speed of a wind turbine to the undisturbed wind velocity and is the most significant parameter in the aerodynamic design of a wind turbine rotor blade (Taylor, 2004). A wind turbine with a (low) design tip speed ratio of ~1 (when wind & blade have same speed) provides a high torque, but would run at a low rotor speed. Wind turbines of the same size can have tip speed ratios of ~5 to 8, and they provide low torque at same power with higher rotor speeds. Such turbines are typically suited for electricity generation (Gasch & Twele, 2012). This is because a smaller gear transmission ratio will be required due to the higher rotational speed of these type rotors. In these rotors, the low start-up torque is not a problem because the generators start working only at higher rotational speeds.

The relation between the efficiency of a wind turbine (expressed via the so-called power co-efficient) and its tip speed ratio indicates that there is an optimum tip speed ratio, TSR (Figure 11). If the wind turbine rotor speed remains constant, then actual operating conditions can represent prolonged excursions from the optimum, as the wind speed varies. To maintain the optimum TSR the undisturbed wind speed varies, the rotor speed must vary too. In the 1990s, constant wind speed rotors were predominant which were controlled to maintain frequency. Consequently, wind turbines spent a significant portion of the time off the optimum Cp-lambda point. In the 2000s, variable speed rotors became available as an option to increase the capture of available wind energy. Overall maintaining the TSR closer to the optimum leads to increases in the wind turbine output and the efficiency of the wind turbine (Taylor, 2004).

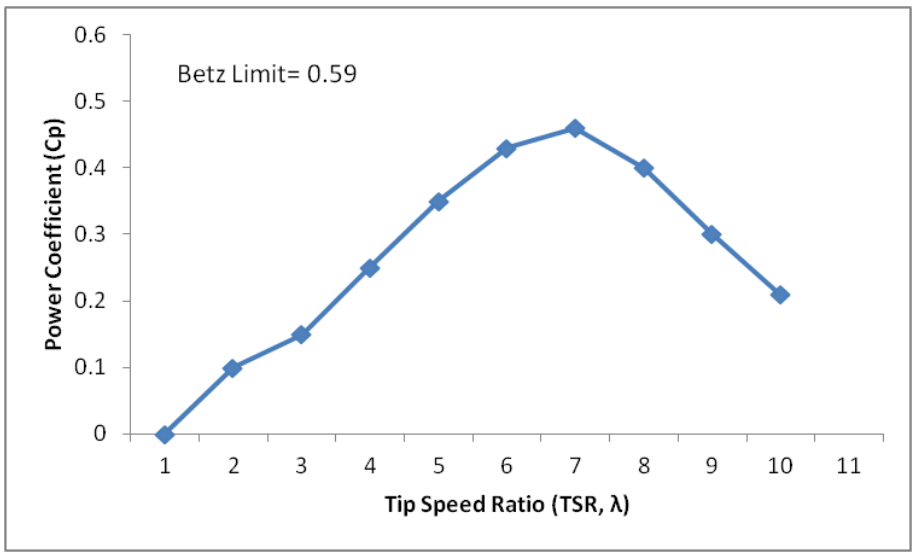

Figure 11: Chart showing the power coefficient and tip speed ratio for a two-bladed rotor (Magdi Ragheb & Ragheb, 2011)

2.4 Wind turbine power curve

According to Betz (as cited in Manwell et al., 2010) proved that the maximum theoretical power maximum Cp that can be harvested from a free stream of flowing air is 59.3% since some kinetic energy that needs to remain in the flow to clear the actuator (rotor). This was determined in 1926 and it is called the Betz Limit.

The incident wind power is given by,

$$Power = 0.5\,\rho A V^3 \tag{6}$$

where, ρ is the density of the air (kg/m^3), A is the area through which the wind is passing (m^2) and V is the wind velocity (m/s).

The tip speed ratio (TSR) is,

$$\lambda = \frac{Blade\ tip\ speed}{Wind\ speed} \tag{7}$$

The blade tip speed is the tangential velocity u, which is given by,

$$u = r\Omega \tag{8}$$

where, Ω is the angular velocity and *r* is the local radius of the blade tip at that point.

Therefore the mechanical power from the wind turbine is,

$$P = \tau * \Omega \tag{9}$$

where τ is torque (Nm).

A typical wind turbine power curve for two different types of control systems, namely stall-controlled and pitch-controlled wind turbines is presented in Figure 12.

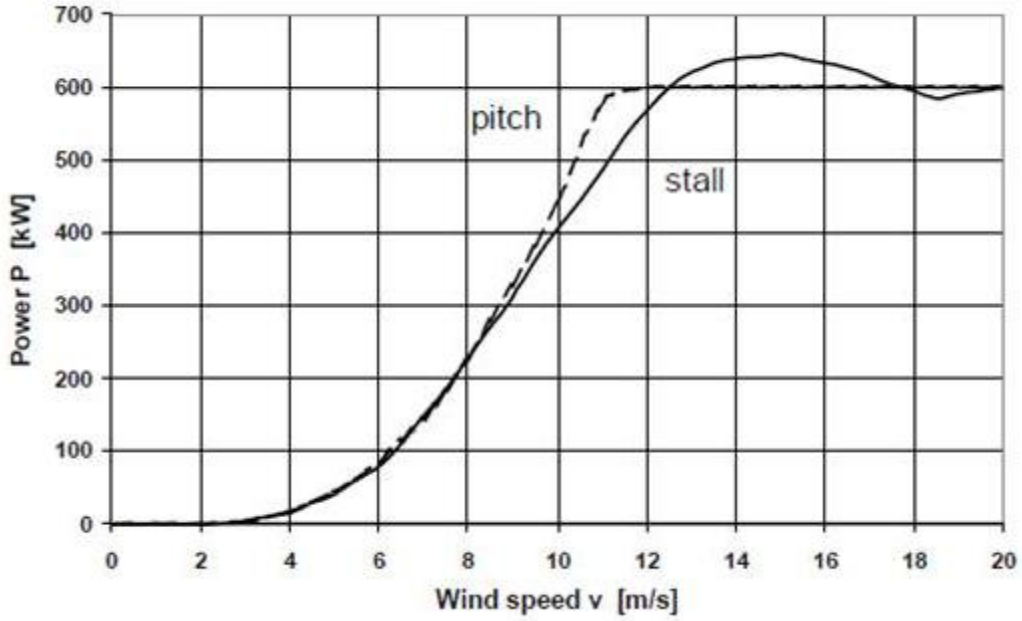

Figure 12: A typical wind turbine power curve for a 600 kW wind turbine for pitch-controlled and stall-controlled system (Gasch & Twele, 2012)

For the stall-controlled wind turbine, the rotor turns at fairly constant speed, and the wind turbine works at its optimum aerodynamics only at one or two wind speeds. The rotor blades of these types of wind turbines are bolted at a fixed angle onto the hub. The blades are designed as such that they will perform worse during high wind speeds to protect the wind turbines. The

power for the stall-controlled wind turbine as shown in Figure 12 is decreasing with increasing wind speed which is due to aerodynamic effects on the turbine blades (Research hubs, 2015). The regions of the blade are stalled, propagating from the hub and outwards with increasing wind speeds. The pitch control technology involves rotation of blade around its own axis to maximise the energy capture (Gasch & Twele, 2012). This control technology uses an active control for the blades that allows the system to have a constant power output above the rated wind speed, as shown in Figure 12. This mechanism is also discussed in Section 2.7.5.

2.5 Torque development from a wind turbine blade

Torque arises from the moment about the centre of rotation due to the driving force imparted by the wind that rotates the blades. For a given amount of power, the lower the angular velocity, the higher the torque, and the higher the angular velocity, the lower the torque. Also low tip speed ratio characteristics result in higher torque values.

Total torque is given by,

$$Q = \sum T\, n \tag{10}$$

$\sum T$ is the sum of all torque at the points along the length of the blade and n is the number of blades. Torque, T at each point is calculated using equation (3). Figure 13 shows how the relative wind angle, ϕ changes along the length of the blade and it also shows visually how torque can be different along the blade length.

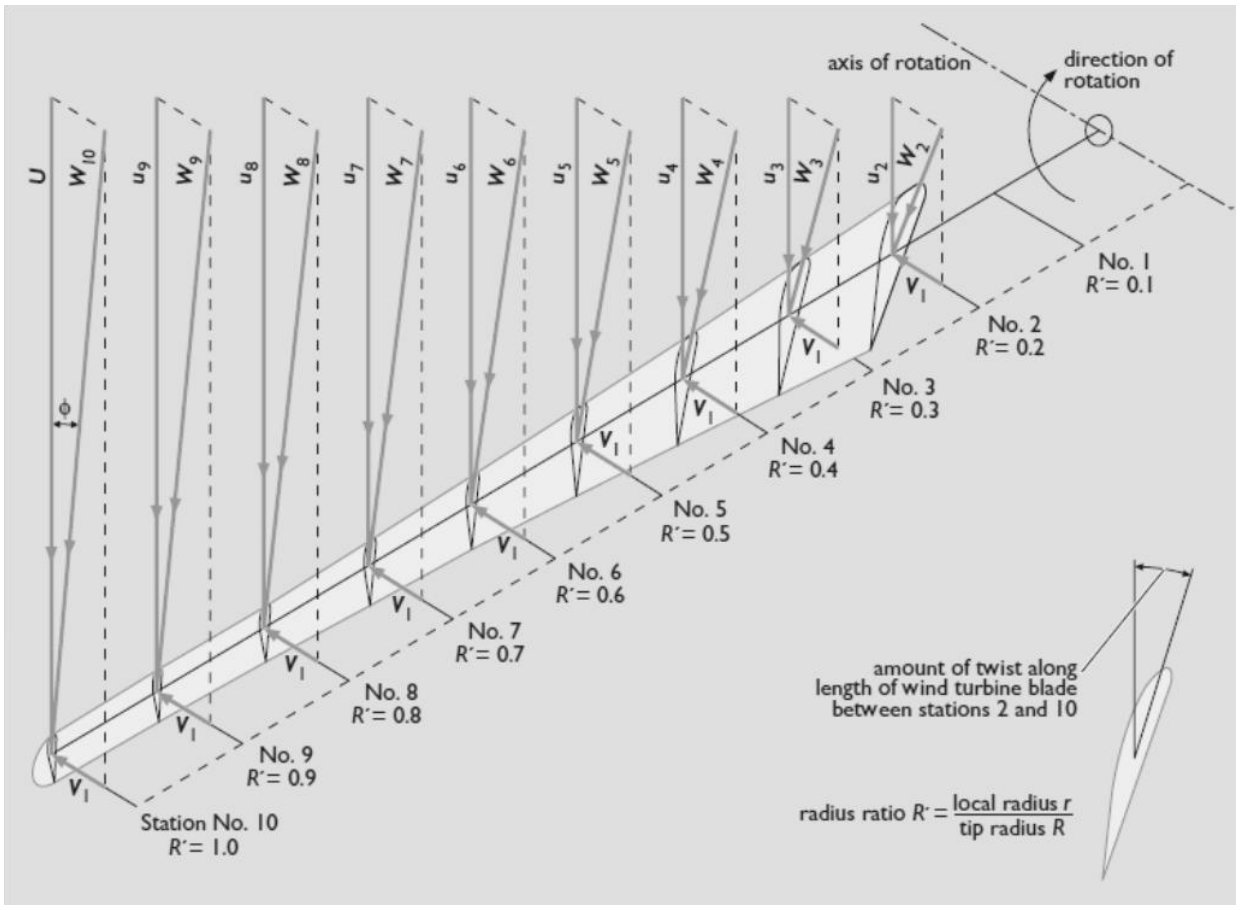

Figure 13: 3D view of an HAWT rotor blade design (Taylor, 2004)

The wind power increases with the cube of the wind speed. Every time the wind speed doubles, there is an eight-fold increase in the amount of power available in the wind. However, the operating design speeds are different for different wind turbine types and also for different locations. Since higher wind speeds can have adverse impact on the wind turbine structure, every wind turbine is designed for specific cut-in and cut-out wind speeds. Therefore, only a constant wind speed is taken into consideration after it reaches certain limit. Many wind turbines have a cut-in wind speed of ~3-5 m/s and the cut-out wind speed of ~25-30 m/s depending on their structural and material properties.

2.6 Optimising wind energy capture with variable speed HAWT

Traditionally, all the wind turbines used to be fixed speed wind turbines, meaning that the wind turbine rotor had constant speed for all the ranges of wind speeds. There is only one wind speed for the fixed speed wind turbine for which the tip-speed ratio is optimum. Therefore, for a particular location, the wind turbine will be not be operating near the optimum tip-speed ratio to a greater extent, unless that particular location has higher probability of getting exactly the same high wind speed (Carlin, Laxson, & Muljadi, 2001). Therefore, the wind turbine will not be able to extract maximum power from the wind. This led to the motivation for the development of the variable speed wind turbines which run efficiently in a wider range of wind speeds, as they could operate close to the optimum tip-speed ratio more frequently. These types of wind turbines can capture as much as 10% more annual incident wind energy than fixed speed wind turbines (Carlin et al., 2001) and means variable speed wind turbine obtain substantially more revenue over the 20- or 30- year lifetime of the wind turbine. A typical power curve for such a wind turbine is presented in Figure 12 (pitch-controlled).

The wind turbine blade inertia plays an important role while designing the control system for the variable speed wind turbines (Butterfield & Muljadi, 2000). Wind turbines have larger inertia than that of a generator because of the wide range of wind speeds they can operate at. This inertia acts as an inductor in an electrical circuit, it helps smooth the rotor speed variation, and it stores energy during acceleration and restores energy during deceleration (Butterfield & Muljadi, 2000). By switching to the variable speed wind turbines, the rotor fatigue loads can also be decreased as the deviations in torque during wind gusts are more severe in the fixed speed wind turbines (Carlin et al., 2001). The added costs of power electronics needed for variable

speed wind turbines can be offset with the added energy capture, reduction in loads and other system costs (Carlin et al., 2001).

2.7 Other HAWT components

In a wind turbine that produces electricity, usually, the rotor in the turbine is connected to the gearbox and the gearbox (or transmission) is connected to the generator. The generator is then connected to a transformer, so that the voltage is raised to that of the utility grid to distribute the electricity produced. The electricity produced by the turbines must not only be at the right voltage, but must also be at the right frequency and phase (synchronized). Thus the transformer and any power electronics integrate the wind turbine generator to the utility grid. This in turn places constraint on the turbine itself, typically this being a need for constant rotational speed. All the components involved in the wind power energy conversion system are depicted in Figure 14.

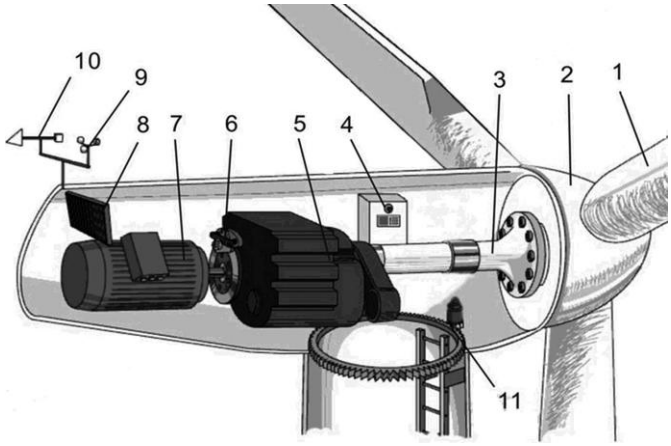

Figure 14: Wind turbine components inside the wind turbine nacelle. 1. Rotor blades, 2. Hub, 3. Main shaft, 4. Controller, 5. Gearbox, 6. Mechanical brake, 7. Generator, 8. Cooling system, 9. Anemometer, 10. Wind vane, 11. Yawing motor and yawing bearing (Jiang, 2010)

As mentioned in Canadian Standards Association, CSA (2008), the CSA is not aware of any Canadian Regulatory requirements for wind turbine blades or rotors, and wind turbine

mechanical systems. However, IEC 61400-1 has a section describing mechanical systems such as gearboxes, brakes, bearings, pitch and yaw actuators, etc., and is supplemented by IEC/TS 61400-13 which is a section on measurement of mechanical loads (Canadian Standards Association, 2008). However, American National Standards Institute, ANSI (2017), state that the wind turbine standards are complemented by ISO, ANSI and other national standards. ANSI (2017) has also presented a list of American and other international wind turbine standards on their webpage. Some of the standards they have listed are, IEC 60050-415 Ed. 1.0 b: 1999 for wind turbine generators, ISO 12494:2017 for atmospheric icing of structures, ANSI/AGMA/AWEA 6006-AO3 (R2010) for design and specification of gearboxes for wind turbines, IEC 60076-16 Ed. 1.0b:2011 for transformers for wind turbine applications, and so on (ANSI, 2017).

2.7.1 Blading

The wind turbine blades are required to convert the kinetic energy in the wind to torque. These blades have to be strong to handle the fatigue failure and extreme bending loads and also to be cost effective in terms of materials and manufacturing process at the same time so that the whole wind turbine system can be cost competitive in the market (Manwell et al., 2010). Therefore the properties of the materials that are used for wind turbine blades should be such that they have high material stiffness to maintain optimal aerodynamic performance have low density to reduce weight forces and have long-fatigue life for a longer life of the whole wind turbine system by preventing the material degradation. Therefore, the blade materials must be optimised in terms of properties, performance, and economy (Brøndsted, Lilholt, & Lystrup, 2005).

Historically, the wind turbine blades were made of wood, which were sometimes covered with cloth. It was not until the mid of the 20th Century, that they were made of steel, but only for larger wind turbines. In around 1970s, the wind turbine blades started to be made with fiber composites (Manwell et al., 2010). The most commonly used composites are the mixture of fibreglass in a polyester resin (Manwell et al., 2010) but Vinyl ester and wood-epoxy laminates are also being used (Manwell et al., 2010). Carbon fibers are comparatively newer composites that have been introduced into the wind turbine blades construction and fabrication. They were not introduced to replace the fibreglass but instead to supplement them (Manwell et al., 2010).

Presently the wind turbine blades are made up of fiber reinforced plastic (FRP) materials surrounded by two FRP shells acting as aerodynamic fairing. Foam is inserted into the aerodynamic trailing to maintain the structural integrity and to limit buckling phenomena (Lachenal, Daynes, & Weaver, 2012). Though aluminum is commonly used for Vertical Axis Wind Turbine (VAWT), it being lighter, it has been used only in few HAWTs (Manwell et al., 2010). Wood laminates, polyester resins, epoxies are the other type of composites that are used for the wind turbine blade manufacturing.

The wind turbine blades face freezing and/or icing problems when they experience lower temperatures. This problem can have significant effect on the wind turbine power production. Other issues associated with the icing on the blades include complete loss of production, reduction of power dues to disrupted aerodynamics, overloading due to delayed stall, increased fatigue of components due to imbalance in the ice load, and damage caused by uncontrolled shedding of large ice chunks as cited in (Homola, 2005). However, many de-icing technologies have been proposed and tested by different companies. Various types of de-icing technologies include: direct and indirect heating, mechanical removal, surface treatment, protection by using

a layer of dry air (Homola, 2005). Anti-icing technologies are also used to prevent the ice formation on the wind turbine blades.

Direct heating is performed either with the use of microwaves or with electrical resistance heating. Indirect heating is when the inside of the blades is heated with warm air or a radiator and heat is transferred to outside of the blades. Mechanical removal of the ice has also been proposed where the blades are flexible enough to crack the ice on them. The anti-icing technology is the surface treatment where a coating is applied to the blades (Homola, 2005).

2.7.2 Transmission systems

The main purpose of transmission/gearbox in a wind turbine is to speed up the rotation per minute (rpm of the wind turbine rotor (low rpm of around tens) to a higher rate (up to hundreds or thousands of rpm)) to drive a standard generator (Manwell et al., 2010). Gearboxes inside the wind turbine nacelle are usually heavy but new techniques are being developed and tested to improve reliability efficiency. The inclusion of the gearbox and the generator in a wind turbine nacelle not only increases the weight of the nacelle but it also increases the installation and maintenance costs (Joselin Herbert, Iniyan, Sreevalsan, & Rajapandian, 2007). The two commonly used gearboxes are the planetary and parallel shafts. Some wind turbines that use multiple generators are connected to the gearbox with multiple output shafts. Low speed generators have also been used in some other wind turbines which means that they do not need a gearbox (Manwell et al., 2010).

Wind turbine gearboxes have a reputation of being the ‘weakest link’ in the power train. As the size of the wind turbines increase, the gearbox design also becomes a challenge, as these transmissions need to handle the greater torque produced by the longer and larger turbine blades. These gearboxes also need to withstand the wind gusts that could result in their

failure. Gearboxes replacement can cost up to 10% of the overall cost of the wind turbine system (A. Ragheb & Ragheb, 2010). Newer wind energy conversion techniques use direct drive ‘gearless’ wind turbines, motivated by removal of low reliability of gearboxes. Using a direct drive power train also helps in reducing the overall weight on the nacelle. Enercon GmbH of Aurich, Germany has developed a solution to the low reliability of the gearbox by using the direct drive train. The solution that Enercon has provided, makes use of an annular multiple pole generator, which not only reduces the number of moving components, but also lowers the amount of repair work and associated turbine downtime (A. Ragheb & Ragheb, 2010). It is shown in Figure 15.

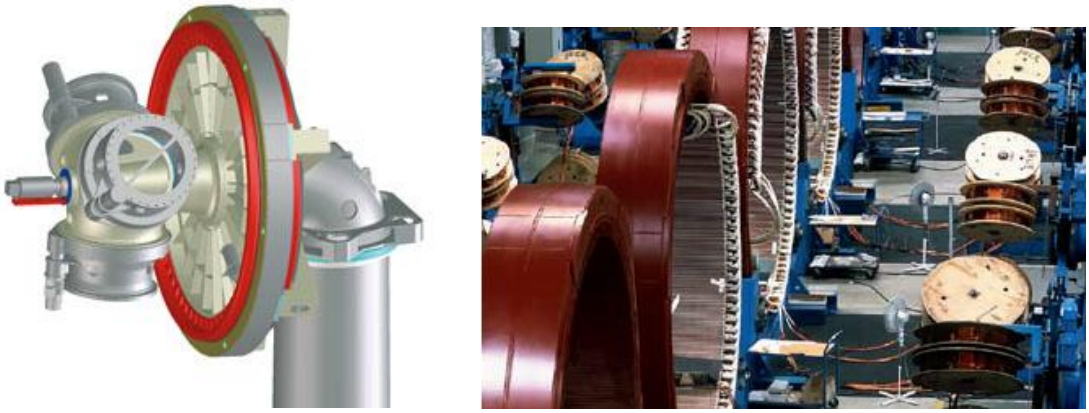

Figure 15: Multiple pole generator (Magdi Ragheb & Ragheb, 2011) *Original source: Enercon GmbH (2016)*

2.7.3 Generator

A generator is required in a wind energy conversion system to convert the rotating shaft work to electrical energy. Reliable, efficient and compact designs of generator have been brought forward to increase the wind power capture and to produce a higher quality output power. These generators are categorised based on their power level, or rating, and their principles of

operation. Most wind turbines use either induction or synchronous generators (Manwell et al., 2010). The wind turbines operate at constant or nearly constant speed if the generators are connected directly to the utility grid and can perform at variable speed if the generators are connected to the utility grid via power electronics (Manwell et al., 2010). Most of the grid-connected applications use squirrel cage induction generators (SQIG) while the doubly fed induction generators (DFIG) are used in variable speed applications. Both are shown in Figure 16. A SQIG operates within a narrow range of operating speeds slightly higher than its synchronous speed. For example, a four-pole generator operating in a 60 Hz grid has a synchronous speed of 1800 rpm.

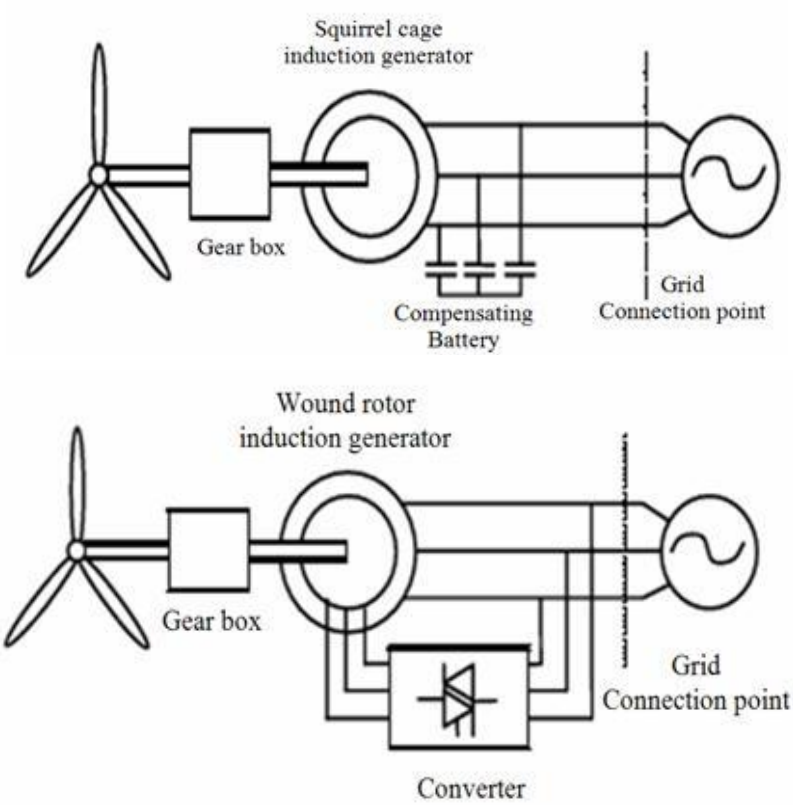

Figure 16: Squirrel cage and doubly fed induction generators for wind turbines (Djemai & Bouktir, 2008)

The variable speed wind turbines are becoming increasingly popular in utility-scale power generation because they result in less wear and tear of the wind turbine system, higher efficiency over a wide range of wind speeds, and increased energy capture. With the proper power electronic converters, either the synchronous or induction generators can run at variable speed (Manwell et al., 2010).

The use of annular generator is gaining more popularity these days. This type of generator is primarily used in the gearless system design. The advantages of using such type of generator are that it avoids the gearbox components and there are less material and mechanical wear which result in longer service life. All these properties of this generator make it perfect for use in heavy demands (A. Ragheb & Ragheb, 2010).

2.7.4 Power electronics

The electricity produced by the turbines must not only be at the right voltage, but must also be at the right frequency and phase (synchronized). Therefore there is need for power converters and electronics that generally convert electrical power from one form to another such as alternating current (AC) to direct current (DC), DC to AC, one voltage to another or from one frequency to another frequency. These are electronic devices that consist of electronic control systems turning off and on switches or valves. Major circuit elements used in the inverters are diodes, silicon-controlled rectifiers, gate turn-off thyristors, and power transistors (Manwell et al., 2010).

Thus the transformer and any power electronics integrate the wind turbine generator to the utility grid. This in turn places constraint on the turbine itself, typically this being a need for constant rotational speed. A significant issue with wind energy, for electrical engineers, is that sudden changes in output from modern wind turbines can be corrected for, but can introduce

harmonics into the distributed electricity signal, as gusts of wind attempt to push a wind turbine out of synchronization. Figure 17 presents a sketch showing different wind turbine components connected to the power system for supplying electricity to the grid.

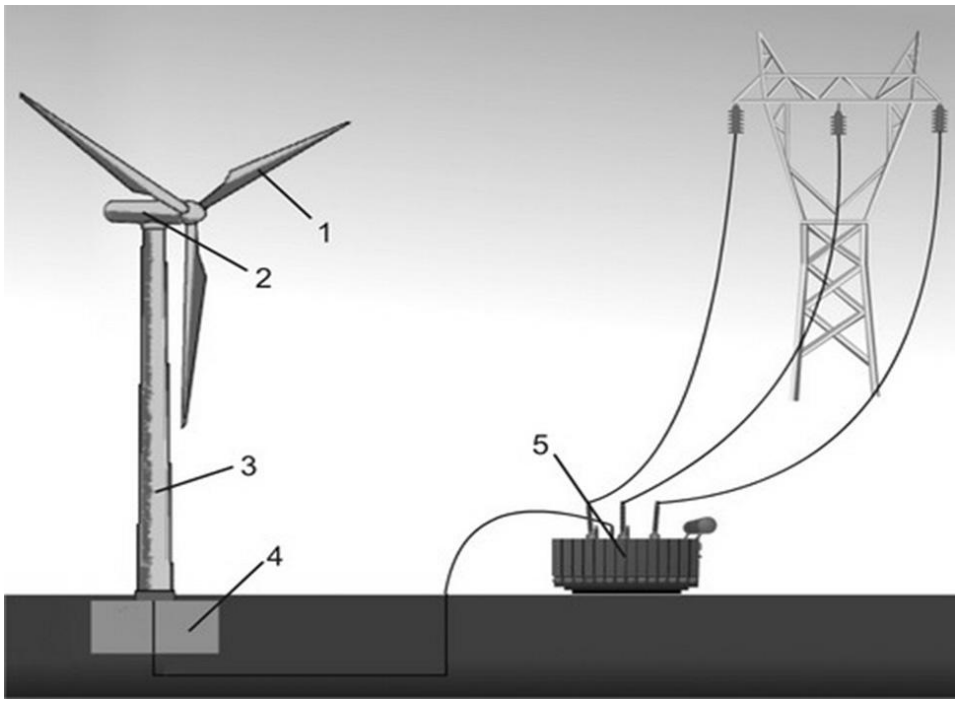

Figure 17: Sketch showing the wind turbine components connected to power system: 1. Rotor/blades, 2. Nacelle, 3.Tower, 4. Foundation, and 5. Transformer (Jiang, 2010)

The predominant wind power interconnection/power conversion methods are: Alternating Current (AC)-connection, Direct Current (DC)-connection or a combination of both connections. In the AC-connection, the output power is directly converted to the power grid and is used as an AC power, whereas in DC-connection the output power from wind is first converted to DC power by the help of a rectifier and then reconverted to AC power of the appropriate frequency by means of an inverter. AC-connections are the most common type due to simplicity; however the DC-connection is gaining popularity because of its gearless design and a wider operating range (Nishikata & Tatsuta, 2013).

Large-scale wind integration with power systems faces challenges including difficulties in controlling the voltage and frequency, as well as stabilizing the electrical grid that is dependent on the supply-demand balance when some fraction of the generating capacity may drop out suddenly due to wind calm. Wind turbines can also be deliberately curtailed because of the disturbances such as voltage dips or frequency variations they cause with gusting winds or because of system efficiencies which make it beneficial to generate without wind contribution. When the installed wind capacity increases on a distribution grid, measures have to be taken so that wind power variations do not decrease the reliability of the power systems. Every 'electron' of power generated on an electrical system must be simultaneously consumed. Maintenance of the supply-demand balance for system operators where there is high wind penetration can be a real problem, which although not insoluble, tends to add to the cost of electricity from these sources and definitely unpopular with electrical engineers. The distance between the sites of wind power production and sites consuming their power can be great which can lead to large I^2R power losses, especially at distribution voltages which become greater with greater distance. Overall as reported by Ibrahim et al. (2011), the fluctuations in wind resources make it difficult to manage the produced energy.

2.7.5 Pitch control system

The control system in a wind turbine system is mainly used for increasing the power production and also to reduce the loads using less number of control inputs in the wind turbine energy conversion system (Joselin Herbert et al., 2007). The most common way of controlling the aerodynamic power produced by the wind turbine system is the pitch control system. The wind turbine blades can be turned into or out of wind with the help of the pitch control. During the below-rated wind speed time, the wind turbine should tend to operate to maximise the wind

power capture so there is no need to vary the pitch angle of the blades. However, pitch control would be needed for the fixed speed wind turbines as the optimum pitch angle for aerodynamic efficiency varies slightly with the wind speed (Burton, Sharpe, Jenkins, & Bossanyi, 2001). This may reduce energy capture but is known to result in higher efficiency and reliability (Manwell et al., 2010), this being the dominant mechanism for technology installed in the early 90s.

For variable speed wind turbines, during part load operation, the wind turbines operate at constant pitch and variable rotor speed to obtain optimum tip speed ratio. When the rated power output is reached, the generator torque is used to control the electrical power and the pitch control mechanism is used to maintain the wind rotor speed within the acceptable ranges (Manwell et al., 2010).

The pitch mechanism can be either hydraulic or electric. Electric mechanism is simpler and requires less maintenance and as a result this is the most commonly used pitch control mechanism at present (Wu, Lang, Zargari, & Kouro, 2011). Wind turbines nowadays are designed to pitch one blade at a time in contrast to the traditional pitch mechanism where all the blades on the rotor hub are used to pitch at the same time. Individual pitch mechanism gives a chance for independent control for each blade (Wu et al., 2011).

2.7.6 Yaw control system

Yaw control system (also known as yaw orientation control) is usually used to control wind turbine power by changing the direction in which wind enters the wind rotor. This control mechanism is generally used in small wind turbines. This mechanism involves either yawing the rotor out of wind or turning the nacelle upwards to bound power control (Manwell et al., 2010).

Yaw control system usually consists of more than one electric motor drive, yaw gear, gear rim and bearing. A set of yaw brakes are inclined around the yaw rims to lock the position of the turbine facing the wind or the turbine is also locked using this mechanism during maintenance. A planetary gear in the yaw drive lowers the rotating speed of the yaw gear. All the motors in the yaw system are provided with the same signals and lock the wind turbine has turned into the desired direction (Wu et al., 2011). However according to Wu et al. (2011), the yaw control mechanism for wind turbine power regulation is no longer used in the newer wind turbines because: the yaw system response is very slow due to the large inertia of the rotor and turbine along the yaw axis, the power capture is insensitive to the yaw angle, and that this mechanism causes mechanical stress on the other wind turbine components, sometimes also resulting in vibration which could lower the overall operating life of a wind turbine system (Wu et al., 2011).

2.7.7 Rotational speed control system

So far, many authors have proposed and applied various control procedures for controlling the wind turbine rotor speed. To capture the maximum energy from the wind, different control strategies are applied. As shown in Figure 18, the power curve is divided into different regions, according to wind speed. Region I is when the wind turbine is not operating as there is no wind blowing. The end of Region II is the region of rated wind speed and rated wind power output. The beginning of Region II is the ‘cut-in speed’ when the wind turbine starts to produce. In Region III the wind turbine operates at high wind speed and outputs its rated power regardless of the high wind speed. If the wind speed gets higher than the so-called ‘cut-out’ wind speed, at the end of Region II, the control system of the wind turbine will shut down the operation because if it continues to operate even with the high wind, the turbine can be damaged due to the power

overloading. Therefore, the only region where the wind power can be maximized is Region II and therefore the control strategy has to be applied in this region. For this study, Region II control strategy is applied for the control of the wind turbine rotor speed as described in various other literatures (K. E. Johnson, Pao, Balas, & Fingersh, 2006), (Varpe, 2008), (K. E. Johnson, 2008), (Rajabhandharaks, 2014). This control strategy is discussed in detail in Section 6.6.

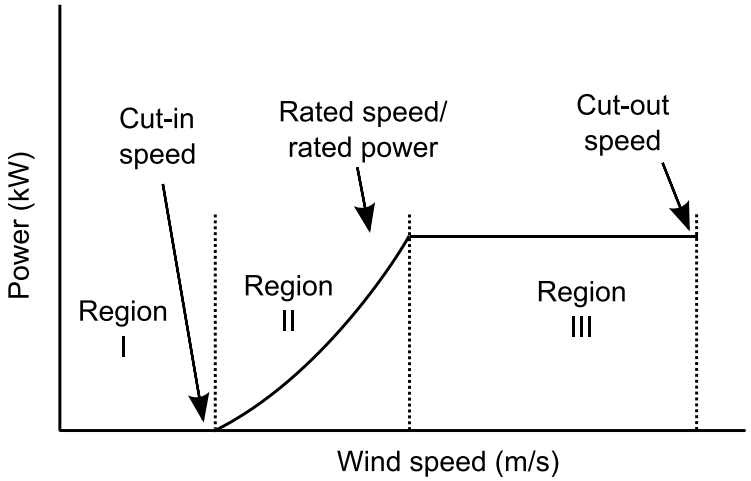

Figure 18: A typical wind turbine power curve showing different control regions (K. E. Johnson et al., 2006) *and* (Rajabhandharaks, 2014)

2.8 Summary

A detailed review on the state-of-the-art and latest developments in the HAWT technology for each component was presented in this chapter. However, some of the materials relevant to conventional wind turbines that produce electricity may have to be omitted or revised for CryoVent concept wind turbines as indicated in Table 1.

Table 1: Relevance of reviewed materials in Chapter 2

Reviewed materials	Relevance
Drag and lift on a blade element	Understanding of drag and lift forces on a blade element is required in both conventional and CryoVent concept wind turbines cases as they are directly related to torque development which in turn is related to power generation.
Cp versus lambda curve	This curve is relevant in both conventional and a CryoVent concept wind turbine as it is useful to determine the optimum tip speed ratio for a turbine that will have higher Cp value.
Wind turbine power curve	This curve is useful in determining the available power at the generator for conventional wind turbine and mechanical power available at compressor drive shaft for CryoVent concept wind turbines.
Torque development	This section explained how torque can be different along the length of the blade which is relavant in both conventional and CryoVent concept wind turbines as the torque development in the wind turbine blade is similar in both cases.
Optimising wind energy capture with variable speed rotor	Variable speed wind rotor can be applied to both conventional and CryoVent concept wind turbines to capture greater wind power than from the fixed speed rotor.
Blading	Blades affect the life of the whole wind turbine system be it for the conventional wind turbine system that produces electricity or the CryoVent concept wind turbine system that produces cryogens.
Transmission	The electrical transmission system reviewed in this chapter is only relevant for the Conventional wind turbine system because CryoVent concept makes use of open loop hydrostatic transmission system which is explained in Chapter 6.
Generator	The generator is required only in the Conventional wind turbine system that produces electricity. For the CryoVent system, a compressor is required which is driven by the hydraulic motor.
Power electronics	Conventional wind turbine system require power electronics for conversion of different electric parameters, however CryoVent system does not require them as electricity is not produced by this system.
Pitch control system	Conventional wind turbines make use of the pitch control system to turn the blades inward or outward. However it has not been determined yet if this system is required for the CryoVent concept.
Yaw control system	Both conventional and CryoVent concept wind turbines would require yaw control system for rotating the tower towards the wind so that more wind energy could be captured.
Rotational speed control system	Both conventional and CryoVent concept wind turbines can acquire control on the rotational speed by torque control mechanisms. For CryoVent concept systems, hydraulic pump displacement can be controlled (presented in Section 6.6) which then controls the wind turbine rotor speed that helps attain optimal tip speed ratio and maximum energy conversion.

Understanding of various mechanisms and wind turbine components reviewed in this chapter are important for achieving a better perception of the CryoVent concept which will be described in the chapters that follow.

3 Statistical analysis of wind climate

Statistical analysis of wind speed data is usually carried out in order to determine the wind energy potential and energy output from the wind turbine installed in that location. This analysis holds an important role in the CryoVent project and in this thesis work as it will be used extensively in the chapter to follow for synthesis of wind speed time series data. The spatial and temporal factors that affect the wind energy in any location are discussed in this chapter.

3.1 Factors affecting wind energy

The economic aspects of a wind turbine and/or a wind farm is closely related to the wind speed variations, especially for the offshore wind power productions (D'Amico, Petroni, & Prattico, 2014). The wind speed variability can be generally divided into short term and long term variability. It is very hard to notice a pattern in short term wind speed data whereas the long term wind speed data can have some distinct patterns (Wan, 2012). However, Manwell et al. (2010) divided the variations of wind speed into four divisions: inter-annual, annual, diurnal and short-term (gusts and turbulences), which are basically the generalized long-term and short-term variations. The inter-annual wind speed variations may be observed in the wind speed data of a specific location of more than one year and it might take a longer time (as many as 30 years) to predict the long term weather and climate data (Manwell et al., 2010). The annual variations can also be sometimes referred as seasonal variations or the monthly variations which are present in the one year long data.

3.1.1 Spatial factors

Spatial variability of wind on a larger scale suggests that there are different climatic regions around Earth that affect the amount of solar insolation. On a smaller scale, within one climatic region, wind varies corresponding to the factors such as the elevation above sea level, elevation above ground level-wind shear, mesoscale surface roughness, fetch and local thermal effects. All of this demonstrates that scale spatial variability to a great extent is dictated by physical geography (Burton et al., 2001). The factors included in the physical geography are the proportion of land and sea, the masses of land, type and amount of vegetation, presence of mountains and valleys. Topography is the major factor in creating variability in wind speed locally (Burton et al., 2001). A global wind map is presented in Figure 19.

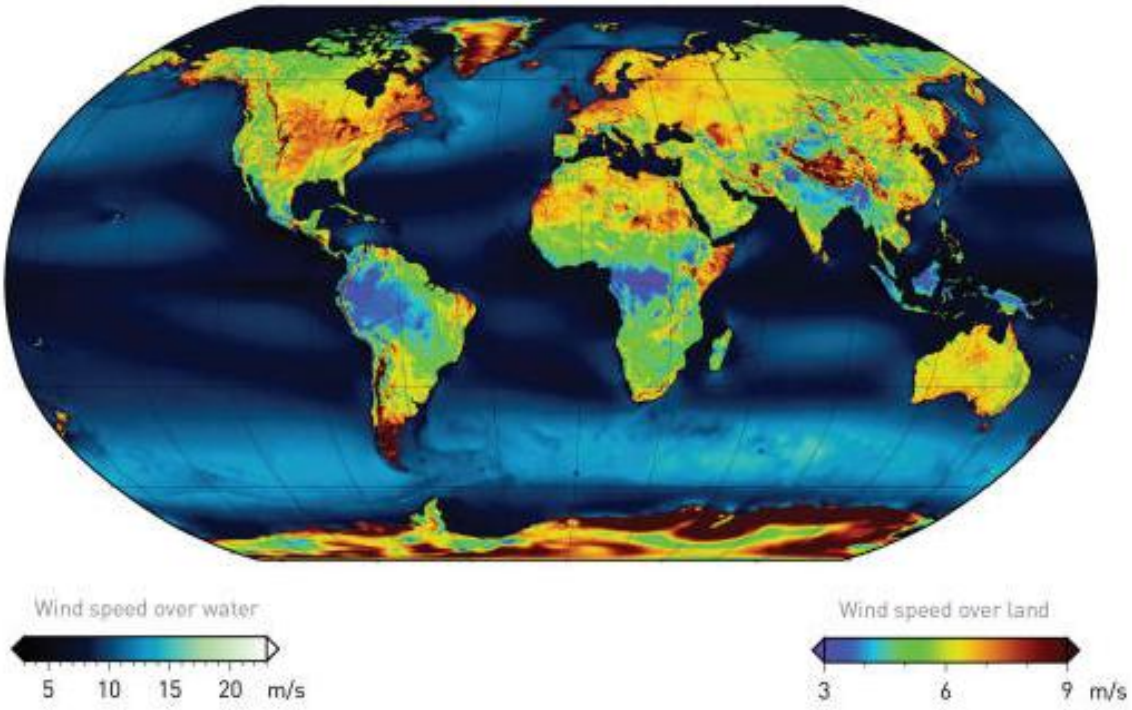

Figure 19: A global wind map showing wind speeds over land and water (Vaisala, 2017)

Thermal effects also help to create the local variations in wind speed. These effects are mainly caused by the differential heating of the land and sea and by altitudinal differences. These are also sometimes defined as sea-land circulation and mountain-valley circulation. The sea-land circulation starts by the heating of the land during the day-time. As it heats up more quickly than the sea, the air above rises, making space for the cold air from above the sea. And the reverse happens during the night as the land cools faster than the sea and the air above the land flows to the sea surface causing the air to flow from land to sea (Gasch & Twele, 2012).

Similarly, for the mountain-valley circulation, the mountains or the slopes of the mountains get heated up faster than the valley, which in turn heats the air masses above them. This process starts early in the morning with the sunrise. The winds on the slope of the mountains thus rise due to the thermal lift produced by differential heating. Later on in the morning, the wind from the valley starts flowing up towards the mountains, causing upward flow. During the night, the masses of air over the slopes get cooled down faster than atmospheric air at the same height. The gravitational force drives the masses of air on the slopes downwards completing the mountain-valley circulation they meet the air that is above the valley (Gasch & Twele, 2012). These processes are depicted in Figure 20.

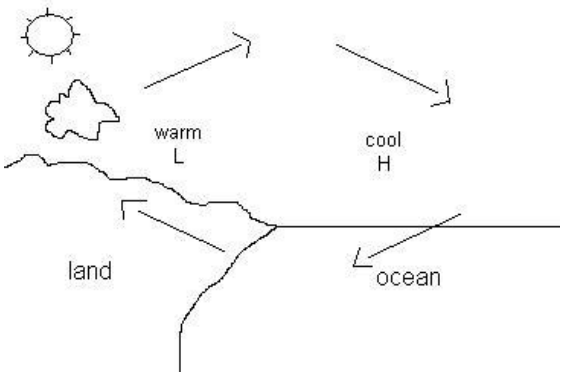

Day time sea breeze conditions

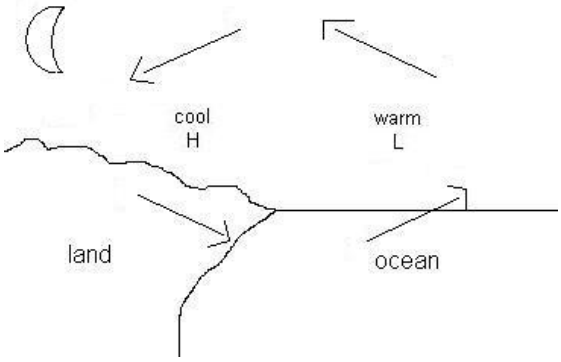

night time land breeze conditions

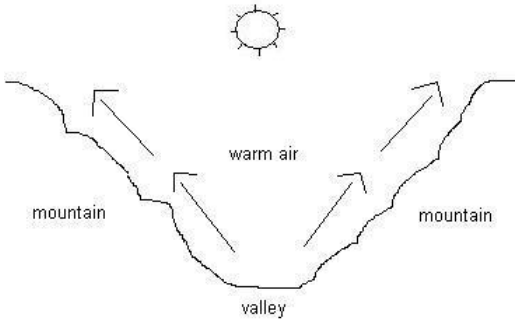

Day time valley breeze conditions

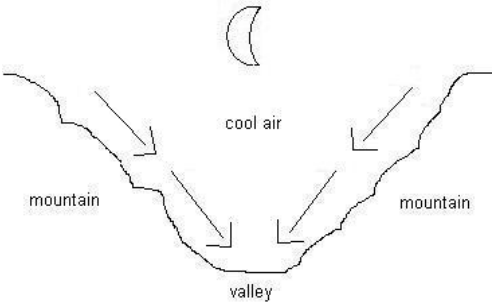

night time mountain breeze conditions

Figure 20: Day and night time breeze conditions in sea and land and mountain and valley respectively (Douglas, 2006)

The effect of surface roughness on the wind speed is that it changes the wind speed and also the direction in which the wind is blowing. The wind speed will change on different sites depending on the surface roughness, for example if the surface changes from smooth to rough, the wind speed will slow down due to the increase in surface frictional stress. The wind speed also tends to decrease as we move closer to the ground. Wind speed at any site is dependent on the surface roughness and the height above the ground. The relation of the wind speed with the height above ground, z (m) is shown in Figure 21.

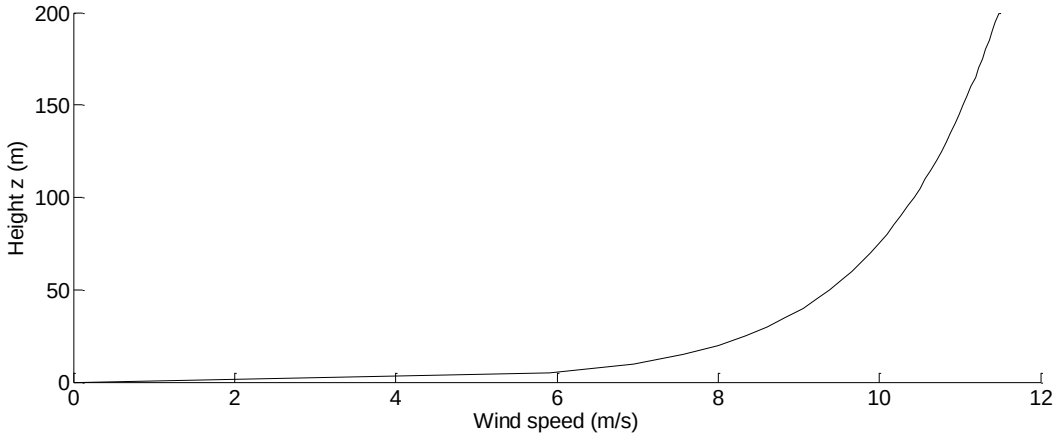

Figure 21: Relation between wind speed (m/s) and roughness above ground (m)

Roughness class and roughness lengths are characteristics of landscape to evaluate wind conditions at a potential wind turbine site (M Ragheb, 2017). For example a roughness class of 4 would have tall building and trees and a calm sea surface would have a roughness of 0. The roughness length is the height above the ground (m) at which the wind speed is theoretically 0. The roughness classes are determined in terms of roughness length in meters by the equations:

$$RC = 1.6999823015 + \frac{lnZ_0}{ln150}, \qquad for\ Z_0 \leq 0.03$$

$$RC = 3.912489289 + \frac{lnZ_0}{ln3.3333}, \qquad for\ C > 0.03$$

The wind speed at a certain height above ground can be estimated as a function of height above ground z and the roughness length Z_0 in the current wind direction from the formula,

$$V(z) = V_{ref}\frac{lnz/Z_0}{lnz_{ref}/Z_0}$$

The reference speed V_{ref} is a known wind speed at a reference height z_{ref} (M Ragheb, 2017).

3.1.2 Temporal factors

Temporal variability factors make the wind speed vary from one time period to another time period. Large scale temporal variability of the wind speed takes place on a yearly, inter-annual scale, evidence for which can be seen in the wind speed data variations from one year to another. There are large scale variations of wind speed within periods of decades or more (Burton et al., 2001). Major factors causing the large scale temporal variations (macro-meteorological range) could be the climate change, sunspots and/or periodic climatic behavior such El Nino.

The peaks in the wind speed spectrum account for annual, seasonal and daily patterns as well as short-term turbulences. A striking phenomenon is the spectral gap between time periods of 10 minutes to 2 hours. These patterns are important not only for yield estimations, but also for forecasting of wind power output.

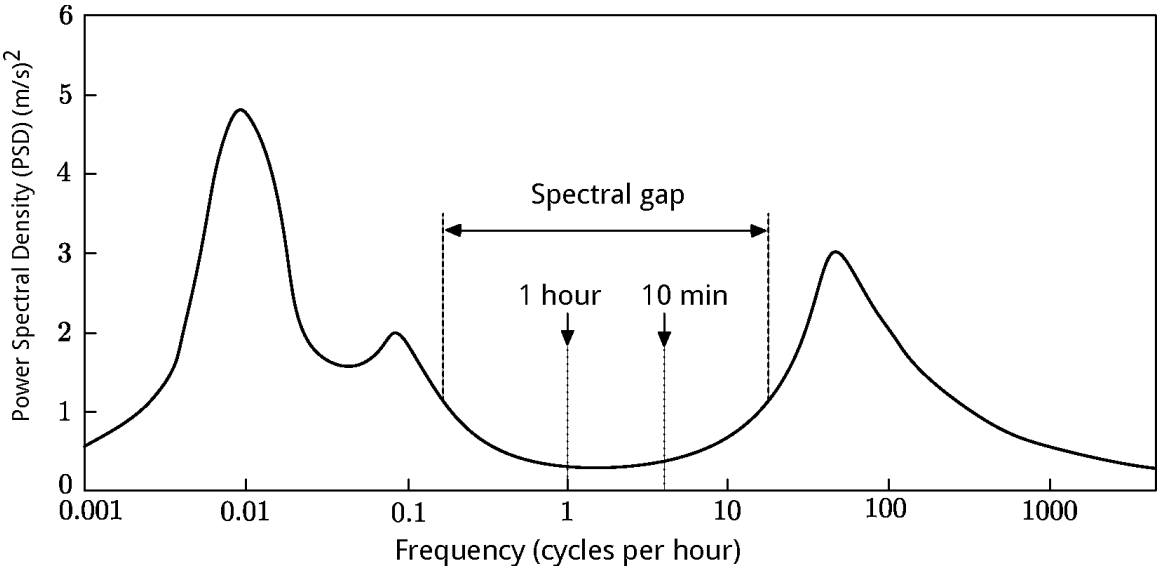

Figure 22: Wind power spectrum (Van der Hoven, 1956)

The variations that occur on a time scale of less than a year are the seasonal variations which are associated with the weather phenomenon (Burton et al., 2001) and planetary orbits, and earth rotation. Seasonal variations are mainly caused by the differences in insolation during different seasons: winter, spring, summer and autumn. Diurnal variations, sometimes also called the sea-land variations are caused by the differential heating of the sea and land during day and night (Gasch & Twele, 2012). These are variations are presented as wind power spectrum as shown in Figure 22.

Turbulence is understood as the variation in wind speed data within even shorter time scale of minutes to seconds or less (micro-meteorological range). This has a great impact on the design and performance of the wind turbines and also on the quality of the power delivered to the network (Burton et al., 2001).

3.2 Statistical measures

The commonly used statistical measures for wind speed such as, the mean wind speed, standard deviation of wind speed and turbulence intensity factor are explained in this section.

3.2.1 Mean wind speed

The mean wind speed is the most commonly used statistical measure for wind speed at or around any location in the globe. It is the average of the wind speeds measured for a given period of time. The mean wind speed, $\bar{v}$ for the total time period of T, is given by,

$$\bar{v} = \frac{1}{T}\int_0^T v(t)dt \qquad (11)$$

v is the wind speed measured at regular time interval t.

3.2.2 Standard deviation of wind speed

The average of the squared difference of the actual wind speed to the average wind speed is the variance, which also reflects the “irregularity” in the wind speed (Gasch & Twele, 2012). The variance is given by,

$$\overline{v^2} = \frac{1}{T}\int_0^T (v(t) - \bar{v})^2 dt \quad (12)$$

The square root of the variance gives the standard deviation. It is formulated as,

$$\sigma_v = \sqrt{\overline{v^2}} \quad (13)$$

It has the same unit as the mean wind speed, $\bar{v}$.

3.2.3 Turbulence intensity factor

The two main types of turbulence prevailing in the atmosphere are the mechanical turbulence and thermally induced turbulence. The mechanical turbulence is usually caused by the wind shear (which is the difference in the horizontal wind speed at the top and bottom of the wind turbine rotor) and it depends on the wind flow from large pressure gradients and also on the surface roughness. Thermal turbulence is caused by heat convection. Therefore it depends mainly on the temperature difference between the ground and the air masses above it (Gasch & Twele, 2012).

Turbulence intensity factor is the ratio of the standard deviation of wind speed to the mean wind speed. Mathematically it is given as,

$$I_v = \frac{\sigma_v}{\bar{v}} \quad (14)$$

This factor usually has a larger range from 0.05 to 0.40 due to various reasons such as, natural fluctuations, different averaging periods of measurements and sometimes also due to the time response of the sensors (Gasch & Twele, 2012).

3.2.4 Weibull distribution

Conventionally, probability distribution functions have been used intensively to model and predict wind speed at various locations. The most commonly described and frequently used distribution for the wind speed is the Weibull distribution. The Weibull probability density function is universally used for the wind energy applications around the globe. Wind varies both geographically and temporally which makes the prediction and forecasting work more difficult (Shu, Li, & Chan, 2015). However, the Weibull probability density function gives satisfactory representation of the variation of hourly wind speed within a year at many different sites (Burton et al., 2001). The Weibull probability density function is given by,

$$p(v) = \left(\frac{k}{c}\right)\left(\frac{v}{c}\right)^{k-1} exp\left[-\left(\frac{v}{c}\right)^{k}\right] \qquad (v > 0; k > 0, c > 0) \qquad (15)$$

where p is the probability of observed wind speed v (m/s), k and c are the Weibull 'shape' and 'scale' parameters respectively. The scale parameter, c (m/s) explains how "windy" a location is and the shape parameter k is dimensionless and it represents the width of the graph, explaining how peaked or how variable the wind distribution is (Shu et al., 2015). If the value of the shape parameter equals 2, the wind speed probability distribution function reduces to a Rayleigh distribution (Carrillo, Cidrás, Díaz-Dorado, & Obando-Montaño, 2014). The Rayleigh distribution is used to represent the wind speed frequency distribution only when the mean wind speed of that location is known (Shu et al., 2015).

The Weibull cumulative distribution function is given by,

$$p(v) = 1 - exp\left[-\left(\frac{v}{c}\right)^{k}\right] \quad (16)$$

3.2.5 Wind roses

A wind speed rose is a diagram showing the temporal distribution of wind direction and azimuthal distribution of wind speed data (Manwell et al., 2010). It is a chart that shows how wind speed and wind direction are distributed at a particular location over a specified time (Bellasio, 2014). This diagram can present the anemometer data in a convenient way. Further, a wind rose can also be used either in the form of speed distribution or frequency distribution. The length of the line in the wind rose is proportional to the frequency of the wind from the compass point. Wind roses are usually used to represent monthly, seasonal or annual wind data. An example of a wind rose is presented in Figure 23.

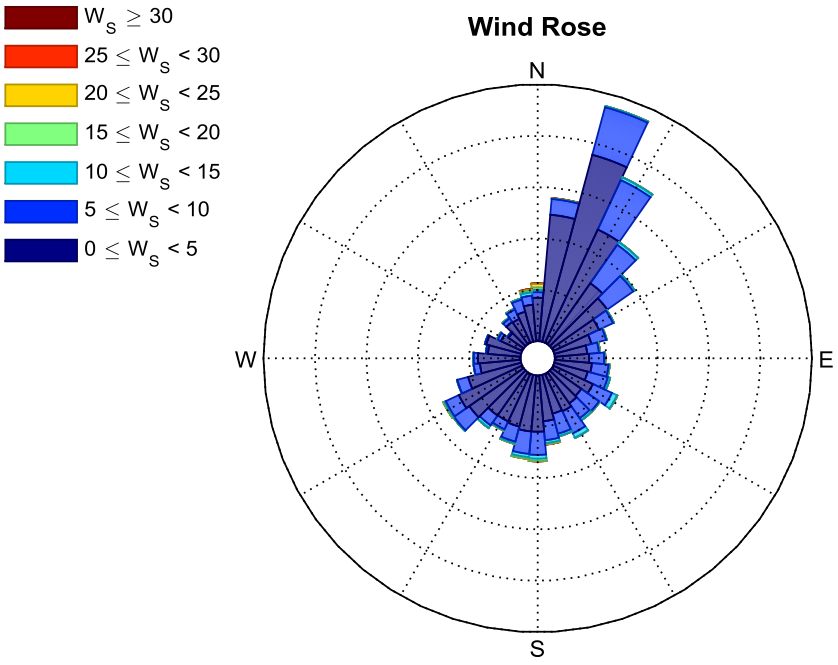

Figure 23: Example of wind rose (Pereira, 2015) *(W_S = wind speed in (m/s))*

3.2.6 Wind atlases (WAsP)

The wind speed and wind direction data of a region can be presented in a chart called wind atlas. Different wind atlases can be found on internet for different regions for example, there are global wind atlases, the European Wind atlases, and wind atlases for different countries and regions. The wind atlas for any region makes use of meteorological data from several monitoring stations and displays the distribution of wind speeds on a broader scale. Wind atlases have been used widely by the governments and developers in estimating the size of resources and regional variations (Wind Energy The Facts, 2017). This information is very important for wind turbine construction and installation in any location.

Many computer programs and software have been developed for the development of the wind atlases. The Wind Atlas Analysis and Application Program (WAsP) is one of them. Some of the applications of WAsP are to calculate the energy yield for a single wind turbine and wind farms, calculating wind farm efficiency, wind resource and turbulence mapping for selected areas, siting of the wind turbine and the wind farms and calculating wind conditions for International Electro-technical Commission (IEC) standard site assessment, such as mean wind speed, wind flow inclination, turbulence, and so on (DTU Wind Energy, 2017).

3.2.7 International Electro-technical Commission (IEC) wind classes for wind turbines

According to IEC (as cited in Burton et al., 2001), there are four different classes of wind turbines that suit different wind conditions according to IEC 61400-1 (IEC, 1998). These classes are presented in Table 2. The reference wind is 10 minute average wind speed at hub-height with a 50 year return period, and the normal value of air density is 1.225 kg/m^3. For the sites that do not fall under these classes, a fifth class has to be provided in which the basic wind parameters have to be provided by the wind turbine manufacturer (Burton et al., 2001).

Table 2: Wind speed parameters for wind turbine classes according to IEC (as cited in Burton et al., 2001)

Parameters	Class I	Class II	Class III	Class IV
Reference wind speed, U_{ref} (m/s)	50	42.5	37.5	30
Annual average wind speed, U_{ave} (m/s)	10	8.5	7.5	6
50 year return gust speed, 1.4 U_{ref} (m/s)	70	59.5	52.5	42
1 year return gust speed, 1.05 U_{ref} (m/s)	52.5	44.6	39.4	31.5

The IEC standard also considers the turbulence intensity as a crucial parameter for wind turbine design and as a result of which has designated two categories, A and B for defining this parameter respectively. Category A is for higher turbulence intensity and B is for lower. The variation in the turbulence in each category with the hub height mean wind speed $\bar{u}$ is given by the formula,

$$I_u = I_{15}(a + \frac{15}{\bar{u}})/(a + 1) \quad (17)$$

where I_{15} is the turbulence intensity at a mean wind speed of 15 m/s, defined as 18 percent for category A and 16 percent for category B; constant a has values of 2 for category A and 3 for category B respectively according to IEC (as cited in Burton et al., 2001).

3.3 Source of wind speed data used in this thesis

The wind speed data used in this thesis are from Roskrow Barton wind farm in Cornwall, England that has on-board wind turbine anemometer and from University of Exeter which has offshore measurement on SWMTF with a sampling rate of 4Hz.

Roskrow Barton is a wind farm located at latitude of 50°10' 31" and a longitude of 5°8'26", at Cornwall, UK. The wind farm consists of 2 Vestas V52/850 (power: 850 kW, diameter: 52 m) wind turbines with a nominal power of 1700 kW. This farm is located about 6 km northwest of central Falmouth, Cornwall, England, constructed in 2008. The towers for each

of the two turbines are 44 metres tall (University of Exeter, 2017). A picture of the wind farm is shown in Figure 24.

Figure 24: Roskrow Barton Wind farm (Wikimapia, 2016)

The South West Mooring Test Facility (SWMTF) is located in Falmouth Bay, Cornwall, UK, near the Manacles rocks, just south of the mouth of the Helford River. The buoy is fully equipped with load cells, motion sensors and other instrumentation to test a variety of catenary and taut mooring arrangements. It transmits data directly to the shore and allows comprehensive evaluation of mooring systems under real sea conditions. It also has a Windsonic wind sensor that logs wind speed data at a frequency of 4 Hz (University of Exeter, 2017). The wind speed data from these two locations were available from private

communication that is used in simulation in this work. The data recorded from Roskrow Barton farm are 10 minute data.

3.4 Summary

This chapter presented the statistical analysis of wind climate. Some of the factors that affect the wind energy such as the spatial and temporal factors were presented in detail. The common statistical measures used in wind speed measurement such as mean, standard deviation, turbulence intensity factor, were also discussed. Wind energy availability of any location is usually determined using the statistical analysis. The review on the statistical analysis of wind speed data as presented in this chapter will be used comprehensively for wind speed time series analysis which will be presented in Chapter 4 that follows.

4 Time series analysis of wind climate

Statistical and time series analyses of wind speed time series data, both are mandatory to determine a site's wind energy resource. The statistical analysis of wind climate was discussed in Chapter 3. By evaluating the parameters such as wind speed and wind climate on site, the wind power engineers are able to provide a correct assessment of the wind potential and the power correction, as adequate as possible. It is feasible to calculate the expected production from a specific wind turbine when the wind speed and its distribution are known for a location. This is usually done with the help of power output curve that is specific for each type of wind turbine and states the power output from the turbine at different wind speeds. The time series analysis and its synthesis for wind speed data is carried out in this work to generate wind speed data for the simulation work.

Some simulation models might need hourly wind speed data but real hourly data may not be available. Sometimes, there might be need of a high sampling frequency, turbulent wind speed with certain specific characteristics as input to a structural dynamics code, which is seldom available. Therefore, there is a need for data synthesis and an accepted way to obtain data for such work is through the application of data synthesis algorithms. Depending on the type of applications and the type of other data available, the type of algorithm that can be applied may be different. Some of the commonly used algorithms are : auto-regressive moving average (ARMA) method, Markov chain method, Shinozuka method, and so on (Manwell et al., 2010).

Any time series data is a set of quantitative observations or measurements arranged in a sequential order. It is also an ordered sequence of values of a variable at equally spaced time

intervals. This set of data play important role in all research areas. Time series models could be used in obtaining an understanding of the underlying forces and structure that produced the observed data and also in fitting a model and proceeding to forecasting, monitoring or even feedback and feed forward control (NIST/SEMATECH, 2003).

The real data files as used in wind energy applications are sampled time series than being continuous analogue records. A single time series referred to a data record, corresponding to a continuous time series signal $x(t)$ can be written as,

$$x_n = x(n\Delta t)$$

where $n = 0,1,2,\ldots,N-1$; N = number of points in data record; $\Delta t = T/N$ = sample interval; T = time length of period; and n = index (point number).

There has been a fair amount of work done towards wind speed modelling and wind speed data synthesis. According to J. Carlin & Haslett, (as mentioned in Brown, Katz, & Murphy, 1984), have modelled spatial correlations of wind speed data ignoring the autocorrelation properties for wind speeds (Brown et al., 1984). Brown et al. (1984) developed wind speed and wind power models taking into account the basic features of wind speed such as, autocorrelation, non-Gaussian distribution and diurnal non-stationarity. However, this approach could only be used for a small set of hourly wind speed data.

D'Amico et al. (2014) used an indexed semi- Markov chain model for one step ahead prediction of wind speeds at different horizon times. Similarly, Gomes & Castro (2012) used ARMA and Artificial Neural Network (ANN) models for forecasting of wind speed and wind power and compared these two methods for forecasting. They concluded both the models produce similar results that worsen with increasing time horizons however, when the ARMA and

ANN models are compared with each other, ARMA model produces slightly better performance in forecasting while the ANN model is faster than ARMA during simulation. On the other hand, both of these models utilise all the available data for prediction of one step ahead or several steps ahead wind speed data. Again in that work, the hourly average wind speeds were used to train the model and then the model was used for forecasting. Lawan, Abidin, Chai, Baharun, & Masri (2014) present an overview of some other wind speed prediction techniques applied historically and also compare their performances. They also introduce some other techniques such as neural networks, support vector machines and genetic algorithms and compare these with the traditional techniques such as: persistence model, ARMA, ARIMA, algebraic curve fitting methods and so on.

J. Liu, Ren, Wan, Guo, & Yu (2016) performed wind speed time series analysis using a variogram function to measure the rate of change of the wind speed. They concluded that higher the instantaneous variogram, the faster the change rate of the wind speeds. They calculated the autocorrelation and cross-correlation coefficients and found the existence of daily periodicity in the rate of change in wind speed, which was faster during daytime and weaker in the night time. From the cross-correlation analysis, they concluded that there was an obvious relationship between the hourly wind speed and its instantaneous variogram. They then developed a three-parameter power model to fit that relationship.

To check the self-similarity prevailing in natural phenomenon such as the disturbance storm time (Dst), la Torre, González-Trejo, Real-Ramírez, & Hoyos-Reyes (2013) used three algorithms namely spectral analysis, rescaled range analysis and Higuchi's algorithm. The self-similarity characteristic of a system can be measured by fractal dimension. They observed that the fractal dimension calculated with Higuchi's method may not be constant over all time scales.

However, when comparing the three methods for determination of fractal dimension, they concluded that FFT-methods lead to very low correlation coefficients, the rescaled range analysis showed good statistical properties but the existence of different dynamics in time series was not presented in detail. Higuchi's algorithm performed the best when determining the fractal dimension, clearly evidencing the complexity of the time series. These complexities are shown by presence of cross-over in the Higuchi plots (Higuchi, 1988), as shown in Figure 36.

This chapter explores the various methods used in wind speed time series analysis such as the frequency domain analysis and multifractal analysis. Since most commonly available wind speed data are hourly averages wind speed data and high frequency wind speed data (1 second average, 30 seconds average or 1 minute average) need to be synthesised as input for simulation and experimental work. The work in this chapter aims to recover the latter from the former.

The commonly available low frequency wind speed data (mostly hourly) is not enough for assessing any location's wind energy potential as the variability and intermittency present in the wind energy is exterminated by averaging. The results obtained by using these average values of wind speed for simulations might not be reliable. Therefore there is a need for high frequency wind speed data. A low frequency data cannot be used for determining the feasibility of proposed concept in this work. Therefore, a new algorithm for the synthesis of wind speed time series needs to be developed. A high sampling frequency wind speed time series can be generated using an available low sampling frequency time series data.

4.1 Sampling frequency and sampling duration

4.1.1 Sampling frequency

A sample is a value or a set of values of an observation/measurement at a point in time and/or space. Sampling frequency of a time series data is the number of samples measured or observed per unit time (generally expressed in seconds). Usually sampling frequency has a unit of Hz that in itself specifies that it is the number of observations or samples per second. It is also called the sampling rate.

$$f_s = 1/T \tag{18}$$

The Nyquist sampling theorem states that the highest frequency that can be determined corresponds to half the sampling rate (Smith, 1997). Therefore, the frequency equal to half of the sampling frequency is the highest detectable frequency and is called the Nyquist or folding frequency. The most effective way of preventing aliasing is by filtering a signal with a low pass filter with the cut-off frequency less than half of the sampling rate. Determining frequencies based on Nyquist sampling theorem is necessary for the reconstruction of the signal or for synthesizing new time series.

4.1.2 Sampling duration

The sampling interval/period is the time interval between each samples/observations. This can be 1 minute, 10 minute, and 1 hour and so on. The sampling interval is given by,

$$T = 1/f_s \tag{19}$$

where f_s is the sampling rate or sampling frequency.

4.1.3 Windowing

When a fast Fourier transform (FFT) is used to measure the frequency component of a signal, the FFT algorithm assumes that the data set is a finite set of data on which the analysis has to be made. The FFT transform also assumes that the data set results in a continuous spectrum that is one period of a periodic signal. The time domain and the frequency domain are circular topologies for the FFT, so it assumes that the two endpoints of the time waveform are connected together. The FFT of a measured signal that is periodic matches this assumption as an integer number of periods fill the acquisition time interval. However, if the number of periods in a signal is non integer, the finiteness of the measured signal may result in a truncated waveform having different characteristics from the original continuous-time signal and can also introduce sharp transition changes into the measured signal. These transitions are discontinuous.

These artificial discontinuities show up in the FFT as high-frequency components not present in the original signal. These frequencies can be much higher than the Nyquist frequency and are aliased between 0 and half of the sampling rate. Therefore the spectrum resulting from FFT, is not the actual spectrum of the original signal, but a chaotic version. It appears as if energy at one frequency leaks into other frequencies. This phenomenon is known as spectral leakage, which causes the fine spectral lines to spread into wider signals. This leakage can be improved using another procedure which is called windowing (National Instruments, 2017).

Windowing has its advantages in reducing the amplitude of the discontinuities at the boundaries of each finite sequence acquired by the measuring/recording instrument. It consists of multiplying the time record by a finite-length window with amplitude that varies smoothly and

gradually toward zero at the edges. This makes the endpoints of the waveform meet and, therefore, results in a continuous waveform without sharp transitions.

Several window functions can be used for FFT purpose. However, the performance of these windows can be compared and a best window for a particular application can be chosen. In general, the Hanning window is satisfactory in 95 percent of cases. It has good frequency resolution and reduced spectral leakage (National Instruments, 2017).

4.2 Autocorrelation of wind speed time series

Autocorrelation of a time series data is the linear dependence of a variable with itself at different points of time. It measures the correlation between data points in a set of data, for example correlation between points yt and $yt + h$, where $h = 0, \ldots, N-1$ and yt is a stochastic process. Wind speed time series data have been found to be highly auto-correlated with the previous data values within a single dataset (Philippopoulos & Deligiorgi, 2005). The autocorrelation for lag h is given by,

$$r_h = \frac{c_h}{c_0} \tag{20}$$

where

$$c_h = \frac{1}{N-1} \sum_{i=1}^{N-h} (y_t - \bar{y})(y_{t+h} - \bar{y})$$

$c_h$is the covariance of the two datasets,

c_0 is the lag 0 covariance which is also called the unconditional variance of the process.

Partial autocorrelation is the autocorrelation between yt and $yt-h$ after removing any linear dependence on $y1$, $y2$, ..., $yt+h-1$. The partial lag-h autocorrelation is denoted by $\phi_{h,h}$.

(a)

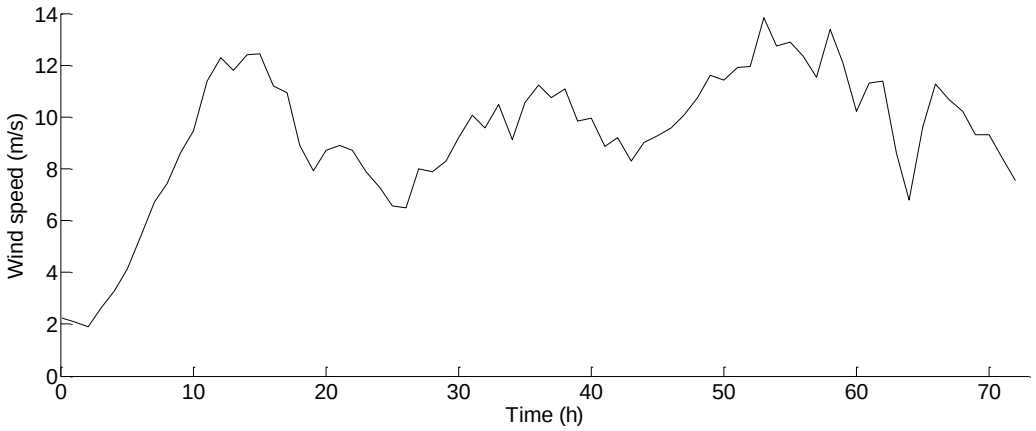

(b)

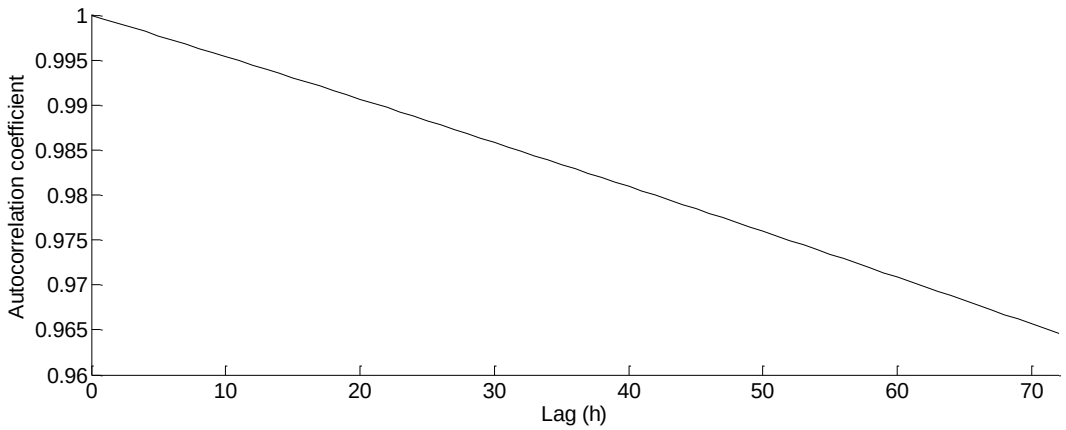

Figure 25: (a) Hourly averages, (b) Autocorrelation coefficients for hourly averages wind speed data at different lags. Data from Roskrow, Barton farm, UK for 3 days (72 hours)

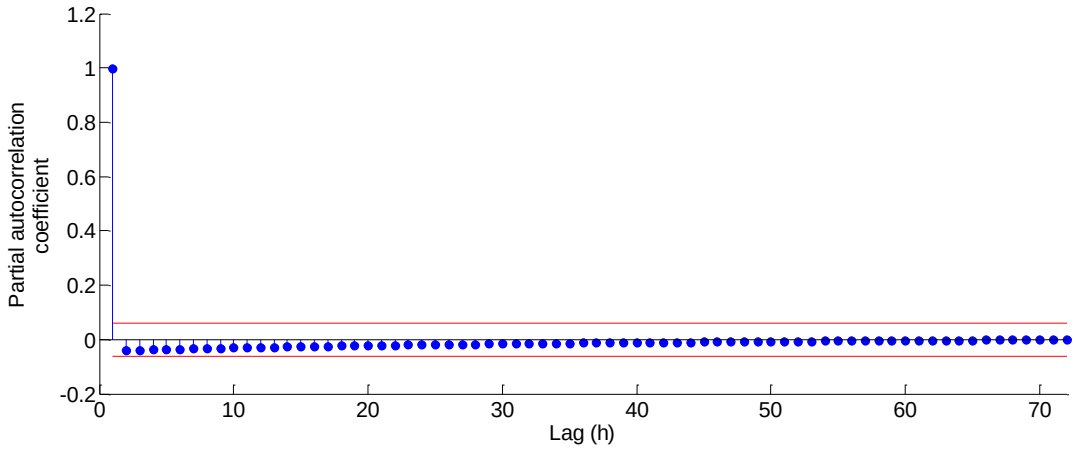

Figure 26: Partial correlation coefficients for hourly averages wind speed data at different lags. Data from Roskrow, Barton farm, UK

Autocorrelation coefficient and partial correlation coefficient are useful measures in determining the order for Auto-Regressive Moving Average, (ARMA) model which is explained later in Section 4.2.3. It becomes very difficult to determine the order of any model with only the autocorrelation coefficient information as presented in Figure 25(b) for the wind speed data shown in Figure 25(a). This is usually the case for the wind speed time series data, as they are highly correlated with themselves for a specific duration. The coefficient however decreases with increasing lag (can be time duration or distance). Therefore, for determining the order for fitting ARMA model, partial autocorrelation coefficient has to be calculated. The partial correlation coefficient information for the same wind speed data (Figure 25(a)) is presented in Figure 26. In MATLAB, this can be done by using the function '*aryule'.*

4.2.1 Lag

The time series data are usually plotted on a scatter plot where the data points are separated from each other by certain values. These values are called lag. The support variable in which the lag is expressed can be either distance or time. But for time series data, it is usually time as

shown in Figure 25 and Figure 26. Lag is usually represented by 'h'. The importance of lag value in time series data analysis is because of the fact that two data close to each other are more likely to have similar values than two data that are far apart. This holds specifically true for wind speed time series data.

4.2.2 Correlation and Correlation coefficient

Correlation is the relation between two datasets or variables from the same dataset. There are three possible patterns that can be observed on a plot defining the relation between two variables. Namely, the variables can be positively correlated, negatively correlated or not related.

Two variables are correlated if one variable tend to be associated with another variable or if the variables have mixed dataset of smaller and larger values, the larger values of one variable tend to be associated with the larger values of another variable. The variables are negatively correlated if the larger values of one variable tend to be associated with the small values of another variable. The possibility of the two variables being not related is when the increase in one variable has no apparent effect on the other and that is why they are said to be uncorrelated (Isaaks & Srivastava, 1989).

The correlation coefficient, ρ, is a measure that is most commonly used to summarize the relationship between two variables and can be written as,

$$\rho = \frac{\frac{1}{N}\sum_{i=1}^{N}(x_i - m_x)(y_i - m_y)}{\sigma_x \sigma_y} \tag{21}$$

where N is the number of data, x_1, x_2,..... x_N are the data points for the first variable, m_x is their mean, σ_x is their standard deviation, y_1, y_2,..... y_N are the data points for the second variable,

m_y is their mean and σ_y is their standard deviation. The numerator in equation (21) is called the covariance, which is given by,

$$C_{XY} = \frac{1}{N} \sum_{i=1}^{N} (x_i - m_x)(y_i - m_y) \quad (22)$$

The covariance between two variables depends on the magnitude of the data values (Isaaks & Srivastava, 1989).

4.2.3 Auto-Regressive Moving Average (ARMA) and variants

The auto-regressive moving average model is known to be a useful tool for defining the individual time series. With the help of this model, one can predict the values of a specific time series which is given by the linear combination of the past values (Lawan et al., 2014). A pth order ARMA model for a stochastic process, y_t can be represented by the equation:

$$y_t = \alpha + \sum_{i=1}^{p} \phi_i y_{(t-i)} + \sum_{i=1}^{q} \theta_i \varepsilon_{(t-i)} \quad (23)$$

where, y_t is the time series data to be modeled, α is the process constant, $(\phi_1, \phi_2, \dots \dots \phi_p)$ are the AR parameters, $(\theta_1, \theta_2, \dots \dots \theta_p)$ are the MA parameters and ε_t is a white noise process. A signal or a sequence ε_t is called a white noise process if each ε_t in the sequence has a zero mean and covariance of σ^2.

The ARMA process involves the computation of a component from known information up to a period of *t-1* that gives the auto-regressive component. Another component, which is the uncertainty of the mean of the time series, y_t, is the moving average component. The ARMA model parameters are often estimated by a least squares minimization process, which looks for the best-fit curve to a set of time series values by minimizing the sum of the squares of the

residuals, the differences between the values of the time series and the same values reproduced by the model (Gomes & Castro, 2012).

For the ARMA model forecasting and prediction, the AR and MA orders are first selected using the autocorrelation and partial autocorrelation coefficients as explained earlier in this Section. The estimation of the model parameters is done through the least squares minimization process and finally the prediction of the future value of the time series is done. The time series used for the ARMA model, the fitted model and the output results for 1 step ahead and 5 step ahead predictions using 4^{th} order ARMA are presented in Figure 27, Figure 28, and Figure 29 respectively. This was performed using system identification toolbox in MATLAB.

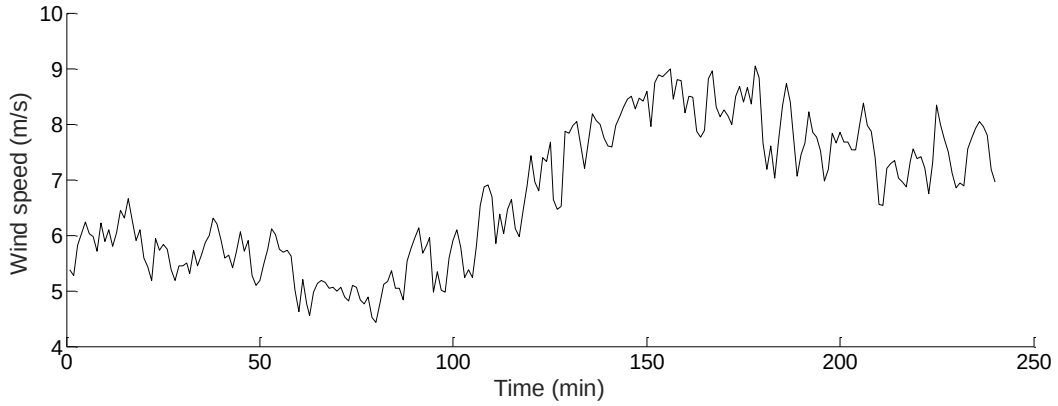

Figure 27: Wind speed time series used for ARMA modelling

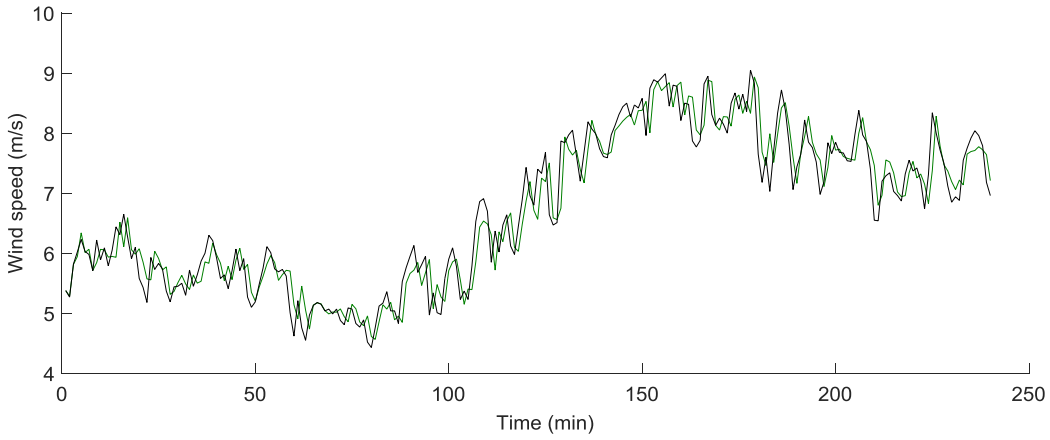

Figure 28: Measured and 1 step ahead predicted wind speed (m/s) using ARMA model

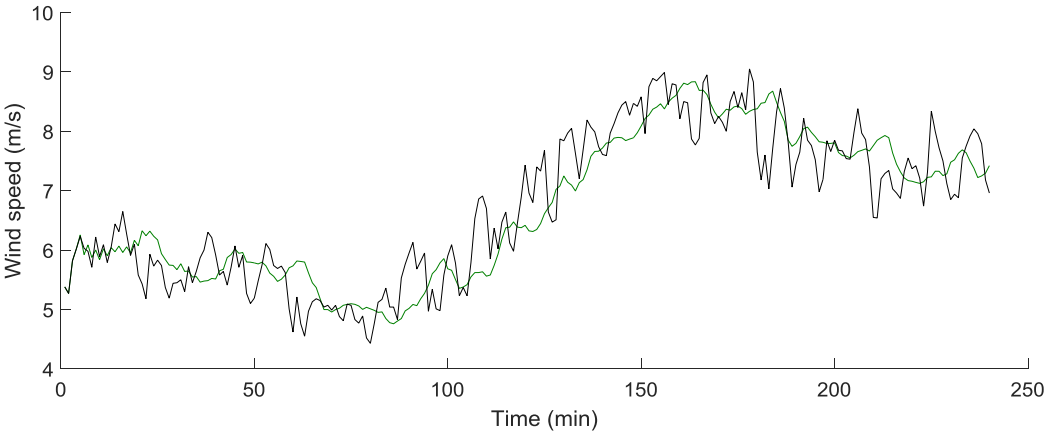

Figure 29: Measured and 5 step ahead predicted wind speed (m/s) using ARMA model

From the results obtained for the ARMA model and prediction, the best fit was 72.6% for a 4^{th} order ARMA model for 1 step ahead prediction and 58.2% fit 5 step ahead predictions. Both the results are obtained with confidence level of 99%. It is obvious that as the number of steps for prediction is increased, the fit of the model decreases. Therefore this may not be the right model for wind speed predictions and simulations of the performance of cryocoolers coupled to wind rotors.

4.3 Frequency domain analysis

Frequency domain representation of a time domain representation is obtained by performing Fast Fourier Transform. It is a different way to look at the same signal. In the frequency domain the magnitudes of data points are amplitudes of periodic signal components present at varying frequencies (National Instruments, 2017).

4.3.1 Fast Fourier transform

Fast Fourier transform (FFT) gives a clear picture of the prevalent cycles in any time series data. Fourier's theorem states that any waveform in the time domain can be represented by the weighted sum of sines and cosines. The FFT decomposes any function into a sum of sinusoidal basis functions. It is a mathematical formula which relates a signal sampled in time or space to the same signal sampled in frequency. Each of these basis functions is a complex exponential of a different frequency. The Fourier Transform therefore gives us a unique way of viewing any function - as the sum of simple sinusoids (Smith, 1997).

$$F\left(g(t)\right) = G(f) = \int_{-\infty}^{\infty} g(t) e^{-2\pi i f t}\, dt \tag{24}$$

The result is a function of f, or frequency. As a result, $G(f)$ gives how much power $g(t)$ contains at the frequency f. $G(f)$ is often called the spectrum of g. In addition, g can be obtained from G via the inverse Fourier Transform:

$$F^{-1}\left(G(f)\right) = \int_{-\infty}^{\infty} G(f) e^{2\pi i f}\, df = g(t) \tag{25}$$

Fast Fourier transforms are performed in this work to retrieve the amplitude and phase spectrum of the available wind speed data. This step will let us determine what information of the wind speed data is contained in the amplitude, power and phase spectrum. This will also let us characterise the phase information contained in the wind speed data, for example to

determine if it is a white noise or a brown noise. The definitions for the white and brown noise in terms are presented in Section 4.3.7. This information is required for the synthesis of wind speed data.

4.3.2 Preparation of frequency array

For the preparation of frequency array, the bin values are assigned first.

$$B = 0, 1, 2, \ldots., N - 1 \tag{26}$$

where N is the total number of data points

Then, frequency in Hz in each bin is given by,

$$f(Hz) = \frac{Bf_s}{N} \tag{27}$$

where f_s is the sampling frequency (data points/sec)

When performing fast Fourier transform, the total data points are divided into half following the Nyquist sampling frequency theorem because the last half are only the mirror images of the first half.

4.3.3 Amplitude spectrum

The FFT function in MATLAB calculates the complex discrete Fourier transform (DFT). Its results are therefore a series of complex numbers that contain both the real and imaginary parts which need to be converted to polar form to obtain magnitude and phase. The amplitude of the FFT is related to the number of points in the time-domain signal. The amplitude spectrum of a signal A can be computed by the following equation,

$$Amplitude\ spectrum = \frac{Magnitude[FFT(A)]}{N} = \frac{\sqrt{[real[FFT(A)]]^2 + [imag[FFT(A)]]^2}}{N} \quad (28)$$

The amplitude information can be extracted in MATLAB using the function 'abs' in the format Abs(fft(signal)). The wind speed data (m/s) from Roskrow Barton, UK used for analysis is presented in Figure 30 and the amplitude spectrum is generated as shown in Figure 31.

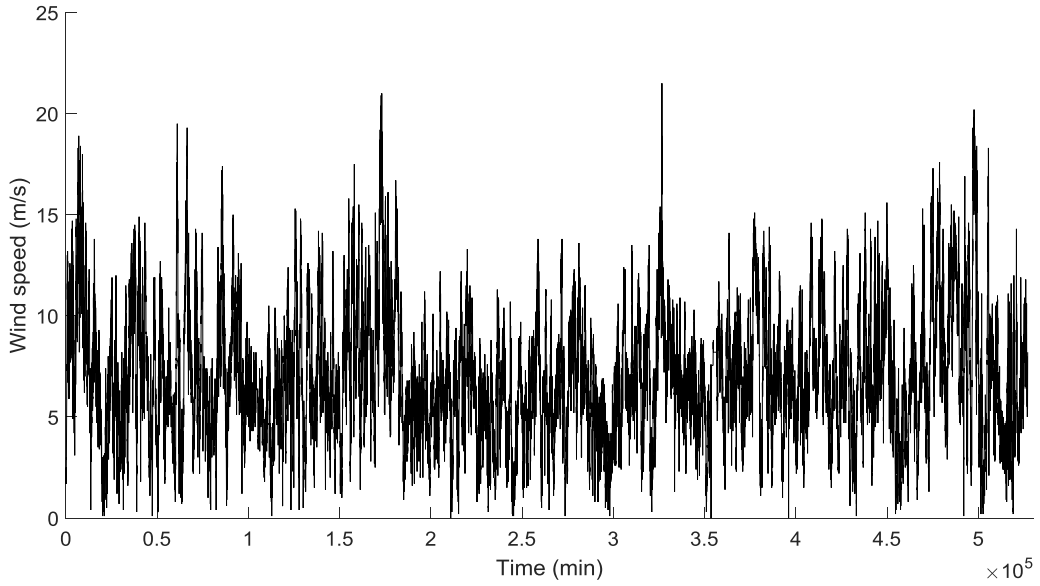

Figure 30: Measured 10 minute average wind speed data (m/s) used for data synthesis. Data from Roskrow Barton farm, UK

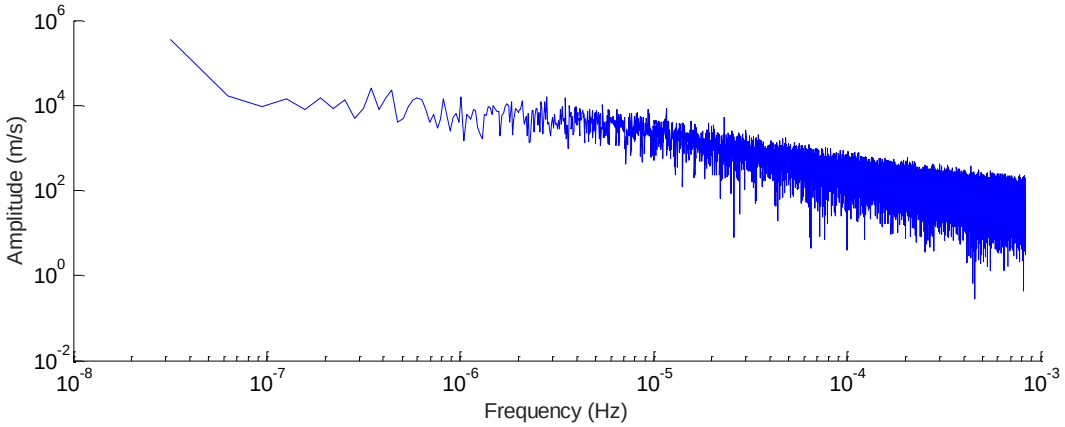

Figure 31: Magnitude spectrum for 10 minute average wind speed data from Roskrow, Barton farm, UK

4.3.4 Power spectrum

A time-domain signal can be converted into frequency domain signal by using the FFT function. The DFT or FFT of a real signal is a complex number, having a real and an imaginary part. The power in each frequency component represented by the FFT is an array that contains the two-sided power spectrum of a time-domain signal. The array values are proportional to the amplitude squared of each frequency component that makes up the time-domain signal. A two-sided power spectrum comprises of negative and positive frequency components at a height of $A_k^2/4$ where A_k is the peak amplitude of the signal at frequency k. The DC component has a height of A_0^2 where A_0 is the amplitude of the DC component in the signal at frequency 0 (National Instruments, 2009).

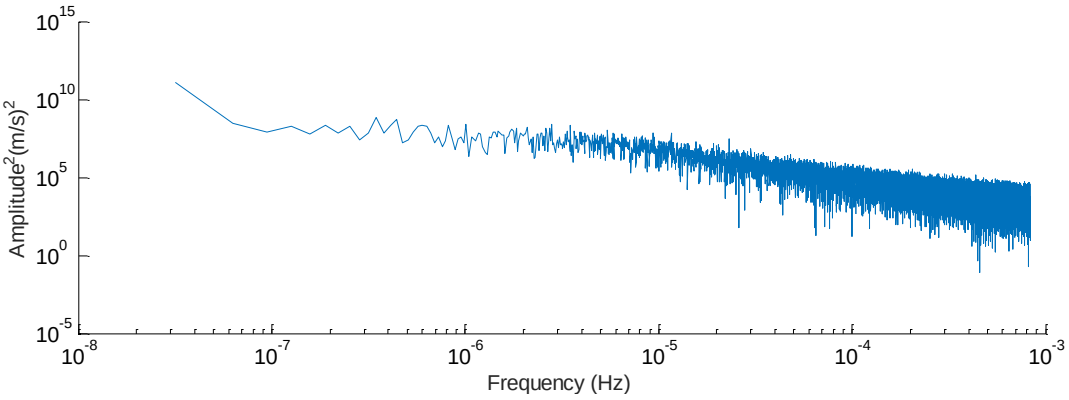

Figure 32: Power spectrum plot for 10 minute average wind speed data from Roskrow Barton farm, UK

Since the two-sided power spectrum consists of both the negative and positive frequency components over the duration of the signal, mostly single-sided power spectrums are considered to determine the power in a given signal. An example of such is presented in Figure 32. Therefore the values for the frequency components in a single-sided power spectrum are at a height of $A_k^2/2$ which can also be written as, $\left(A_k/\sqrt{2}\right)^2$ where $A_k/\sqrt{2}$ is the root mean square

(rms) amplitude of the sinusoidal component at frequency k (National Instruments, 2009). Thus, the power in the kth frequency component—that is, the kth element of the DFT or FFT is given by,

$$Power = S(f) = A_k^2/2 \quad (29)$$

where A_k is the magnitude of the frequency component k.

The power spectrum shows power as the mean squared amplitude at each frequency line but includes no phase information.

4.3.5 Phase spectrum

The phase information returned by the FFT is the phase that is relative to the start of the time-domain signal. For example a sine wave shows a phase of -90° at the sine wave frequency whereas a cosine shows a 0° phase (National Instruments, 2009). Since the FFT returns the spectrum in a complex form which is a mixture of real and imaginary parts, these must be converted to polar form to obtain the magnitude and phase as explained earlier in Section 4.3.3. The following equation is used to extract the phase information from the FFT of a signal A.

$$Phase = arctan\left(\frac{imag[FFT(A)]}{real[FFT(A)]}\right) \quad (30)$$

In MATLAB, it can be obtained by using the function, angle(FFT(A)), and can be plotted as Figure 33 and Figure 34.

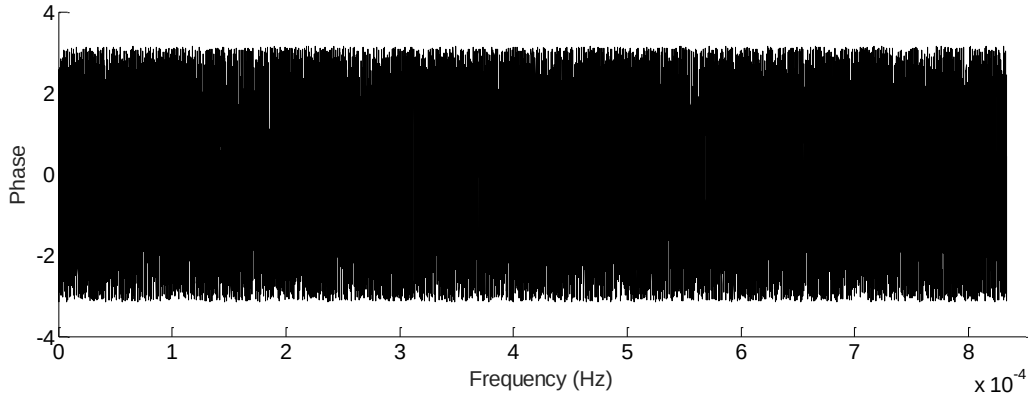

Figure 33: Phase spectrum presenting phase values at different frequency for 10 minute average wind speed data from Roskrow Barton farm, UK

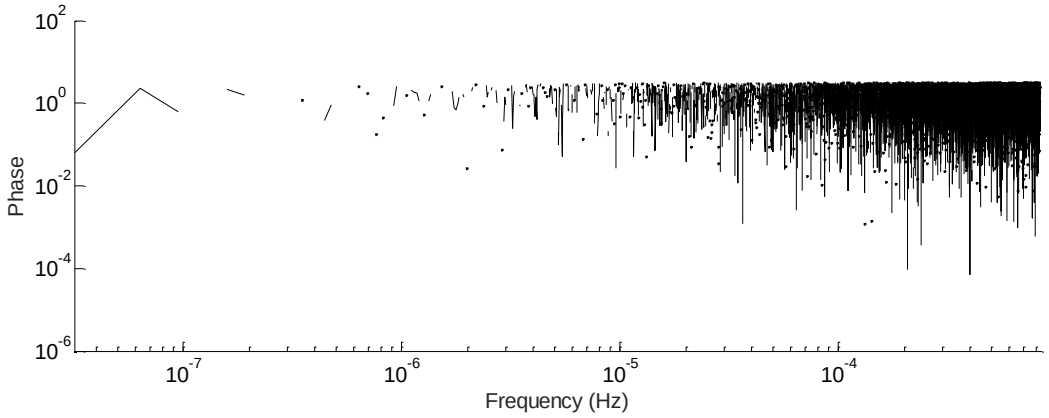

Figure 34: A logarithmic plot of the phase spectrum for 10 minute average wind speed data from Roskrow Barton farm, UK

The logarithmic plot for the phase spectrum is shown in Figure 34. The breaks between the data points is due to the presence of negative values in the phase information of the data, that varies from $+2\pi$ to -2π, as was presented in Figure 33. However, the curve in Figure 34 had a fractal dimension of 1.97, indicating that it is random.

4.3.6 Modelling the power spectrum

The discrete implementation of the power spectrum $S(f)$ is given by equation (29). The power spectrum results are always real unlike the FFT. The power spectrums obtained from the FFT are fitted using a power law equation of the form,

$$y = af^{\beta} \tag{31}$$

where a is the amplitude, f is the frequency and β, is the power exponent which is also called the decay rate. The power exponent β is related to the fractal dimension of the time domain signal by the relations explained in the section that follows immediately. Different types of noise in a signal can also be defined in terms of β values.

4.3.7 Fractal dimension from power spectrum

The relation between the fractal dimension and power exponent β is given by (Higuchi, 1988),

$$D = \frac{5-\beta}{2} \tag{32}$$

The power spectral density of a time series $X(t)$ can also be written as,

$$S(f) \propto af^{-\beta} \tag{33}$$

The quantity is the power in time series associated with the frequency in the interval, β is the power exponent which defines the dynamic behaviour of the time series $X(t)$. For example, $\beta = 0$, for white-noise processes, which are uncorrelated and have a power spectrum that is independent of frequency. When $\beta = 1$, the systems are moderately correlated. The systems are highly correlated for $\beta = 2$, or brown noise type systems (la Torre et al., 2013).

4.3.8 Relation between average wind speed and magnitude spectrum

The average wind speed of any dataset is reflected as the first component of the magnitude spectrum when FFT is performed on the dataset. It represents the average of all the samples within the window of the signal considered. It is real for a set of data containing real values and does not contain imaginary part. For example, the first component of the magnitude spectrum in

Figure 31 is 364700, which divided by the number of samples (i.e. 52704), gives the mean wind speed of 6.92 of that dataset.

4.3.9 Relation between wind speed variability and power spectrum

A power spectrum has also been defined as a measure of the contribution of oscillations of continuously varying frequencies to the variability of a variable. For example when wind speed is taken as the variable, the variance is proportional to the kinetic energy of the wind speed fluctuations (Van der Hoven, 1956). The power spectrum presents the information on the frequencies on which the power of the signal is distributed. It is very helpful in determining the major cycles for the signal and their occurrences for the total time period considered. For example in Figure 31 for the magnitude and/or power spectrum for one whole year, the major cycle in the wind speed variability is one year cycle, the second highest is the monthly cycle and the third highest is the daily or ~24 hours cycle.

4.4 Multifractal analysis

The fractal dimension (D) is a measure of self-similarity of an object. It can also be taken as a measure of irregularity of a time series data. Larger the fractal dimension, more random the data (Chang et al., 2012). Therefore, the concept of fractal dimension in chaos theory can be applied for characterizing the wind speed behaviors. The algorithm chosen for the fractal analysis of the wind speed data is presented in this section, which will be used in the sections that follow for the synthesis of a new wind speed time series data, for simulation purposes.

4.4.1 Higuchi algorithm

Several analyses such as spectral analysis, rescaled analysis, semi-variogram analysis, Higuchi's algorithm, (as cited in la Torre et al., 2013; Chang et al., 2012; & Tetsuya, 2002) have been published for the calculation of fractal dimension of a signal. However, for this work, Higuchi's algorithm has been used to determine the fractal dimension of wind speed time series data. This is because the variability evident in the wind speed time series at different time scales are revealed very well with the help of this algorithm. The algorithm for calculating fractal dimension is as follows (Higuchi, 1988).

1. A finite set of time series is considered which is taken at a regular interval:

   $X(1), X(2), X(3), \ldots . X(N)$

2. A new time series is constructed from the given time series which is:

   $$X_k^m; X(m), X(m+k), X(m+2k), \ldots, X\left(m + \left[\frac{N-m}{k}\right].k\right) \quad (m = 1,2, \ldots, k)$$

where [ ] denotes Gauss notation and both k and m are integers, m and k are initial time and interval time respectively. Therefore for a time interval of k, we get k sets of new time series.

An example for a list of time series generated with a time interval of $k = 3$, and $N = 100$, is as follows (Higuchi, 1988):

$X_3^1; X(1), X(4), X(7), \ldots, X(97), X(100)$

$X_3^2; X(2), X(5), X(8), \ldots, X(98)$

$X_3^3; X(3), X(6), X(9), \ldots, X(99)$

The length of the curve, X_k^m, is defined as (Higuchi, 1988):

$$L_m(k) = \left\{\left(\sum_{i=1}^{\left[\frac{N-m}{k}\right]} |X(m+ik) - X(m+(i-1).k)|\right)\frac{N-1}{\left[\frac{N-m}{k}\right].k}\right\}/k. \quad (34)$$

The term $N-1/\left[\frac{N-m}{k}\right].k$ represents the normalization factor for the curve length of subset time series. The length of the curve for the time interval k, $L(k)$ is defined as the average value of k sets of $L_m(k)$. According to (Higuchi, 1988), if $L(k) \propto k^{-D}$, then the curve is fractal with the dimension – D.

4.4.2 Modeling Higuchi plots

Higuchi plot is generated by plotting the lag length versus the length of the curve in logarithmic scale. A straight line is fitted to the points by the least-square method. The slope of the line as shown in Figure 35 represents minus fractal dimension (Higuchi, 1988).

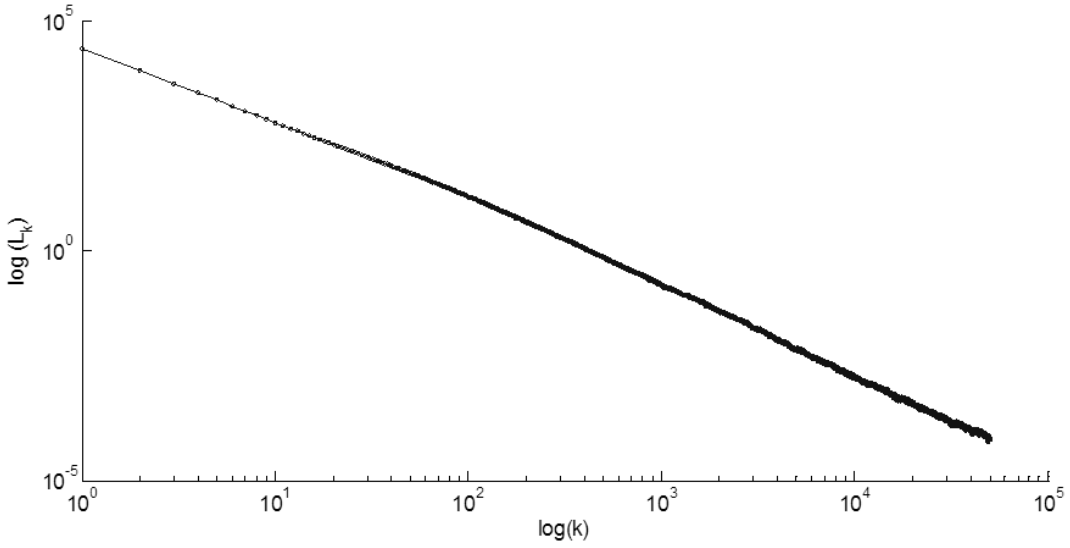

Figure 35: A typical Higuchi plot generated for wind speed time series data from a wind farm in Roskrow Barton, Cornwall, UK

Higuchi plot in Figure 35 presents a logarithmic plot of average length of time series, $L(k)$, versus that lag length, k, for the wind speed data for Roskrow Barton wind farm, Cornwall, UK. The wind speed time series samples are contiguous 10 minute averages so that

fundamental lag dimension is 10 minutes. The number of samples used to compute the average length is 300, where the starting indices in the time series, m, are equally interspaced over the complete time series sampling interval. The total length of time series is 8784 hours.

4.4.3 Domains of self similarity & calculation of domain fractal dimension

The fractal dimension is calculated as the slope of the line from the $log(Lk)$ Vs $log(k)$ as is shown in Figure 35. A best fit line is fitted to the Higuchi plot on MATLAB. According to (Higuchi, 1988), the self-similarity of the data points are determined by the slope of the line. The fractal dimension ranges between 1 and 2. Greater the fractal dimension, greater is the self-similarity of the data-points with each other.

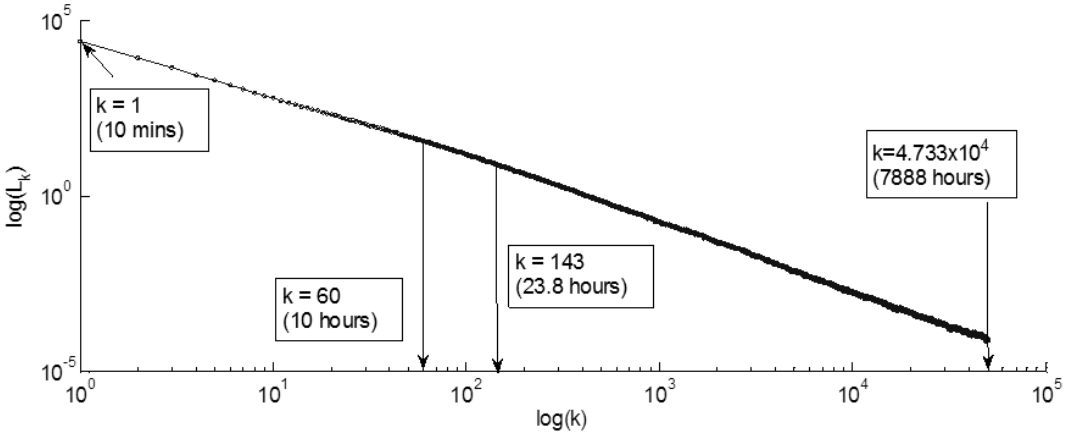

Figure 36: Higuchi plot showing cross-over indicating that the fractal dimensions for this set of wind speed data could be more than one slope (more than one value for fractal dimension)

As shown in Figure 36, the wind speed data over a year can have different values of fractal dimensions over different time scales. For example, it can have one value of fractal dimension for lags of $k = 1\ to\ 60$ (time period of 10 minute to 10 hours), another value for $k = 61\ to\ 143$ and so on. When the fractal dimensions were calculated for this particular wind speed time series data, the first fractal dimension D_1 was found to be 1.587 for lag of $k = 1\ to\ 60$ (time

period of 10 minute to 10 hours), the second fractal dimension D_2 was found to be 1.765 for lag $k = 61\ to\ 143$ and the third fractal dimension D_3 was found to be 1.999 for lag $k = 143\ to\ 47330$. The changes in the fractal dimensions for the time series data, referred as 'cross-over' can be related to the changes or the dynamics in the wind speed data over those time periods.

4.4.4 Comparison of the methods for determination of the fractal dimension

The determination of fractal dimension for time series data is important in this work so that one can generate self-similar time series data that can be essential to perform simulation works. On the assumption that a wind speed time series contains self-similar characteristics, quantifying and characterizing that self-similarity through determination of the fractal dimension then permits said fractal dimension to be used to condition synthesis of high frequency time series from lower frequency time series (to meet the needs of the cryogen production from wind energy simulator).

4.4.5 Options for computing fractal dimension

Fractal dimension can be determined by various other techniques. The techniques applied in this work for comparison reasons are spectral analysis, Higuchi process, variogram method, and correlogram method. The power spectrum obtained by FFT presents appreciable fluctuations, which can make the determination of the power exponent β from plots such as Figure 32 difficult. On the other hand, with Higuchi's method for determining fractal dimension, determining fractal dimension is clearer. The power exponent β and Hurst exponent H can then be derived from the fractal dimension D (Higuchi, 1988). Use of Higuchi's algorithm for fractal dimension D is also useful in indicating the presence of cross-over in the time series data (if

any). Cross-over indicates non-stationary wind speed variability character over different time periods, and is deemed to be an (intuitively) desirable facility to embed within the wind speed time series synthesis process. This non-stationarity is evident in Figure 36 and discussed in Section 4.4.3.

4.4.6 Characterisation of white and brown noise

Any digital signal can be analysed for different types of noise depending on different measures such as the mean, standard deviation, power exponent (derived from the power spectrum), the fractal dimension (the self-similarity feature), and the Hurst exponent.

The white noise and brown noise are defined in terms of the power exponent β. If $H = 0$, the signal contains the white noise and if $H \approx 0.5$, then the signal contains the brown noise.

The power exponent β is related to the fractal dimension D by the following equation,

$$D = \frac{5-\beta}{2} \tag{35}$$

The relation between the fractal dimension $D$and the Hurst exponent H is given by,

$$D = 2 - H \tag{36}$$

Finally the Hurst exponent and the power exponent are related by the equation,

$$\beta = 2H + 1 \tag{37}$$

Therefore, the required exponents can be calculated using the equations provided to determine if the signal contains or indeed is white noise or brown noise.

4.4.7 Using Higuchi algorithm to compute the fractal dimension of the phase spectrum

Given any time series data, the Fast Fourier Transform (FFT) is calculated. The phase and amplitude spectrum of the transform are calculated. Subjecting Figure 33 (the phase spectrum of a wind speed time series) to analysis to determine its fractal dimensions and other metrics reveal that the phase spectrum of the wind speed time series data behave as a white noise with a mean of zero and defined standard deviation. This is useful because it means that phase spectral components of a wind speed time series can be generated randomly (or pseudo-randomly). Knowing that the phase spectrum is a white noise, we can randomise it for the purpose of synthesising new wind speed time series data. To illustrate this can be done by calculating the fractal dimension using the Higuchi's algorithm as discussed earlier in Section 4.4.1.

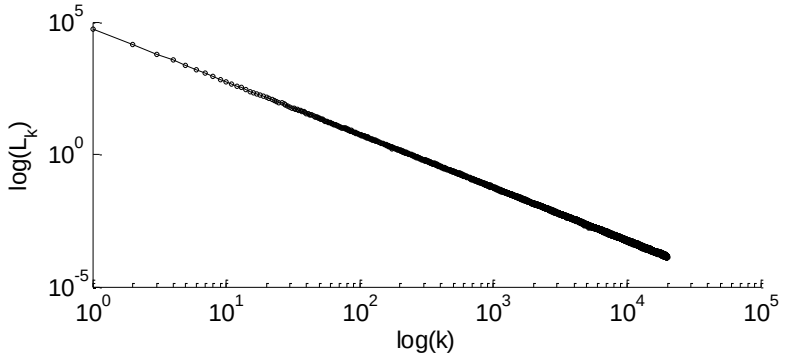

Figure 37: Higuchi plot for phase spectrum of one year worth of wind speed data from Roskrow Barton wind farm, UK

From Figure 37, the fractal dimension of the phase spectrum of Figure 37 is 1.97, which means the Hurst exponent, H is 0.034 which is close to 0, indicating the phase spectrum is completely a white noise.

4.4.8 Steps for generating high sampling frequency wind speed time series data preserving the variability in them

A novel method introduced in this section is expected to generate higher sampling frequency wind speed time series data such as 4Hz from the available lower sampling frequency data of 10 minute averages. For illustrations, the SWMTF 4Hz data is taken, and 10 minute averages were then calculated. Then assuming that we were given only 10 minute averages, model was developed further.

A power spectrum is first plotted after performing the FFT on the available wind speed time series data. Further, for illustration and comparison purposes, the power spectrum for 4Hz data (in red) is also presented in Figure 38. The gradients of lines on the power spectrum plot are defined by the fractal dimensions obtained from the Higuchi plot, as discussed in Section 4.4.1 and Section 4.4.2. As wind speed data records from a site are almost always hourly, the power (Amplitude^2) value at a frequency corresponding to 1 hour can be obtained from the experimental Fourier power spectrum – by averaging over a small window and plotted over the power spectrum to provide an 'anchor point' for fitting, as shown in Figure 38.

The power spectrum components of different sampling frequencies are found to be related by,

$$W(0)_{4Hz} = W(0)_{10\min} \cdot (f_{4Hz}/f_{10min})^2 \quad (38)$$

where, $W(0)_{4Hz}$ is the first power component of the higher sampling frequency (in this case 4Hz) power spectrum when transposing, $W(0)_{10\min}$ is the first power component of the available lower sampling frequency (in this case 10 min) power spectrum, f_{4Hz} is the sampling frequency of the higher sampling frequency wind speed time series data (in this case 4Hz) and

$f_{10\min}$ is the sampling frequency of the available lower sampling frequency wind speed time series data (in this case 10min).

The following steps can be applied for the synthesis of higher sampling frequency such as 4Hz from a lower sampling frequency wind speed time series data such as 10 minute.

Step 1: Plot the power spectrum of the available wind speed time series data (green in Figure 38).

Step 2: A line is then fitted that envelopes the high frequency components of power spectrum in the lower bound, which was found to be a line with a fractal dimension of 1.0 to 1.4 in this analysis.

Step 3: Apply a power transformation to the 10 minute data, so that the power values correspond to those that would be logged at 4 Hz, using equation (38). The result is magenta coloured power spectrum in Figure 38.

Step 4: Apply Higuchi procedure to establish the fractal dimensions of either the 10 minute data or the transformed 4 Hz data.

Step 5: Transform the power spectrum fit to 4 Hz from 10 minutes.

Step 6: Extend the fitted model to the 4 Hz sampling frequency.

Step 5: Randomly generate power values within the specified zone (in this case yellow zone in Figure 38), for frequencies above the highest in the hourly data. Invert the resulting power spectrum (with random phases for each frequency) back to the time domain using inverse FFT.

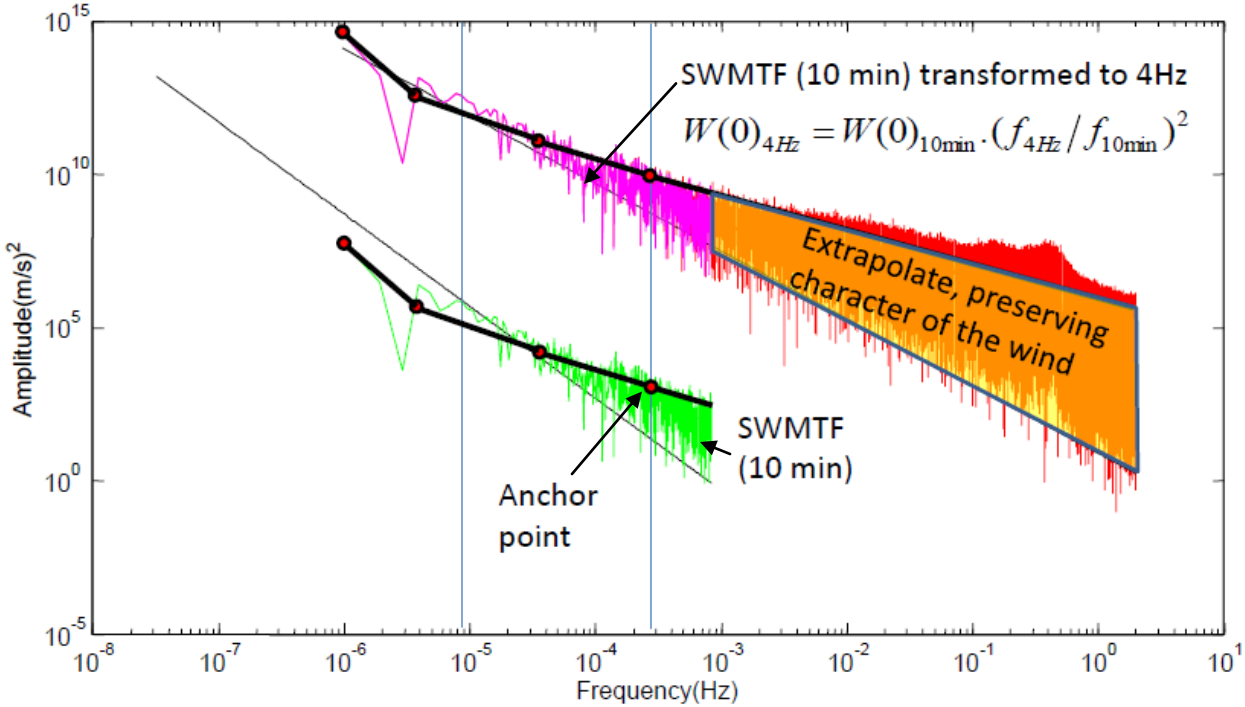

Figure 38: Pictorial representation of the novel method for generation of high sampling frequency wind speed time series data from available lower sampling frequency data. Synthesis of wind speed time series data using this method is in progress.

The desired higher sampling frequency wind speed time series data can now be generated. However, further work is needed on the synthesis of wind speed time series data using this method, which was out of scope of this thesis but the work will be presented in a peer-reviewed journal article when completed.

4.5 Summary

This chapter started with the definitions of some of the general terms for time series and frequency analysis. It then presented detailed time series analysis of wind speed time series data, reviewed some of the works completed earlier, and presented a novel method for the wind speed time series analysis. It also presented the methods for performing time series analysis such as the frequency domain analysis and fractal analysis. Introduction of Higuchi algorithm in wind speed time series data was done. This chapter then ended with a novel method that will be used in the synthesis of higher sampling frequency wind speed time series data, such as 4Hz when only low frequency wind speed time series data such as 10 minutes or 1 hour averages are available. This method can be applied to any time series data.

There might be a relationship between the Weibull shape parameter and fractal dimension for a time series data. However, existence of such a relationship can only be concluded with further investigations. It was also conceived that the first component of the magnitude spectrum is the average of the dataset whenever an FFT is performed on any dataset. It was concluded that the ARMA prediction model allows obtaining results that worsen with increasing time horizons.

The fractal analysis executed in this chapter suggested that wind time series data is multifractal (trifractal) for the particular wind speed data obtained from Roskrow Barton wind

farm for the year 2010. The Higuchi algorithm used in this chapter is a clear way to exhibit the multifractal character of wind speed time series as the changes in the fractal dimensions for the time series data at different lags can be easily depicted. These cross-over present in the Higuchi plot can be related to the dynamics in the wind speed data over time periods. For our knowledge, the Higuchi algorithm has been used for the first time for the wind speed time series data analysis till date. However, to confirm if all the wind speed time series data exhibit the multifractal behavior, further work may be required for the same wind speed data source (for different years) and also with different wind speed data.

A relation for the power components of the higher sampling frequency data and lower frequency data was also established which allowed the transformation of different sampling frequency power spectrums possible as shown in Figure 38 and discussed in Section 4.4.8. For our knowledge, this relation has also been reported for the first time. This relation was the crucial step towards the development of novel method presented in Section 4.4.8. The novel method developed in this chapter that is based on frequency and fractal studies can be used for the generation of higher sampling frequency time series data which is the end product of this chapter. The method has been developed but the synthesis part could not be covered in this thesis and will be presented in a peer-reviewed journal article. A high sampling frequency wind speed time series can be generated from available low sampling frequency wind speed time series data using this novel model introduced in this chapter. The higher sampling frequency wind speed time series data are necessary as input for the simulation work for large scale CryoVent systems, such as those presented in Chapter 10 to determine system performance and also to determine major specifications for some of the system components such as hydraulic accumulator. Hydraulic accumulators are discussed in detail in Chapter 6 and the simulations for large scale CryoVent system are presented in Chapter 10.

5 A review of gas refrigeration and liquefaction systems

The production of liquefied gases evolved from the basic vapor compression system. The Joule-Thomson effect (which is the cooling effect obtained when a compressed gas is allowed to expand) was first discovered in 1852 and oxygen was first liquefied between 1877-1883. Carl Von Linde produced 3 liters/hr of liquid oxygen for the first time in 1895 and the tonnage scale production started in 1910 (Radebaugh, 2007). Following Linde's production of liquid oxygen, other inventors liquefied other gases such as hydrogen, nitrogen, helium, and natural gas. Some used the same concept as Linde's while others modified this system to reach the boiling points of other gases.

A full scale CryoVent includes a variable speed wind turbine rotor coupled to a hydrostatic transmission which is then coupled to the gas liquefaction system. This compressor will be the key input work component to a refrigeration or gas liquefaction system. A review on the gas refrigeration and liquefaction techniques, and the different components used in these systems are therefore necessary. These are presented in this chapter. This chapter presents the introduction and working principles of Joule-Thomson effect, vapor compression refrigeration, reversed Brayton refrigeration, ideal liquefaction system, simple Linde-Hampson cycle, Stirling cycle refrigeration, Gifford-McMahon cryocooler, and pulse tube cryocooler. A thermodynamic performance comparison of some liquefaction systems is also presented in this chapter. This chapter is helpful in determining the amount of energy that will be required drive a gas liquefaction system in the context of CryoVent project.

5.1 Joule-Thomson effect

Lower temperatures are produced for the gas liquefaction systems mostly by using an expansion valve or Joule-Thomson valve (Barron, 1985). The expansion process is usually (but not always) isenthalpic and allows for an increase in the volume of the fluid; however the temperature decreases when a high pressure fluid is allowed to expand. Despite the fact that the flow within the valve is irreversible and not an isenthalpic process, the inlet and outlet states lie on the same enthalpy curve (Barron, 1985). Expansion devices reduce the high pressure of the condensing refrigerant to low evaporating pressure and also regulate the liquid-evaporator flow. The isenthalpic expansion method requires no moving parts and is easy to apply, explaining its wide use (Van Sciver, 2012). For example, different types of expansion valves used in current refrigeration and air conditioning systems are capillary tubes, constant pressure or automatic expansion valves, thermostatic valves, orifices, float valves, manual and electronic expansion valves (Dincer & Kanoglu, 2010). Air motors, expansion turbines are examples of non-isenthalpic expansion devices among others that produce work. Although reciprocating compressors are required to provide work input to the cryocooler for Cryovent, there is more flexibility in the choice of expander, particularly in recuperative systems, and use of a working expander will reduce the net work input to the liquefaction cycle.

The function of an expansion valve is to allow a high pressure gas to expand, thus reducing its pressure. Isenthalpic devices are well represented by a Joule-Thomson valve. Upon expansion, the formerly pressurized gas attains a much lower pressure and increases its volume. The temperature of the gas, which was increased initially during the compression process, is also lowered. The main function of the Joule-Thomson valve is to allow isenthalpic

expansion of the gas, thus reducing its temperature enough to liquefy the gas (Van Sciver, 2012) as shown in Figure 39. The Joule-Thomson coefficient is given by,

$$\mu_{J-T} = (\frac{dT}{dP})_h \quad (39)$$

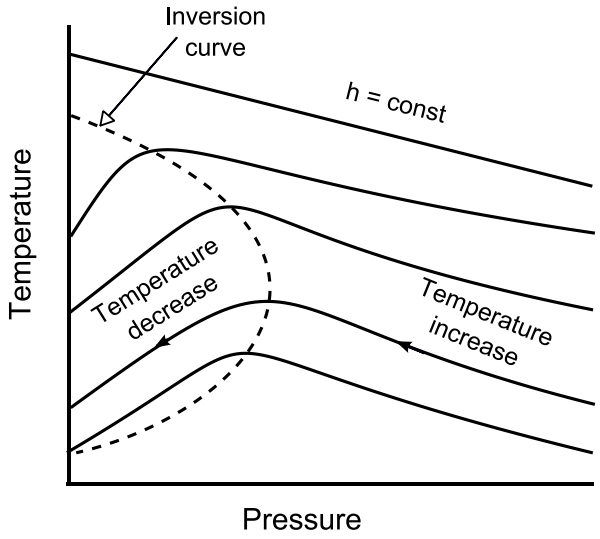

Figure 39: Isenthalpic expansion of a real gas (Barron, 1985)

Therefore when a gas expands from a high pressure to a lower pressure, the temperature will decrease if $\mu_{J\text{-}T}$ is positive or it will increase if $\mu_{J\text{-}T}$ is negative and it will remain constant if $\mu_{J\text{-}T}$ is zero.

5.2 Reversed Brayton refrigeration Cycle

In a Brayton cycle, atmospheric air is compressed in a compressor, then mixed with a fuel in a combustion chamber and finally the mixture of pressurized air and fuel is ignited in a combustion chamber to increase the enthalpy of the fluid, and then the gas is expanded and cooled in an expansion device, such as a turbine, releasing the energy and delivering work in some form. In this case, the compression process is initially assumed isentropic, the combustion process is isobaric and the expansion process is isentropic.

The reverse Brayton cycle is also known as the air-standard refrigeration cycle and is a refrigeration method frequently used in passenger aircraft. This is also an alternative to the vapor compression refrigeration cycle. This process is reverse of the Brayton cycle because although the working fluid passes around the same components in the same order, the sense of the heat transfers in the heat exchangers is reversed; a cooling effect is achieved by cooling the fluid after the compressor to ambient temperature rather than heating it. A non-condensing gas such as air is usually used instead of the condensing vapor refrigerant (Dincer & Kanoglu, 2010). The cooled fluid passes to an expansion device and assumes a very low temperature, which causes heat to be transferred from the medium requiring cooling. The work needed to produce the refrigerating effect is provided by the compressor. The steps in the reverse Brayton cycle as shown in Figure 40 are: a) an isentropic compression process 1-2, where the pressure of the gas is increased from its initial value to a desired highest value, b) an isobaric heat rejection in a heat exchanger where the heat of compression is removed with the help of cooling air or water 2-3, c)further cooling below ambient temperature, d) an isentropic expansion process 3-4 in an expansion valve or an expander where the high pressure cooled gas is allowed to expand to lower the pressure to produce low enough temperature to bring about a cooling effect, and e) an isobaric heating 4-5, where heat is added to the returning refrigerant and results in a cooling effect (Dincer & Kanoglu, 2010): for the fluid travelling from the compressor, the process is isobaric cooling; for the fluid travelling to the compressor, the process is isobaric reheating.

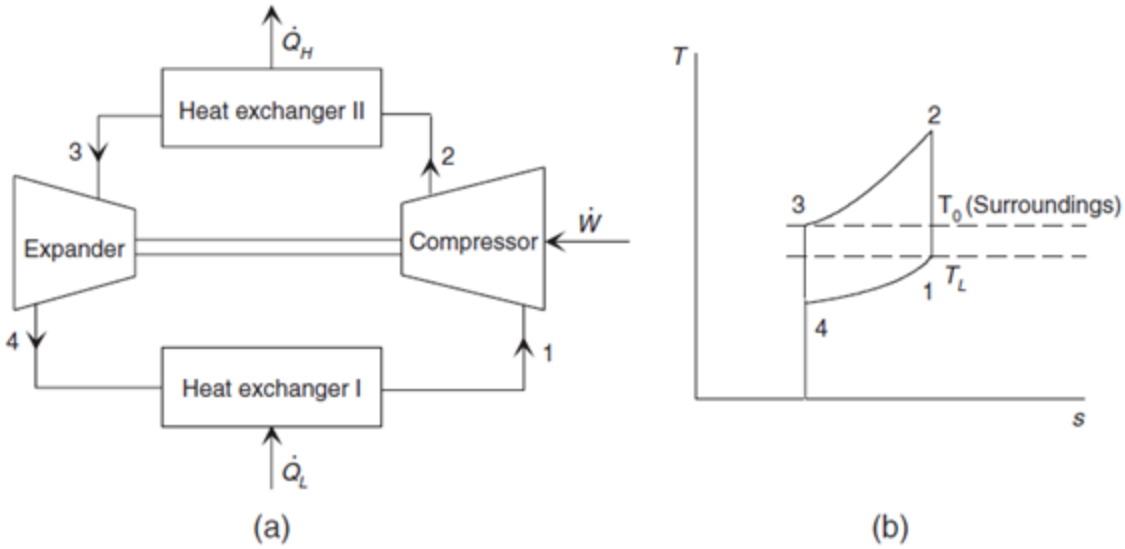

Figure 40: a) A reverse Brayton refrigeration cycle, b) its T-s diagram (Dincer & Kanoglu, 2010)

5.3 Ideal liquefaction systems

An ideal liquefaction system is a system in which all of the working fluid that is compressed gets liquefied. The pressure at point 2, as shown in Figure 41 (b), could be as high as 10, 000 bar. Therefore the liquid yield and efficiency are assumed to be 100%. The diagram in Figure 41 (b) shows that the wetness fraction is about 60% meaning that when the nitrogen is expanded, 60% of it liquefies, and 40% of it is cold, but dry vapor. Thus it cannot be 100% efficient as shown, if the efficiency measures the proportion of liquid produced, one time around the cycle. This type of system is ideal in nature and therefore does not exist in reality but is helpful as a benchmark for comparison with other liquefaction systems. The ideal system consists of a compressor, an expander and a Dewar vessel/flask for collecting the liquid air as shown in Figure 41(a). In the ideal case each component in the cycle is assumed to be 100% efficient. The system undergoes an ideal isothermal compression and isentropic expansion process to produce liquefied gas (Venkatarathnam, 2008) & (Van Sciver, 2012).

(a)

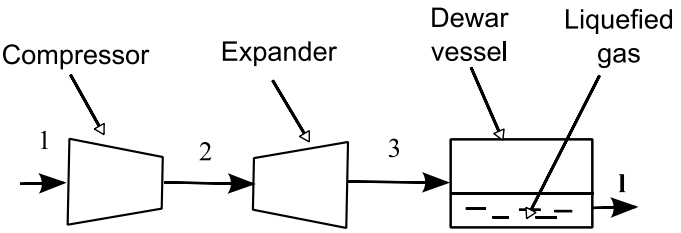

(b)

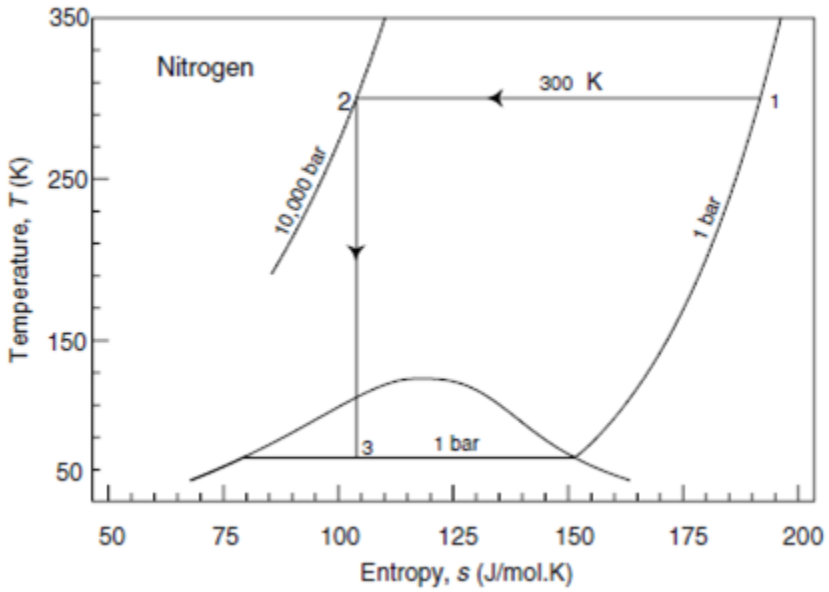

Figure 41: Schematic (a) and T-s diagram (b) of an ideal liquefaction system for nitrogen (Venkatarathnam, 2010)

5.4 Simple Linde-Hampson cycle

The Linde-Hampson liquefaction system (Figure 42) is the most straight forward type of practical liquefaction cycle and was developed separately by Carl Von Linde and William Hampson in 1895 (Krasae-in, Stang, & Neksa, 2010). This system consists of a compressor, a heat exchanger, an expansion valve, a pressure vessel or a phase separator and the required

pipes and fittings. The system requires a very high pressure to operate which is a challenge to work with due to the risk of explosion in the absence/failure of a pressure relief valve (Thomas, Ghosh, & Chowdhury, 2012).

The simple Linde-Hampson system operates as follows. Atmospheric air is first compressed (pressure ratio typically 200) then passed through heat exchangers to cool it down. Next it is allowed to expand, either through an expansion valve or an expansion turbine. In the latter instance some work can be extracted from the fluid. In either case, a proportion of the air condenses and is collected in a Dewar vessel. The remaining non-condensed air is sent to the cold side of the heat exchanger to cool the compressor delivery air, then is returned to the compressor, completing the cycle as shown in the Figure 42(a). The overall production rate of the liquefied air (or any other working fluid) depends on the effectiveness of the heat exchangers (Thomas et al., 2012). The overall specific work of liquefaction (kWh/kg) depends on the efficiency of the compressor.

This is actually no different than the reversed Brayton cycle other than expander replaced by expansion valve/turbine. Temperature at 5 is so low, some of the air in Reversed Brayton Cycle liquefies. Also this cycle is open cycle for the compressor and semi-open-cycle at the expander.

(a)

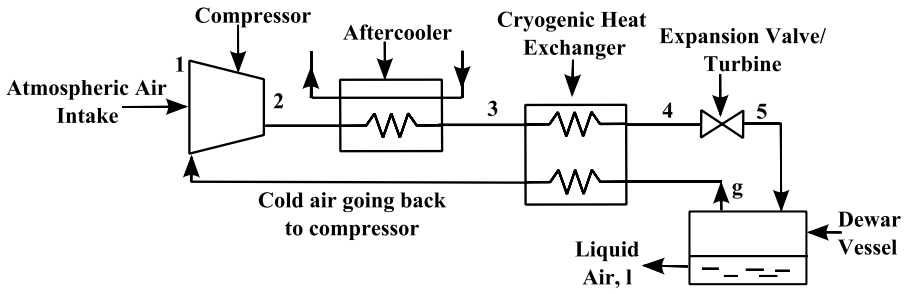

(b)

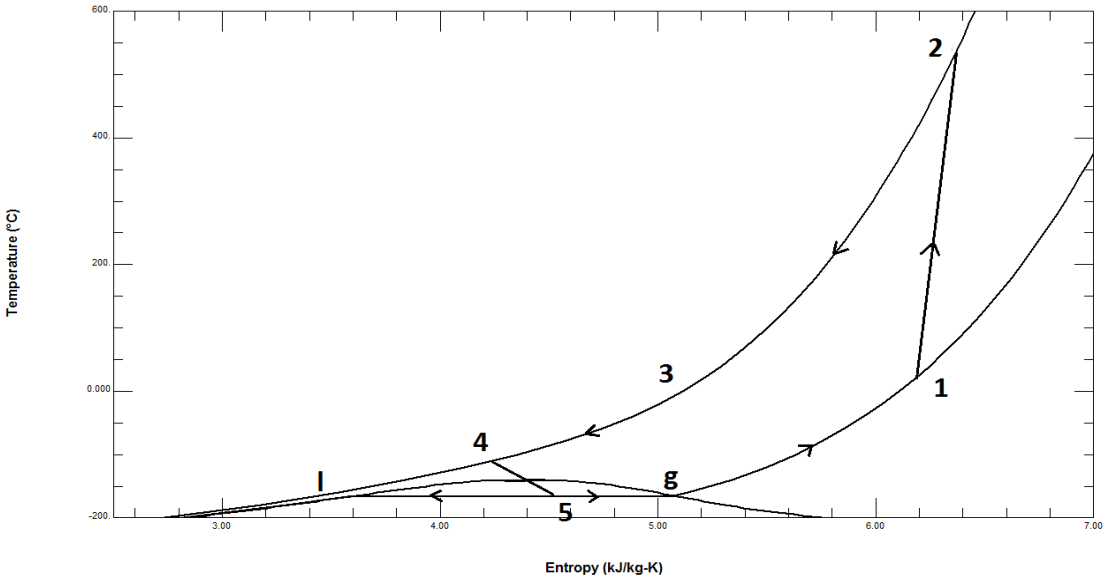

Figure 42: Schematic (a) and T-s diagram (b) of the Linde-Hampson liquefaction system for air

The derivatives of the simple Linde-Hampson system are: the pre-cooled Linde-Hampson system, the dual pressure Linde-Hampson system, the Claude system named after French scientist Georges Claude (U.S. Patent No. 981748, 1909), the Kapitza system named after the Russian scientist Pytor Kapitza (Reif-Acherman, 2009), the Collins system invented by Sameul C. Collins (Thomas et al., 2012; Van Sciver, 2012) and the Heylandt system invented by Paul Heylandt and Christian Wilhel (U.S. Patent No. 1777040, 1927).

A thermodynamic performance comparison of some of the cycles for production of cryogens is presented in Section 5.9. In the Linde-Hampson and derivative cycles, heat is recuperated in the cryogenic heat exchangers (meaning that the waste heat in the main cryogenic heat exchanger is utilised to warm up the cold air going back to the compressor to ambient temperature as the atmospheric air at 1). Along with these conventional and modified systems, there are cycles and machines which have heat exchangers that regenerate heat rather than recuperate it, and these, called cryocoolers, are explained in the sections that follow.

5.5 Stirling cycle refrigeration

The Stirling engine has been used for various purposes since its invention in 1816 by Robert Stirling in Scotland. The reverse Stirling cycle has long been used for cryogenic refrigeration and liquefaction processes (Thombare & Verma, 2008). The Philips Company was the first company to commercially produce refrigerators that operated on the reverse Stirling cycle (Van Sciver, 2012).

In contrast to earlier presented cycles, the Stirling cycle is a closed cycle involving a single mass of gas rather than a flow through mass flow, as shown in Figure 43. The refrigeration process consists of four different sub-processes, namely compression, expansion, heat addition and rejection. The three main components responsible for these processes, as indicated in Figure 44, are the regenerator (R), compressor/expander, and the displacer (D). The working fluid is compressed at point 1 at which point the high temperature refrigerant passes through the regenerator at constant volume and into the expansion chamber, while the displacer is moved to its upper position through 1 to 2. Heat rejection and a small pressure reduction of the compressed refrigerant takes place during the process of passing through the regenerator (2-3). Next the isentropic expansion takes place (step 3-4), while displacer is moved

upward with the compressing piston head. In steps 4-1, the displacer is moved to its lower position, which displaces the cold expanded refrigerant through the regenerator and back to the compression chamber. Refrigeration is obtained by the isentropic expansion of the working fluid. The fluid does not flow continuously as in a recuperative system but the flow reciprocates due to the periodic nature of the cycle. Therefore the cooling is also not produced continuously (Van Sciver, 2012).

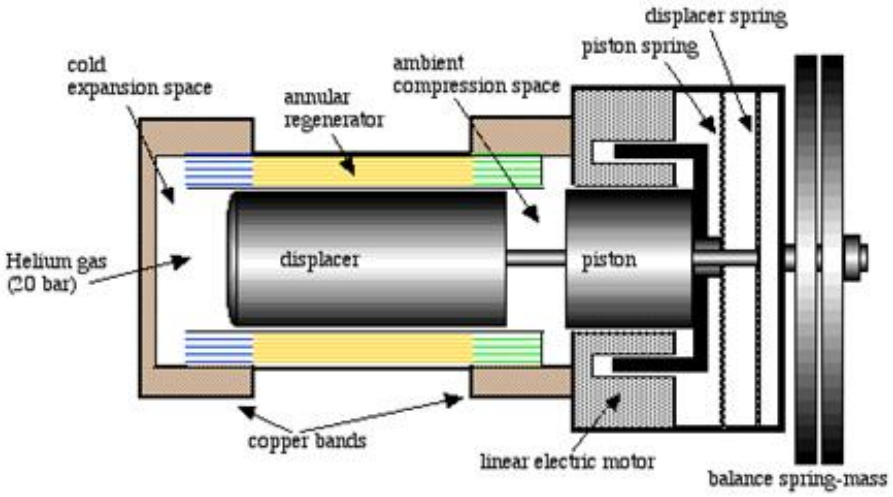

Figure 43: Schematic of a Striling cryocooler (Urieli, 2010)

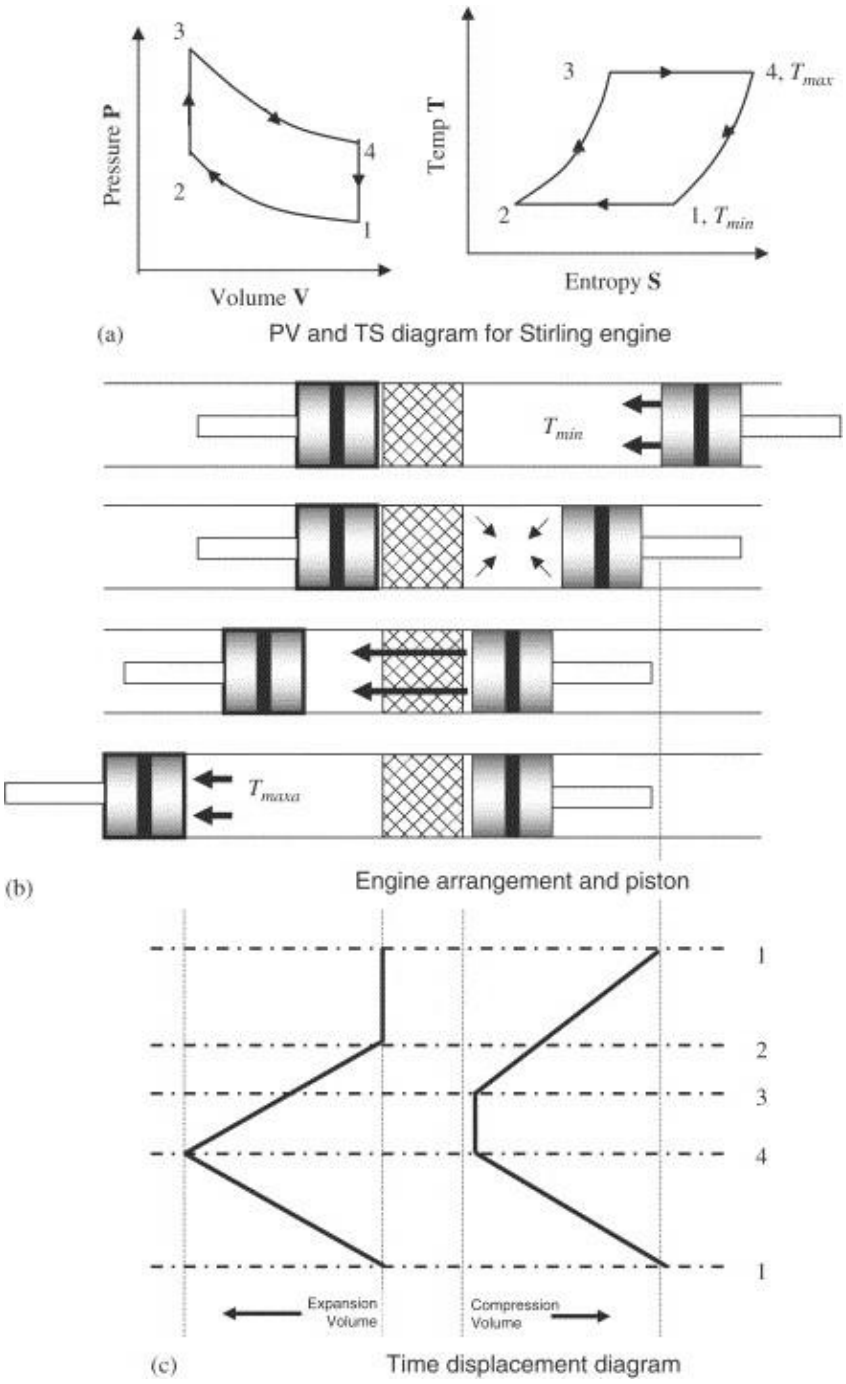

Figure 44: Schematic of the Stirling cycle refrigerator (Van Sciver, 2012)

Through each repetition of the cycle, heat is removed from the working fluid at the hot end of the machine by conduction through the machine walls. At the same time, heat is added

to the working fluid at the cold end of the machine, again by conduction through the machine walls – this is the cooling effect. When the work added to the Stirling engine is used to drive this cycling refrigeration process, the cold end of the engine becomes progressively colder; the average temperature of the contained gas is reduced since the rate of heat transfer to the environment at the hot end is greater than the rate of heat conduction at the cold end. In order to liquefy gases, the gases are brought into contact with the cold end of the Stirling refrigerator, which eventually becomes so cold that the gas condenses on its outer surface. The liquefied gas that drips off the cold end is then collected in a Dewar vessel. Although this refrigerator has several advantages and is highly efficient, it has more vibration due to the reciprocating motion and controlling losses can be problematic. These limitations are however overcome by pulse tube refrigerators which are discussed later in Section 5.7.

5.6 Gifford-McMahon cryocooler

The Gifford-McMahon (GM) refrigerator was developed by W.E Gifford and H.O McMahon in 1959 (U.S. Patent No. 2906101, 1957). It is a regenerative refrigerator/cryocooler similar to the Stirling cycle refrigerator but has rotary valves that alternate between high and low pressure sources (Radebaugh, 1999). The GM cycle starts with the displacer at its lowest position, and the return valve closed. The schematic of the GM cryocooler is shown in Figure 45.

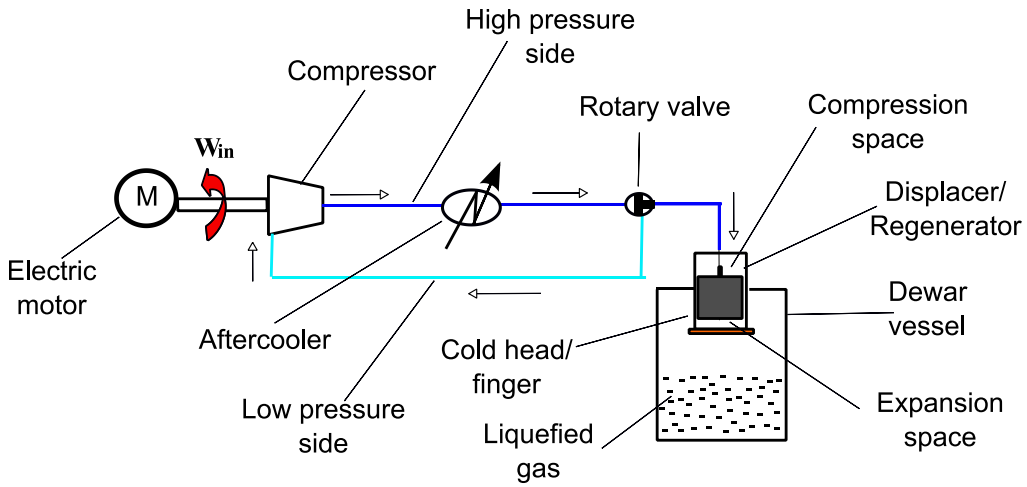

Figure 45: Schematic of the GM showing the process more visually

The inlet or the high pressure valve is opened to allow the high pressure helium gas to fill the regenerator and space above the displacer at room temperature. Then with the inlet valve still open, the displacer is moved to its upper position. The high pressure gas passes through the regenerator and is cooled more or less isobarically by the matrix. The cold gas then fills the space below the displacer. Now the inlet valve is closed and the outlet valve is opened with the displacer at its upper position. The gas in the regenerator and cold space below the displacer therefore undergoes expansion, the fluid temperature lowers, which produces the refrigeration. Finally the displacer moves back to the lowest position with its outlet valve still open. As such, the low temperature gas is warmed isobarically by the matrix refilling the space above the displacer at room temperature, which completes the cycle (Van Sciver, 2012).

All valves and seals used in GM cryocoolers operate at room temperature therefore the problems with low-temperature valves and seals are eliminated. The opportunity to multistage also makes it possible to attain lower temperatures when using a GM refrigerator. The multistage GM refrigerator also has better thermodynamic efficiency than the single-stage refrigerator for the same upper and lower temperature limits (Barron, 1985).

Various authors have experimented with the GM refrigerator cooling capacity by optimizing the inlet and outlet valves (R. Li, Onishi, Satoh, & Kanazawa, 1997) and changing the regenerator materials (Masuyama, Fukuda, Imazu, & Numazawa, 2011), (Masuyama, Matsui, Tamura, & Numazawa, 2012). They have shown that the cooling capacity of the GM cryocoolers can be increased by these optimization methods.

A major concern with the GM cryocoolers is the vibration of their cold head. Tomaru et al. (2004) carried out a comparative study on the cold stage vibration of the 4K Pulse tube and 4K GM cryocoolers and found out that the vertical vibrations of cold head for the 4K GM cryocoolers were higher than that for the 4K Pulse tube cryocoolers. However, the cold stage vibration for both the 4K GM and the pulse tube cryocoolers were of the same magnitude and the differences in vibrations in pulse tube and GM cryocoolers did not come from the cold stage vibration but from the cold head vibration. Tomaru et al. (2004) concluded that the cold stage vibration was due to the elastic deformation of the pulse tube and that these are major problems for the cryocoolers that use pressure oscillations of the working gas for obtaining lower temperature (Tomaru et al., 2004).

5.7 Pulse tube cryocooler

The pulse tube cryocooler is another regenerative type of cryocooler, yet, compared to other cryocoolers, it has low vibration, is compact and has no moving parts in the cold end (Qiu, Wang, Gan, & Dong, 2012). It was developed by Gifford and Longsworth in the 1960s (W.E Gifford & Longsworth, 1963) and (de Waele, 2000). According to Radebaugh (2009), the presence of an orifice in the pulse tube refrigerator and changes in the position of the orifice made it possible to achieve temperatures lower than 60K in the 1980s. With continuous technological development as well as the addition of the double inlet in 1990 and the inertance

tube in mid 1990s, these cryocoolers have reached efficiencies as high as those of Stirling cryocoolers (Radebaugh, 2009). The pulse tube cryocoolers can be of either Stirling or GM type. In the GM type, the oscillating pressure is created by connecting the high and low pressure sides of a compressor using a rotary valve. In contrast, for the Stirling type pulse tube cryocooler, the frequency of the pressure oscillations in the tube is given by the driving frequency of the piston (Nissen, 2010).

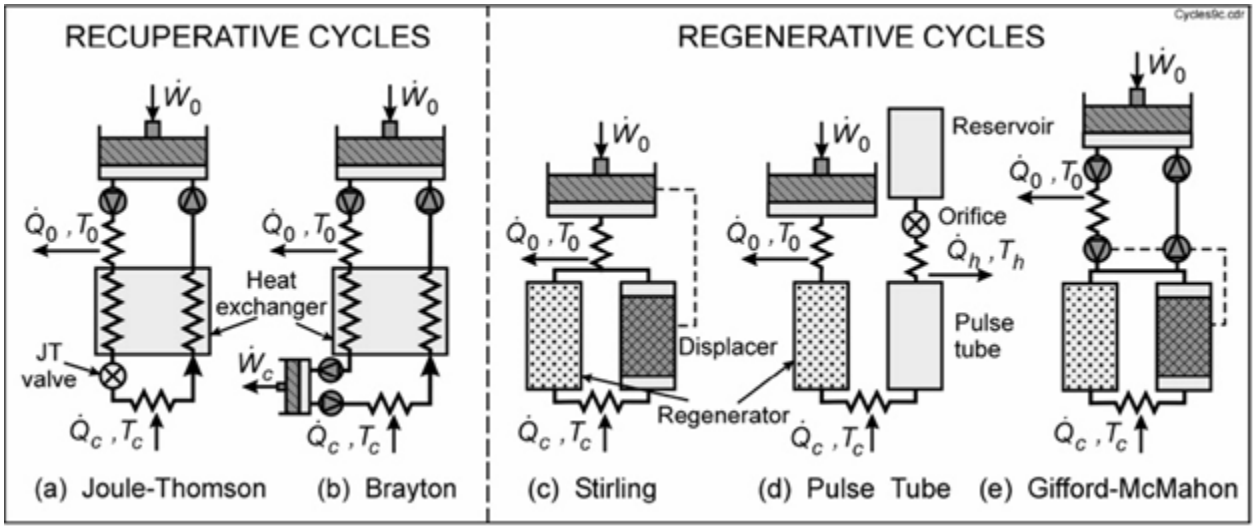

Figure 46: Schematic of five common cryocoolers (Radebaugh, 2009)

As shown in Figure 46, the pulse tube cryocooler consists of a compressor at room temperature; a heat exchanger that takes the heat from the compressed fluid and brings it to room temperature; a regenerator that absorbs heat from the gas when it flows to the right and releases heat again when it flows back to the left; and another heat exchanger at the low temperature absorbs the cooling power. There is also a tube that acts as nothing but a passage for the gas to flow back and forth. The last heat exchanger rejects heat to room temperature. The orifice is used as a flow resistance, and is usually adjusted to obtain optimum production; the reservoir is used as a buffer (de Waele, 2000).

Also as shown in Figure 46, the Joule-Thomson and Brayton cycles, there is a steady flow of gas in one direction with steady low and high pressures. These cycles are classified as recuperative cycles.

In all these cycles, compression takes place at ambient temperature T_0, whereas expansion takes place at the cold end at a temperature T_c. The heat of compression is rejected to ambient atmosphere. Refrigeration effect is achieved during the expansion process at the cold end where Q_c is absorbed.

The expansion process is constant enthalpy in JT cycle and constant entropy in Brayton cycle. The Stirling, pulse tube and GM cryocooler shown in operate with oscillating flows and oscillating pressures that are analogous to AC electrical systems. These all are regenerative cycles and use helium as the working fluid almost always probably because helium has the lowest boiling point and can produce more cooling. In the regenerative type of cryocoolers, heating occurs when pressure is increasing and cooling occurs as pressure is decreasing. Striling and GM cryocoolers make use of a displacer to move most of the gas to the hot end during the compression process and to the cold end during the expansion process. In the pulse tube cryocooler, the gas is moved with the help of oscillating flow in the warm-end orifice, but without a moving part.

The regenerator used in these cycles is filled with a porous matrix with high surface are and heat capacity. It is packed with metallic screens and spheres. The heat is transferred from the hot end to cold end via this matrix, where the heat is stored for a half cycle.

5.8 Dewar vessels for cryogen storage

Dewar vessel is named after Sir James Dewar, who developed the vacuum-insulated double-walled vessel in 1892 according to Dewar (as cited in Barron, 1985). The Dewar vessel is the same type of container as the regular thermos bottle which is used for storing tea, coffee, and water and so on. But its development in 1892 was a huge step forward in cryogenic-fluid storage vessel design. Although numerous improvements have been made in the original design, the basic construction of the containers is still based on Dewar's original principle. A basic Dewar container is a double walled container with space in between two vessels which is evacuated.

The Dewar vessel contains an inner vessel which stores the liquefied cryogenic fluid. The inner vessel of Dewar container is also called the product container. This container is then enclosed by an outer vessel or the vacuum jacket which holds the high vacuum necessary for the effectiveness of insulation and serves as a vapour barrier to prevent transportation of water vapour or air to the cold inner vessel (Barron, 1985). These storage vessels come in different shapes, such as cylindrical, conical and spherical, or a combination of these. The most economical shape among these is the cylindrical shape.

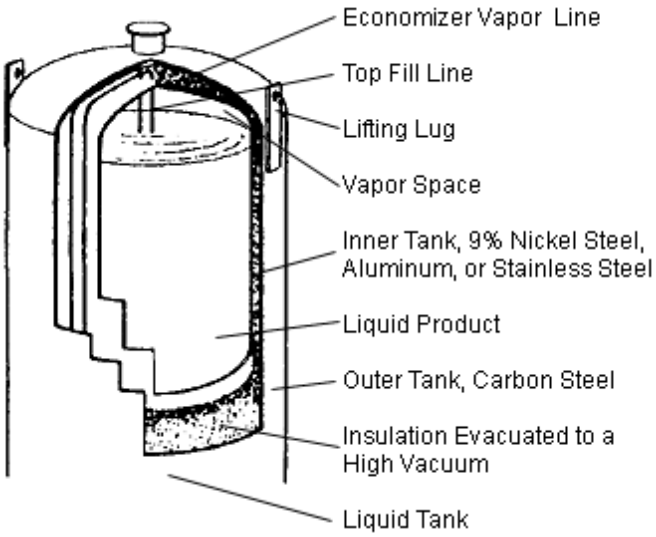

Figure 47: A cut-view of a typical cryogenic storage tank (Air products, 2017)

The cryogenic Dewar vessel usually consist of several elements and safety devices as shown in Figure 48, such as the liquid nitrogen extraction tube, level indicator, cold head, penetrations for pressure relief valves. These elements and devices can also act as a good source of heat conductors for conduction and radiation type heat transfer (gain) mechanisms. The major part on the Dewar vessel lid through which most of the heat is conducted is at the neck part, which holds the cold head (or cold finger).

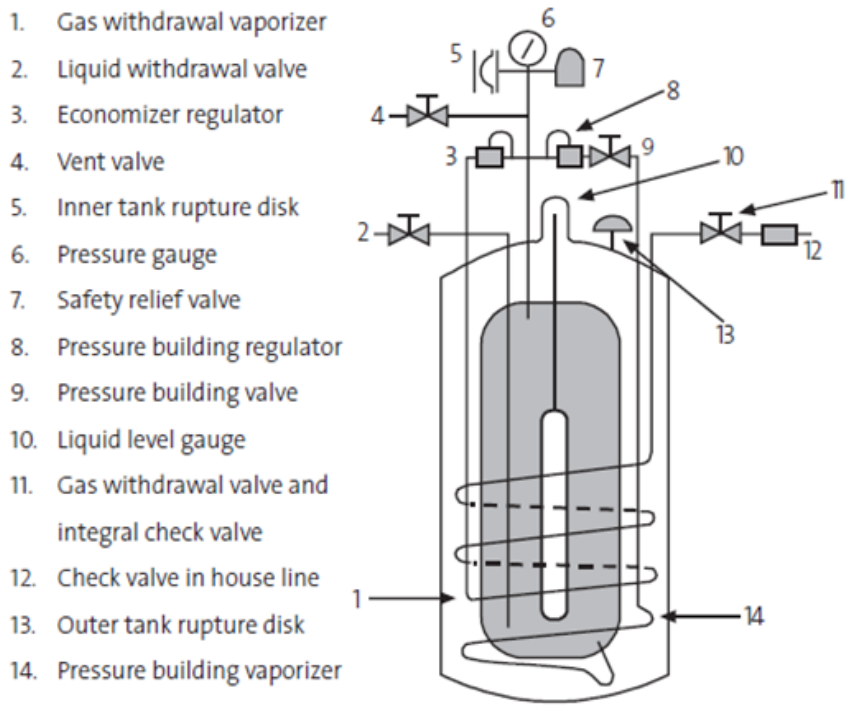

Figure 48: Cryogenic storage tank with required valves and gauges (Air Products and Chemicals, 2013)

5.9 Thermodynamic performance comparison of some liquefaction systems

The theoretical minimum work input required for the liquefaction of gases can be determined for Carnot refrigerator, an ideal to which real liquefaction systems can be compared. Practically the work input requirement is dependent on the inlet and the outlet gas stream properties, as well as the temperature of the surroundings. It has also been found that with an increase in liquefaction temperature and decrease in the inlet gas stream temperature, there is an increase in the mass of the liquefied fraction, and the coefficient of performance (COP) of the system, while there is a decrease in the actual and reversible work input consumption. The fraction of the liquid yield is dependent upon the refrigeration effect. The refrigeration effect, amount of work input required, and COP of the system following a more practical Linde-Hampson cycle are given in Table 3 according to (Kanoglu, Dincer, & Rosen, 2008).

Table 3: Performance parameters of a simple Linde-Hampson cycle for various fluids: (T_1= 25^{o}C; P_1= 1 atm, P_2= 20 MPa) (Kanoglu et al., 2008)

	Air	Nitrogen	Oxygen	Argon	Methane	Fluorine
Liquefaction temperature (^{o}C)	-194.2	-195.8	-183.0	-185.8	-161.5	-188.1
Fraction of gas liquefied	0.0823	0.0756	0.107	0.122	0.199	0.076
Cooling effect (kWh/kg liquid)	0.117	0.120	0.112	0.075	0.253	0.095
Work input (kWh/kg liquid)	1.522	1.720	1.043	0.736	1.080	1.239
Minimum Work input (kWh/kg liquid)	0.204	0.212	0.175	0.131	0.3	0.157

The specific power consumption for liquid nitrogen production by the Claude cycle is 0.18-0.2 kWh/kg of liquid nitrogen, as compared to 0.45-0.5 kWh/kg of liquid nitrogen for conventional plants, which do not use any Liquefied Natural Gas (LNG) refrigeration for pre-cooling the working fluid (U.S. Patent No. 5139547, 1991). The specific power consumption for hydrogen liquefaction by pre-cooled Claude cycle is 12.5-15 kWh/kg of liquid hydrogen. The detailed summary of hydrogen liquefaction process with different cycles, as performed by Krasae-in et al. (2010) is presented in Table 4.

Table 4: Specific power consumption for hydrogen liquefaction using different cycles (Krasae-in et al., 2010)

Cycle used	kWh/kg liquid hydrogen
Pre-cooled Claude cycle	12.5-15
Theoretical simple Linde-Hampson system	Cannot liquefy hydrogen
Theoretical pre-cooled Linde-Hampson system	64.5-71.7
Theoretical pre-cooled Claude system	24.8-35.0
Theoretical helium-refrigerated system	29.3-49.5
Large-scale Praxair, Air Products, Air Linde plant system	~12-15
Large-scale Claude system in Ingolstadt in stream in 1994	13.58
WE-NET: Nitrogen pre-cooled large-scale Claude plant	~8.5
Large-scale conceptual plant by Quack	-without pressure drop = 7 -with pressure drop ~7.3
Four helium Joule-Brayton cascade cycle by Valenti	5.04

Table 3 and Table 4 taken together show that it is difficult to generalize the specific work of gas liquefaction because it depends on the gas being liquefied and the cycle used to do the liquefaction.

5.10 An analysis of the cryogenic air separation plant at Copper Cliff Smelter

In 1954, a large oxygen plant with a production capacity of 1,000 tonnes/day of 95% pure gaseous oxygen via a cryogenic oxygen production method was installed and operated by Inco at the Copper Cliff Smelter in Sudbury Ontario by Air Liquide. The oxygen plant had a total production cost of $4/tonne (then) with an electricity price of $0.04/kWh (CAD 35.72/tonne and $0.36/kWh in 2014 terms). The gaseous oxygen was used for oxygen pyrometallurgy in the Copper Cliff Smelter, thus storability and transportability were important factors to consider. Various methods can be applied for the production of gaseous oxygen but cryogenic methods have been the most economic for large tonnage applications. In contrast, for oxygen requirements less than 100 tonnes/day, the vacuum swing adsorption process is preferred (Queneau & Marcuson, 1996).

The most recently constructed oxygen plant at the Copper Cliff Smelter, now owned by Vale Canada Ltd, produces 1500 tonnes of oxygen per day at 96.5% purity and had a capital cost of $40M (KSH, 2015), former KSH Dick engineering. The production and operating costs of the oxygen plants and their power consumption are shown below in Figure 49, as was analysed by (Queneau & Marcuson, 1996).

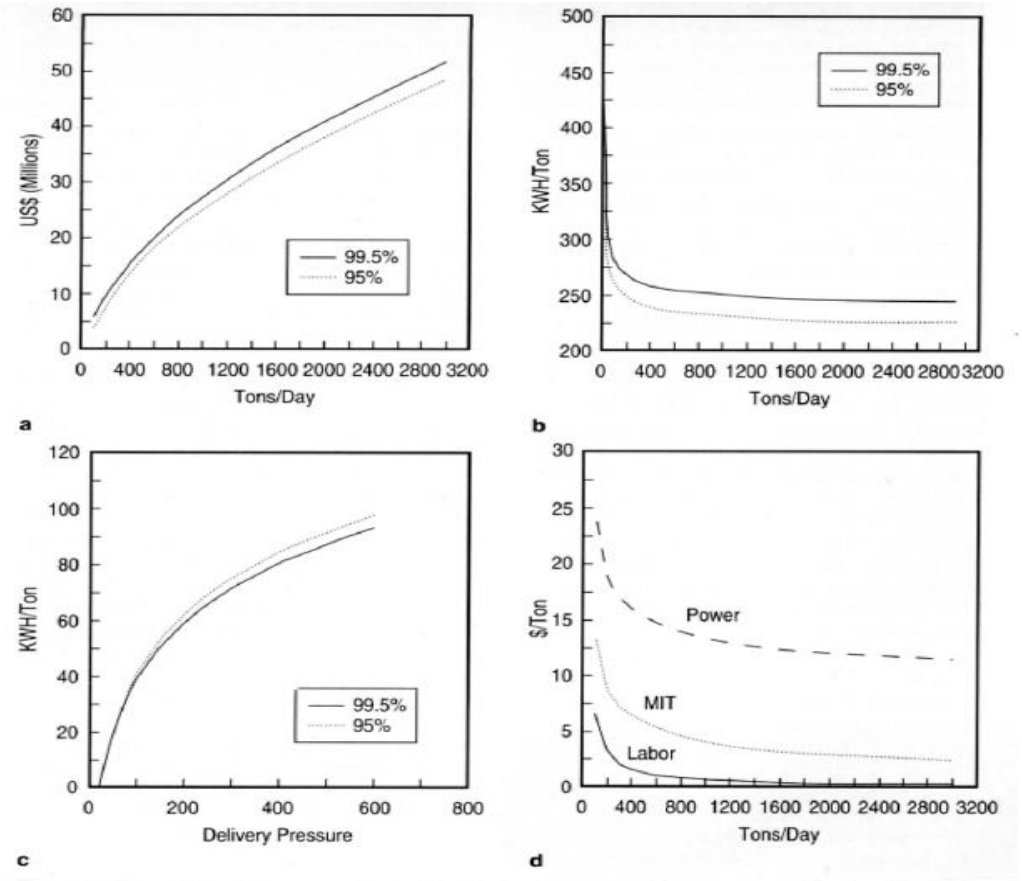

Figure 49: Oxygen production requirements shown with costs and oxygen purity percentage: (a) plant investment for oxygen at 20 psig; (b) power requirements for oxygen at 20 psig; (c) power requirements for oxygen at pressures above 20 psig; and (d) operating costs. (MIT- maintenance, insurance, and taxes) taken from Queneau & Marcuson (1996)

Although there have been distinct developments in the area of cryogenics, gas refrigeration and liquefaction systems, all systems use grid electricity rather than a renewable source of energy for the production of cryogens.

Some companies have started producing cryogens, storing them and using them on demand for power generation. For example, Highview Power Storage in London, England, founded in 2005, produces and stores liquid air and subsequently allows the liquid air to expand and generate power from this process when needed (Highview Power Storage, 2014).

5.11 Summary

This chapter of the document has reviewed refrigeration and gas liquefaction systems. Two common factors for all the liquefaction systems whether they are recuperative or regenerative, are that all of the systems rely on the compression and expansion of a gas to bring about temperature changes. It is clear that the choice of cycle to adopt depends on the specific energy of liquefaction (kWh/kg liquid), and this would be as true for electric motor driven systems designed to operate in steady-state as it would be for systems with dynamic and transient work input (as with Cryovent). In either case, one would want to make the best of the work input available. The marginal cost of the work input is not zero for the steady state systems that are driven by electric motors. However, for Cryovent systems it would be close to zero because the source of work input that drives the systems is renewable and free of cost, i.e. wind energy.

To prove or disprove the hypothesis of this work, it actually mattered little on which cycle was to be chosen, as whether variable input work to the compressor leads to relatively steady cryogen production applied in all cases. A higher priority was safety during the research investigations, which pointed to nitrogen as the gas to liquefy, but even this does not restrict the

cycle to select much. For research investigations, flexibility is key and it is for this reason that the GM cryocooler cycle was chosen as the one to adopt for the laboratory experimental phase of the work. Detailed modeling and simulations for such a system is presented in Chapter 7, the experimental verification is presented in Chapter 8, detailed comparison of the simulation and experimental results are then presented in Chapter 9 that follow immediately.

6 A review of fluid power for wind turbines

Although use of a hydrostatic transmission is among the recent developments in the integration of wind power, this type of transmission system has been used only for mechanical coupling and storage for power generation.

Hydraulic transmissions in wind energy systems started several years ago, however the development in the modern production technology has given rise to the commercial development of very compact and efficient drives that make this option more attractive than the traditional drives. The idea of using oil hydraulic circuits for wind turbine application is solely the replacement of the gearbox and frequency converter. The general principle behind the 'fluid power for wind turbine applications' concept is that the rotating mechanical power from the prime mover is converted into a fluid flow at high pressure, by a positive displacement pump. At the other end of the hydraulic circuit, the fluid power is converted back to mechanical power by a hydraulic motor. A schematic of such a system is shown in Figure 50.

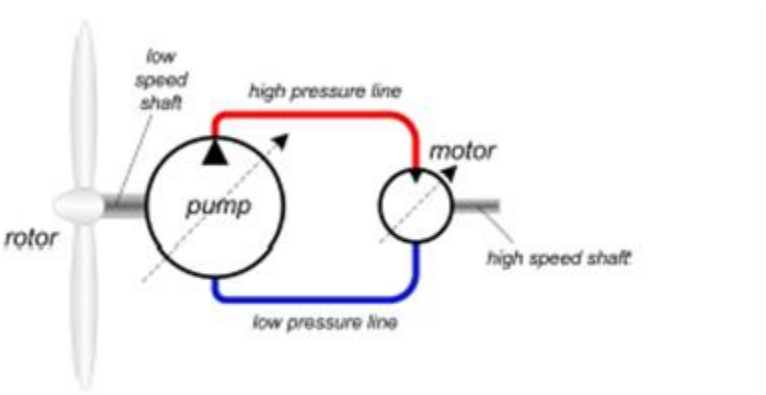

Figure 50: Schematic showing working principle of fluid power transmission for wind turbine application (Diepeveen, 2013)

This Chapter reviews the prior work done in the fluid power transmission for wind turbine applications, describes the power transmission system, develops a model for open loop and closed loop hydrostatic transmission, presents results from simulation performed in MATLAB/Simulink, and compares the obtained results with some of the published research works.

6.1 Prior work

Most of the studies conducted to date focus on the steady state behaviour of the wind energy integration system with the hydrostatic transmission, with improvements for the dynamic behaviour yet to be reported. One exception is Diepeveen (2013), who presents a theoretical model of the fluid power transmission and an analysis of the main design parameters on the dynamic behaviour of the system. The main advantage of using a hydrostatic transmission is the possibility of varying the transmission ratio, which makes it possible to operate the wind turbine at variable speed while using a synchronous generator directly coupled to a grid driven by a hydraulic motor; and therefore the need for an AC frequency converter and a voltage transformer is eliminated. In turn this reduces the nacelle mass (Diepeveen, 2013). However, the study performed by reference Diepeveen (2013) did not take into account the presence of accumulators (pressurized tanks) for short term energy storage but considered only the hydraulic hoses in their transmission system. That system was closed loop with zero storage capacity which makes it different from the concept described in this work, which includes accumulating storage as a design feature specifically to mitigate short term wind variability.

Izadian, Hamzehlouia, Deldar, & Anwar (2014) present a novel method for using a hydraulic wind power transfer system to connect several wind turbines to a single power generation unit but this really follows the concept set out by Millar & Parish (2010). Izadian et al.

(2014) present a mathematical modelling of the wind power transfer technology and its dynamic behaviour. It was concluded that the system proposed and tested would help eliminate the need for a variable speed transmission and also lead to most of the equipment being moved from the nacelle to ground to obtain greater accessibility to the generator unit and also to reduce the maintenance costs (Izadian et al., 2014).

In another study, a dynamic model of an open–circuit low speed high torque hydrostatic drive system with pump loading was developed (Dasgupta, Mandal, & Pan, 2012). The model developed was validated through experiment with respect to the variation of inertial and the resistive loads. However, the fluid inertia was neglected and the loss coefficients of the pumps and motor were estimated through steady-state analysis (Dasgupta et al., 2012).

6.2 Hydrostatic transmission components

6.2.1 Hydraulic pumps and motors

A hydraulic transmission circuit consists of a displacement pump, hoses and a hydraulic motor. The variable speed wind rotor is coupled directly to the drive shaft of the hydraulic pump, which rotates the pump. Therefore, the rotor speed is equal to the pump shaft speed. The input rotational power drives the hydraulic pump to generate high hydraulic pressure. Many control strategies have been applied for the control of the wind rotor so that maximum power could be captured.

A piston pump works on the principle that a reciprocating piston can draw in fluid when it retracts in a cylinder bore and discharge it when it extends. The main type of the piston pumps are the radial and axial piston pumps. The radial piston pump design consists of a pivot which directs fluid in or out of the cylinders, a cylinder barrel with pistons, and a rotor containing a

reaction ring (Esposito, 2009). For the pumping action, the reaction ring is moved eccentrically with respect to the pivot or shaft axis. As the cylinder barrel rotates the pistons on one side travel outward. This draws in fluid as each cylinder passes the suction ports of the pivot. When a piston passes the point of maximum eccentricity, it is forced inward by the reaction ring. This forces the fluid to enter the discharge port of the pivot. If the hydraulic pump is a radial piston pump, the hydrostatic transmission capacity can be easily increased with the increase in the number of cylinders or stages that constitute the hydraulic pump and motor (Sasaki, Yuge, Hayashi, Nishino, & Uchida, 2014). Figure 51 shows a typical hydraulic radial piston pump or motor which works on a digital displacement technology recently developed by (Artemis Intelligent Power, 2016).

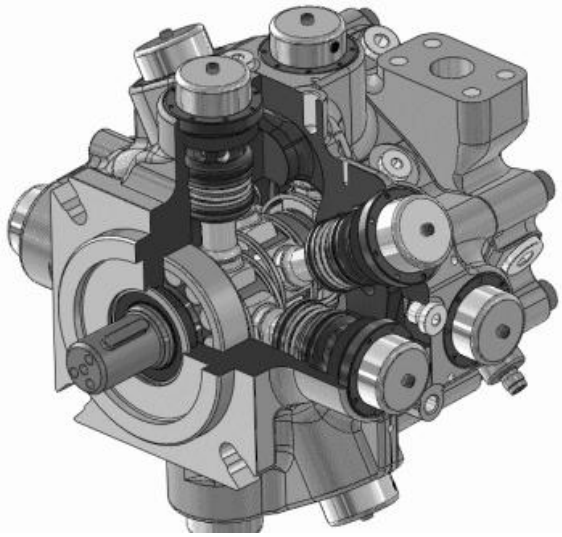

Figure 51: A typical radial piston pump/motor (Artemis Intelligent Power, 2016)

Piston motors generate torque by pressure acting on the ends of pistons reciprocating inside of a cylinder block. The motor driveshaft and cylinder block are centered on the same axis. Pressure acting on the ends of the pistons generates a force against an angled swash plate. This causes the cylinder block to rotate with a torque that is proportional to the area of the

pistons. The torque is also a function of the swash plate angle. The swash plate angle in the piston motor determines the volumetric displacement (Esposito, 2009).

6.2.2 Valves

The valves that are necessary for any hydrostatic transmission are the check valves, pressure relief valves and proportional control valves. Check valves are the simplest type of direction control valves. These are needed in the hydraulic circuit to prevent the fluid from flowing backwards. These valves are one-directional valves which do not allow back-flows in the system when the system is shut down. The ball valves are the most common type of the check valves. They are a form of quarter-turn valves which use a hollow, perforate and revolving ball to control flow through them. The valve opens when the ball is in line with the flow and is closed when it is rotated perpendicular to the line with the help of the handle. A spherical ball membrane is present in the ball valve which blocks the flow. This ball is loaded with a spring which prevents the flow from passing through.

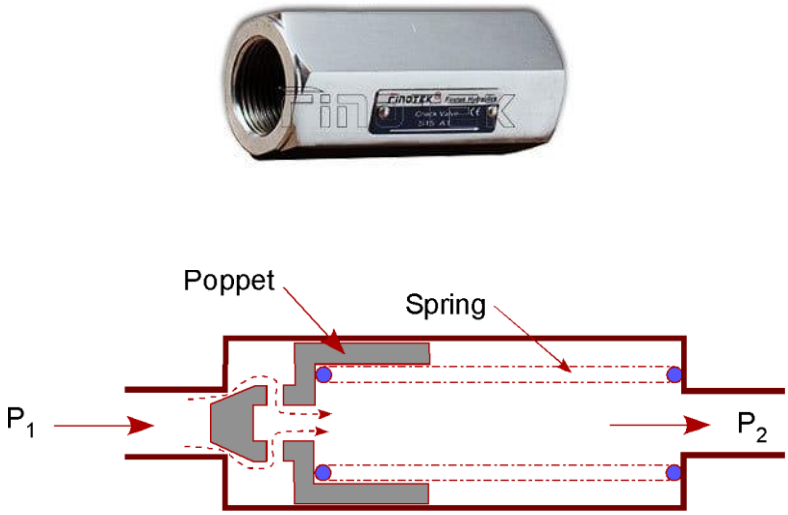

Figure 52: A check valve (Finotek, 2006) *and its cut view* (Design Aerospace LLC, 2013)

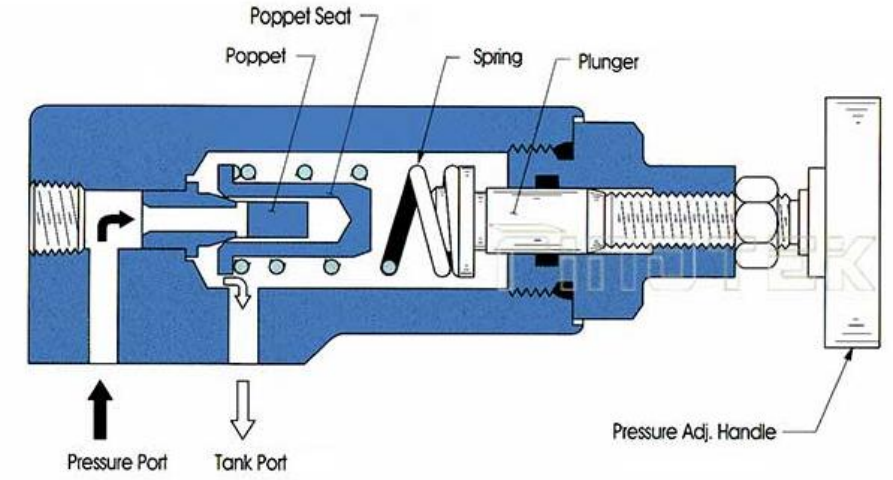

Figure 53: A pressure relief valve with its components (Finotek, 2006)

A typical pressure relief valve is normally a closed valve, as shown in Figure 53, whose function is to limit the pressure to a specified maximum value by diverting pump flow back to the tank. Pressure in a circuit is created by the resistance in the system which keeps on increasing

unless there is a relief system like the pressure relief valve. The pressure relief valves can be set to a specific pressure value, which when overcome by the system pressure, the valve will open to get rid of the excess pressure in the system.

The pressure at the full pump flow is the pressure level that is specified when referring to the pressure setting of the relief valve. It is the maximum pressure permitted by the relief valve. If the system does not accept any flow, then all the pump flow must return to the tank via the relief valve. The pressure relief valve also provides protection against any overloads experienced by the actuators in the hydraulic system. Another important function of the pressure relief valve is to limit the force or torque produced by the hydraulic motor.

Some of the hydraulic circuits also use a proportional control valve, sometimes also called an electro-hydraulic proportional valve. The main purpose of a proportional control valve is to distribute the flow between the primary motor and the auxiliary motor. The primary motor is active during all the situations (for example in this work during high or low wind speed conditions). The auxiliary motor is active when the system needs to store the extra hydraulic fluid during high wind speed condition and/or when the system has to make use of the stored hydraulic fluid from the hydraulic accumulator during low wind speed condition. The position of the valve is regulated to control the angular velocity of the motors. These valves can also be equipped with a controller to regulate the valve position to maintain a reference primary motor angular velocity. It uses a solenoid that produces a force proportional to the current in its coils. Therefore by controlling the current in the solenoid coil, the position of the spring-loaded spool can also be controlled. A proportional valve can provide both directional and flow control capability in a single valve, unlike the standard solenoid valve (Esposito, 2009).

6.3 Hydrostatic transmission wind turbine model

The power from the wind is given by equations (6) and (9).

The available rotor power however is given by,

$$P_{rotor} = P_{wind} C_p(\lambda, \beta) \tag{40}$$

P_{rotor} is the mechanical power available at the low speed shaft, $C_p(\lambda, \beta)$ is the characteristic power coefficient of the wind turbine.

The aerodynamic torque at the low-speed shaft is given as,

$$\tau_{rotor} = P_{rotor}/\omega_r = \frac{1}{2} \rho_{air} A R C_q(\lambda, \beta) v^2 \tag{41}$$

C_p is given as,

$$C_p(\lambda, \beta) = c_1 \left(\frac{c_2}{\lambda_i} - c_3\beta - c_4\right) e^{-\frac{c_5}{\lambda_i}} + c_6\lambda \tag{42}$$

$$\frac{1}{\lambda_i} = \frac{1}{\lambda + 0.08\beta} - \frac{0.035}{\beta^3 + 1} \tag{43}$$

where, $c_1 = 0.5176$, $c_2 = 116$, $c_3 = 0.4$, $c_5 = 21$ and $c_6 = 0.0068$ respectively.

The wind turbine rotor rotational motion is converted to fluid flow by the hydraulic pump. This is expressed as,

$$\tau_{rotor} - \tau_{pump} = J_r \dot{\omega}_r \tag{44}$$

J_r is the moment of inertia of the rotor and τ_{pump} is the resistant torque imposed by the hydraulic pump on the turbine rotor. This resistance torque from the hydraulic pump is given by,

$$\tau_{pump} = \frac{D_p \Delta p_p}{\eta_{mech,p}} \tag{45}$$

Δp_p is the differential pressure between high and low side of the pump, $\eta_{mech,p}$ is the pump mechanical efficiency, D_p is the pump displacement that can be fixed or variable. The above equation can now be written as,

$$\dot{\omega}_r = \frac{1}{J_r}\left(\tau_{rotor} - \frac{D_p \Delta p_p}{\eta_{mech,p}}\right) \tag{46}$$

6.4 Dynamic simulation of a closed loop hydrostatic transmission

A radial piston pump directs fluid in and out of the cylinders, a cylinder barrel with pistons, and a rotor containing a reaction ring. The pistons remain in constant contact with the reaction ring due to the centrifugal force and back pressure on the pistons. The pump delivers flow to the system, which is given by,

$$Q_p = D_p \omega_p - k_{l,p} P_p \tag{47}$$

$$k_{l,p} = \frac{k_{HP,p}}{v\rho} \tag{48}$$

$$k_{HP,p} = \frac{D_p \omega_{nom,p}(1-\eta_{v,p}) v_{nom,p} \rho}{P_{nom,p}} \tag{49}$$

where Q_p is the pump flow rate (m^3/s), D_p is the pump volumetric displacement (m^3/rad), ω_p is the pump angular velocity (rad/s) which is equal to the rotor speed, $k_{l,p}$ is the pump leakage coefficient, P_p is the pump differential pressure (Pa), $k_{HP,p}$ is the Hagen-Poiseuille coefficient for pump which can be calculated using nominal angular velocity ω_{nom} (rad/s), v is the fluid kinematic viscosity (m^2/s), v_{nom} is the nominal fluid kinematic viscosity (m^2/s), P_{nom} is nominal pressure (Pa), ρ is fluid density (kg/m^3) and η_v is the volumetric efficiency.

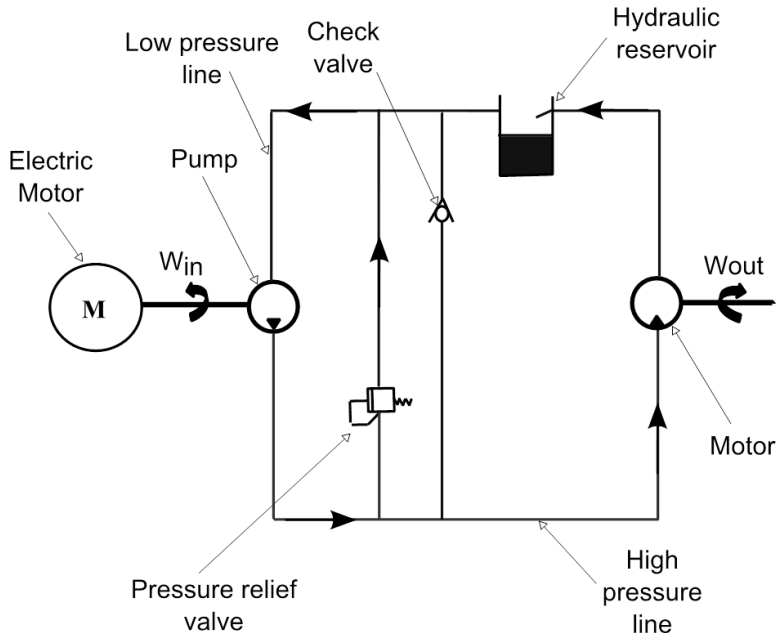

Figure 54: Schematic of closed loop hydrostatic transmission

The pressure relief valve is modeled at a pre-set pressure value. It is open if the pressure exceeds the pre-set value, and for pressures below this value, the valve is closed. The flow rate through the pressure relief valves are given as:

$$Q_v = k_{zb}(P - P_b) \quad \text{if } P > P_b \tag{50}$$

$$Q_v = 0 \quad \text{if } P \leq P_b \tag{51}$$

where Q_v is the flow rate through the valve (m^3/s), k_{zb} is the flow discharge coefficient and P_b is the valve preset pressure setting (Pa).

The check valve is used to permit flow in one direction and the flow rate through this valve is,

$$Q_{cv} = k_{zb} l_b \frac{(P - P_b) A_{disc}}{k_s} \quad \text{if } P > P_b \tag{52}$$

$$Q_{cv} = 0 \quad \text{if } P \leq P_b \tag{53}$$

where Q_{cv} is the flow rate through the valve (m^3/s), l_b is the hydraulic perimeter of the valve disc (m), A_{disc} is the area in which fluid acts on the valve disc (m^2), and k_s is the spring stiffness.

If the flexible hoses are used in connecting the wind turbine to the motors, then the dynamics of these pressurized hoses can be modeled as volume with a fixed bulk modulus. The fluid compressibility relation is given by

$$\frac{dP}{dt} = \frac{\beta}{V}(Q_p - Q_m - Q_v) \tag{54}$$

where β is the fluid bulk modulus (Pa) and V is the fluid volume subjected to the pressure effect (m^3).

The hydraulic flow supplied to the hydraulic motor is given as:

$$Q_m = D_m\omega_m + k_{l,m}P_m \tag{55}$$

where Q_m is the motor flow rate (m^3/s), D_m is the motor volumetric displacement (m^3/rad), ω_m is the motor angular velocity (rad/s), $k_{l,m}$ is the motor leakage coefficient and can be determined similarly as the pump leakage coefficient discussed earlier, P_m is the motor differential pressure (Pa). The torque at the motor shaft is given by the equation:

$$T_m = D_m P_m \eta_{mech,m} \tag{56}$$

The total torque produced in the hydraulic motor is the sum of torque from the motor loads, which can be written as,

$$T_m = T_i + T_B + T_L \tag{57}$$

where T_m is the total torque (Nm), T_i is the inertial torque (Nm) and T_L is the load torque (Nm). Rearranging the above equation, we get,

$$T_m - T_L = I_m(\frac{dw_m}{dt}) + B_m\,\omega_m \tag{58}$$

$$T_m = (\frac{D_m P}{2\pi}) \tag{59}$$

where I_m is the motor inertia (kg/m^2), ω_m is the motor angular velocity (rad/s) and B_m is the motor damping coefficient (Nm/(rad/s)).

The output shaft velocity of the motor under loading condition can be determined as:

$$I_m \dot{\omega}_m = T_m - B_m \omega_m - T_L \quad (60)$$

$$\dot{\omega}_m = \frac{T_m - B_m \omega_m - T_L}{I_m} \quad (61)$$

A model for the hydraulic wind turbine system was built and simulated in MATLAB/Simulink environment. The experimental setup in laboratory consisted of a VFD driven GM cryocooler system for nitrogen gas liquefaction. Therefore, for the validation purpose of the hydraulic wind turbine system, work of the authors Hamzehlouia et al. (2013), Hamzehlouia, Izadian, Pusha, & Anwar (2011) & Rajabhandharaks (2014) were used extensively. The first part of this section included the modeling and simulation of the hydrostatic transmission part on its own and then to compare the results with Hamzehlouia et al. (2013) .

Since the wind turbine rotor was mechanically coupled with the hydraulic pump, variable speeds were supplied to the hydraulic pump to simulate the variable wind speed conditions. Authors Hamzehlouia et al. (2013); Rajabhandharaks (2014) did not consider the wind speed model and/or the wind turbine model. In both works, the wind turbine model was represented with variable speeds supplied to the hydraulic pump. The model was first simulated to check the system response for a closed loop hydrostatic transmission. This model consisted of a hydraulic pump, a check valve, a pressure relief valve, a primary hydraulic motor, and hydraulic hoses. Some of the major parameters for this model are listed in Table 5. The detailed parameter list and MATLAB code are presented in Appendix C.

Table 5: List of parameters for closed loop hydrostatic transmission

Symbol	Definition	Quantity	Unit
D_p	Pump displacement	0.0226	m^3/rev
D_{mA}	Primary motor displacement	0.00013	m^3/rev
D_{mB}	Auxiliary motor displacement	0.00013	m^3/rev
I_{mA}	Primary motor inertia	0.0005	kg. m^2
I_{mB}	Auxiliary motor inertia	0.0005	kg. m^2
β_{mA}	Pump damping coefficient	0.0026	Nm/(rad/s)
β_{mB}	Motor damping coefficient	0.0022	Nm/(rad/s)
η_{total}	Pump/motor total efficiency	0.90	
η_v	Pump/motor volumetric efficiency	0.95	
β	Fluid bulk modulus	1266394	kPa
P	Fluid density	850	kg/m^3
v	Fluid viscosity	0.00000712	m^2/s

The mathematical model was simulated in MATLAB/Simulink environment. The fixed displacement pump with a displacement of 0.0226 m^3/rev was used to supply hydraulic fluid to the primary motor and an auxiliary motor. Both of these motors have displacement of 0.097 m^3/rev. A set of variable speeds were supplied to the hydraulic model to start the simulation. The pump speed was changed from 500 rpm to 600 rpm and from 600 rpm back to 500 rpm as shown in Figure 55. MATLAB code used for initializing the system is provided in Appendix C. The results obtained from the simulation have been presented in Figure 55 to Figure 58.

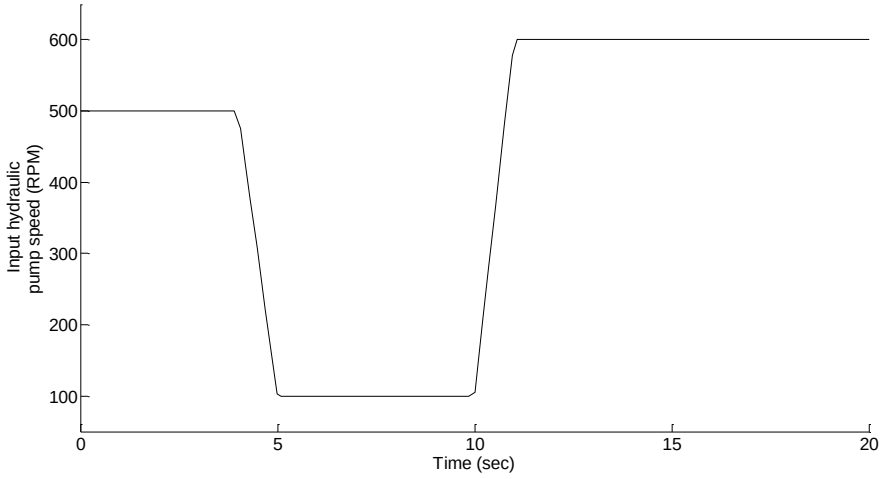

Figure 55: Variable pump speed (RPM) signals provided to the hydraulic pump with respect to time (sec) representing the changes in wind speed

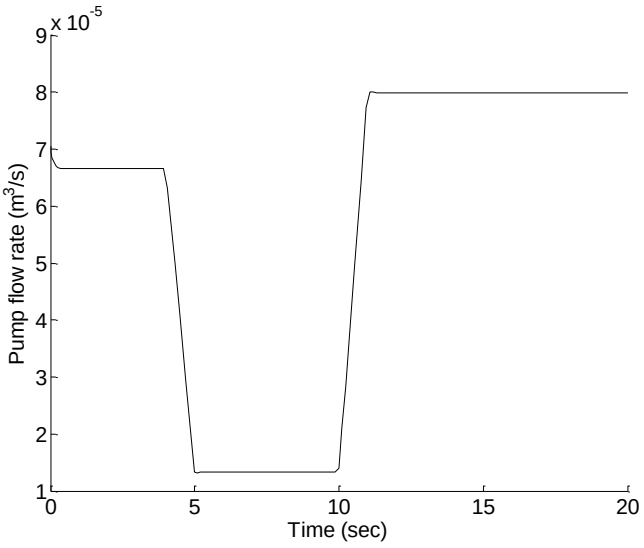

Figure 56: Corresponding hydraulic pump flow (m^3/s) as a result of change in pump speeds with respect to time (sec)

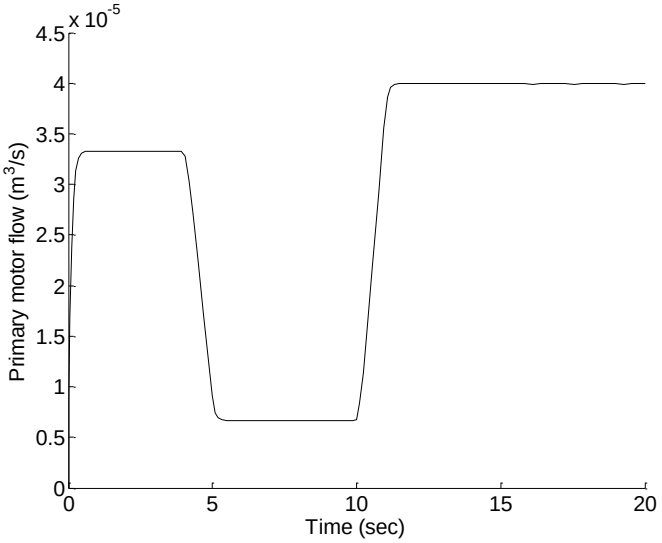

Figure 57: Motor flow (m^3/s) with respect to time (sec)

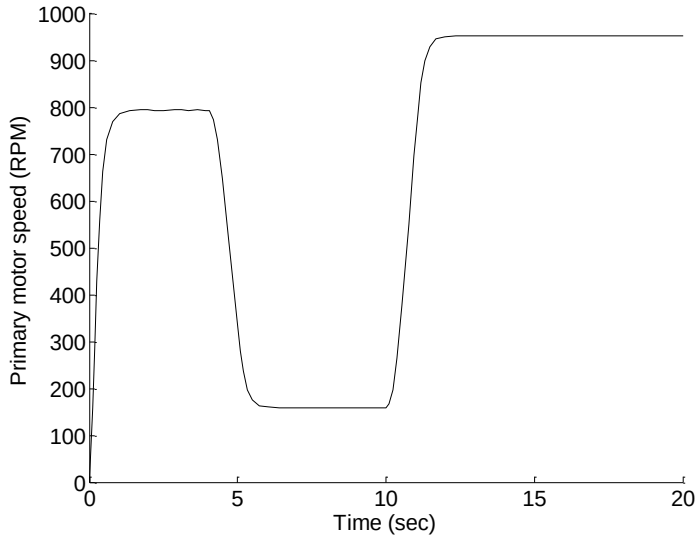

Figure 58: Hydraulic motor speed (RPM) with respect to time (sec)

The simulation results showed that the hydrostatic system or the hydraulic wind turbine system was stable during the high and low hydraulic pump speeds (that resembled the wind speed fluctuations). The results also demonstrated that the model responds fairly to the changes in wind speed. Figure 56 shows the change in pump flow generated as a result of change in the pump shaft. The transients are clearly seen in Figure 56. Corresponding changes in the primary motor flow is depicted in Figure 57. Finally, the primary motor speed is presented in Figure 58, which also responds to the change in system flow.

6.5 Reservoirs and accumulators

A reservoir is usually used as storage for the hydraulic fluid in the hydrostatic transmission. It would have pipes connecting both the hydraulic pump and hydraulic motor. A reservoir provides a large volume required for the fluid to transfer heat with the surrounding, a space for the fluid to settle the heavier contaminants, help the fluid lower its velocity, the presence of baffle inside the reservoir (as shown in Figure 59) helps to separate the fluid entering the reservoir from the fluid

entering the pump suction line, air space above the fluid to accept air that gets bubbled out of the fluid (Hydraulics & Pneumatics, 2012).

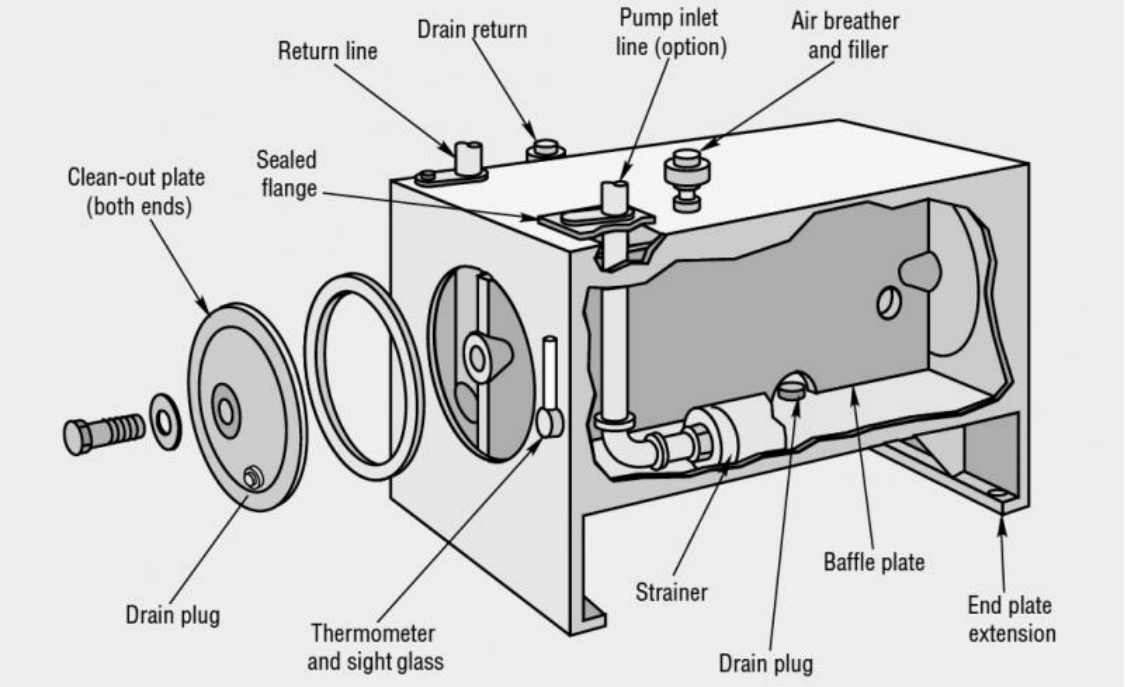

Figure 59: A cut-view of a rectangular reservoir (Hydraulics & Pneumatics, 2012)

Hydraulic accumulator stores the pressurized hydraulic fluid. It is a device which stores potential energy by means of gravity, mechanical springs or compressed gases. The stored potential energy in the accumulator is a quick secondary source of fluid power capable of doing useful work as required by the system (Esposito, 2009). Fluid pressure is maintained via an external source, based on which the accumulators are divided into two main types, mechanical and hydro-pneumatic. The mechanical accumulators can be loaded either by a spring or via a weight (Rapp, 2015). Therefore, the three basic types of accumulators used in hydraulic systems are: weight-loaded or gravity type, spring-loaded type, and gas-loaded type, as shown in Figure 60. The main applications of accumulators include their use as an auxiliary power source, a leakage compensator, an emergency power source and a hydraulic shock absorber.

Hydraulic accumulator in this work is used for the purpose of energy storage when the wind energy is not enough to power the gas liquefaction system and/or to provide rotational speed to the wind turbine rotor when it faces start-up problem during low wind conditions. The hydraulic fluid is stored when the system pressure reaches value higher than rated system pressure (during high wind conditions) and is released when there is not sufficient power from wind turbine rotor to drive the gas liquefaction system.

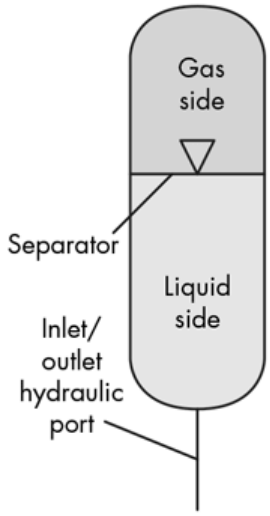

Figure 60: Bladder type hydraulic accumulator (J. Johnson, 2014)

6.6 Control system

The controls applied in this project are namely the wind turbine rotor speed control and the hydraulic motor speed control. Wind turbine torque control is attained by controlling the torque of the hydraulic pump and the wind turbine rotor. While the hydraulic motors speed control is attained by regulating the system pressure. The hydraulic fluid displacement is regulated and also the system pressure is controlled which in turn controls the speed of the hydraulic motor. A proportional integrator derivative (PID) controller is used to control the system pressure. A

feedback from the hydraulic motor speed is sent to the controller which then tries to output the set point speed for the hydraulic motor.

The control strategy applied in Region II, as discussed in Section 2.7.7, helps to attain optimum power coefficient, $C_{p.}$ The power coefficient, C_p is the efficiency of the wind turbine rotor for converting wind energy to rotational energy. It is given as,

$$C_p = \frac{P_{rotor}}{P_{wind}} \tag{62}$$

The power coefficient is maximised at steady state by the use of following equation.

$$\frac{D_p \Delta p_p}{\eta_{mech,p}} = K\omega^2 \tag{63}$$

where,

$$K = \frac{1}{2}\,\rho_{air} A R^3 \frac{C_{p,max}}{\lambda_{opt}^3}$$

Rearranging,

$$D_p = \frac{K\omega^2 \eta_{mech,p}}{\Delta p_p} \tag{64}$$

Using this equation, the pump displacement can be controlled as a result of which, the wind turbine rotor speed converges to the speed which gives optimal tip speed ratio and also helps in gaining maximum energy conversion (K. E. Johnson et al., 2006). Rajabhandharaks (2014) developed a linear approximation equation for the calculation of the optimal motor displacement, $D_{m,optimal}$ which is given by,

$$D_{m,optimal} = 0.0002\,\frac{\omega_r R}{\lambda_{opt}} - 0.0003 \tag{65}$$

Same approach has been used in this thesis for the purpose of simulation of the large scale hydraulic wind turbine system for liquefaction of gases. For the control of hydraulic motor

speed, a model based control system as explained in Hamzehlouia et al. (2011) and Vaezi & Izadian (2014) was used. This controller helped to maintain the hydraulic motor speed at a specified set point under load or input flow variations. Most control techniques make use of a proportional flow control valve to distribute the flow to the hydraulic motor and bypass the excess flow to the hydraulic pump as done by various authors Bai, Xie, Yu, & Zhou; Mohammad & S. E. (as cited in Hamzehlouia et al., 2011). However these techniques are mainly used in control of displacement in hydraulic cylinders. In this work, a Proportional Integral (PI) control technique is used for controlling the speed of hydraulic motor, which in turn controls the compressor speed. The control mechanism for the hydraulic motor frequency control is given as,

$$C(s) = K_p + \frac{K_i}{s} \tag{66}$$

where K_p is the proportional gain and K_i is the integral gain which can be adjusted for faster and accurate speed regulation purposes. The controller proportional gain used was 0.0025 and the integral gain was 0.15. The PI gain values can be tuned in Simulink which helps in finding the most appropriate values that could be used in a model. The high integral gain and low proportional gain are used. This has various advantages to the model such as fast dynamic response, reduced settling time and undershoot, and this also reduces steady state tracking error (Hamzehlouia et al., 2011).

The controller signal $C(s)$ from equation (66) is then passed to a proportional valve, which helps in regulating the pressure in the system, and thus controlling the speed of hydraulic motor. The hydraulic motor pressure, returning pressure and hydraulic pump pressure are given by,

$$P_m = PC(s) \tag{67}$$

$$P_{BP} = P\left(1 - C(s)\right) \quad (68)$$

where, P_m is the hydraulic motor pressure (Pa), P_{BP} is back pressure or pressure in the returning line (Pa).

6.7 Dynamic simulation of an open loop hydrostatic transmission with short term energy storage

The open loop hydrostatic transmission model is different from the closed loop hydrostatic transmission model as described in Section 6.4 in having short term energy storage. Therefore, an auxiliary motor and an energy storage system were added to the model from Section 6.4, and the model was simulated both for the high wind and low wind speed conditions. The open loop hydrostatic transmission model consisted of a hydraulic pump, a check valve, a pressure relief valve, a primary hydraulic motor, an auxiliary hydraulic motor, hydraulic hoses and a hydraulic accumulator for storage. An electrical storage was considered in this section, so that the dynamic system response could be compared with the work presented by Hamzehlouia et al. (2013).

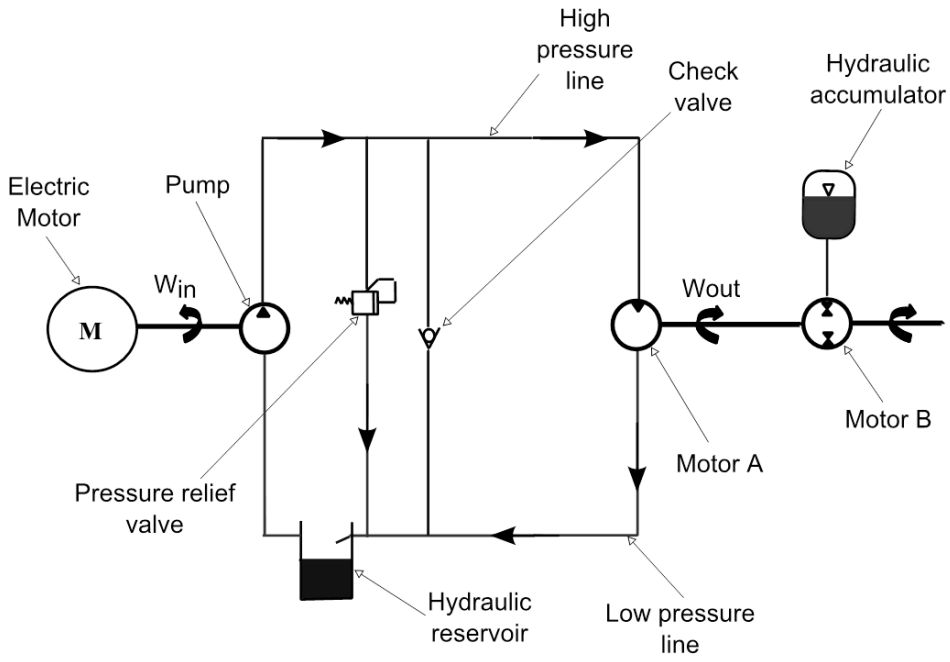

Figure 61: Schematic of open loop hydrostatic transmission

The purpose of the auxiliary hydraulic motor, as shown in Figure 61, was to capture the excess energy during high wind speed conditions and store it in the electrical storage for the low wind speed conditions. Hamzehlouia et al. (2013) considered the electrical storage; however, the high pressure fluid can itself be stored in its own form as backup energy for the low wind conditions. For all the other simulation works presented in this thesis, the high pressure hydraulic fluid is stored in the accumulator instead of storing excess energy in the electrical form.

For the high wind speed conditions, hydraulic pump provided a constant flow of high pressure hydraulic fluid to drive the hydraulic motor and stored the excess high pressure fluid in the storage. The system pressure was controlled using a proportional integrator (PI) controller as presented in Section 6.6 that helped in the regulation of the high pressure fluid flow to the primary hydraulic motor that in turn provided constant speed to the primary hydraulic motor. With the natural flow configuration, the high pressure fluid was divided between the primary

hydraulic motor and the auxiliary hydraulic motor based on the fluid properties of the hydraulic fluid. But the flow was maintained such that the primary hydraulic motor could run at desired constant speed. The only input to the system in this configuration type was the hydraulic pump angular velocity. The flow diagram for the high wind speed condition is presented in Figure 62 in which the excess energy is stored in battery.

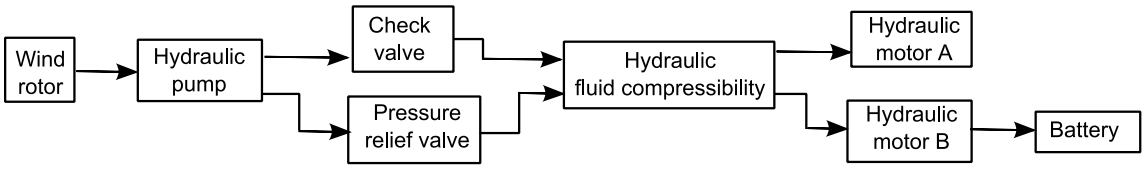

Figure 62: Flow diagram for the high wind speed condition (Hamzehlouia et al., 2013)

However, the hydraulic pump would fail to start up on its own when there are low wind conditions. This is when the system requires the stored energy. The electrical storage system will discharge enough energy to drive the hydraulic pump. In this case, the auxiliary motor will behave as a hydraulic pump which regulates the flow to drive the hydraulic motor. Auxiliary motor will capture enough amount of energy to provide constant speed to the primary hydraulic motor. The flow diagram for a low wind speed condition is presented in Figure 63, in which the auxiliary motor behaves as a pump to keep the system functional.

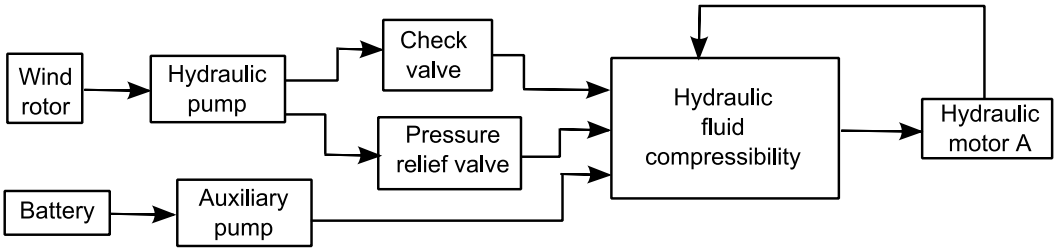

Figure 63: Flow diagram for the low wind speed condition (Hamzehlouia et al., 2013)

The storage was considered to be a battery storage so that the model comparison could be made with Hamzehlouia et al. (2013). The excess energy captured by the auxiliary motor is stored in battery and transformed into electrical energy with the help of a generator. This stored

energy would then be utilized during low wind periods when the system needs to keep running. The charge current in battery is given as,

$$I_B = \frac{T_{mB}\omega_{mB}\eta_{gen}}{V_B} \tag{69}$$

where T_{mB} is auxiliary pump/motor torque (Nm), ω_{mB} is the auxiliary pump/motor speed (rad/s), η_{gen} is efficiency of generator, and V_B is the battery voltage (Volts).

The state of the charge of battery is given as,

$$SOC = \frac{C_i}{C_0} \tag{70}$$

where, C_i is available or initial charge of the battery and C_0 is the nominal capacity of the battery. Since the auxiliary pump/motor is coupled with the generator, its speed is given by,

$$\omega_{mB} = kI_B \tag{71}$$

where k is the current coefficient of the generator.

The parameters used for this model are listed below in Table 6. The detailed parameter list is presented in Appendix C.

Table 6: Parameters used for simulation of the open loop hydrostatic transmission model (Hamzehlouia et al., 2013)

Symbol	Definition	Value	Unit
k	Current Coefficient	10	
V_B	Battery voltage	12	Volts
C_0	Initial battery capacity	31.25	Amp.hr
SOC_0	Initial state of charge	50	%
k_p	Proportional gain	0.001	
k_i	Integral gain	10	

The results from the simulation work are presented in Figure 64 to Figure 68. The hydraulic motor speed is controlled by controlling the system pressure. These simulation results showed that the excess energy during high wind speed conditions can be stored in the form of

electric energy in battery and then released during the low wind conditions, when the system has problem during start-up.

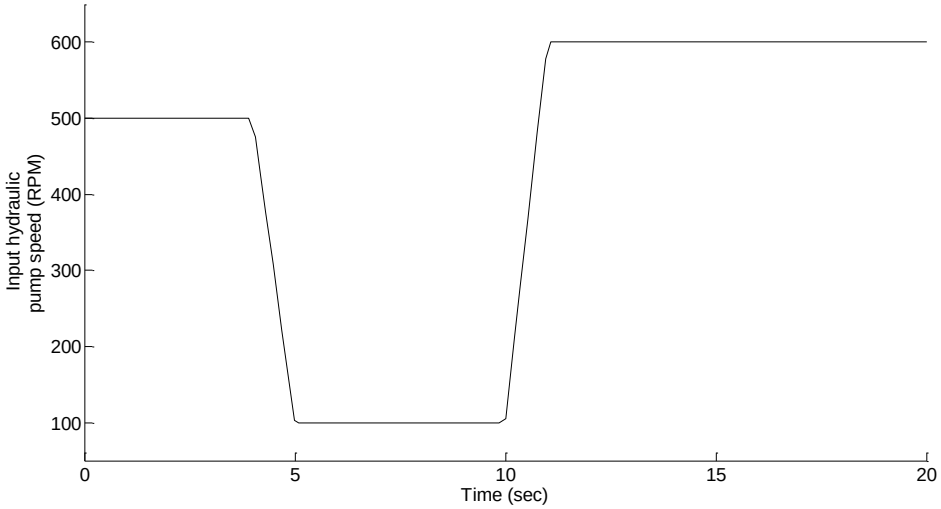

Figure 64: Variable pump speed (RPM) signals provided to the hydraulic pump with respect to time (sec) representing the changes in wind speed

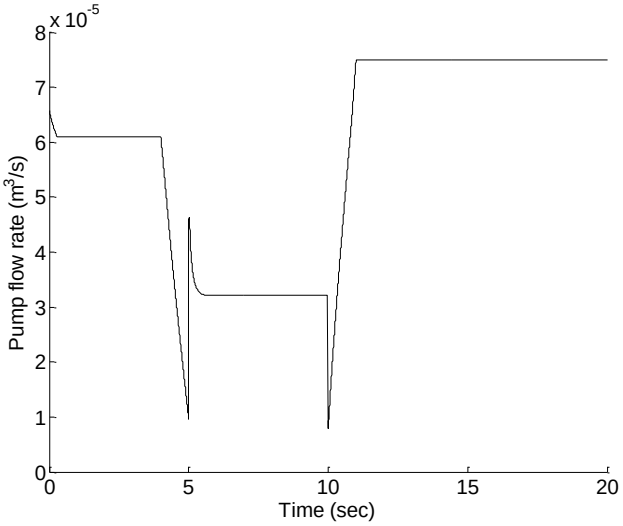

Figure 65: Pump flow rate (m^3/s) with respect to time

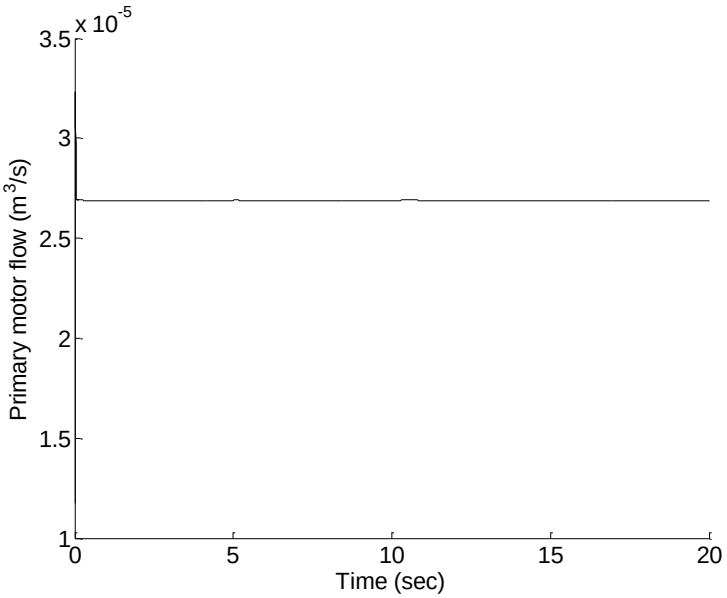

Figure 66: Hydraulic motor flow (m^3/s) with respect to time

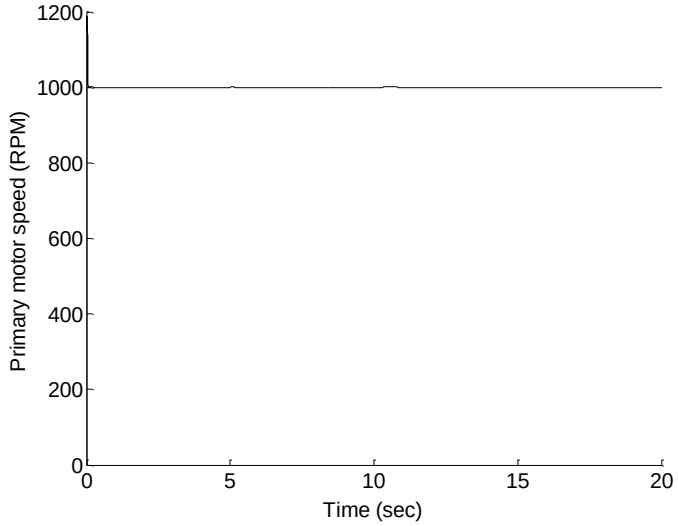

Figure 67: Hydraulic motor speed (RPM) with time

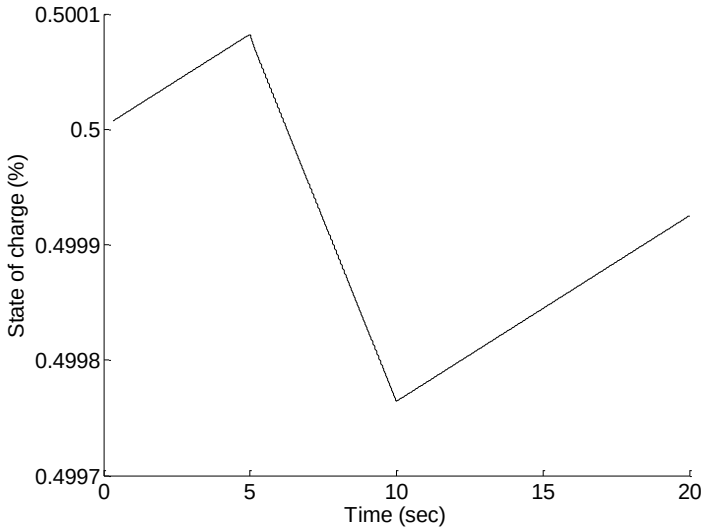

Figure 68: State of charge (%) of the storage with respect to time (sec)

Figure 65 shows the change in pump flow generated as a result of change in the pump shaft. The primary motor flow is depicted in Figure 66. Finally, the primary motor speed is presented in Figure 67, which also responds satisfactorily to the change in system flow. As it can be seen from Figure 68, the state of charge (SOC) of the storage responds satisfactorily to the input conditions. The SOC (%) rises sharply during high wind conditions, meaning the energy is stored in the battery and it decreases immediately during low wind conditions, meaning the energy stored in battery is released. The hydraulic motor flow and the hydraulic motor speed however are maintained constant during all these processes, as depicted in Figure 66 and Figure 67 respectively.

The results obtained from Hamzehlouia et al. (2013) are presented in Table 7 which show that the simulation results agree to some extent with the results acquired by Hamzehlouia et al. (2013). The slight differences present in the results between Hamzehlouia et al. (2013) and this study could possibly be due to the effect of the PI controller present in the system that was used for controlling the hydraulic motor speed. According to (Hamzehlouia et al., 2013), the

spikes resulting at 5 seconds and 10 seconds such as in Figure 65 to Figure 67 is due to the PI controller which makes the open loop hydrostatic transmission switch between different configurations to maintain the reference angular velocity of the hydraulic motor by controlling the hydraulic fluid flow rate in the system. However, this could be determined with some further investigation.

6.8 Summary

This chapter started with a review on the previous works that utilized fluid power technology, specifically hydrostatic transmission for wind energy conversion systems. Then the details on the closed and open loop hydrostatic transmission systems including their dynamic modeling and simulation were presented. The Chapter then presented comparisons for simulation results obtained from the open loop hydrostatic transmission model with those presented by Hamzehlouia et al. (2013). The open loop hydrostatic transmission model also included a temporary storage system (battery storage) that supplied energy to the system during low wind speed conditions. The results obtained were found to be in agreement with those acquired from Hamzehlouia et al. (2013) with some slight differences that could be due to the PI controller used for controlling the speed of hydraulic motor. This needs further investigation.

The electric form of energy storage was considered in this chapter simply to be able to compare the developed model on open loop hydrostatic transmission with already published journal articles, to analyse the system performance and to gain confidence in the model so that it could be extended to large scale simulation work, such as that presented in Chapter 10. The original idea for this research work however, is to store the high pressure hydraulic fluid in the hydraulic accumulator without converting it into electricity.

Table 7: Comparing obtained simulation results with those from Hamzehlouia et al. (2013)

Time (sec)	Input hydraulic pump speed (RPM)		Pump flow (m^3/sec)		Hydraulic motor flow (m^3/sec)		Hydraulic motor speed (RPM)		State of charge (%)	
	Hamzehlouia et al. (2013)	This study	Hamzehlouia et al. (2013)	This study	Hamzehlouia et al. (2013)	This study	Hamzehlouia et al. (2013)	This study	Hamzehlouia et al. (2013)	This study
0	500	500	$6.9x10^{-5}$	$6.4x10^{-5}$	$3.0x10^{-5}$	$3.0x10^{-5}$	1190	1180	0.50000	0.50000
5	100	100	$1.3x10^{-5}$	$1.0x10^{-5}$	$2.5x10^{-5}$	$2.7x10^{-5}$	1000	1000	0.50020	0.50009
10	100	100	$1.3x10^{-5}$	$1.0x10^{-5}$	$2.5x10^{-5}$	$2.7x10^{-5}$	1000	1000	0.49800	0.49975
15	600	600	$7.6x10^{-5}$	$7.5x10^{-5}$	$2.5x10^{-5}$	$2.7x10^{-5}$	1000	1000	0.49840	0.49985
20	600	600	$7.6x10^{-5}$	$7.5x10^{-5}$	$2.5x10^{-5}$	$2.7x10^{-5}$	1000	1000	0.49970	0.49993

7 Dynamic simulation of a wind energy driven Gifford McMahon cryocooler

A complete dynamic simulation of a wind energy driven Gifford McMahon (GM) cryocooler system, as shown in Figure 4 (see Section 1.2.2), is presented in this chapter. This chapter starts with the introduction and overview of the system components, discusses the options for the hydrostatic transmission. This chapter also illustrates in detail the geometry, numerical procedures and algorithms, and test scenarios considered for the simulation. The thermo-mechanical process for the Dewar storage vessel is also presented in this chapter. Different heat transfer mechanisms for Dewar heat transfer are listed and governing equations for the thermo-mechanical model are presented.

After the development of the model, simulations are performed for the cool down of the cold head, and condensation and evaporation of nitrogen within the liquid nitrogen generation unit. Following this, simulations are extended and performed for the cryocooler unit driven by an electric motor at steady compressor motor frequencies, at sinusoidal varying set points, at random frequency set points, and at frequency set points that follow a wind speed pattern of Roskrow Barton farm, UK for 10 hours period. The simulation results are presented in this chapter and later on compared with the experimental results in Chapter 8.

The simulations at steady state frequencies and varying set point frequencies are carried out in this chapter as the main objective of this research is to determine the feasibility of producing cryogens fairly continuously using wind energy (which is variable).

7.1 Introduction – overview of components and component options

The GM cryocooler unit driven by an electric motor, as described in Section 5.6 is used as a unit to produce liquid nitrogen for experimentation in the laboratory. The driving component for this system could be a constant frequency electric motor or a variable frequency electric motor that is controlled by a VFD. For simulation purposes, both techniques have been used to analyse the system response. Steady state experiments at steady frequencies were also performed for the system response analysis and also for comparison of the simulation results. A 6 kW variable speed wind turbine is selected to drive an open loop hydrostatic transmission drive, which in turn drives the helium compressor of the GM cryocooler system. The major parameters for an appropriate wind turbine, the hydrostatic transmission and the GM cryocooler system are given in Table 8 and Table 9 respectively. Detailed component description is presented in the Appendix E.

Table 8: Parameters for wind turbine rotor and hydrostatic transmission

Symbol	Description	Value	Unit
ρ_{air}	Air density	1.225	kg/m^3
R	Rotor radius	3.2	m
J_r	Rotor shaft inertia	890	kg.m^2
D_p	Hydraulic pump displacement	0.0000149	m^3/rad
D_{mA}	Hydraulic motor displacement	9.9e-7	m^3/rad
ρ	Fluid density	852.8	kg/m^3
v	Fluid viscosity	18.78e-6	m^2/s

Table 9: Parameters for GM cryocooler system

Symbol	Description	Value	Unit
V_0	Compressor dead volume	0.0000013	m^3
V_s	Swept volume	0.0000375	m^3/rev
V_{comp}	Compressor cylinder volume	0.0022	m^3
L_{reg}	Regenerator length	0.10	m
D_{reg}	Regenerator diameter	0.02	m
Pr	Regenerator porosity	0.4	-
Lt	Displacer length	0.141	m
dt	Displacer diameter	0.046	m

7.2 Options for the hydrostatic transmission drive

7.2.1 Dynamic model of electric motor with constant rotation speed set point

The electric motor considered in this simulation is used for supplying constant and variable rotational speeds to the hydrostatic transmission drive. The rotational speed supplied of the electric motor was related to the volumetric flow delivered by the hydraulic pump by the equations (47) to (49) presented in Section 6.4.

7.2.2 Wind turbine rotor

For this simulation work, a variable speed wind turbine rotor with a rotor radius of 3.2 m was used. The parameters for the wind turbine rotor are presented in Table 8. The governing equations for a hydrostatic transmission are already discussed in Sections 6.4, 6.6 and 6.7.

7.3 Options for Helium compressor drive

In the simulation, the helium compressor can be operated by two driving mechanisms, namely, an electric motor with constant speed and/or an open loop hydrostatic transmission as described in Section 6.7.

7.3.1 Dynamical model of an electric motor with rotational speed varying between set point to set point

For the dynamical model of an electric motor the helium gas pressure values were assumed to be known from measurements. The pressures in the system were taken to be constant. Initial low pressure for working fluid (helium) was taken to be 260.325 kPa. The pressure ratio was assumed to be 6.4 so that the discharge pressure is ~1666 kPa. Knowing these values, the work input needed for the compression process in Watts is given by,

$$\dot{W}_{cp} = \dot{m}\left(\frac{n}{n-1}\right)\left(\frac{P_2}{\rho_2} - \frac{P_1}{\rho_1}\right) \tag{72}$$

where $\dot{m}$ is the helium mass flow rate (kg/s) and can be calculated as,

$$\dot{m} = V_s\, \rho_1 f \tag{73}$$

n is the specific heat ratio for helium (which is 1.667), P_1 is the initial helium pressure (kPa), P_2 is the final helium pressure (kPa), ρ_1 is the initial helium density (kg/m^3) and ρ_2 is the final helium density (kg/m^3), V_s is the compressor swept volume (m^3/rev), f is the driving motor frequency (Hz). The shaft power and the motor power can be determined by knowing the motor efficiency.

7.3.2 Open loop hydrostatic transmission

The helium compressor can also be driven using the open loop hydrostatic transmission, where the hydraulic motor drive shaft is coupled with the helium compressor. Model for open loop hydrostatic transmission has been explained in Section 6.7.

7.4 Thermo-mechanical dynamic process simulation of the GM cryocooler

The geometry and parameters of the GM cryocooler are presented in Table 9. The related numerical equations used for the model are also presented in Section 7.5. The cold head temperature (K) for the initial cool down from room temperature to liquid nitrogen boiling point is given by,

$$T(t) = T_a + (T_0 - T_a)e^{-kt} \quad (74)$$

where, $T(t)$ is the cold head temperature (K) at time t , T_a is the ambient temperature (K) or the temperature to which the cold head has to be cooled down, T_0 is the initial temperature (K) of cold head, and k is the rate of cooling (K/sec). For this model, it was assumed the temperature of cold head after 15 minutes was 80 K, the ambient temperature was taken to be 300 K. After calculating the rate of cooling, it was possible to predict the cold head temperature (K) decline with respect to time.

The simulation for the cold head temperature and cool down time was performed taking the initial temperature of ~300 K and the temperature of the object to be cooled down to 77.325 K.

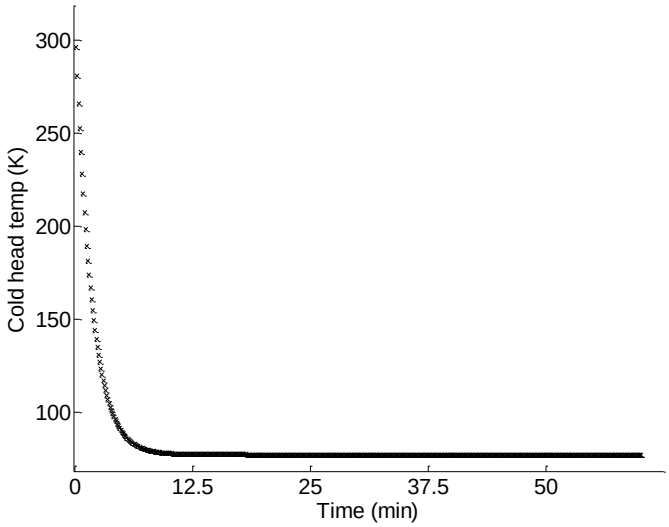

Figure 69: Cool down of the cold head when starting from room temperature (300K)

As can be seen from the graph it takes around 25 minutes for the cold head to reach the liquid nitrogen boiling point of ~77.325 K.

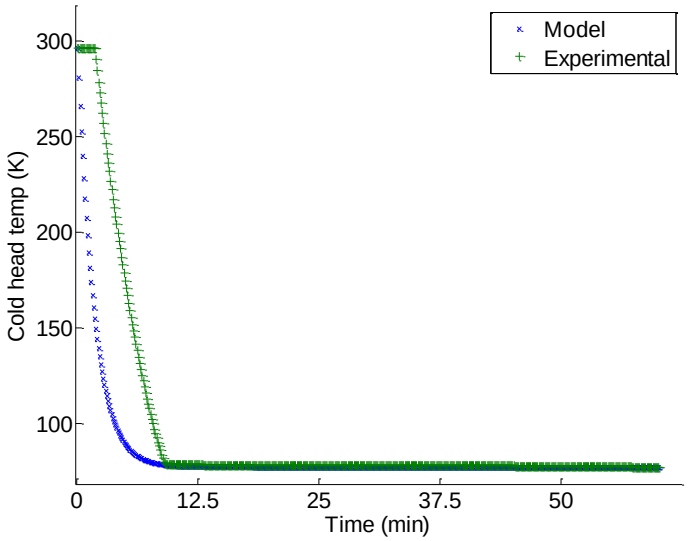

Figure 70: Cold head temperature (K) versus time taken (min) showing the simulated and experimental results

The comparison between the simulated and experimental cold head temperature (K) is presented in Figure 70. The time taken by the cold head temperature is also depicted in the

figure. The time taken by the cold finger to reach the boiling point was same both in the simulation and experiment, with difference in the nature of cool down curve as is seen in Figure 70.

7.5 Dynamical model for nitrogen liquefaction within a Dewar storage vessel

7.5.1 Geometry, configuration and materials

The Dewar vessel is a storage vessel for liquid nitrogen produced by the GM cryocooler system in the laboratory. It is fabricated by Cryofab and is made up of 304 SS Stainless steel double-walled containers mainly designed for collecting and storing liquid nitrogen. This vessel also has multilayer insulation in its vacuum annulus. With development in welding and fabrication, Cryofab has provided solutions to the problems like rust and scratches in the bottom of the Dewar flask (Cryofab, 2017).

The laboratory Dewar flask consists of several elements and safety features as already discussed in Section 5.8. A schematic of Dewar vessel with all the features is shown in Figure 71. The Dewar flask fabricated by Cryofab, was part of the liquid nitrogen generator unit from Cryomech. This container has been modified by Cryomech. But due to confidentiality issues, the detailed dimensions of this container could not be obtained from neither of these companies. Therefore, the required parameters for the heat loss model were calculated with the help of available literature.

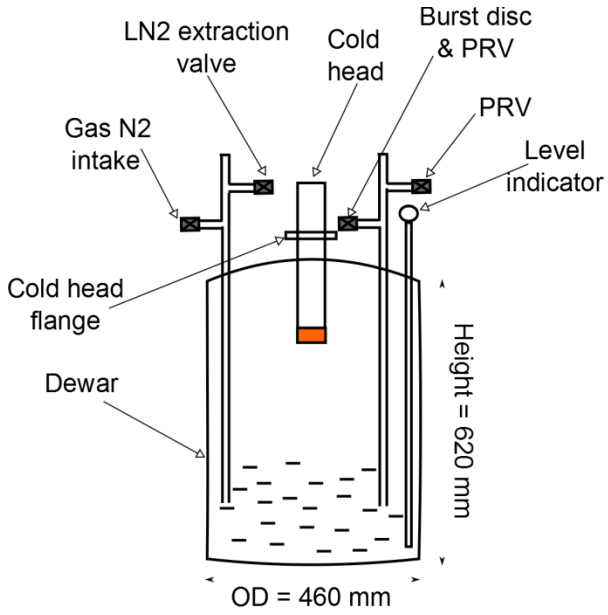

Figure 71: Schematic of Dewar vessel with installed safety features (PRV = Pressure Relief Valve)

While designing the inner vessel, the thickness of the inner vessel should be selected such that it can withstand only the internal pressure and bending forces. This is also because if the inner vessel is too thick, it will take longer time to cool down and more liquid will be wasted for the cool down process. The minimum thickness for a cylindrical vessel, according to ASME Code, Section VIII (as cited in Barron, 1985), is given by,

$$t = \frac{pD}{2s_a e_w - 1.2p} = \frac{pD_0}{2s_a e_w + 0.8p} \tag{75}$$

where p is the design internal pressure (absolute pressure for vacuum-jacketed vessels), D is the inside diameter of the shell, D_0 is the outside diameter of the shell, s_a is the allowable stress (approximately one-fourth minimum ultimate strength of material), and e_w is the welding efficiency and is taken as 0.6 for this work following Barron (1985).

However, the outer vessel cannot be made with very smaller thickness. Though the outer vessel has to withstand only the atmospheric pressure acting on it, it would fail from the standpoint of elastic instability which can be collapsing or buckling. The collapsing or critical

pressure for a long cylinder exposed to external pressure is given by Timoshenko and Gere (as cited in Barron, 1985),

$$p_c = \frac{2E(t/D_0)^3}{1-v^2} \quad (76)$$

where E is the Young's modulus of shell material, t is the shell thickness, D_0 is the outside diameter of the shell and v is the Poisson's ratio for shell material.

A long cylinder is defined as the one for which the length-to-diameter ratio meets the following conditions:

$$L/D_0 > 1.140\,(1-v^2)^{1/4}\,(D_0/t)^{1/2} \quad (77)$$

where L is the unsupported length of the cylinder (distance between the stiffening rings for the outer shell). The cylinder was found to be a long cylinder for this work.

Similarly, the lid thickness was calculated using the equation for a flat circular plate loaded centrally

$$t_{lid} = 1.65 * \left(\frac{F}{\sigma_t}\, log_e \frac{d}{d_0}\right)^{0.5} \quad (78)$$

where, F is the load on the lid (N), σ_t=s_a is the allowable design stress, d is the diameter of the whole plate (which is the Dewar vessel lid outer diameter) and d_0 is the diameter of the area loaded centrally (m). The diameters of the cold head, extraction valve, the pressure relief valve, burst disc, level indicator and the vacuum release port were added together to find the diameter of the area which was loaded centrally on the Dewar vessel lid.

7.5.2 Delivery of nitrogen (air to drying system to nitrogen filtration)

Atmospheric air in the laboratory is compressed to a higher pressure of ~790 kPa, passed through an attached after-cooler, and then passed to a refrigerant air dryer. The air is compressed to a higher pressure so that it can be passed through the air dryer and the set of filters to remove moisture, oil, and carbon that might be present in it. The refrigerant air dryer is a miniature vapor compression refrigeration unit. A typical process flow diagram for a refrigerated air dryer is shown in Figure 72. The warm compressed air from the compressor enters the air-to-air heat exchanger. It gets pre-cooled by the air that is already cold. Then this pre-cooled air is passed through the evaporator to further lower its temperature. While doing so, the water vapor condenses forming liquid droplets and gets collected in the moisture separator. These droplets are discharged from the separator with the help of an automatic drain as shown in Figure 73. This condensate works on the float valve mechanism. The cooling is generated by the vapor compression refrigeration system of the refrigerant (here R134a) as shown as the refrigerant flow loop in Figure 72. The cold and dried air is returned to the air line through the heat exchanger where it is reheated before it is released.

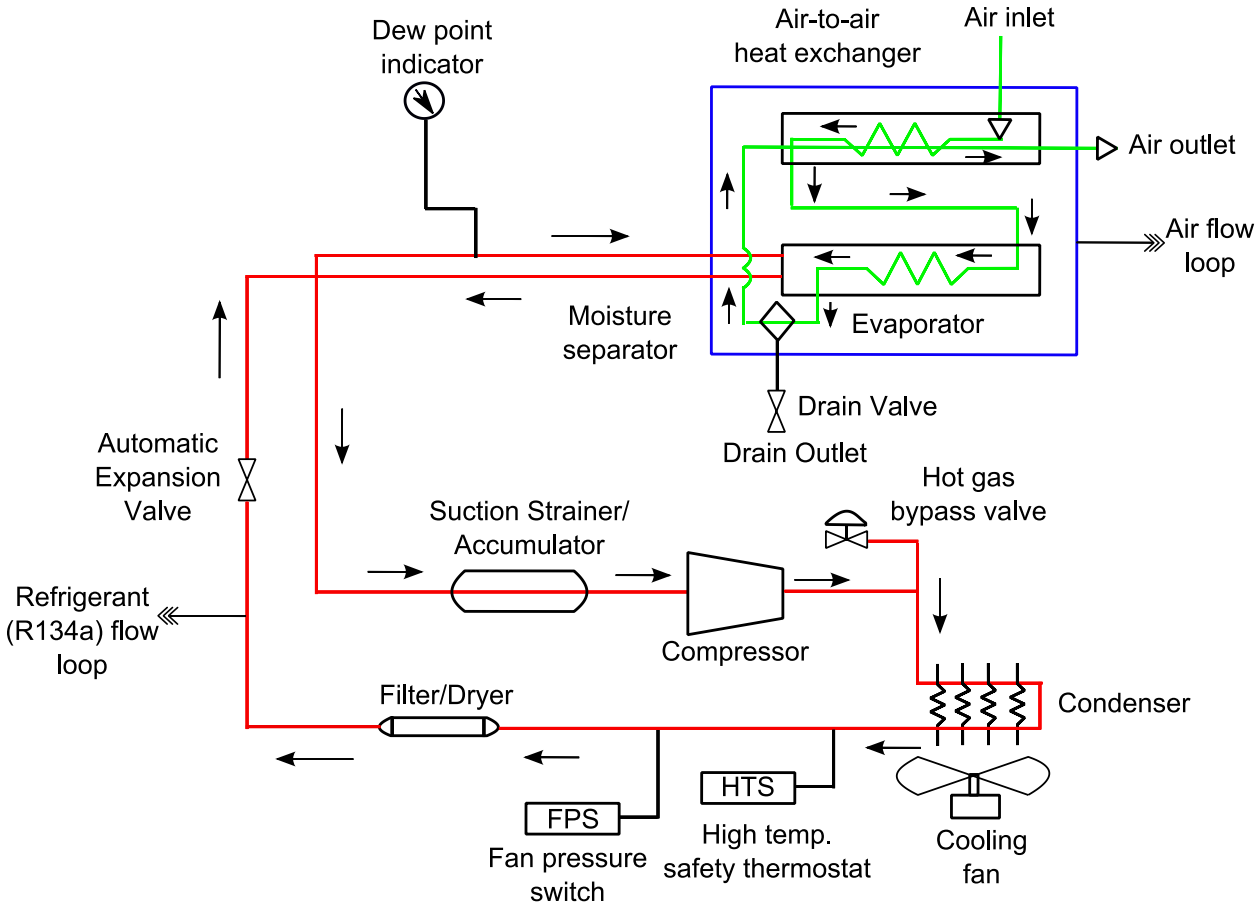

Figure 72: A typical refrigerated air dryer (eCompressedair, 2017)

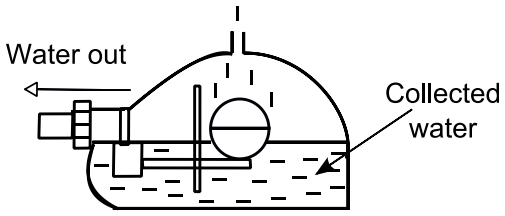

Figure 73: A hyper drain condensate which works on float valve mechanism

The dried and cold compressed air is then passed through the filter bank to remove any remaining condensate, oil contaminants, and charcoal. The filter bank assembly, along with the nitrogen separator are discussed in detail in Section 8.1.4.

7.5.3 Heat transfer by conduction

Fourier's law states that the rate of heat flow through a single homogenous solid is directly proportional to the area A of the section at right angles to the direction of heat flow, and to the change of temperature with respect to the length of the path of the heat flow, $\frac{dT}{dx}$. A thin slab of material of thickness dx and surface area A has one face at a temperature t and the other at a temperature (T+dT). Then from Fourier's law, we have the rate of heat flow in the direction x as (Eastop & McConkey, 1993),

$$\dot{Q} \alpha A \frac{dT}{dx} \tag{79}$$

$$\dot{Q} = -KA \frac{dT}{dx} \tag{80}$$

The heat flow in the direction of x is always positive but since dT is always negative, $\dot{Q}$ is also negative. Here, K is the thermal conductivity of the material which is the amount of heat flow per unit area per unit time when the temperature decreases by one degree in unit distance. The unit for λ is W/mK or kW/mK.

Integrating the above equation and considering K as a constant, we get the following equation,

$$\dot{Q} = \frac{KA}{x}(T_1 - T_2) \tag{81}$$

Since the thermal conductivity of stainless steel changes with temperature, the average thermal conductivity from low to high temperature can be taken for the calculations (Barron, 1985). The mean thermal conductivity of stainless steel is given by,

$$K_{avg} = \frac{1}{T_1 - T_2} \int_{T_1}^{T_2} K dT \tag{82}$$

The heat transferred by conduction can be calculated using the following equation,

$$\dot{Q} = K_{avg}\ \frac{A}{x} \tag{83}$$

A molecule at higher energy has to travel short distances and strike a lower energy molecule and transfer energy in case of heat transfer at atmospheric conditions. The gaseous conduction heat transfer is directly proportional to gas pressure. The energy transfer rate by molecular conduction can be given by (Barron, 1985),

$$\dot{Q} = GPA_1(T_2 - T_1) \tag{84}$$

where G is the property dependent function and is given by,

$$G = \frac{\gamma+1}{\gamma-1}\left(\frac{g_c R}{8\pi T}\right)^{1/2} * F_a \tag{85}$$

P is the vacuum pressure of the gas, A_1 is the inner vessel area, T_1 and T_2 are the initial and final temperatures, γ is specific heat ratio, g_c is gravitational constant, R is gas constant. F_a is the accommodation coefficient factor, which is given by,

$$\frac{1}{F_a} = \frac{1}{a_1} + \frac{A_1}{A_2}\left(\frac{1}{a_2} - 1\right) \tag{86}$$

A_2 is the outer vessel area. Subscript 1 and 2 are for the inner and outer vessel respectively and a is the accommodation coefficient, which is 0.85 for air.

7.5.4 Heat transfer by radiation

Heat is transferred across the annular space of a vacuum-insulated vessel by radiation from the hot outer vessel to the cold inner vessel and by gaseous conduction through the residual gas with the annular space. The radiant heat transfer rate between two surfaces is given by the modified Stefan-Boltzmann equation,

$$\dot{Q} = F_e F_{1-2}\sigma A_1(T_2^4 - T_1^4) \tag{87}$$

where, F_e is emissivity factor, F_{1-2} is configuration factor, σ is Stefan Boltzmann constant and is taken as 5.67×10^{-8} $Wm^{-2}K^{-4}$, A_1 is the inner vessel area, and T is the absolute temperature. The configuration factor F_{1-2} is assumed a value equal to that for cryogenic-fluid storage vessels in which the inner vessel is completely enclosed by the outer vessel (Barron, 1985). The subscripts 1 and 2 refer to the inner vessel and outer vessel respectively. The emissivity factor, F_e for diffuse radiation for concentric spheres or cylinders is given by,

$$\frac{1}{F_e} = \frac{1}{\varepsilon_1} + \frac{A_1}{A_2}\left(\frac{1}{\varepsilon_1} - 1\right)$$

Simplifying the above equations, we get,

$$\dot{Q} = \frac{\sigma\left(T_1^4 - T_2^4\right)}{\frac{1-\varepsilon_1}{\varepsilon_1 A_1} + \frac{1}{F_{1-2}A_1} + \frac{1-\varepsilon_2}{\varepsilon_2 A_2}} \qquad (88)$$

ε is the emissivity of the surface and A is the surface area (m^2).

The heat emitted by radiation is propagated as electromagnetic waves and the energy will be absorbed by another surface on which the radiation is incident. The absorption coefficient of a surface is equal to its emissivity. Therefore the greater value of emissivity means that larger quantity of heat is absorbed. Emissivity of a surface can be reduced by polishing the surface or even by plating the surface with materials having low emissivity.

7.5.5 External conditions assumed

The surface area, cross-section area and volume for Dewar vessel and the elements of Dewar for conducted and radiated heat transfer were calculated using the equations as discussed in Sections 7.5.3 and 7.5.4. The helium gas property constants taken for this model are: the specific heat capacity for helium was taken as 5192 J/kgK, the gas constant as 2074.6 J/kgK,

gamma as 1.67 and the dynamic viscosity as 19.81e-6 (Ns/m^2) respectively. Similarly, the specific heat capacity for liquid nitrogen was taken to be 2.04 kJ/kgK, and for 304 SS Stainless steel as 0.51 kJ/kgK respectively. The room temperature was taken to be 296.15 K. Since the thermal conductivity of the metal changes with temperature, an average thermal conductivity of 12.3 W/mK was taken for 304 Stainless steel for the temperature range of 300-77 K as suggested by Barron (1985). Also the emissivity factor was taken to be 0.04215 following ASME Boiler and Pressure Vessel Code Section VIII (as cited in Barron, 1985). Other parameters and the code used for modeling are presented in detail in Appendix D.

7.5.6 Differential equation for heat transfer between gas and cold finger

The total heat transfer due to conduction and radiation are calculated for the Dewar vessel lid, the neck area (via cold head), extraction valve, pressure relief valve and burst disc, level indicator and vacuum release port, is represented by q_1 (as shown in Figure 74) and is calculated by the equations presented in Sections 7.5.3 and 7.5.4 respectively. The total radiant heat transfer from the outer vessel to inner vessel, represented by q_w was also calculated. The total heat transferred from gaseous nitrogen supplied from the nitrogen generator, represented by q_2 was derived. q_L in Figure 74 is the latent heat of vaporization of liquid nitrogen.

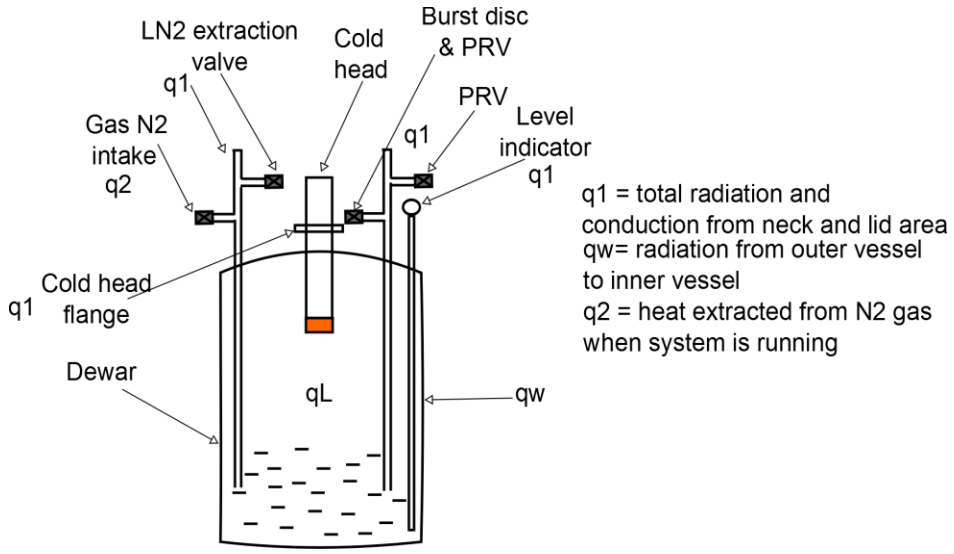

Figure 74: Dewar vessel configuration used for heat loss calculations

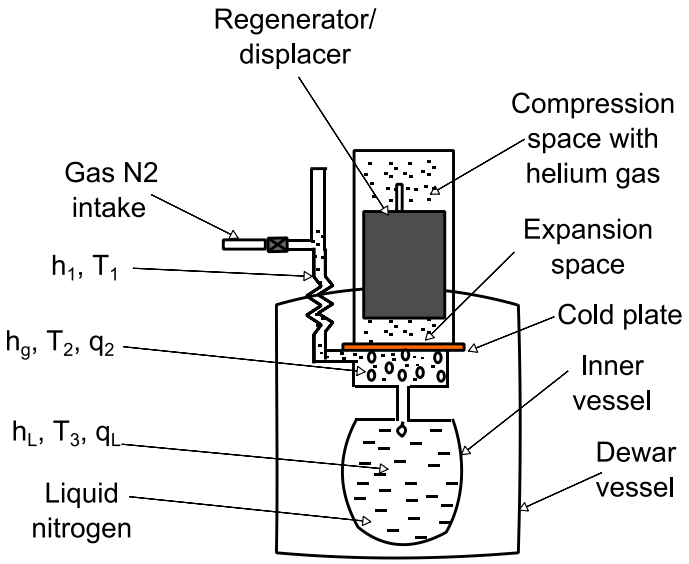

Figure 75: Dewar vessel configuration showing energy distribution for the nitrogen liquefaction process. Drawing adapted from Wang (2005)

The following energy equations were used to calculate the latent heat of condensation q_L, and the heat carried by gaseous nitrogen q_2. The heat carried with the gaseous nitrogen q_2 as pointed out in Figure 74, is given by Wang (2005),

$$q_2 = \dot{m}(h_1 - h_g) \tag{89}$$

And the latent heat of condensation is given by

$$q_L = \dot{m}(h_g - h_L) \tag{90}$$

Rearranging these equations, we get,

$$q_2 = \dot{m}(h_1 - h_L) - q_L \tag{91}$$

Finally, the enthalpy of the saturated vapour inside the Dewar vessel can be determined by,

$$h_g = (q_2 - \dot{m}h_1)/\dot{m} \tag{92}$$

From the known pressure and enthalpy of gaseous and liquid nitrogen inside the Dewar, the temperature of the gaseous nitrogen can be determined using REFPROP (Lemmon, Huber, & McLinden, 2013). The temperature of gaseous nitrogen immediately after it enters the Dewar vessel (T_2) was estimated to be 79.46 K. The heat conducted by gaseous nitrogen can also be calculated using the equation,

$$q_2 = \dot{m}(h_1 - h_L) = \dot{m}\left[h_L + \int_{T_{BP}}^{T_{Ambient}} C_{p,v}dT\right] \tag{93}$$

The heat transferred by the intake of gaseous nitrogen into the Dewar vessel was determined to be 23.88 W. The total heat leak into the Dewar vessel system is then given by,

$$q_T = q_1 + q_2 + q_{Lc} - q_{Lv} \tag{94}$$

q_{Lc} is the latent heat of condensation and q_{Lv} is the latent heat of vaporisation of nitrogen. Now for the GM cryocooler system with the helium gas as the working fluid, the work requirement per unit mass for the compressor is (Barron, 1985),

$$-W/m = [T_2(s_1 - s_2) - (h_1 - h_2)]/\eta_{c,0} \tag{95}$$

The state points are presented in Figure 76. In equation (95), T_2 is the temperature of helium gas (K) at point 2 after compression, s_1 and s_2 are the entropy at point 1 and 2 (kJ/kgK) respectively, h_1 and h_2 are enthalpies at point 1 and 2 (kJ/kg) respectively, and $\eta_{c,0}$ is the compressor efficiency.

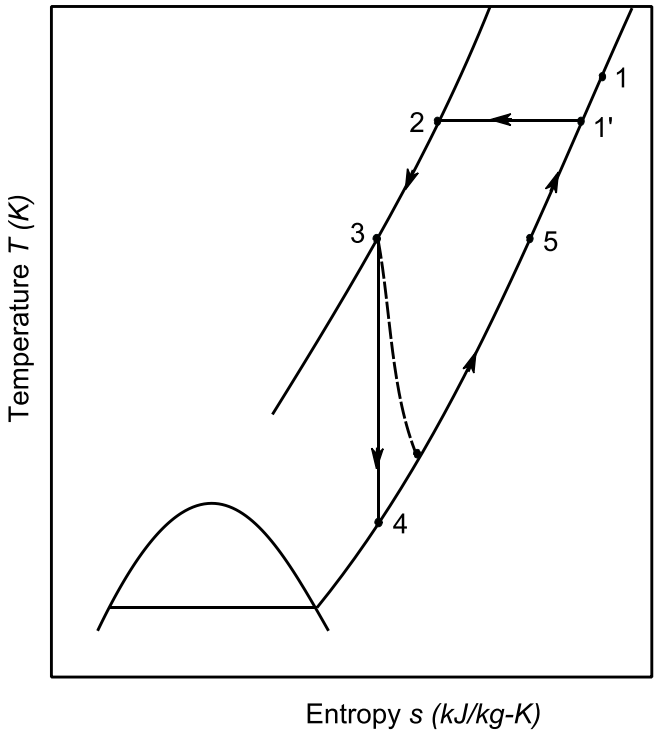

Figure 76: The temperature entropy diagram for the GM refrigeration process (Barron, 1985)
The actual enthalpy at the end of the expansion process 3-4 in Figure 76 is determined from

$$h_4' = h_4 + (1 - \eta_{ad})(h_3 - h_4) \quad (96)$$

h_3 and h_4 are enthalpies (kJ/kg) at point 3 and 4 respectively, η_{ad} is the expansion efficiency.

The refrigeration effect per unit mass of helium gas is then given by,

$$q_a/m = (m_e/m)(h_5 - h_4') = \eta_{ad}(m_e/m)(h_5 - h_4) \quad (97)$$

m_e is the mass of gas within the expansion space at the end of the expansion process 3-4, and m is the total mass of compressed gas. Since the volume of the expansion space remains constant during the expansion process, the mass ratio can be determined in terms of density ratio as (Barron, 1985),

$$m_e/m = \rho_4^{'}/\rho_3 \tag{98}$$

ρ_3 is the helium gas density at point 3 and $\rho_4^{'}$ is the actual density of at the end of expansion process. The COP for the cryocooler/refrigerator is,

$$COP = -q_a/W \tag{99}$$

Therefore, the excess refrigeration effect from the cold head after balancing the heat leak into the system is given by,

$$q_{rem} = q_a - q_T \tag{100}$$

The rate of nitrogen liquefaction is then given by,

$$\dot{m}_{LN2} = \frac{q_{rem}}{L} \tag{101}$$

where L is the latent heat of nitrogen (kJ/kg). The liquid nitrogen mass inside Dewar vessel is then given by,

$$m_{LN2} = \dot{m}_{LN2} * \Delta t \tag{102}$$

The corresponding mass of gaseous nitrogen, volume of liquid nitrogen, and the volume of gaseous nitrogen in Dewar vessel were then calculated. The heat transfer energy (Wh) is given by,

$$HT_{energy} = \frac{\Delta t}{3600} * q_{rem} \tag{103}$$

The temperature change in the cold head is now given by,

$$\Delta T = \frac{HT_{energy}}{(Cp_{Cu} * m_{Cu})} \tag{104}$$

where HT_{energy} is in kJ, Cp_{Cu} is specific heat capacity of Copper block (kJ/kgK) at the end of cold head, m_{Cu} is the mass of Copper block (kg) respectively.

During the liquefaction process, the mass of liquid nitrogen inside the Dewar vessel keeps on increasing whereas the mass of vapour nitrogen inside the vessel decreases at the same time. The cold head temperature is then finally given by,

$$T = T_0 - \Delta T \tag{105}$$

where T_0 is the initial temperature for the cold head. For the liquefaction model, the cold head was assumed to be at 77.325 K whereas for the cool down model, the cold head was assumed to be at room temperature and the cold head temperature is given by equation (74) The liquefaction model was fed with a new calculated cold head temperature with respect to time. The rate of condensation or the rate of nitrogen liquefaction was found to be decreasing with time whereas the mass of liquid nitrogen in Dewar vessel increases with time.

7.5.7 Simulation of nitrogen condensation with defined cold finger temperatures

The simulation results of nitrogen condensation with the cold head temperature at 300 K and 77.325 K are presented in this section. The parameters used for this simulation are presented in Appendix D in detail. Figure 77 shows the cool down time and temperature of the cold head when starting to run the GM cryocooler system from room temperature. It takes around 25 minutes to reach to 80 K. Figure 78 shows the cold head temperature during the continuous system operation when starting from liquid nitrogen boiling point, ~77.325K.

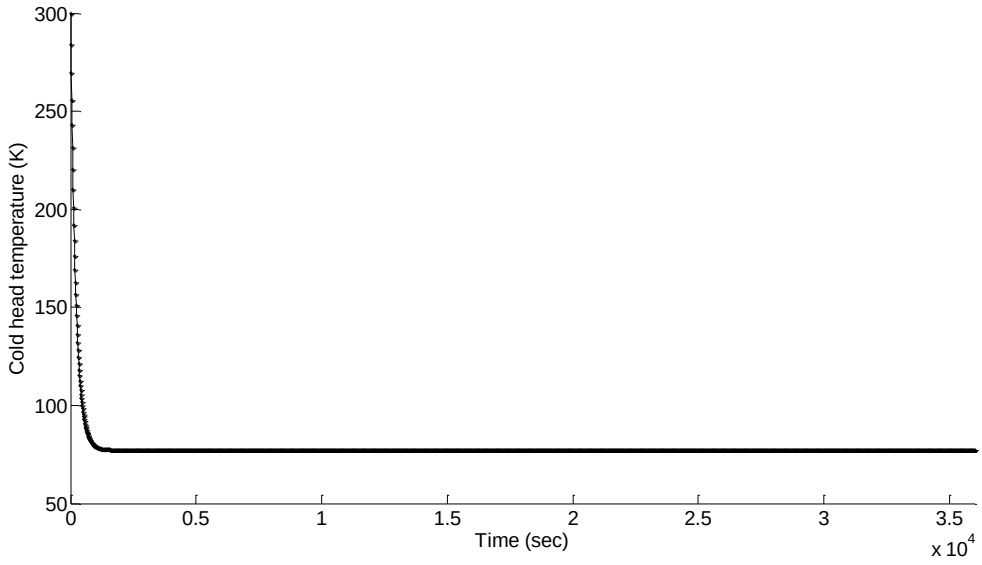

Figure 77: Simulated cool down of the cold head when starting from room temperature of 300K

Ten hour long simulations, with a time step of 15 seconds were performed using MATLAB/Simulink for the GM cryocooler system with the cold head temperature at ~77.325K and the Dewar pressure at 128.9 kPa. Figure 78 shows the cold head temperature with respect to time. Cooling produced by the cryocooler is shown in Figure 79. The liquid nitrogen mass flow rate with respect to time is presented in Figure 80. These simulations were performed for 10 hours (simulation time) so that these results could be compared with the experimental results.

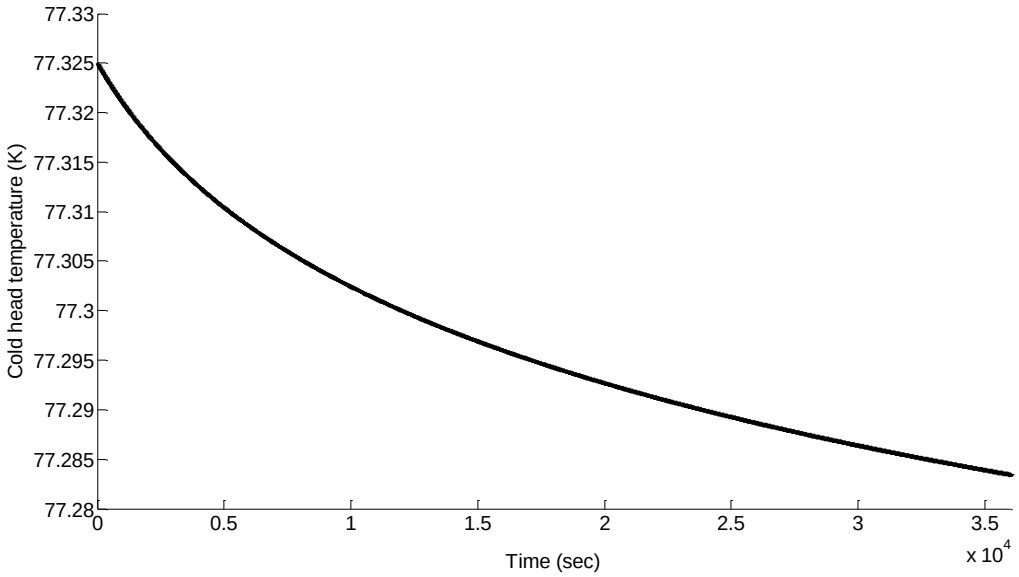

Figure 78: Simulated cold head temperature (K) when starting from liquid nitrogen boiling point

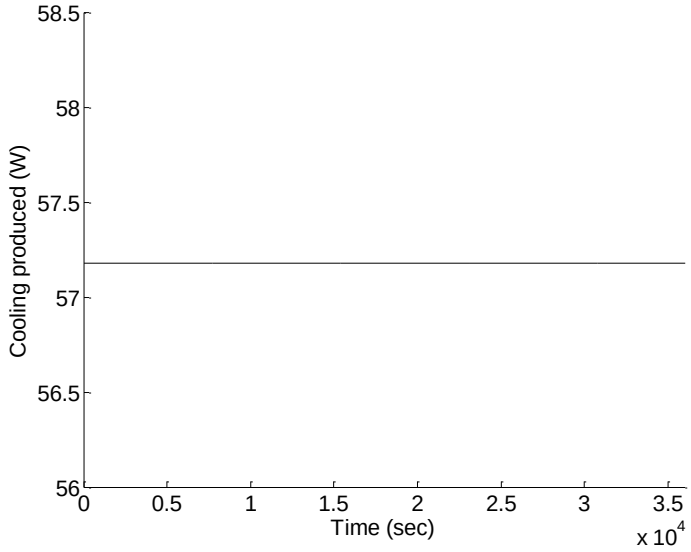

Figure 79: Cooling produced by the cold head

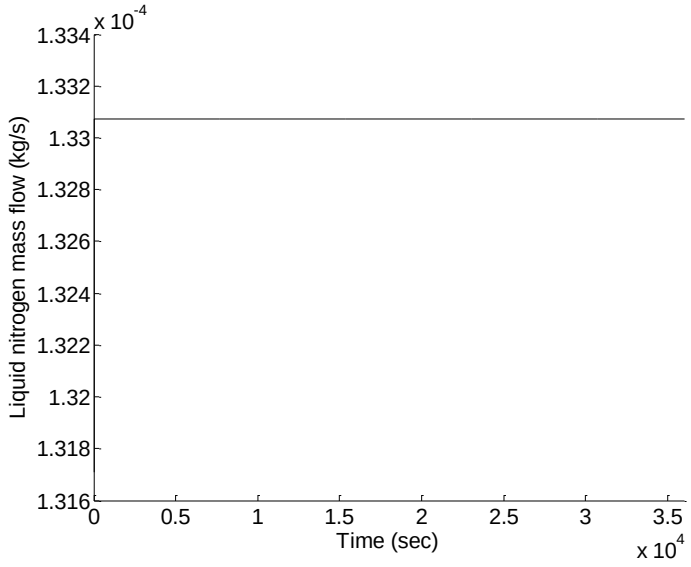

Figure 80: Liquid nitrogen mass flow rate (kg/s) with respect to time

The obtained simulation results showed that the condensation rate of liquid nitrogen attains a steady state value when the cold head temperature has already reached the liquid nitrogen temperature (~77.325K).

7.5.8 Simulation of nitrogen evaporation with defined cold finger temperatures

Liquid nitrogen evaporation will take place when the GM cryocooler system is stopped; i.e. there is no production of the refrigeration effect. The incoming gaseous nitrogen is also stopped from entering the Dewar vessel and the heat load into the Dewar system is only the conduction and radiation heat load from the surrounding. However, there will be some amount of heat entering the Dewar from gaseous nitrogen that is left on the gas port and from helium that is left on the compression/expansion space of the displacer. Although the rate of heating is small, being governed solely by conduction through the non-flowing gas, the heat can penetrate to the cold head tip and will raise the cold head temperature, the inner Dewar vessel and will also result in heating and evaporating liquid nitrogen. The equations used for this model are same as those

used in Section 7.5.6 except there was no cooling produced in the system rather there was heating by means of conduction through the gas, simulated by holding the temperature of helium and nitrogen at around 300 K in the simulation. This heat leak into the Dewar vessel will raise the temperature of the cold head, the inner vessel, and the sub-cooled liquid nitrogen. The total heat leak into the system in this case is given by,

$$q_T = q_1 + q_h + q_v - q_n - q_{th} \tag{106}$$

q_h is the heat from helium gas that might have been left on the compression and expansion space in the cold head. q_v is the heat from vapor nitrogen which occupies the top layer in Dewar vessel. q_n is the heat absorbed by liquid nitrogen and q_{th} is amount of heat required to raise temperature of the inner vessel mass.

The rate of evaporation of liquid nitrogen from the Dewar vessel is given by,

$$\dot{m}_{evap} = \frac{q_T}{L} \tag{107}$$

where L is the latent heat of nitrogen in J/kg.

The simulation results are presented to demonstrate verification of the Dewar model. Simulations were carried out for four different scenarios. Based on the simulations, the expectation generally was that the rate of evaporation of liquid nitrogen was less when the volume liquid nitrogen in Dewar was greater than when the liquid nitrogen volume in the Dewar was lesser.

For the first two scenarios, experimental cold head temperature was taken, while for the other two test scenarios; calculated cold head temperature was used for determining the rate of evaporation of liquid nitrogen from Dewar. These results are presented in the charts that follow.

1. When the liquid volume in Dewar was ~8.75 Liters and the cold head temperature was taken from experiment

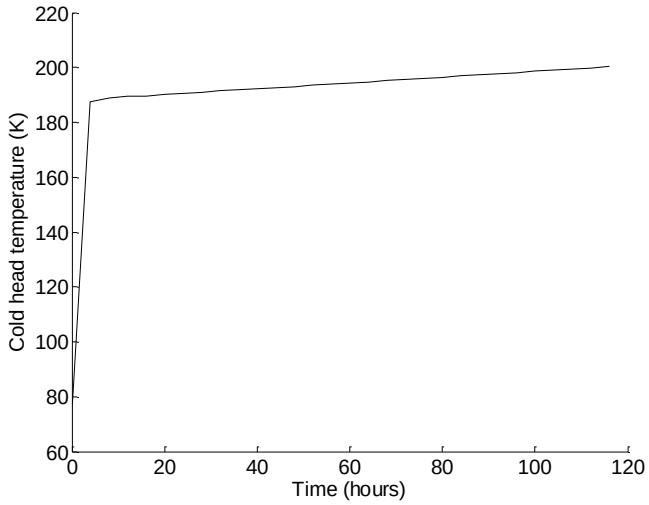

Figure 81: Experimental cold head temperature rise (K) when the cryocooler system was shut down (compare with Figure 84)

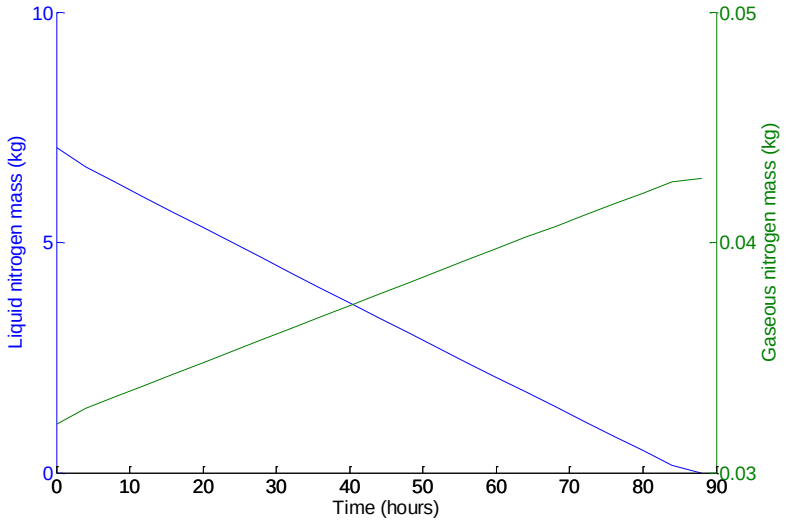

Figure 82: Liquid nitrogen mass (kg) and gaseous nitrogen mass (kg) inside Dewar showing time taken to evaporate when Dewar was filled with ~8.75 Liters of liquid nitrogen

2. When the liquid volume in Dewar was ~10.5 Liters and the cold head temperature was taken from experiment

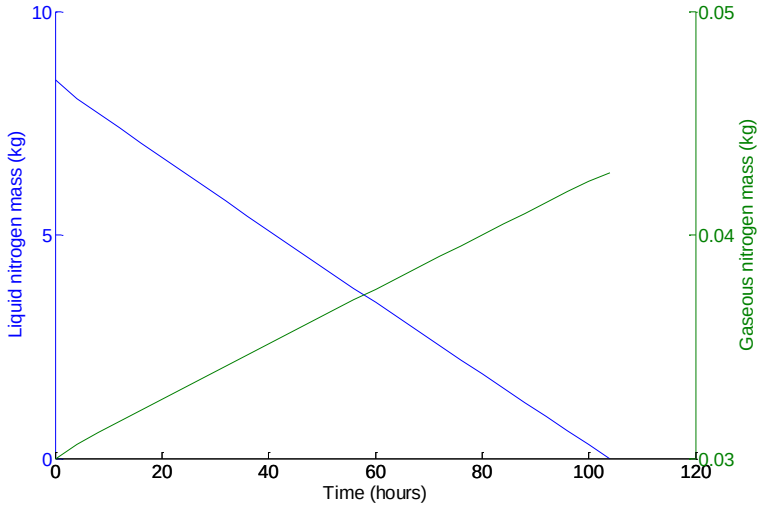

Figure 83: Liquid nitrogen mass (kg) and gaseous nitrogen mass (kg) inside Dewar showing time taken to evaporate when Dewar was filled with ~10.5 Liters of liquid nitrogen

3. When the liquid volume in Dewar was ~8.75 Liters and the cold head temp was taken from simulation

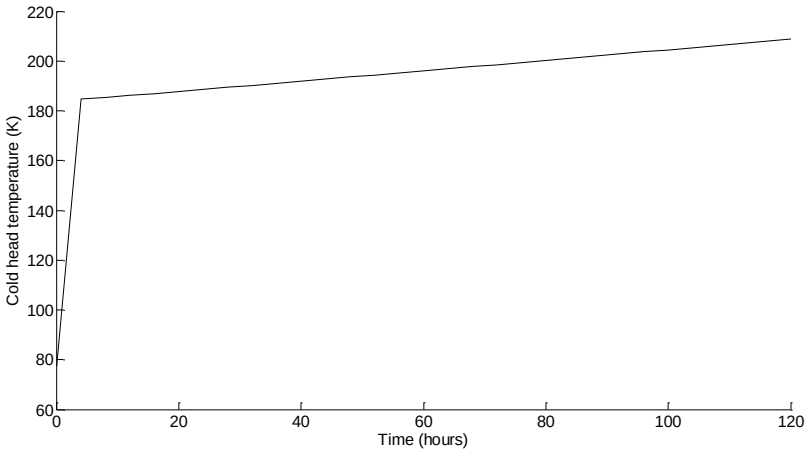

Figure 84: Simulated cold head temperature rise (K) during system shut off (compare with Figure 81)

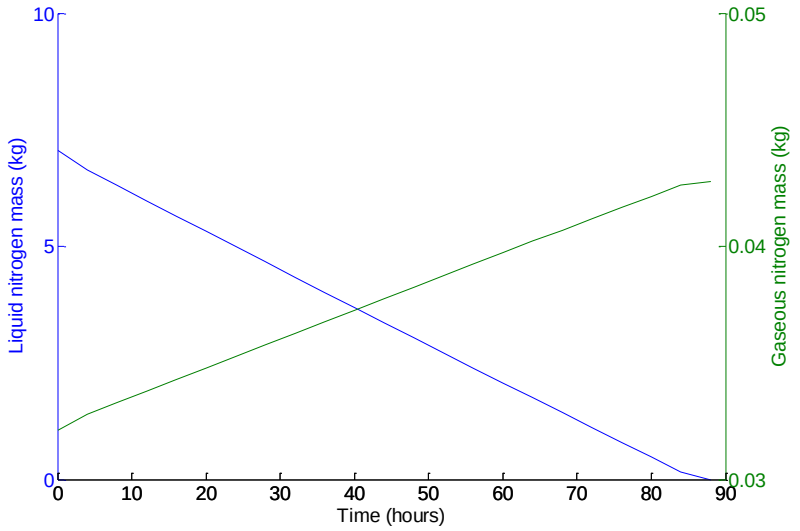

Figure 85: Liquid nitrogen mass (kg) and gaseous nitrogen mass (kg) inside Dewar showing time taken to evaporate when Dewar was filled with ~8.75 Liters of liquid nitrogen

4. When the liquid volume in Dewar was ~10.5 Liters and cold head temperature was taken from simulation

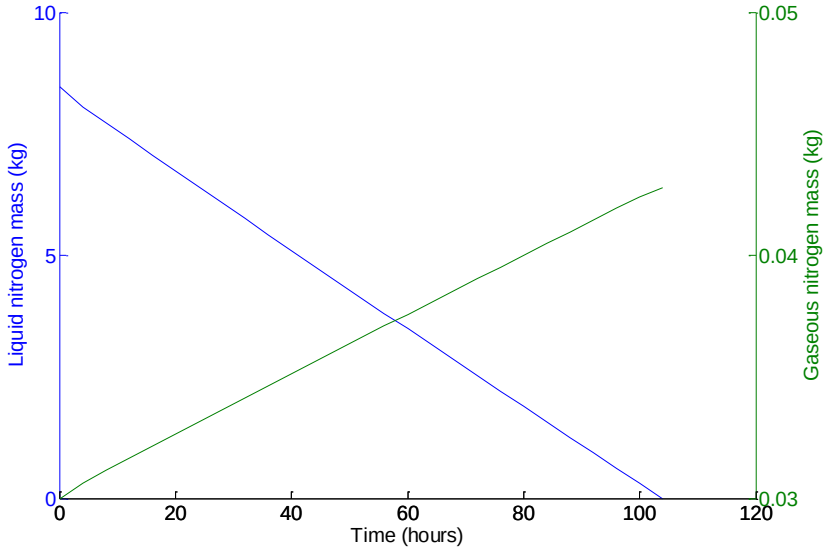

Figure 86: Liquid nitrogen mass (kg) and gaseous nitrogen mass (kg) inside Dewar showing time taken to evaporate when Dewar was filled with ~10.5 Litres of liquid nitrogen

When considering ~10.5 Liters of liquid nitrogen in Dewar and taking both the experimental and simulated cold head temperature into account, it took around 104 hours for it to evaporate liquid nitrogen to vapor, as shown in Figure 83 and Figure 86. However experimentally it was determined to be around 120 hours. When considering ~8.75 Liters of liquid nitrogen in Dewar, it took around 84 hours for it to evaporate all of the liquid nitrogen, as shown in Figure 82 and Figure 85. However, the stay time for liquid nitrogen (hours) determined experimentally was around 72 hours.

Section 7.5.7 and Section 7.5.8 presented the results for simulation of nitrogen condensation and evaporation in different test scenarios. The difference in the liquid nitrogen evaporation rate in the simulation and experimental work is due to the properties of gaseous nitrogen in upper Dewar region, nitrogen vapour just above the liquid nitrogen will have different properties from the bulk nitrogen vapor that could not be predicted well in absence of temperature measurements at different points inside Dewar vessel. Also, the heat leak into the system is “used” for the sensible heating of the inner vessel itself, sensible heating of liquid nitrogen and in vaporisation of liquid nitrogen. Similar issues have been reported by authors Notardonato (2006) and Partridge (2010). The evaporated nitrogen occupies the Dewar vessel while the pressure setting on the Dewar vessel is not reached. This is usually the case (as was with the simulations performed in this section) when very little amount of liquid nitrogen, as compared to vapor nitrogen is contained in Dewar. However, when the Dewar is almost full and there is very small space for evaporated nitrogen, the pressure inside Dewar rises quickly and the pressure relief valve sets on to release the pressure.

The model predicted evaporation rate when Dewar was filled with 10.5 Liters of liquid nitrogen was 2.42 L/day and the experimental evaporation rate was 2.1 L/day, as compared to

the manufacture data of ~1 L/day. Again, the evaporation rate is lower when the Dewar is filled with high volume of liquid nitrogen than when partially filled. The laboratory Dewar has a capacity of 35 Liters (0.035 m^3). The evaporation rate calculated in this Section is for the situation when the Dewar vessel was filled with 10.5 Liters and 8.75 Liters of liquid nitrogen. Also, the evaporation rate can be accelerated or decelerated depending on the room temperature and pressure outside the Dewar vessel and pressure inside Dewar vessel. More penetrations (such as the cold head on Dewar neck, liquid level indicator, extraction valve and line) cause more heat leak into the Dewar vessel than in the standard cryogens storage tank which do not have these penetrations. The results of system shut-down performance monitoring and comparison with simulation of that state, has resulted in increased confidence in the simulation model.

7.6 Simulations with integrated dynamical models

7.6.1 Simulations at steady speeds

This section presents simulation results performed for 10 hours at different compressor driving frequencies. The schematic of the system is presented in Figure 87. The simulation was run at different constant motor speeds, simulating for 10 hours and the average values from the 10 hours simulation were taken. The results for running the system at different frequencies are presented in Figure 88 and Figure 89. The compressor input work at different constant frequencies is shown in Figure 88 and the liquid nitrogen mass flow rate (kg/s) with respect to time is presented in Figure 89.

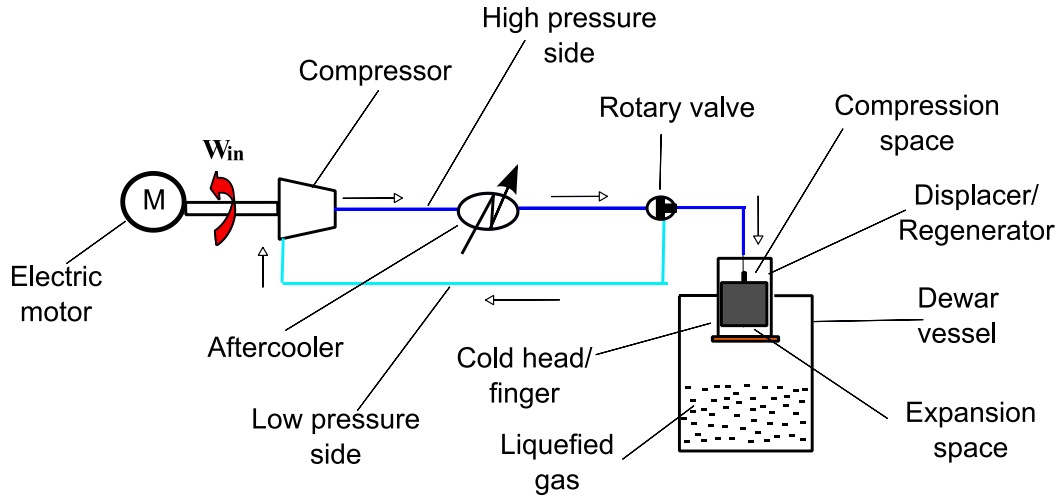

Figure 87: Schematic of the electric motor driven GM cryocooler system

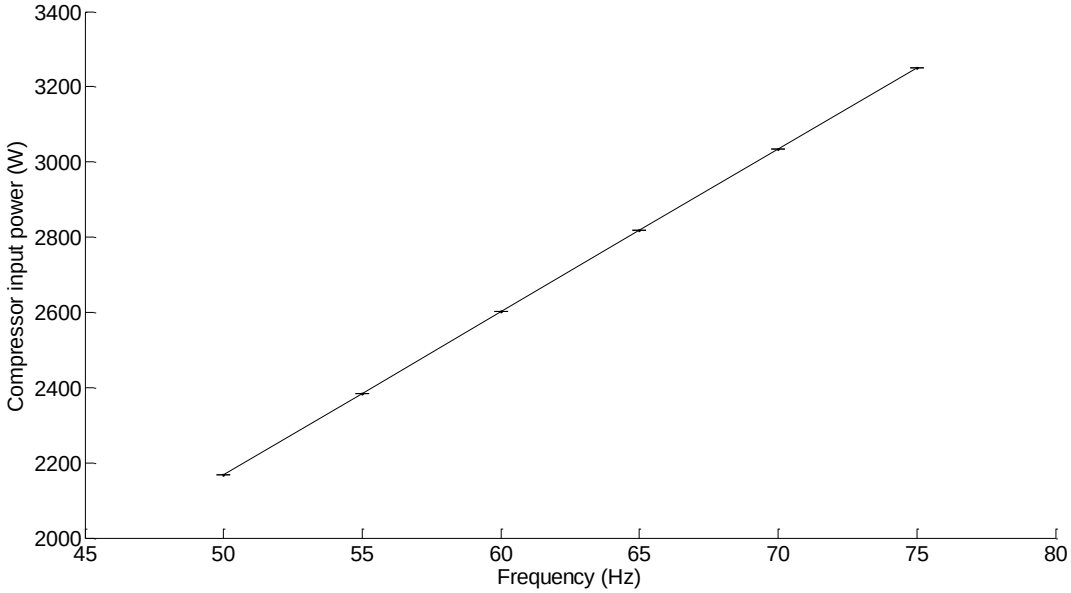

Figure 88: Compressor power input required for different driving frequencies

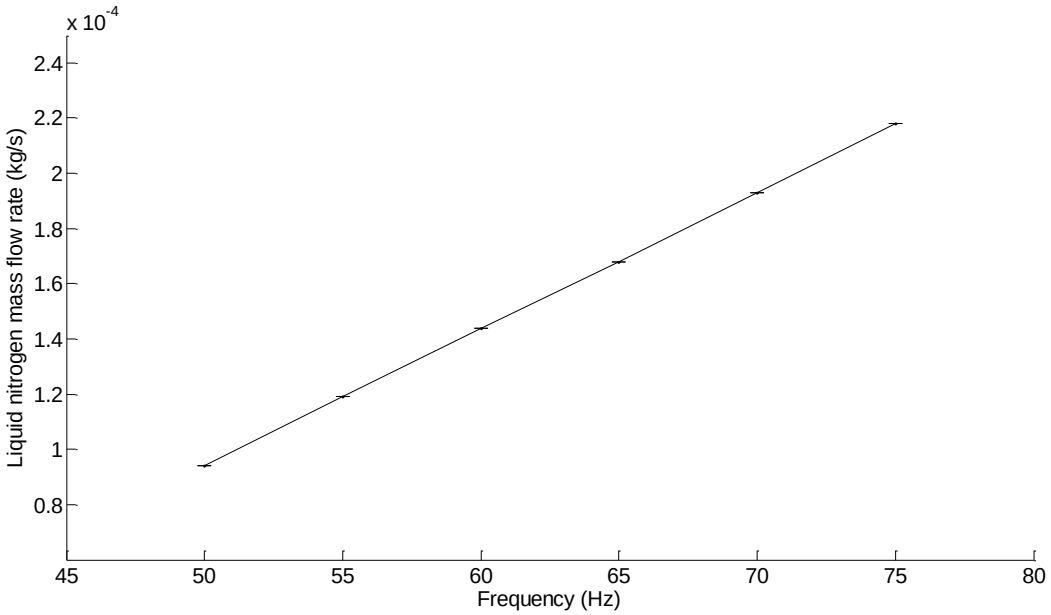

Figure 89: Average liquid nitrogen mass flow rate at different frequencies with error bars

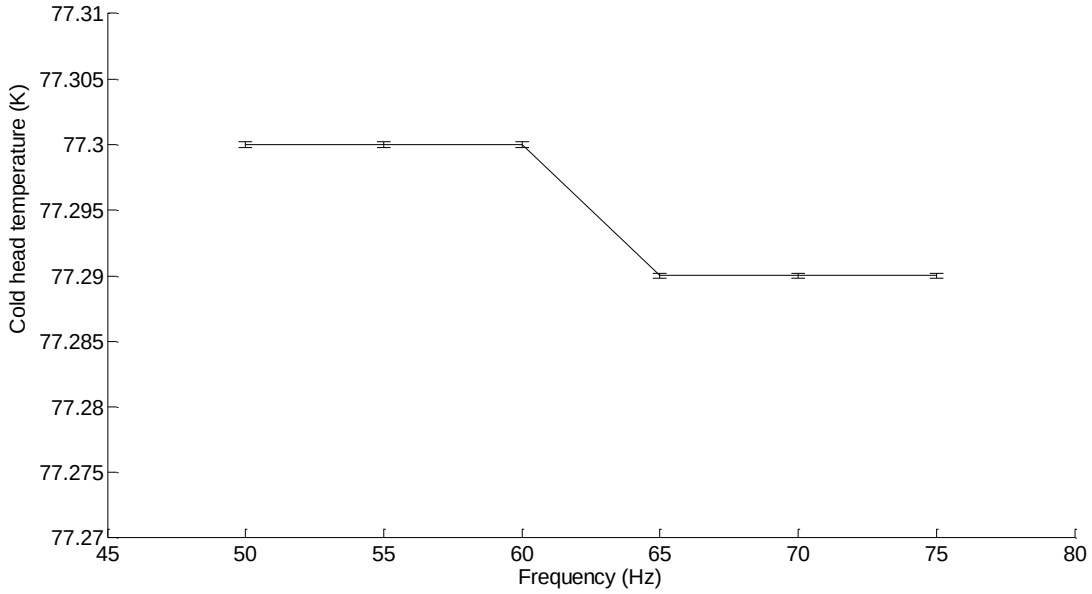

Figure 90: Cold head temperature (K) at different frequencies with error bars

The average compressor input work at different driving frequencies, the average liquid nitrogen mass flow rate (kg/s) and the average cold head temperature (K) were determined from the simulations in MATLAB/Simulink. The results are also presented in Table 10.

Table 10: Simulation results

Frequency (Hz)	Compressor motor power input (W)	Cold head temp (K)	Liquid nitrogen mass flow rate (kg/s)	Mass flow rate/Power input
50	2167.61	77.300	0.000095	4.38E-08
55	2384.37	77.300	0.000119	4.99E-08
60	2601.13	77.300	0.000144	5.52E-08
65	2817.90	77.290	0.000168	5.98E-08
70	3034.66	77.290	0.000193	6.37E-08
75	3251.42	77.290	0.000218	6.70E-08

7.6.2 Simulations at sinusoidal varying set points

Another set of simulations was performed in which sinusoidal input of compressor motor driving frequency was applied as input frequency. First set of simulations were performed with a sine signal input for 2 hours, in which the compressor frequency was changed every minute as shown in Figure 91. The results from the simulations were logged with a time step of 15 seconds as shown Figure 92 and Figure 94.

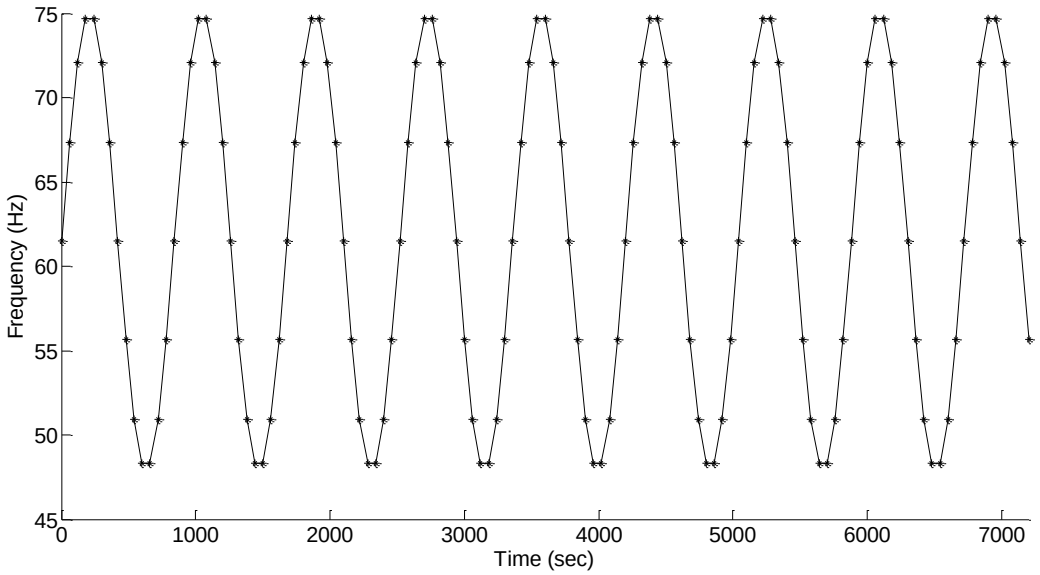

Figure 91: Sinusoidal input of compressor driving frequency with frequency changing every minute

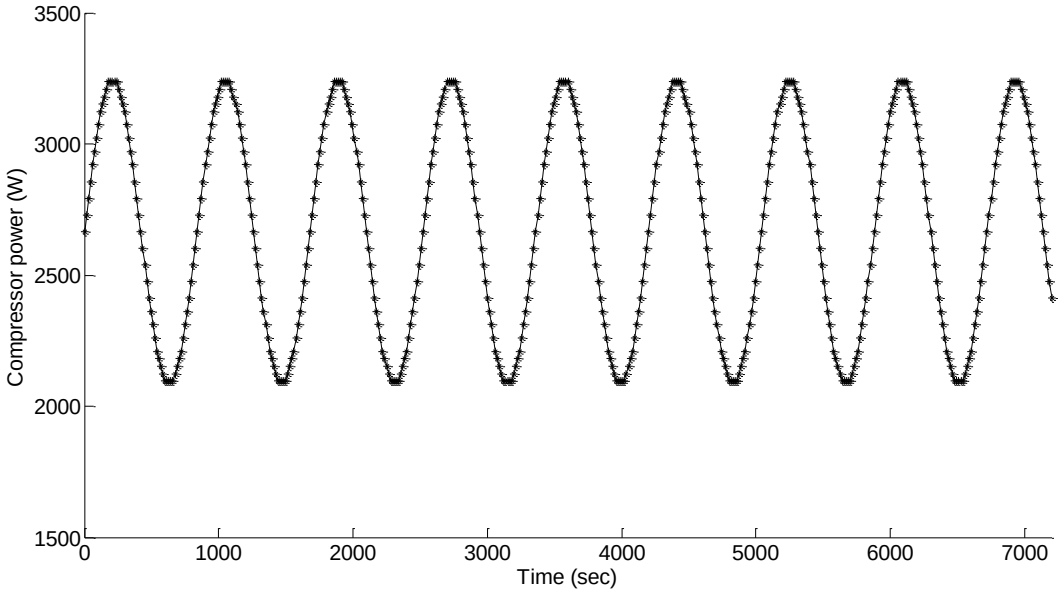

Figure 92: Compressor input power (W) with respect to time

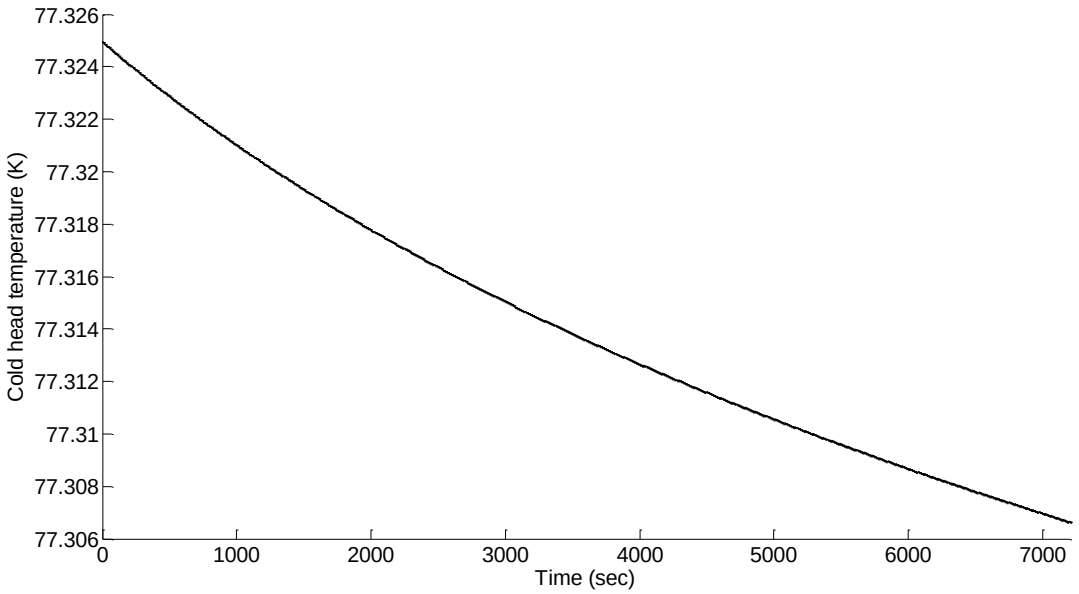

Figure 93: Cold head temperature (K) with respect to time

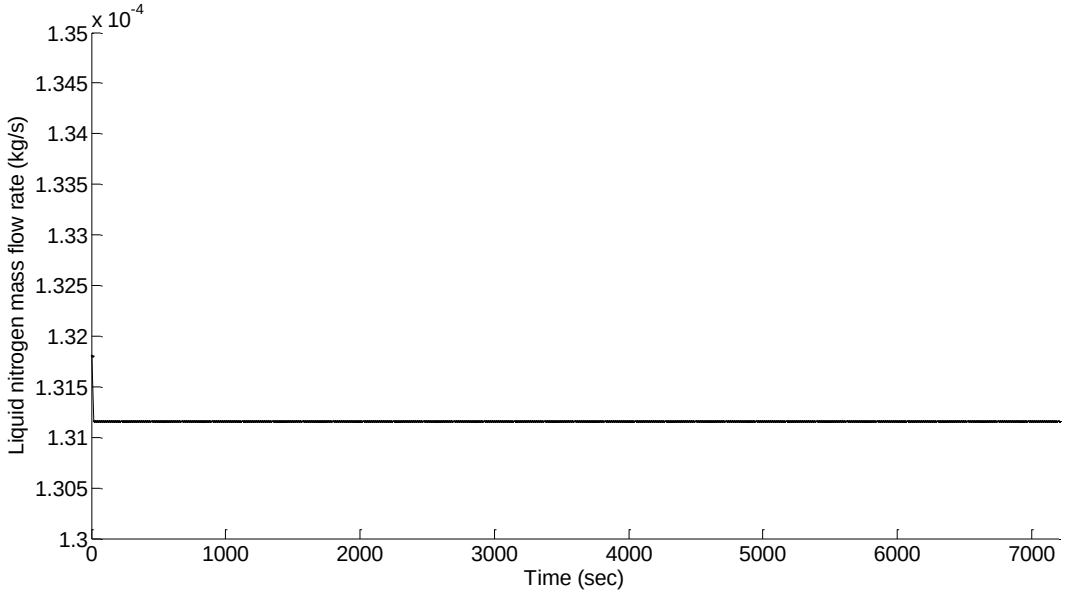

Figure 94: Liquid nitrogen mass flow rate (kg/s) with respect to time

The simulations showed that the liquid nitrogen mass flow rate (kg/s) remains fairly constant irrespective of varying frequencies and/or time.

7.6.3 Simulations at random set points

For this simulation, random set points of frequencies were used as input driving frequencies for 10 hours, changing the motor frequency randomly as shown in Figure 95. The input power required to drive the compressor (W) is shown in Figure 96. Similarly, the liquid nitrogen mass flow rate (kg/s) is shown in Figure 99.

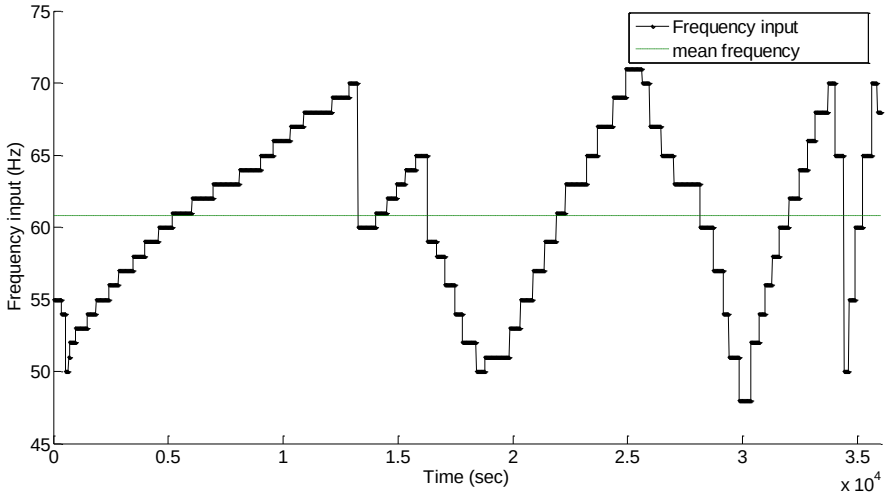

Figure 95: Random frequency set points (Hz) used for simulation

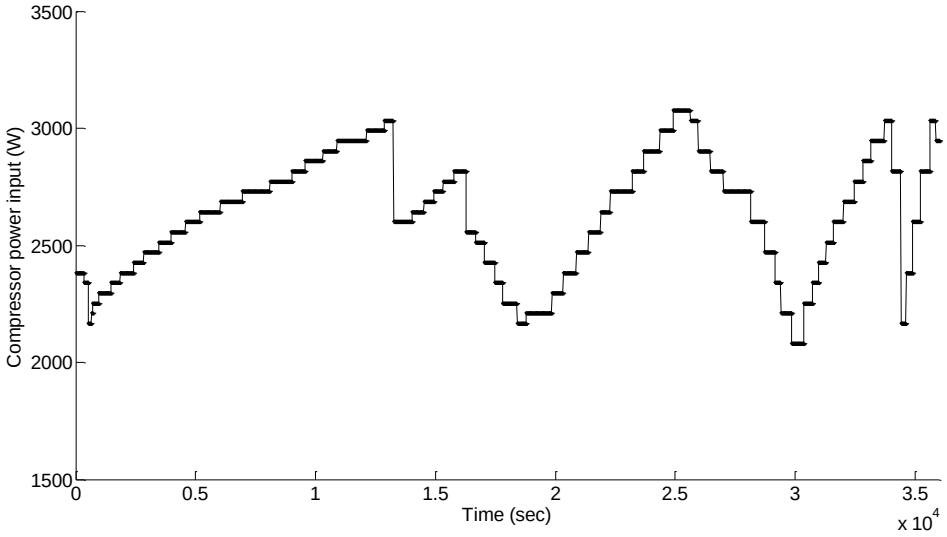

Figure 96: Compressor input power (W) with respect to time

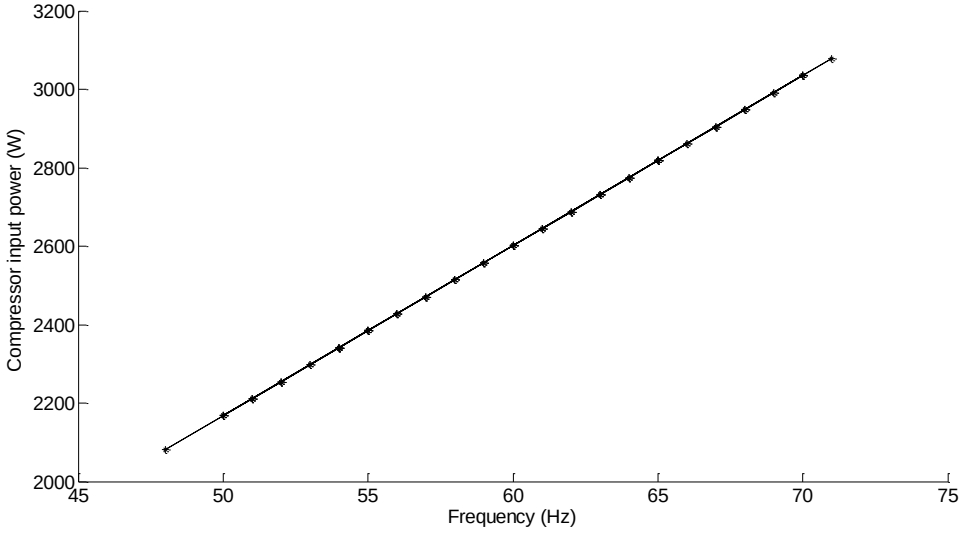

Figure 97: Compressor input power (W) with respect to frequency (Hz)

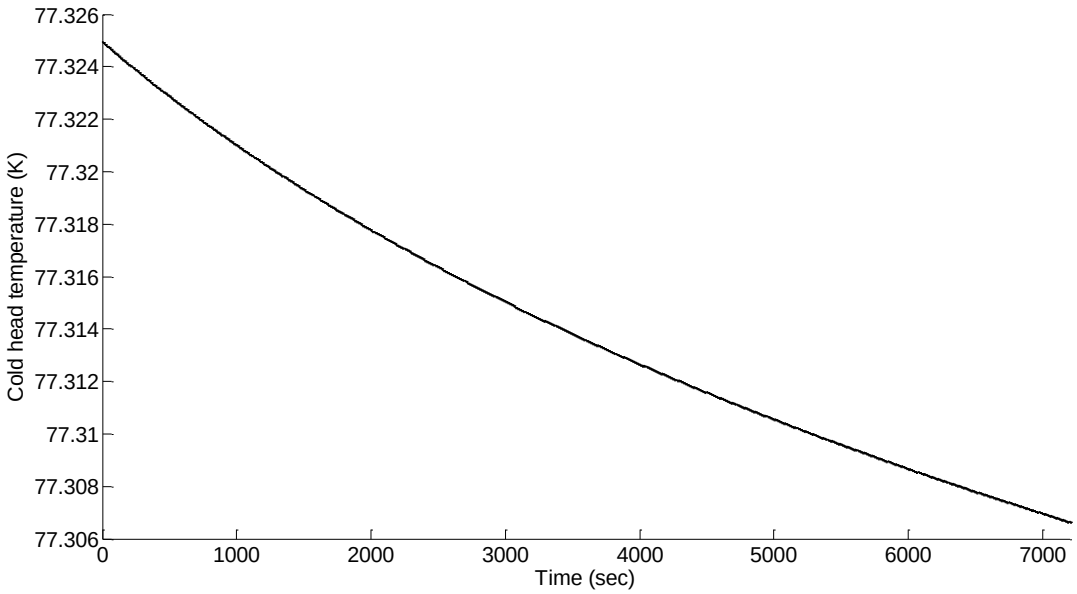

Figure 98: Cold head temperature (K) with respect to time

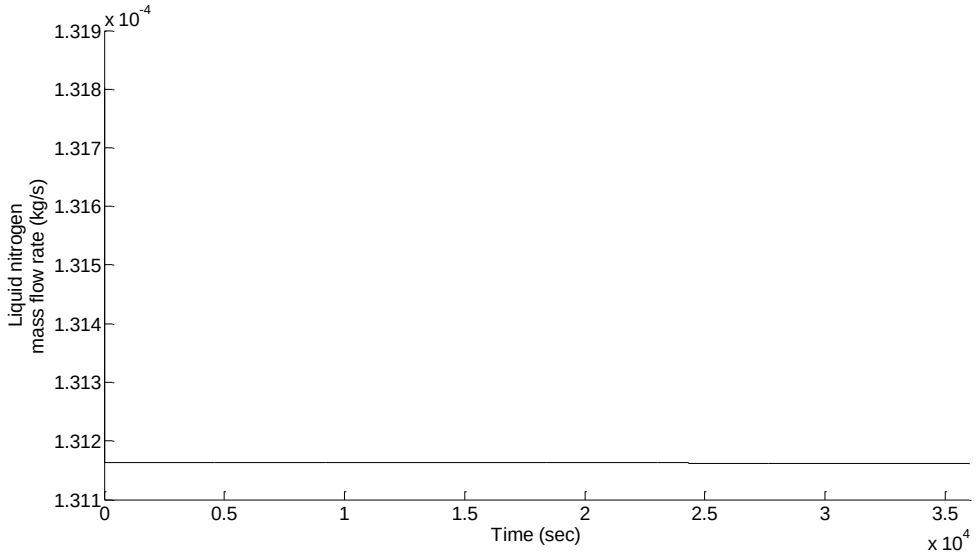

Figure 99: Liquid nitrogen mass flow rate (kg/s) with respect to time

These results also showed that the liquid nitrogen mass flow rate (kg/s) remained constant irrespective of the frequencies applied to the helium compressor. The liquid nitrogen mass flow rate had an average value of 1.31e-04 kg/s and a standard deviation of 1.3e-08 kg/s.

The average value is fairly close to the value obtained in Figure 89 (1.4e-04 kg/s) for a compressor motor frequency of 60.82 Hz.

Another set of simulation was carried out, for a relatively shorter time period of around 22 minutes, changing the frequency randomly every minute as shown in Figure 100. The liquid nitrogen mass flow rate (kg/s) is shown in Figure 103.

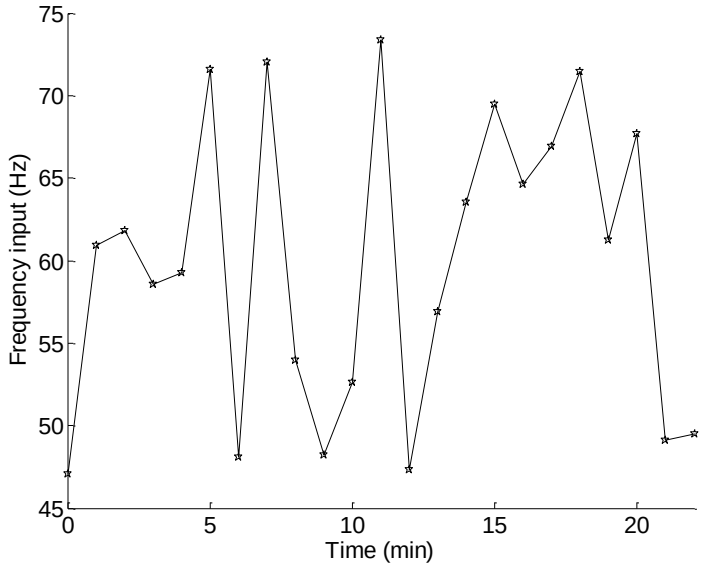

Figure 100: Frequency input (Hz) with respect to time (min)

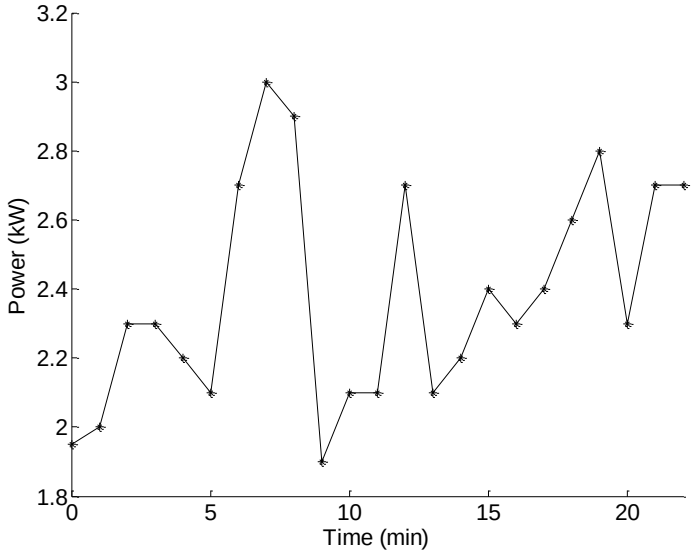

Figure 101: Compressor input power (kW) with respect to time (min)

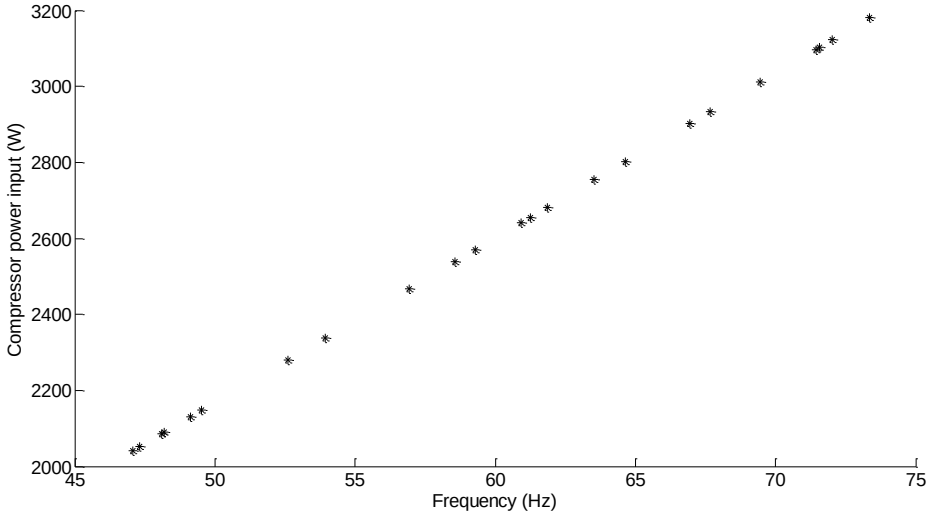

Figure 102: Compressor input power (W) with respect to frequency (Hz)

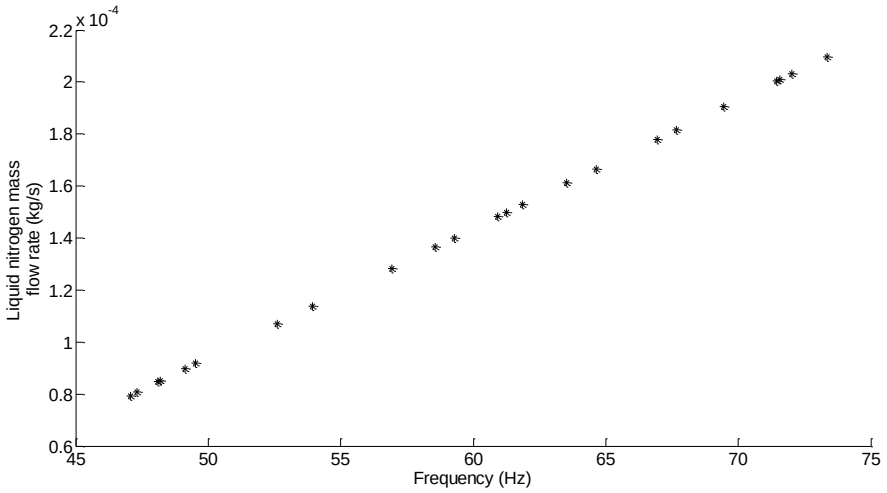

Figure 103: Liquid nitrogen mass flow rate (kg/s) with respect to frequency (Hz)

These results showed that the liquid nitrogen mass flow rate (kg/s) tend to follow the compressor input frequency trend. It can be seen from Figure 103 that the production rate increases with increase in compressor motor frequency. The average input frequency was 50.98 Hz and the average liquid nitrogen mass flow rate was 0.00014 kg/s, which agrees with the values presented in Table 10.

7.6.4 Simulations following wind speed data

This section presents results from simulation in which the compressor driving frequencies were changed every minute. The motor driving frequencies correspond to the wind speed trend but they are within the limits of 48 Hz and 75 Hz. The wind speed data used for this simulation are 10 minute average data from Roskrow (13th Nov, 8:00 am to 6:00 pm) as shown in Figure 104. 10 minute average data were treated as 1 minute average while running the simulation so the driving frequency was changed every minute. The corresponding compressor input frequency is presented in Figure 105.

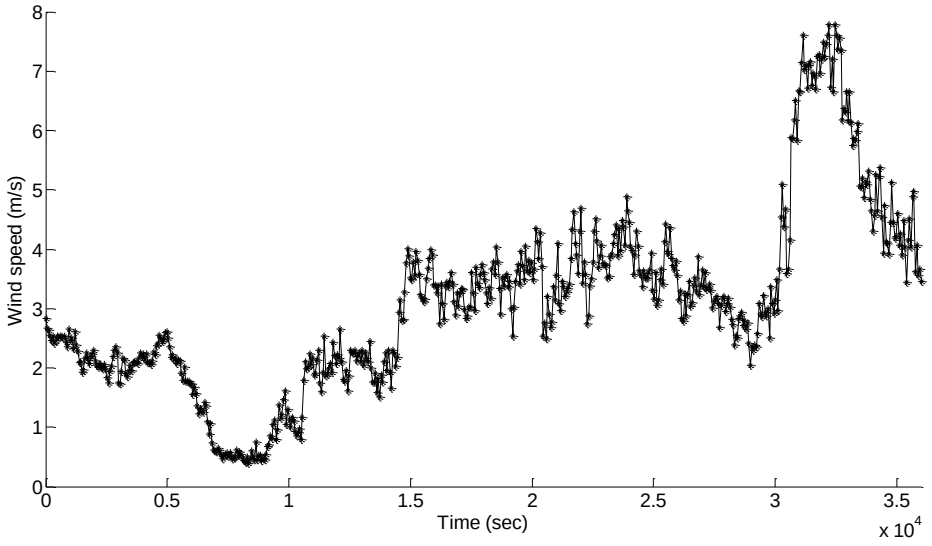

Figure 104: Wind speed (m/s) data used for scaling to compressor input frequency (Hz)

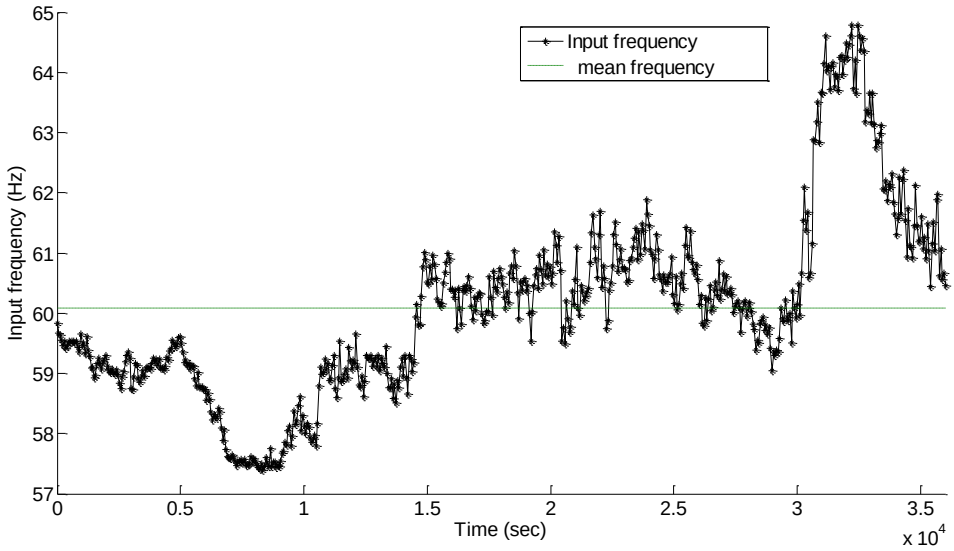

Figure 105: Input frequency (Hz) in proportion to wind speed of Figure 104 changing every minute

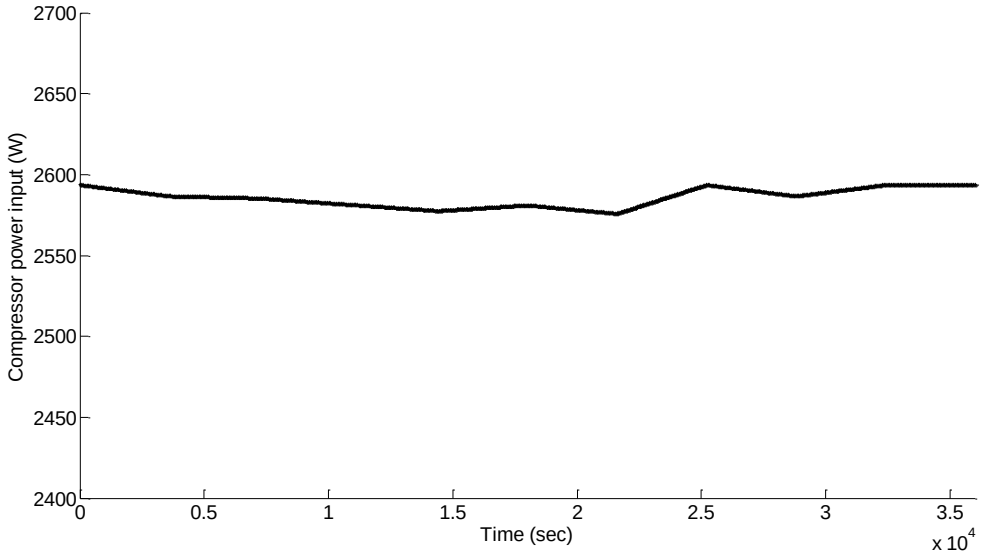

Figure 106: Compressor power input (W) to drive the cryocooler system

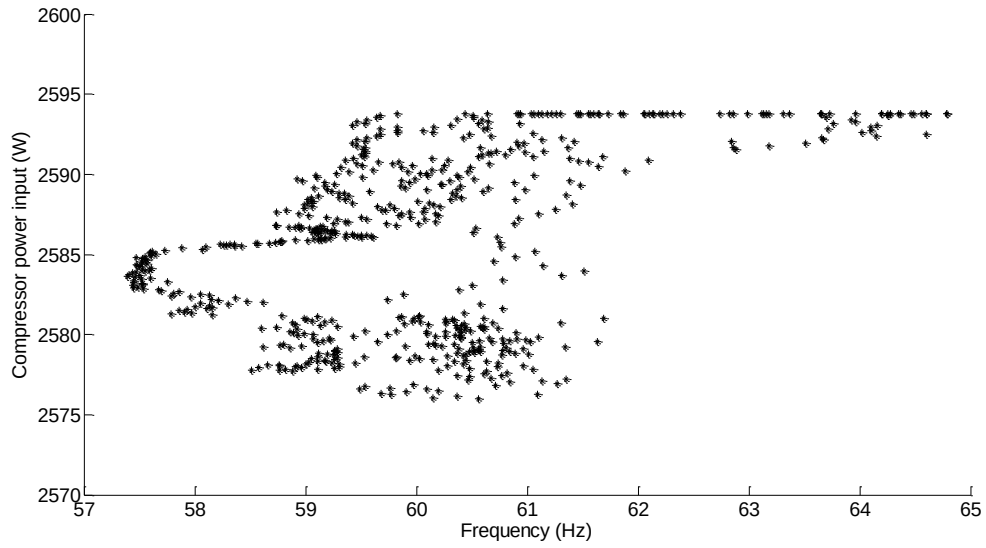

Figure 107: Compressor power input (W) with respect to frequency input (Hz)

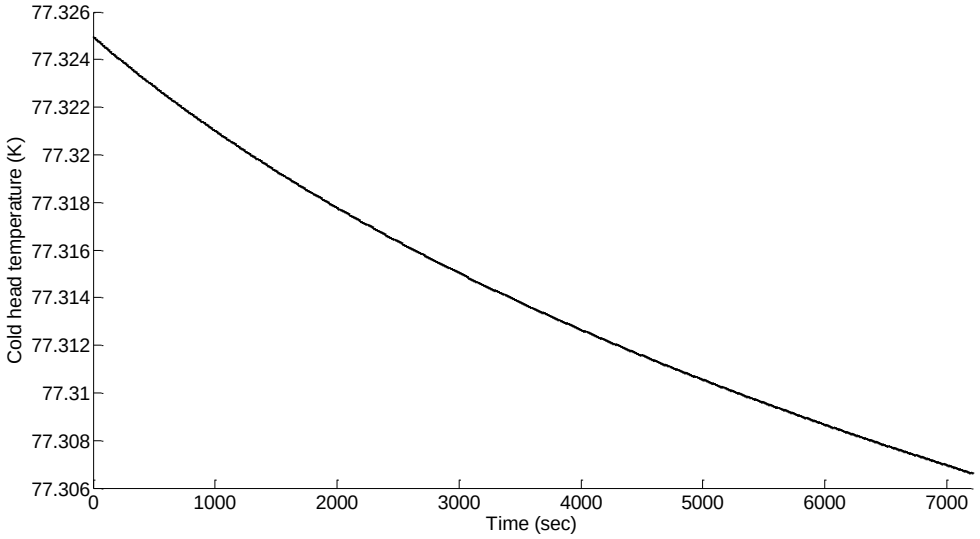

Figure 108: Cold head temperature (K) with respect to time

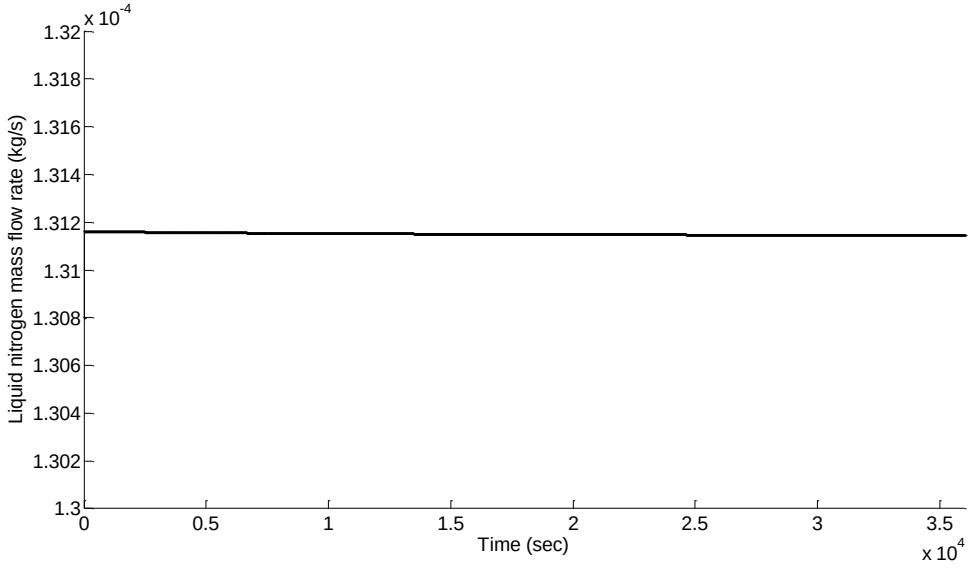

Figure 109: Liquid nitrogen mass flow rate (kg/s) with respect to time

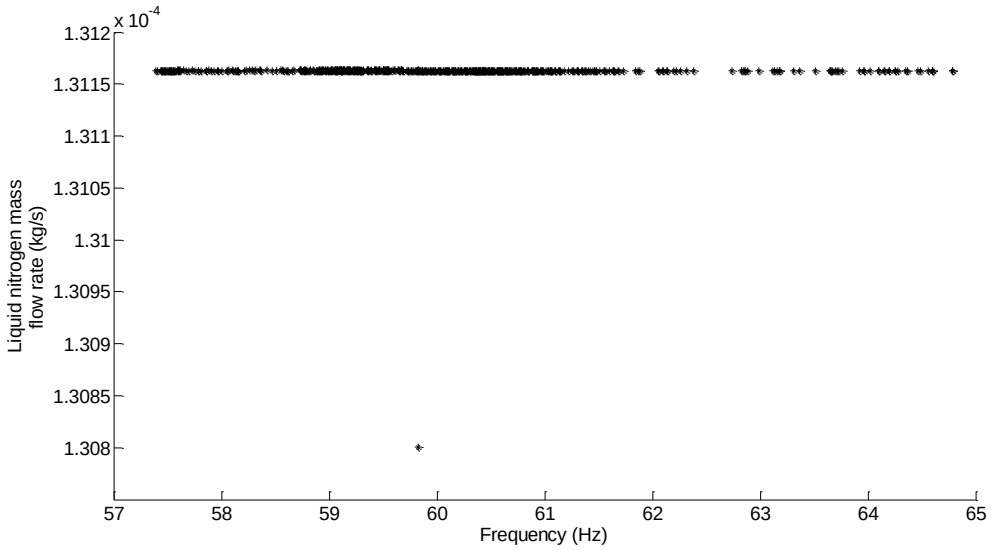

Figure 110: Liquid nitrogen mass flow rate (kg/s) with respect to frequency (Hz)

The compressor input work (W) and the liquid nitrogen mass flow rate (kg/s) are presented in Figure 106 and Figure 109. The mean and standard deviation for the liquid nitrogen mass flow rate (kg/s) was 0.00013 kg/s and 1.4e-08 kg/s. The average value is fairly close to the value obtained in Figure 89 (1.4e-04 kg/s) for a compressor motor frequency (Hz) of ~60.09 Hz.

Finally a set of simulation was performed using 1 second average data from Exeter, SWMTF, UK. The following set of charts present results from simulation where the driving compressor frequencies are in proportion to the wind speed data from 4Hz SWMTF. The 4Hz (4 wind speed data per second) wind speed were averaged to get 1 second average wind speed data (m/s). These 1 second average wind speed data were then used to represent the compressor driving frequency within the limits of 48Hz and 75Hz, and changing the frequency every second. These are better shown in Figure 111 and Figure 112 respectively. The compressor input power (W) is presented in Figure 113. The liquid nitrogen mass flow rate (kg/s) is shown in Figure 115.

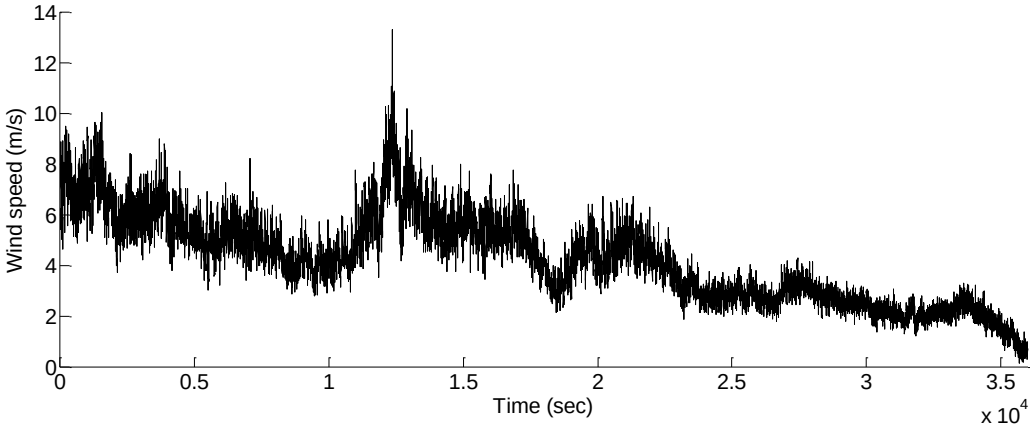

Figure 111: 1 second average wind speed (m/s) data

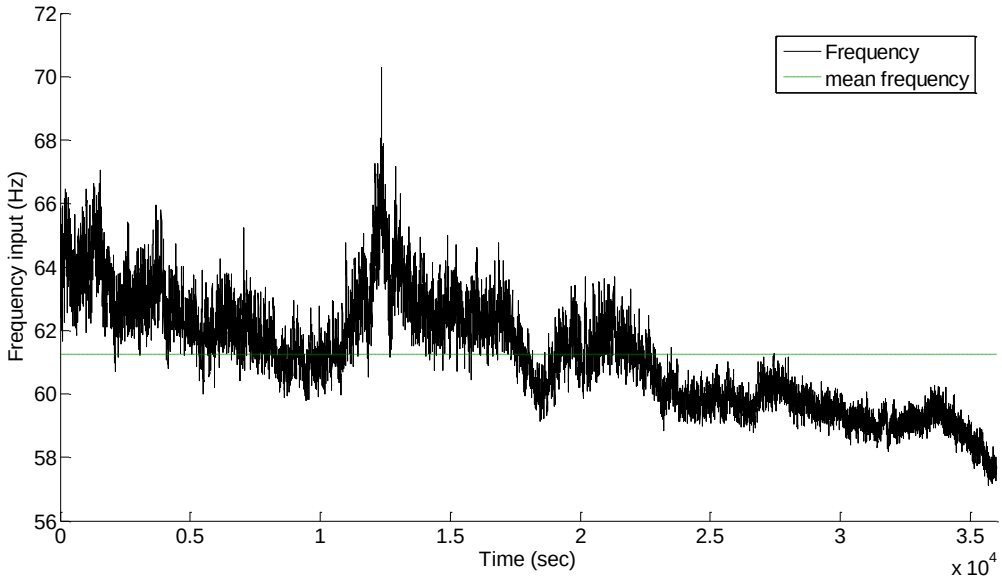

Figure 112: Proportional compressor driving frequency (Hz) with respect to time

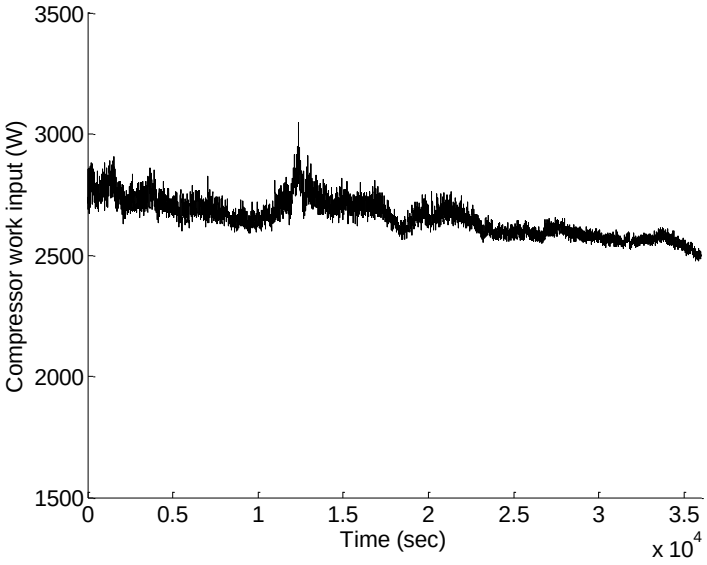

Figure 113: Compressor input power (W) to drive the cryocooler system

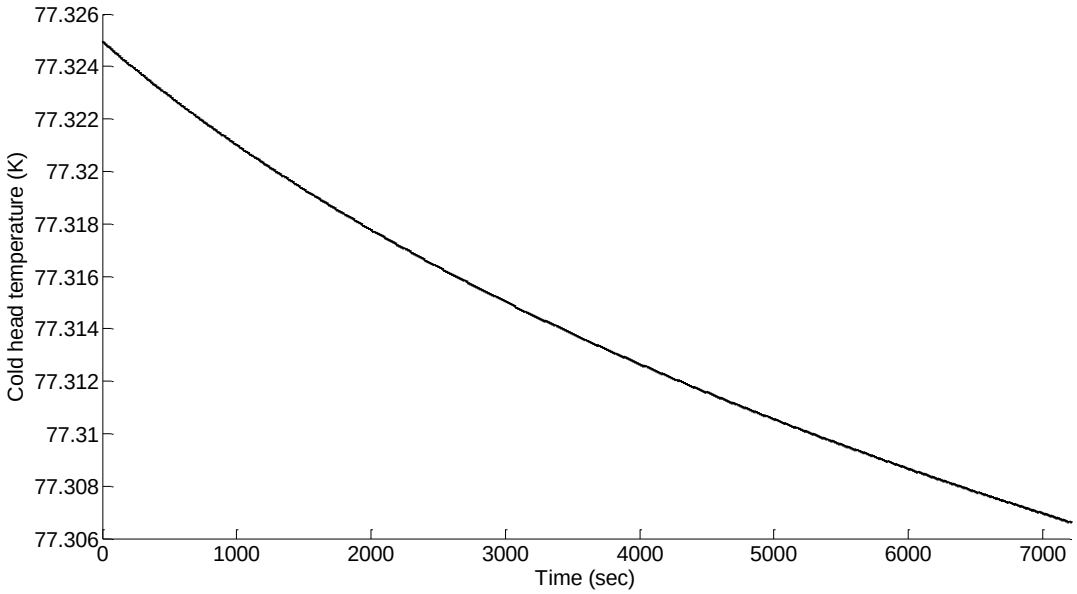

Figure 114: Cold head temperature (K) with respect to time

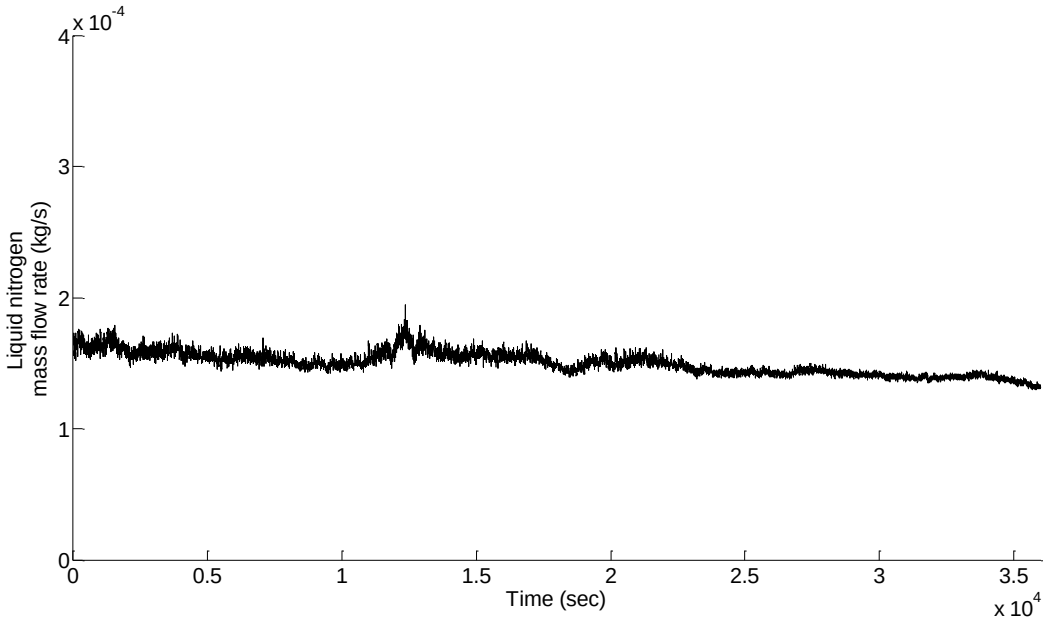

Figure 115: Liquid nitrogen mass flow rate (kg/s) with respect to time

The mean liquid nitrogen mass flow rate (kg/s) for this simulation was 0.00014 kg/s and the standard deviation was 8.7e-06 kg/s. The average value is fairly close to the value obtained in Figure 89 (1.4e-04 kg/s) for a compressor motor frequency (Hz) of ~61.26 Hz.

7.7 Summary

A complete dynamic simulation of a wind energy driven Gifford McMahon (GM) cryocooler system was presented in Chapter 7. Geometry, numerical procedures and algorithms, and test scenarios considered for the simulation were also presented in detail. The chapter also included the thermo-mechanical process for the Dewar storage vessel and the results obtained from the simulations performed were also presented. The simulation results for the GM cryocooler system at different settings for compressor driving frequencies were also presented in this Chapter.

The model and the results obtained in this Chapter were essential for this research work so that the model predictions could be verified with the experimental results that will be presented in the upcoming Chapter 8. From the simulation results obtained, we found that the average liquid nitrogen mass flow rate reasonably tended to attain its steady state value irrespective of the random driving frequencies applied to the motor/compressor shaft. The drawback in the model was that some helium gas properties was assumed constant at various state points due to the lack of measurement values of the parameters such as the after cooled helium gas temperature and return helium gas temperature.

8 Laboratory verification of liquid nitrogen production model

This chapter presents all the experimental work performed in the laboratory for the verification of the integrated dynamic model developed for the liquid nitrogen production. The experimental setup used represents a wind energy conversion system where the induction motor and variable frequency drive was designed to physically simulate work input from either a wind rotor or a hydrostatic transmission. There is no gearbox in the CryoVent concept (replaced by the hydrostatic transmission). The induction motor produces a torque which is applied to the shaft of the helium compressor. The motor frequency is controlled by a variable frequency drive (Hitachi inverter SJ700D-037L series) which has a power monitoring and display capability of 0.0 to 9999 in steps of 0.1 kW (Hitachi, 2014). This chapter presents the experimental results which are then compared with the simulation results presented earlier in Chapter 7. It starts with the introduction and overview of the experimental equipment, process flow diagram, the development of the supervisory control and data acquisition system, the experimental program at different settings, corresponding results and discussions.

8.1 Experimental equipment

8.1.1 Process flow diagram for Cryomech Helium compressor unit with variable frequency drive electric motor

The experimental setup as shown in Figure 116 (b), consists of several sub-systems including compressor, rotary valve, regenerator/displacer, heat exchangers, and flexible connecting hoses. The system was fabricated specifically for the purposes of this work by Cryomech Inc.

based on their established model- LNP10 unit and was used for the experimental purpose after commissioning.

(a)

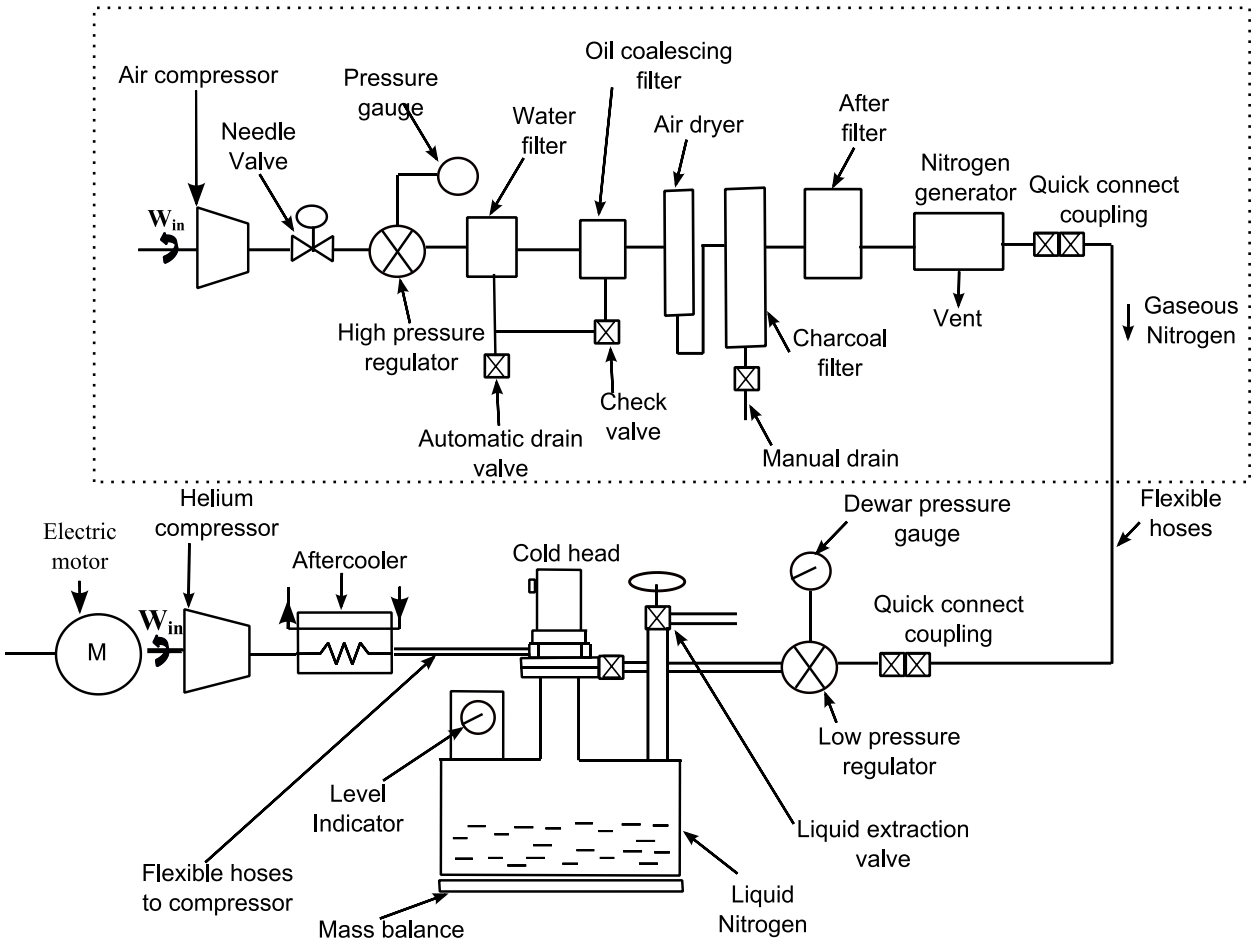

(b)

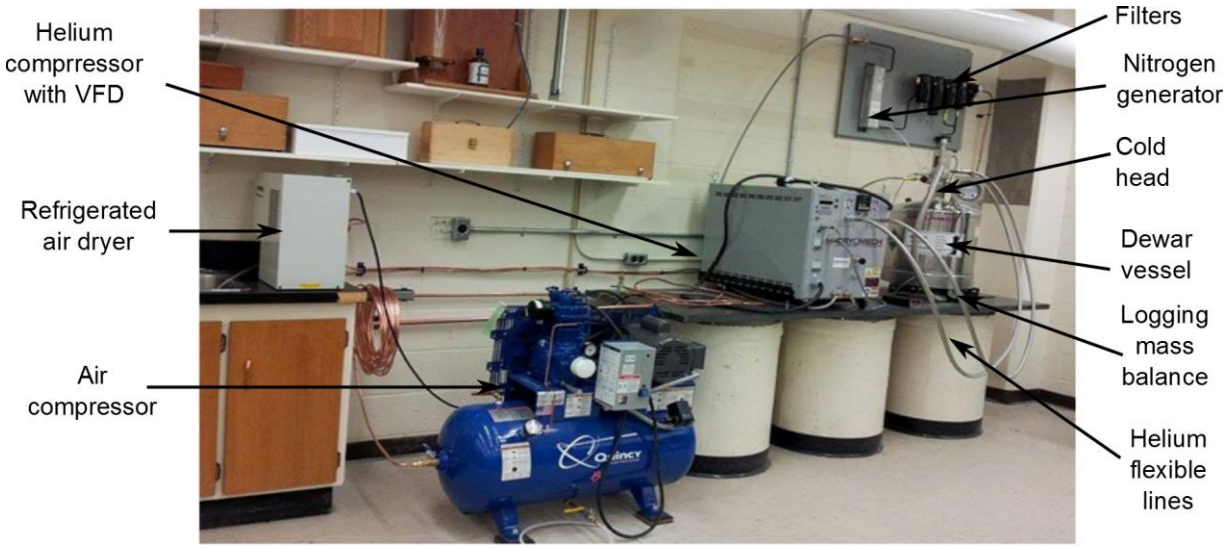

Figure 116: (a) Experimental setup schematic (Items shown within the dashed box are those required simply to provide a safe source of gas to liquefy for experimental purposes), and (b) laboratory setup

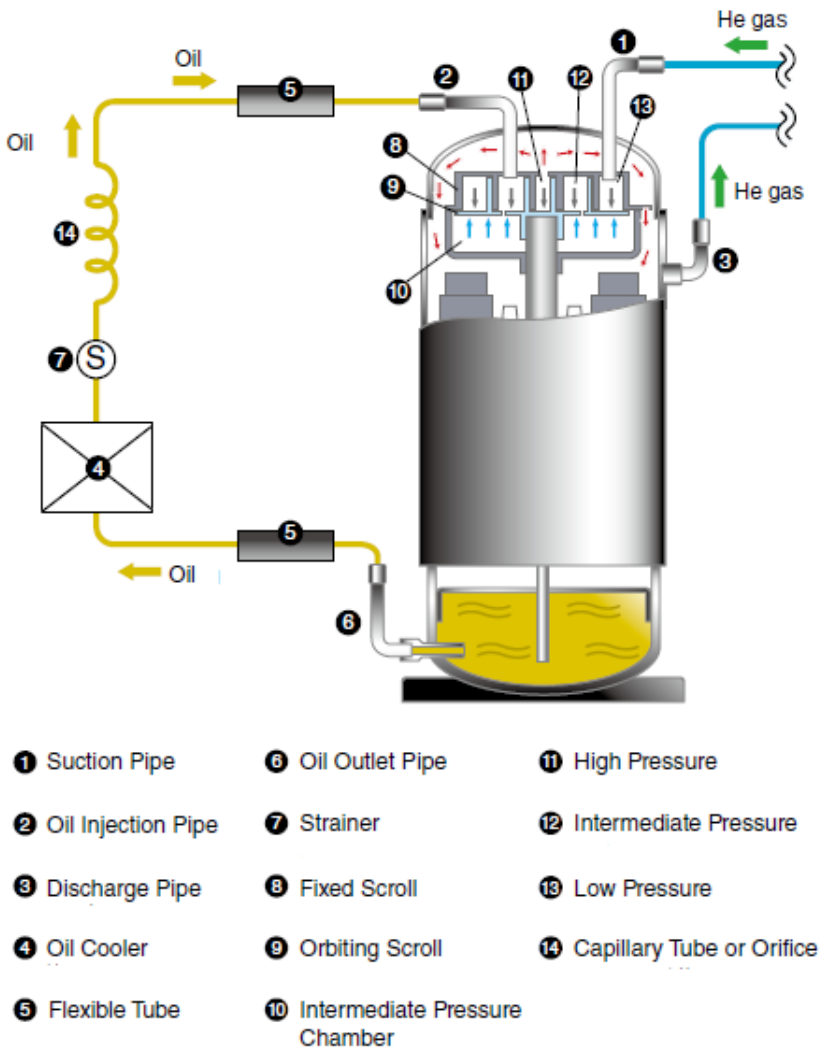

Figure 117: Process flow of helium refrigeration and oil injection cooling mechanism (Hitachi America Ltd., 2015)

The working principle of a GM cryocooler has been presented earlier in Section 5.6. The helium compressor contains high purity helium gas and builds high and low pressure sides by developing pressures of ~260 kPa on the delivery side and ~1600-1700 kPa on the return side. The process flow diagram for the helium compressor from Hitachi is shown in Figure 117. The rotary valve alternately connects the high pressure and low pressure helium lines to the

regenerator hot end. The high pressure and low pressure helium gas is delivered by the flexible hoses. The average mass flow rate of helium gas so delivered was estimated to be ~0.10 g/s.

The thermal energy of the system is stored in the regenerator, which is made up of high-heat capacity material. The regenerator cools the incoming fluid stream to the working temperature and warms the exhaust stream to ambient temperature. Hot end heat exchanger is where the working fluid rejects heat of compression in every periodic cycle of operation and the cold end heat exchanger is the part where minimum temperature is achieved in the refrigeration system (Roy, Das, & Sarangi, 2006). This is where the gaseous nitrogen comes into contact with the cold produced by the refrigeration system and where it gets liquefied.

8.1.2 Heat exchanger and auxiliary systems

The process flow diagram of the overall system showing heat exchanger and auxiliary systems is shown in Figure 118. The helium compressor can be either air-cooled or water-cooled. For this work, a water cooled heat exchanger was selected. The specification for the cooling water required is given in Figure 119. The compressor provides the high purity helium flow necessary for the cryogenic refrigeration process. The compression process also generates heat of compression and saturate helium with oil particles. Oil is passed into the compression chamber with a venturi. Most of the heat during the compression process is in the helium/oil mixture and therefore needs to be removed with the help of heat exchangers. There are oil separating devices installed in series with the compressed helium flow line, which take the oil out of the compressed helium. One of the separators has two circuits for returning cool oil to the compressor. One circuit injects oil directly to the compression chamber and cools the compression chamber and another circuit cools the compressor module frame. Other oil

separators purify the compressed helium from oil and the remaining amount of oil is sent back to the compressor.

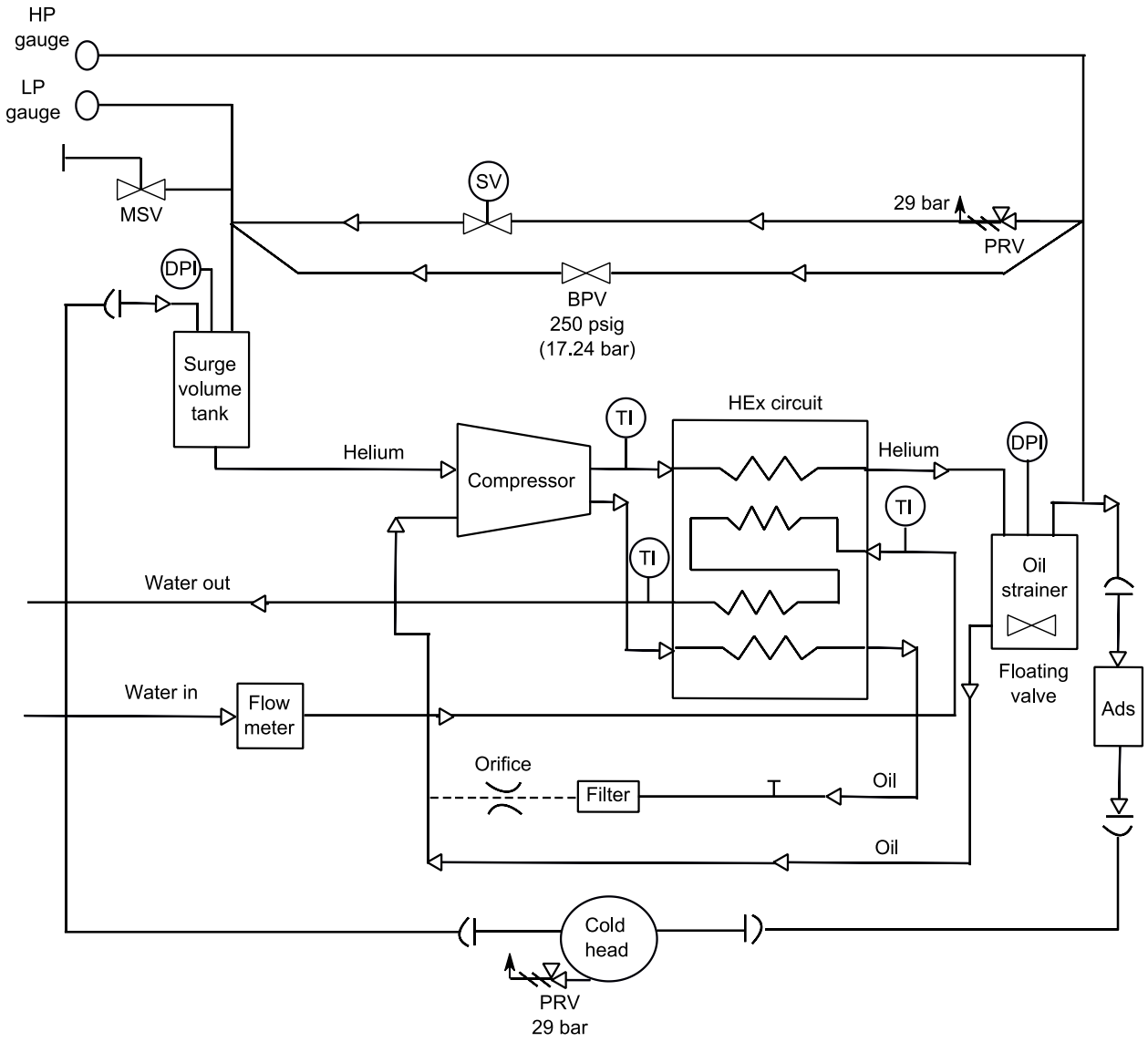

Figure 118: Process flow diagram for the overall system showing helium gas lines and cooling water lines (courtesy: Cryomech Inc.)

In the figure, LP = Low Pressure, HP = High Pressure, MSV = Manual Shut down Valve, SV = Safety Valve, PRV = Pressure Relief Valve, BPV = Back Pressure Valve, DPI = Differential Pressure Indicator, HEx = Heat Exchanger, Ads = Adsorber.

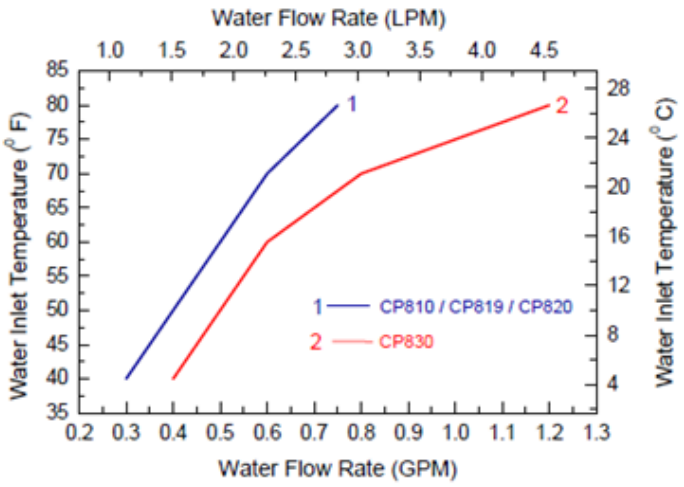

Figure 119: Cooling water requirement for compressor CP830 (Cryomech, 2017)

Most of the oil separation occurs in the strainer and from the strainer, there are two routes through which oil is sent back to the compression chamber. The oil exiting from the lowest fitting on the strainer feeds the injection circuit and the remaining oil is returned to the compressor sump through the oil return line. The level in the strainer keeps on increasing until the high pressure gas activates the float and a valve mechanism to push the oil out from the strainer. After exiting from the strainer, the oil mixture then passes through the agglomerator, where the traces of oil which did not get removed from the strainer are trapped. The trapped oil from the agglomerator is then returned to the compressor sump via the oil return line.

Any vaporous contaminants will be adsorbed in the adsorber using activated charcoal, which allows only pure helium to pass through the cold head. Without the adsorber, the build up of moisture will migrate to the cold head which might result in the cold head malfunction. Therefore for better performance of the cryocooler system, charcoal adsorber should be replaced at every 10000 hours of operation and it must be reconditioned (Cryomech, 2014).

8.1.3 Cold head including rotary valve

The compressed helium from the compressor system, which is free of moisture and oil and any other gas contaminants, is sent to the cold head through the flexible stainless steel pipes. The cold head is the part of the GM cycle where it allows the expansion of the compressed helium from high pressure to low pressure. The timing of the displacer is controlled by the rotary valve frequency, which is 144 times per minute with this specific cold head model. The function of the rotary valve in this system is to assist in movement of displacers and flow of helium through the regenerator, across the heat exchanger and charging the expansion volume with high pressure helium. The rotary valve then turns 45^0 and the high pressure helium is allowed to expand out of the expansion volume, across the heat exchanger and through the regenerator back to the suction side/low pressure side of the compressor (Cryomech, 2017).

The cold head is divided into two parts: the motor assembly and the tubular base assembly as shown in Figure 120. The motor is screwed to the motor mount, which includes the rotary valve and the rotary valve plate. The motor for this cold head assembly is an AC synchronous motor with a speed of 72 rpm. Speed of this motor determines the number of cycles per minute of the cold head. The motor is sealed from the outside by the motor tube and motor top as shown in Figure 120. Electrical supply to the motor is provided through a hermetic feed through with a plug and receptacle configuration.

The base tube assembly is mainly for housing the displacer, regenerator and the heat exchanger. This tube is made up of 304 SS stainless steel. It is held by a flange which has holes to secure the cold head to the vacuum flange of the Dewar. A high conductivity, oxygen free copper heat exchanger is attached to the base of the tube. The spring seals in the displacer separate the warm end of the cold head from the cold end. The displacer moves up and down

as a piston in a compressor, inside the tube assembly. The regenerator located inside the displacer is a heat exchanger matrix, which cools the incoming gas and retains cold from the outgoing gas. The stem and stem seal retainer are necessary to direct and seal the pressure differential in the system. The displacer is driven in both directions by the gas pressures applied in the stem and sealed from the rest of the system by the stem seal (Cryomech, 2014).

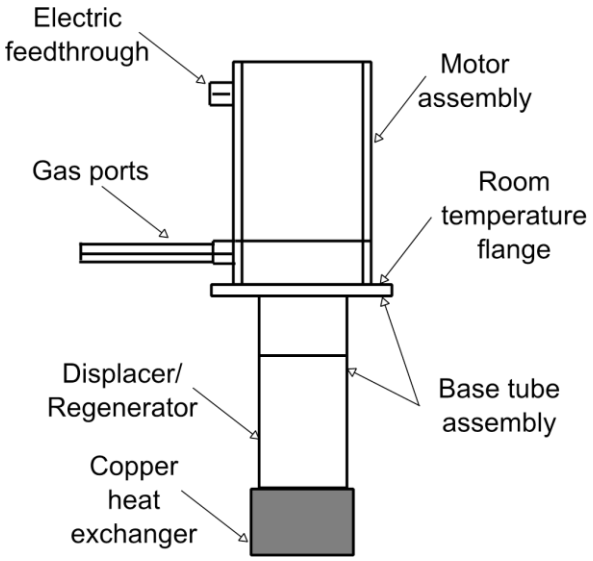

Figure 120: Cold head assembly showing its component locations(Cryomech, 2014)

8.1.4 Nitrogen generation, drying and purification system

Nitrogen generator uses a membrane technology to separate nitrogen from the compressed air and deliver >98% pure gaseous nitrogen. The compressed air must be pressurized to ~120 psig (828 kPa) before it can be sent to the nitrogen generator. The gaseous nitrogen should be free from moisture and impurities before it could be sent to the nitrogen generator. Therefore, for the delivery of pure and dry gaseous nitrogen, four filters are provided in the system which filters out the moisture, oil and carbon in the compressed air inlet before it is passed through the membrane separator. The compressed air from the compressor is first passed through a refrigerant air dryer, then the dry compressed air is passed through a water filter, then an oil

coalescing filter, air dryer, charcoal filter and an after filter as shown in Figure 121 and Figure 122. Nitrogen gas was chosen for the experimental purpose in this thesis as it was safe and flexible for use in a laboratory scale work.

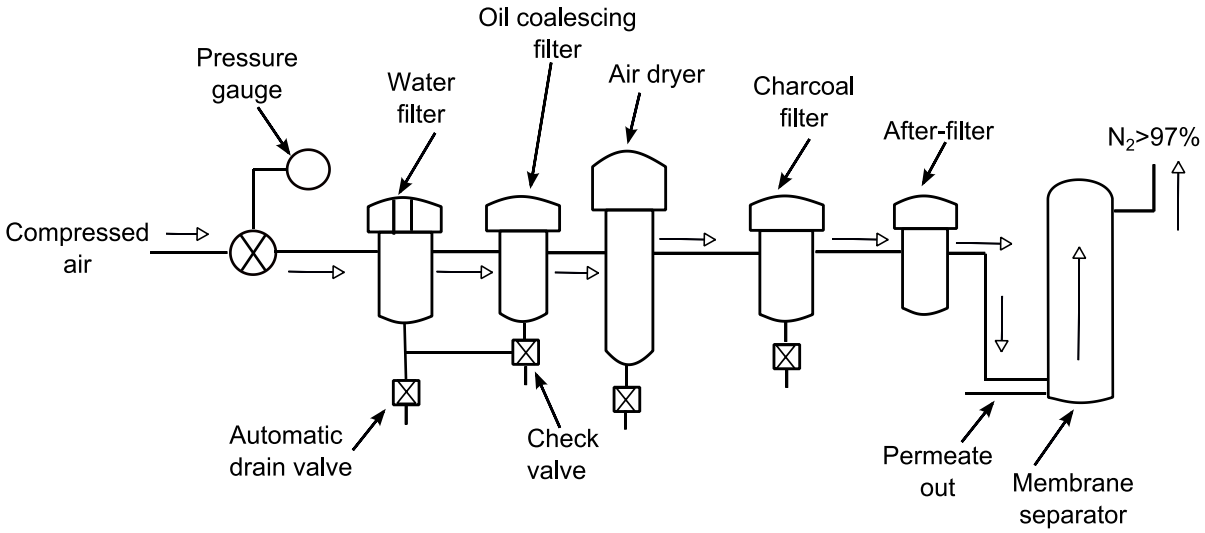

Figure 121: Set of filters in the nitrogen filter bank to remove water, oil, and carbon from the compressed air feed

The first two filters are the coalescing filters which have functions to remove water and any bulk-oil from the compressed air stream. These are equipped with a timer-operated automatic drain valve as shown in Figure 122.

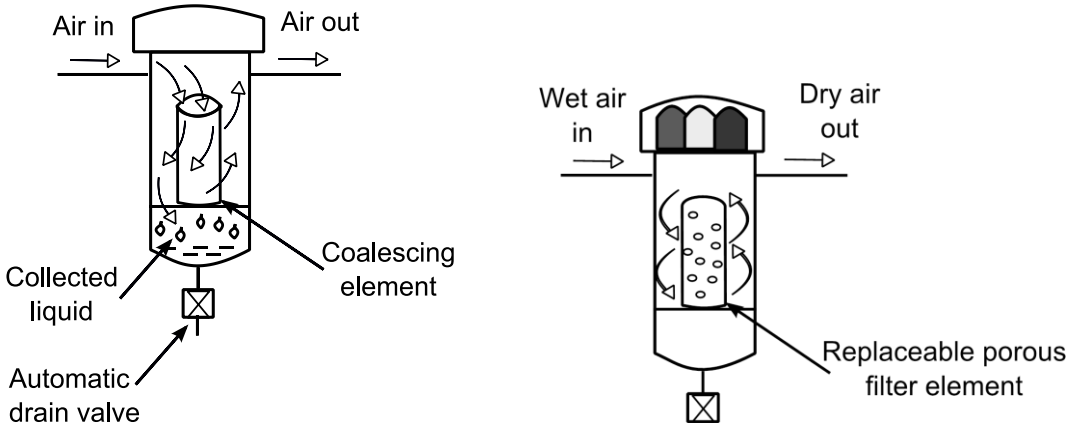

Figure 122: Coalescing filter and water filter with the band of color-change medium

The third filter contains an activated carbon element to further eliminate any hydrocarbon contaminants in aerosol form. This filter is equipped with a manual drain to remove any condensed moisture, and also has a band of color-change medium built into the element that turns brown. The filter element must be replaced before the color change reaches the brown label. When the compressed air is free of contaminants and is dry, then it is passed through the fibre membrane as shown in Figure 123 to remove other gas constituents from the air and only to keep pure and dry nitrogen gas.

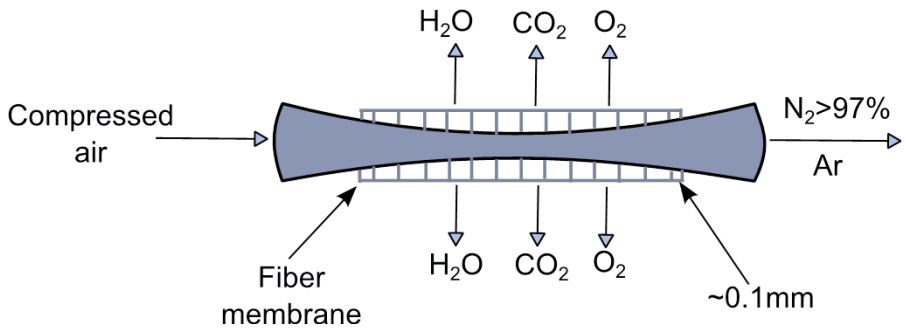

Figure 123: Membrane separator showing the separation process (Kopeliovich, 2017)

8.1.5 Dewar flask

The Dewar flask is required for the storage of low temperature fluid. It is a 35 liter (0.035 m^3) container which is double walled container and is sealed from the outside environment so that only gaseous nitrogen can enter the container. This sealing is done to prevent heat leak into the container, which results in evaporation of liquid nitrogen. The boil off losses from this Dewar vessel is reported to be less than 1 liter/day. There are other components attached to the Dewar which are: the low pressure regulator, level indicator/switch, pressure gauge, pressure relief valve, burst disk, bleed valve and the liquid nitrogen extraction line as shown in Figure 124. The pressure relief valve is activated and it opens when the pressure inside the Dewar is approximately 10 psig (68.9 kPaG). The burst disk is an additional safety feature which

activates at approximately 45 psig (310.3 kPaG) for the protection of Dewar if the relief valve fails.

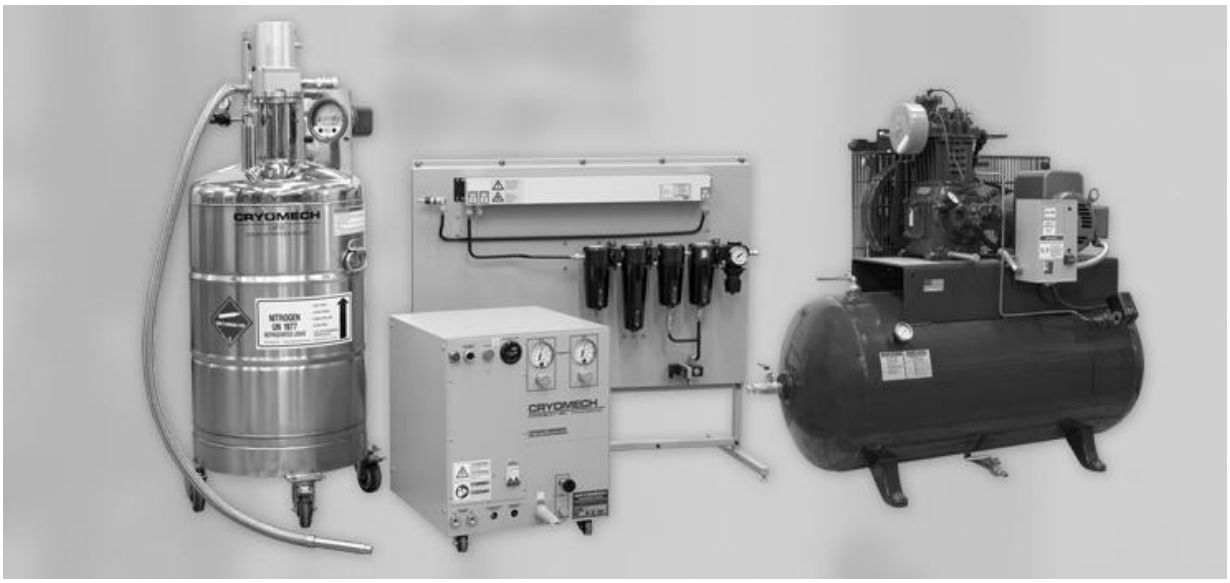

Figure 124: LNP10 liquid nitrogen generator system with air compressor, helium compressor, filter bank and Dewar vessel (Cryomech, 2017)

8.1.6 Mass balance

The logging mass balance used was a shipping balance, Ultegra Max flat top from Fairbanks scales, USA as shown in Figure 125. The specifications of the balance are listed in Table 11.

Table 11: Mass balance parameters

Dimensions	20”x20”x2.5”
Capacity	113kg factory set
Rounding	Nearest division per NIST H-44 requirements
Power requirements	5VDC or USB
Capacity	250 lbs/113.5 kg
Readability	0.05 lbs/0.02 kg

Figure 125: UltegraMax Flat top logging mass balance from Fairbanks Scales (Fairbanks Scales, 2017)

8.2 Development of the supervisory control and data acquisition system

This section describes the part of the research work that was dedicated to the development of the supervisory control and data acquisition system. Data collection and logging was done using LabVIEW software extensively. This development program includes developing programs on LabVIEW for monitoring of lab environmental data, monitoring parameters from helium compressor, interfacing with VFD, monitoring data from the cold head, and monitoring data from logging mass balance. This program is also depicted in the block diagram Figure 126.

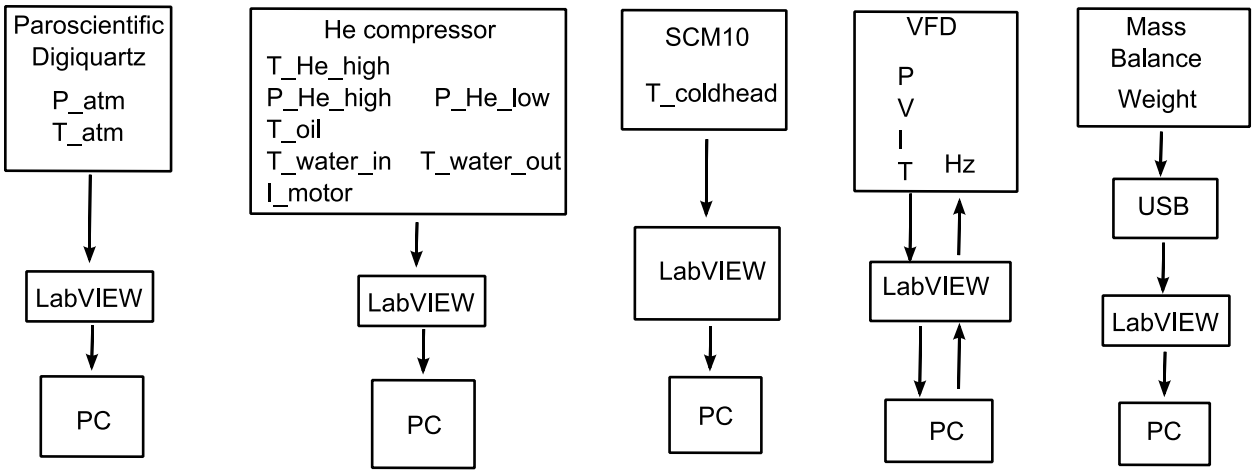

Figure 126: A block diagram showing the supervisory control and data acquisition system development

8.2.1 Monitoring of lab environmental data

Room temperature and pressure were monitored using a Paroscientific Inc. pressure standard. This monitor features an accuracy of 0.01%, digital output, high resolution and ±2 psig for upto 40,000 psia pressure values. The data were logged into computer using a standard RS 232 cable utilizing the Graphical User Interface provided by the manufacturer.

8.2.2 Cryomech Helium compressor data acquisition software

The high and low helium gas pressures, the helium gas temperature, water inlet and outlet temperatures, compressor oil temperature were recorded using the Cryomech Helium compressor data acquisition software (in LabVIEW) provided by Cryomech Inc. Screenshot of the program for monitoring the data and logging to a file is shown in Figure 127. The first virtual panel is to monitor the low and high pressures, motor current, helium gas temperature, oil temperature, water inlet and outlet temperatures. The baud rate for this interface was 115200. As shown in the figure, the virtual panel also shows the minimum temperature recorded, maximum temperature recorded and the current temperature. It also displays the total number

of hours compressor is operated until current time. The second virtual panel is to log the same data to the computer. This program asks for a path to store the data and stores the data in text format.

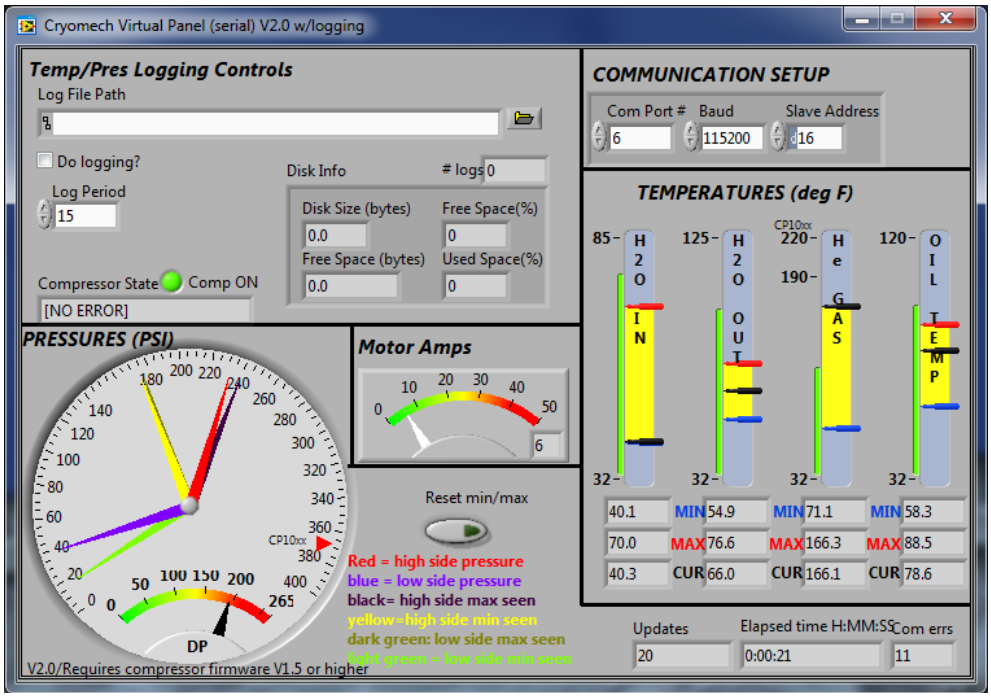

Figure 127: Cryomech Virtual panel for logging all the parameters(Cryomech, 2017)

8.2.3 Development of the VFD interface in LabVIEW

One of the motivating and difficult interfacing was that of the variable frequency drive, which was done on LabVIEW. There were numerous registers that could be read and written, among which the most useful ones were the: input current and voltage, input power, torque (constant and variable). The commands were sent to the Hitachi variable frequency drive via RS 485 to RS 232 (RS-Recommend Standard) cable.

The two modes of communication with the inverter were in ASCII mode and Modbus-RTU mode. The communication made in this case was in the standard Modbus-RTU (Remote

Terminal Unit) mode, where the communication was between the inverter which acted as the slave and the external control system which was the master. The external control system was LabVIEW from where the commands were sent to read, write or read & write the registers. The inverter manual provides the list of coils and registers, which are memory addresses. A coil is a single-bit physical output (boolean) and a register is a 16-bit integer output. There are numerous registers which are available for read, write or for read & write both.

The command message that is sent to the slave device by the master device is called “query” and the response message that are sent to the master device from a slave device when a “query” is sent is called “response”. The query and response frame formats are as follows:

Query ⇨ *<Slave address><Function code><Query data><Error check code (CRC-16)>*

Response ⇨ *<Slave address for confirmation><Function code for confirmation><Response data><Error check code (CRC-16)>*

(i) Slave address

The slave address is a number 1 to 247 that is assigned to the inverter (i.e. slave) beforehand. Since we had only one inverter connected to our system, the slave address was ‘1’.

(ii) Function code

The function to be executed by the inverter is specified by the function code. The function codes supported by SJ700 series inverter with their functions are listed in Table 12.

Table 12: Function codes supported by SJ700 series inverter and their functions (Hitachi, 2014)

Function code	Function	Maximum number of data types in a message	Maximum data count in a message
01h	Reads the coil status	4	32 coils (in units of bit)
03h	Reads registers	8	16 registers (in units of byte)
05h	Writes data to a coil	2	1 coil (in units of bit)
06h	Writes data to a register	2	1 register (in units of byte)
08h	Performs a loopback test	-	
0Fh	Writes data to multiple coils	4	32 coils (in units of bit)
10h	Writes data to multiple registers	8	16 registers (in units of byte)
17h	Writes/Read data to multiple registers	32/32	16 registers (in units of byte)

The read function query was sent in the form: *<Slave address>function code><starting register number (upper digit)><starting register number (lower digit)><Number of registers to read (upper digit)>< Number of registers to read (lower digit)><CRC-16 code (upper digit)><CRC-16 code (lower digit)>.*

The response of this form would be: *<Slave address>function code><number of data bytes><starting register number (upper digit)><starting register number (lower digit)><Number of registers to read (upper digit)>< Number of registers to read (lower digit)><CRC-16 code (upper digit)><CRC-16 code (lower digit)*. The number of data bytes requested will be responded by the slave. The data contains a functional instruction. The sending format of the data is different depending on the function code. The inverter supports the following Modbus data format as depicted in Table 13.

Table 13: Modbus data format (Hitachi, 2014)

Data name	Description
Coil data	1-bit binary data that can be referenced and changed
Register data	16-bit data that can be referenced and changed

The Modbus RTU protocol uses a cyclic redundancy check (CRC) as the error check method. The CRC is a 16-bit data generated for a data block that has an arbitrary data length

(in unit of 8 bits). A generative CRC-16 ($X^{16} + X^{15} + X^2 + 1$) is used to generate CRC code. The block diagram for finding the CRC code is shown in Figure 128. At first, the CRC code was calculated separately and then combined with the main data before sending the query. But later, the CRC code was embedded in the main block diagram which made it easier to send the query.

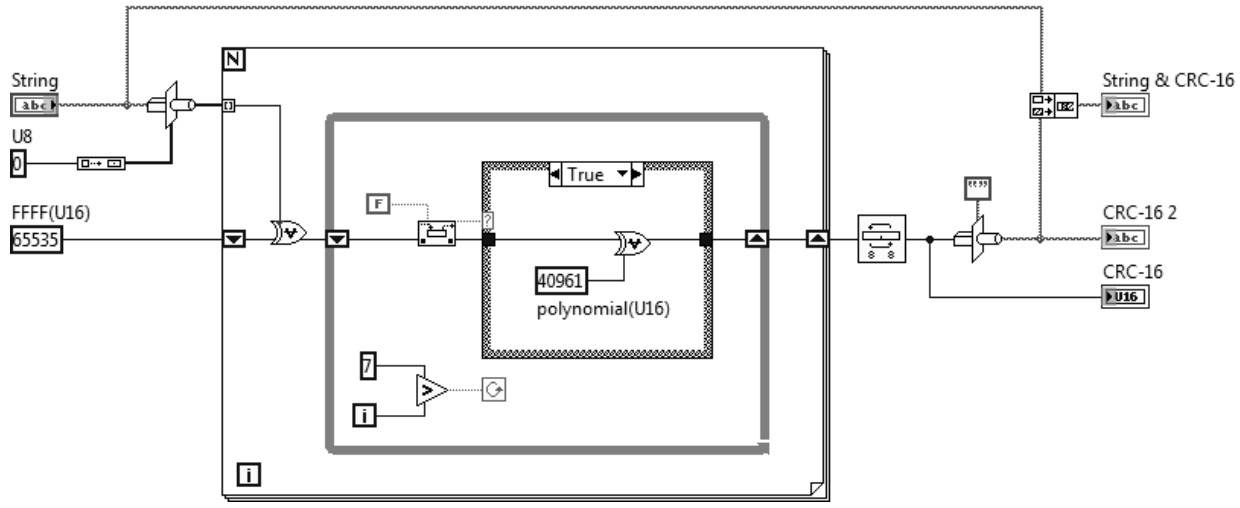

Figure 128: LabVIEW block diagram error check code for inverter

The baud rate for interfacing this device was 9600, data bits of 8, no parity, 1.0 stop bits and no flow control. The block diagram shown below is for a function that writes /reads data to multiple registers. This function is used to change the frequency setting (F001) and for reading the output power (d014) in the inverter at slave address “1”. The block diagram was also developed to be able to monitor current, voltage, and torque from the variable frequency drive. The normal response of the inverter is expressed as an example in the next page, but if the query sent to the inverter contains an error, it would send an response with an error or the exception code in the format: <*Slave address*><*Function code*><*Exception code*><*CRC-16*>.

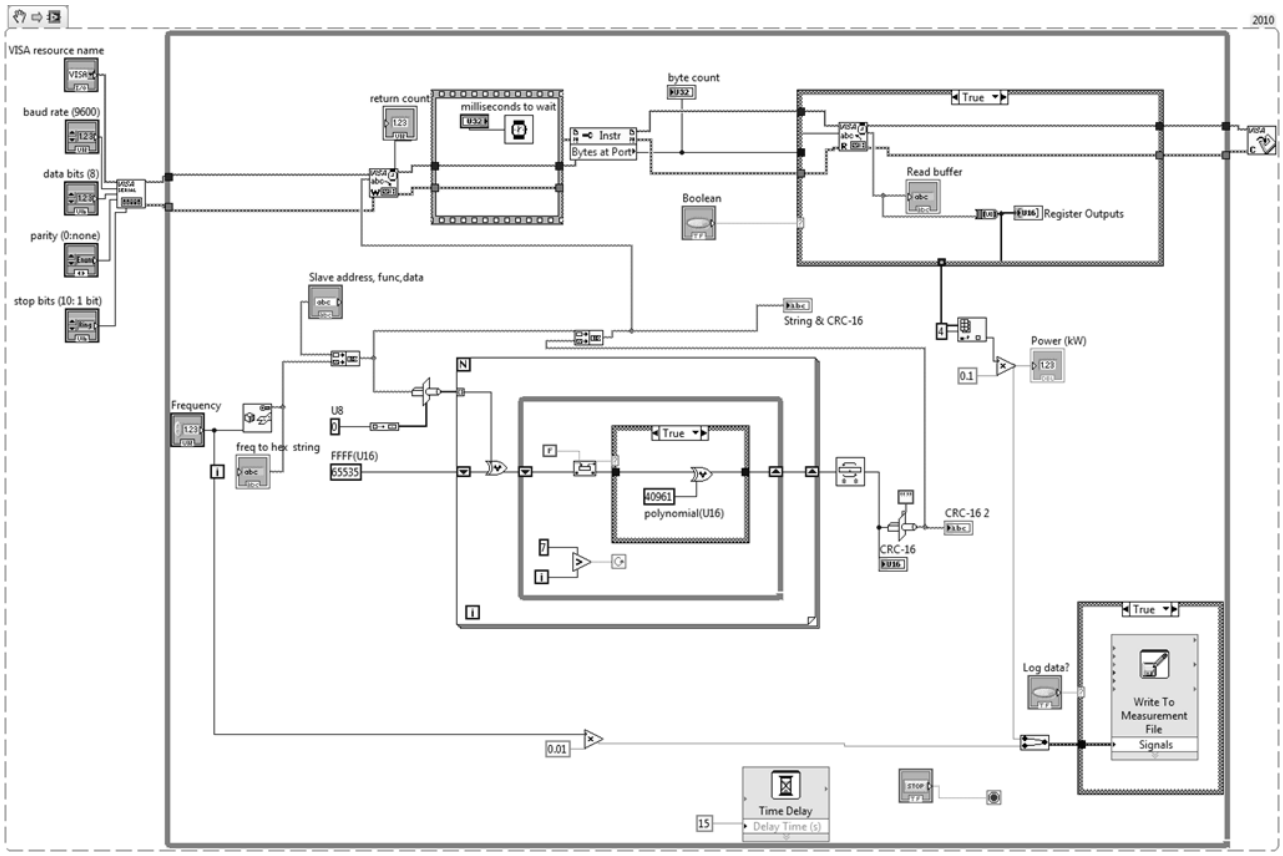

Figure 129: LabVIEW block diagram for interfacing with inverter

The variable frequency drive allowed monitoring the torque, however controlling the torque was not an option with this drive. The registers monitored from the variable frequency drive are listed in Table 14.

Table 14: List of monitored registers (Hitachi, 2014)

Register number	Function name	Function code	Read(R)/ Write(W)	Monitoring and setting items	Data resolution
1001h	Output frequency monitoring	d001 (high)	R	0 to 40000	0.01 [Hz]
1002h		d002 (low)			
1003h	Output current monitoring	d002	R	0 to 9999	0.1[A]
1010h	Torque monitoring	d012	R	-200 to +200	1[%]
1011h	Output voltage monitoring	d013	R	0 to 6000	0.1[V]
1012h	Power monitoring	d014	R	0 to 9999	0.1[kW]

8.2.4 Integration of the ultra low temperature sensor into LabVIEW HMI

The temperature of the cold head was measured using a silicon diode and was logged to computer via Scientific Instruments temperature monitor, SCM10. SCM10 is a single channel monitor which measures temperature from 1.5 K to 800 K, the results can be displayed either in temperature units, degree Centigrade (^{0}C), Kelvin (K) or degree Fahrenheit (^{0}F) or in sensor units Volts (V) or Ohms (Ω). The range of this temperature monitor is 0-10 Volts and 4-20 mA. The monitor sensitivity for Silicon diode is ±3.7mK at 4K, ±87mK at 77 K ±66mK at 273 K. The monitor came with a Graphical User Interface by which the data could be logged and recorded into the computer by means of an RS 232 straight through 9 pin cable. A LabVIEW program was created for the monitor to log the temperature of the cold head. The baud rate for interfacing this device was 9600, data bits of 8, no parity, 1.0 stop bits and no flow control. The ASCII message strings were sent in the format:

<Query string><?><space><parameters><terminators>

The terminators can be line feed (‘*n*’) or a carriage return (‘*r*’). The parameters are usually not necessary when sending a query. This program was used to send a temperature query in the

form “*T?\r*” which would return the query and give the response as “*T xxx.xxx\r*”, where *xxx.xxx* is temperature reading in Kelvin. The block diagram is presented in Figure 130.

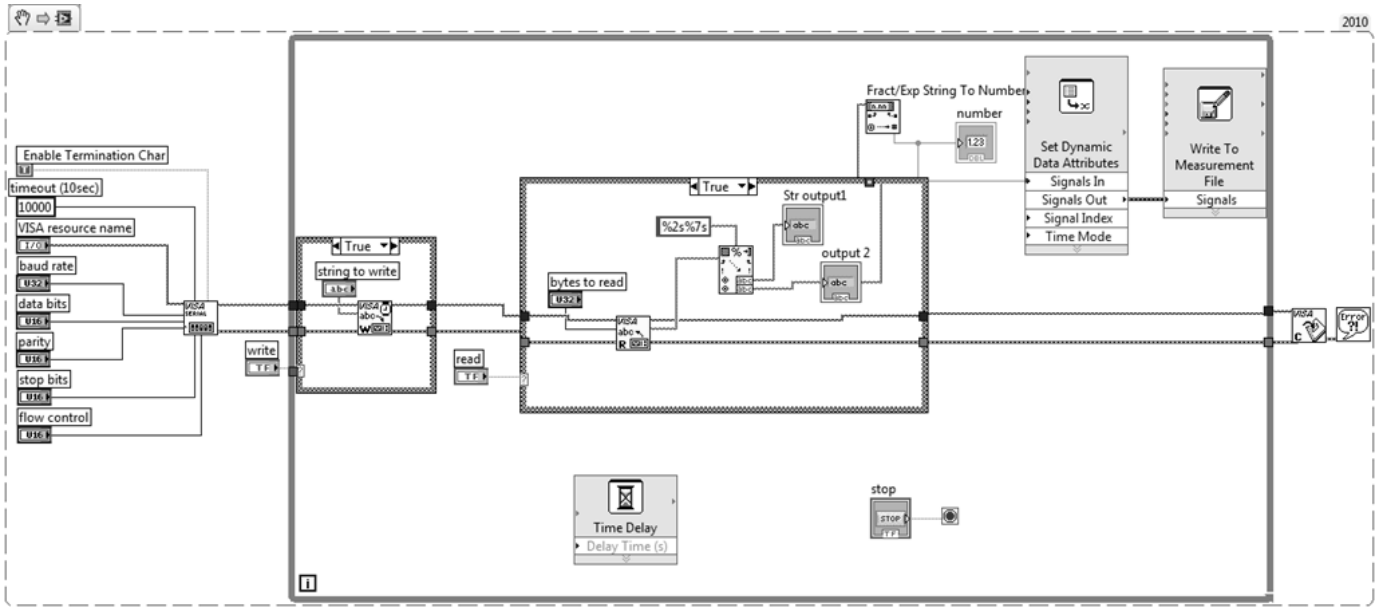

Figure 130: LabVIEW block diagram for interfacing with the temperature monitor

8.2.5 Enhanced measurement resolution procedure for the Fairbanks UltraMax digital mass balance and integration to the LabVIEW HMI

As delivered, the logging mass balance did not comprise manufacturer software driver. Therefore an NI-VISA driver was created for a Human Interface Device (HID)-USB utilizing the tutorial provided by the National Instruments on their website, so that the balance could be programmed in LabVIEW. The driver worked perfectly until some time when the program would not recognise the device. After then, another program had to be built but there was no other option to interface it without using the DLL provided by the manufacturer. The DLL was then embedded in LabVIEW and the mass balance interfaced smoothly again. Figure 131 shows the block diagram for the logging mass balance. As supplied this balance had a readability of 0.05 lbs or 0.02 kg which was later improved to 0.01 kg with the help of the manufacturer. The

balance display was improved to a readability of 0.001 kg but it was only limited to its display. The highest readability possible for logging the data was 0.01 kg.

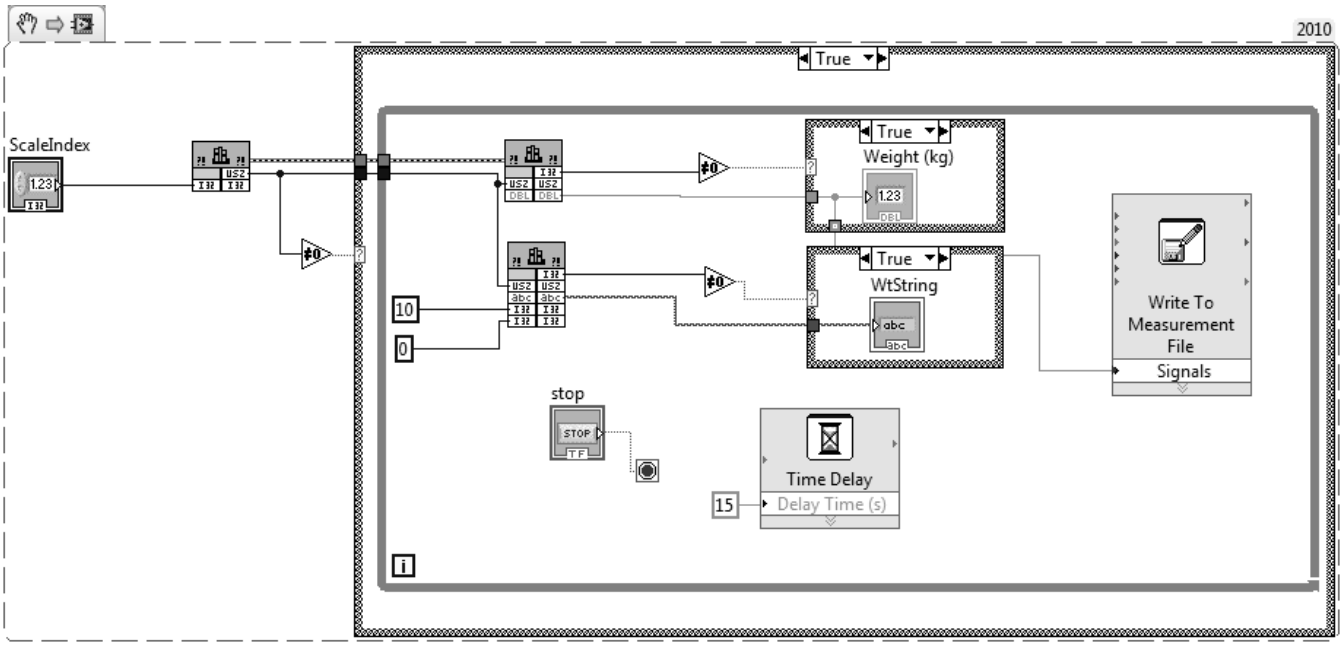

Figure 131: LabVIEW block diagram for interfacing with the logging mass balance

8.3 Experimental program

An experimental program was designed and implemented for obtaining results that could be compared with the simulation results. This program was also performed to test some of the hypotheses listed in each sub-sections that follow. The major hypothesis tested in all the experimental scenarios was whether or not the cryogen production remains comparatively steady when the electric motor that drives the compressor is fed with variable work input.

Prior to undertaking of the experimental program in the laboratory, some commissioning checks were performed to familiarize the system behavior and response. Once the commissioning checks were completed, then experimental works were carried out.

First, some tests were carried out at standard normal operating frequency of 60 Hz. Then the experiments were performed using other steady frequencies such as 50 Hz, 65 Hz, 70 Hz and 75 Hz. Experiments could not be performed below 50 Hz and above 75 Hz for 10 hours period because the electric motor would either draw less than normal current (below 50 Hz) or higher than normal current (near or above 75 Hz) that would make the motor heat up and the safety system on the unit would shut the system down. Following these, experiments were performed at sets of other frequencies including: random frequency experiments, sinusoidal varying set points, and set points following wind speed patterns were also carried out. Section 8.3 presents each tests carried out, method adopted, reduced results from raw results, discussion, conclusion and recommendations.

8.3.1 60Hz testing

This section presents the purpose, experimental method, obtained results, discussion and conclusions on the experimental work performed. The GM cryocooler system was operated at an operating frequency of 60 Hz for 10 hours and the system parameters were monitored and recorded. The parameters that were recorded using the data acquisition system were: the helium pressure at compressor inlet, helium pressure and temperature at compressor outlet, VFD power consumption, cooling water inlet and outlet temperature, cold head temperature and cumulative liquid nitrogen produced. The purpose of carrying out this test was to determine if the system performs as it was tested by the manufacturer. The hypothesis set out for this experimental work was that the system operates at a constant frequency, and that it produces liquid nitrogen in a constant rate.

The system was started when the cold head was at room temperature ~294-300 K. It takes around 15 minutes for the cold head to reach the ~77 K, and around 2 hours to cool down

the Dewar vessel. It is only after the Dewar is cooled down, nitrogen gas starts condensing and is collected in Dewar vessel. The cool down process indicating time taken to cool down has been presented in Section 7.4. The data collection was started when liquid nitrogen starts producing. The balance was zeroed out and the results were recorded.

The average input power consumed by the compressor unit at 60 Hz over the 10 hour period was 2.2 kW. Similarly the average helium low pressure and high pressure were 269.1 kPa and 1655.6 kPa respectively. The cooling water inlet temperature was 15.2 ^{0}C and the cooling water outlet temperature was 18.9 ^{0}C respectively. The minimum cooling water flow rate necessary for this compressor model was ~2 LPM. Similarly the helium gas temperature at compressor outlet was 70.7 ^{0}C, the motor oil temperature was 27.5 ^{0}C and the motor current was 6 Amps. The average cold head temperature was 77.307 K and the total mass of liquid nitrogen accumulated over the 10 hours period was 4.65 kg. The average room temperature was 27.4 ^{0}C and the average room pressure was 98.830 kPa respectively. The system was operated at a driving frequency of 60 Hz repeatedly to determine the system performance and to compare it with the manufacturer provided results. The constant compressor driving frequency is presented in Figure 132 while Figure 133 and Figure 134 attached below present the results.

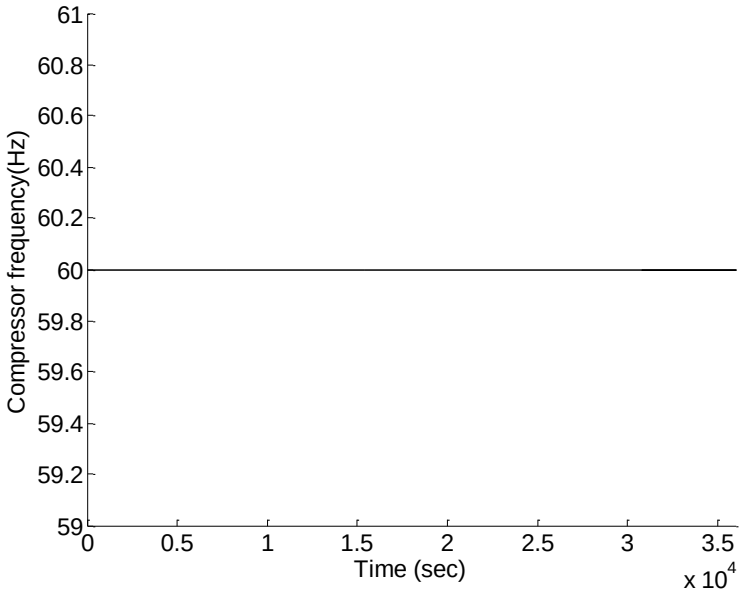

Figure 132: Constant compressor input frequency of 60 (Hz)

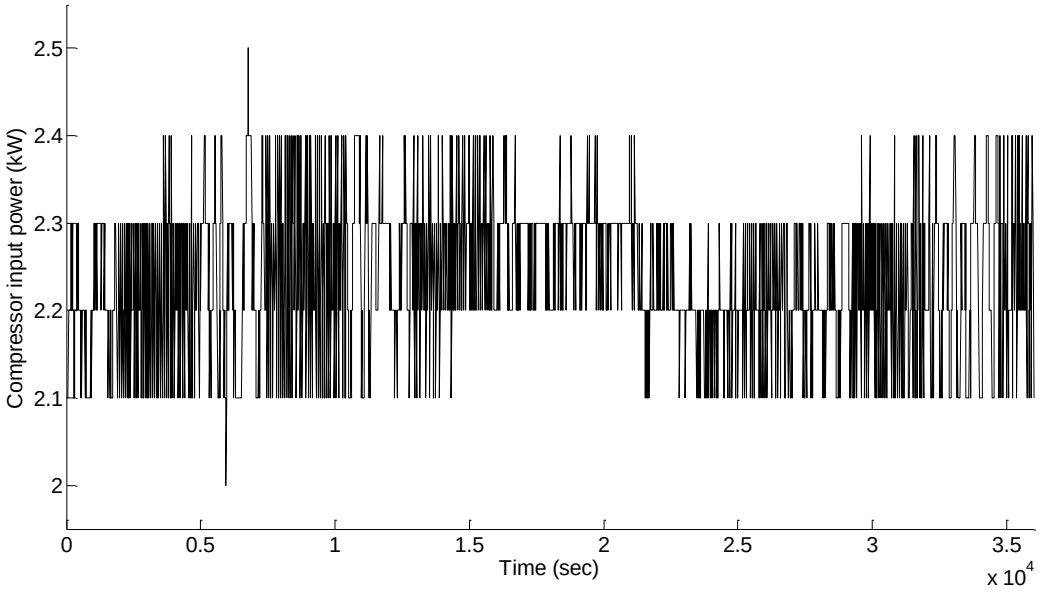

Figure 133: Compressor input power (kW) at constant frequency of 60 Hz

The fluctuations seen in Figure 133 in the compressor input power is partly due to voltage fluctuations and mainly due to the quantization of signal by the VFD controller.

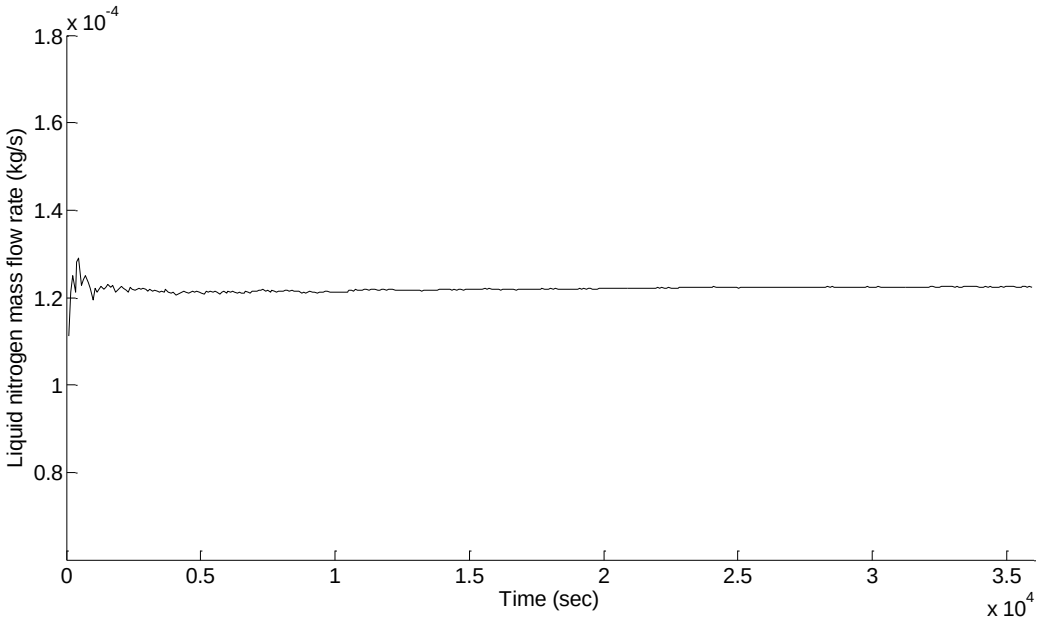

Figure 134: Liquid nitrogen mass flow rate (kg/s)

The compressor input power (kW) during 60 Hz testing for 10 hours is presented in Figure 133, and the liquid nitrogen mass flow is shown in Figure 134. Detailed results including helium gas discharge temperature, helium suction and discharge pressures, cooling water inlet and outlet temperatures, motor oil temperature, motor current are presented in Appendix G. The 60 Hz testing was the base study which allowed gaining information on the system behavior on its operation at standard operating frequency that could be used as a support when comparing the results with other frequencies in terms of differences and similarities.

8.3.2 Prolonged tests at other driving frequencies

Experiments were carried out at various constant driving frequencies of 50Hz, 55Hz, 65Hz, 70Hz, and 75Hz for 10 hours each. The purpose, experimental method, obtained results, discussion and conclusions on the experimental work performed are also presented. The GM cryocooler system was operated at an operating frequency of 60 Hz for ~2-3 hours until the unit

started producing liquid nitrogen. Data was recorded after that. The parameters that were recorded using the data acquisition system were: the helium pressure at compressor inlet, helium pressure and temperature at compressor outlet, VFD power consumption, cooling water inlet and outlet temperature, cold head temperature and cumulative liquid nitrogen produced. The purpose of carrying out this test was to determine how system performs at constant frequencies but different than the normal operating frequency. The hypothesis set out for this experimental work was that the power consumed by the compressor motor increases linearly with the driving frequency and the liquid nitrogen mass flow rate (kg/s) or the total liquid nitrogen mass produced (kg) also increases linearly with the driving frequency.

In each of these tests, the system was run at 60 Hz to lower cold finger temperature to around nitrogen boiling point ~77K. The data were all logged with a step time of 15 seconds for 10 hours. The compressor motor input power, the cold head temperature, and the liquid nitrogen mass flow rate are presented in the graphs (Figure 135 to Figure 137). These are average values from 10 hours data. For each frequency, the test was repeated 3 times, except for 75 Hz. The standard deviations from mean for the parameters at various motor driving frequencies in each of the tests are presented as error bars in the plots. The system was operated at 75 Hz for 10 hours once and this experiment could not be repeated 3 times on this particular frequency for the reasons discussed earlier. The safety feature on the unit would stop the system to prevent compressor motor and motor oil from being overheated. The system would operate for maximum of 30-45 minutes ≤45 Hz and/or ≥75 Hz and would stop (when tried to operate continuously). Therefore, error-bars are not plotted for this frequency Figure 135 to Figure 137. However, the parameter values for this frequency are tabulated on the tables that follow, which are from one 10 hour experiment.

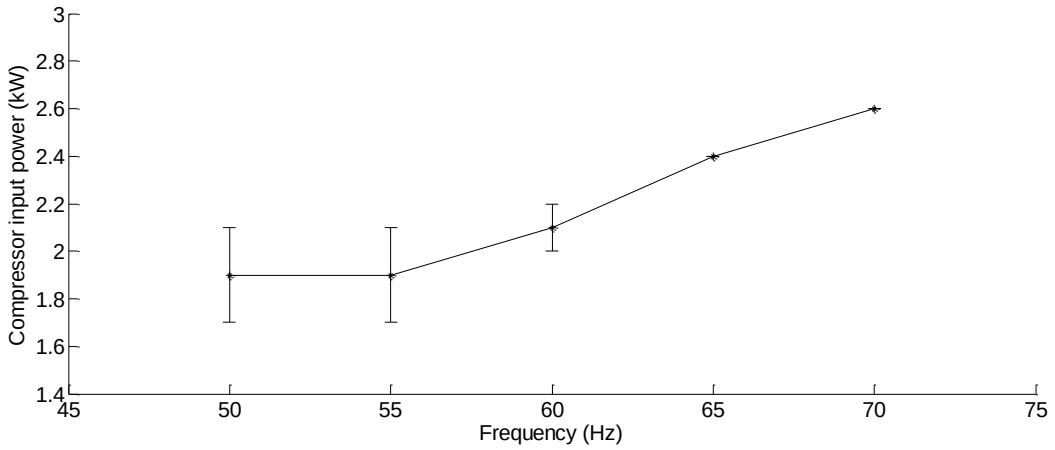

Figure 135: Average compressor input power (kW) at different driving frequencies

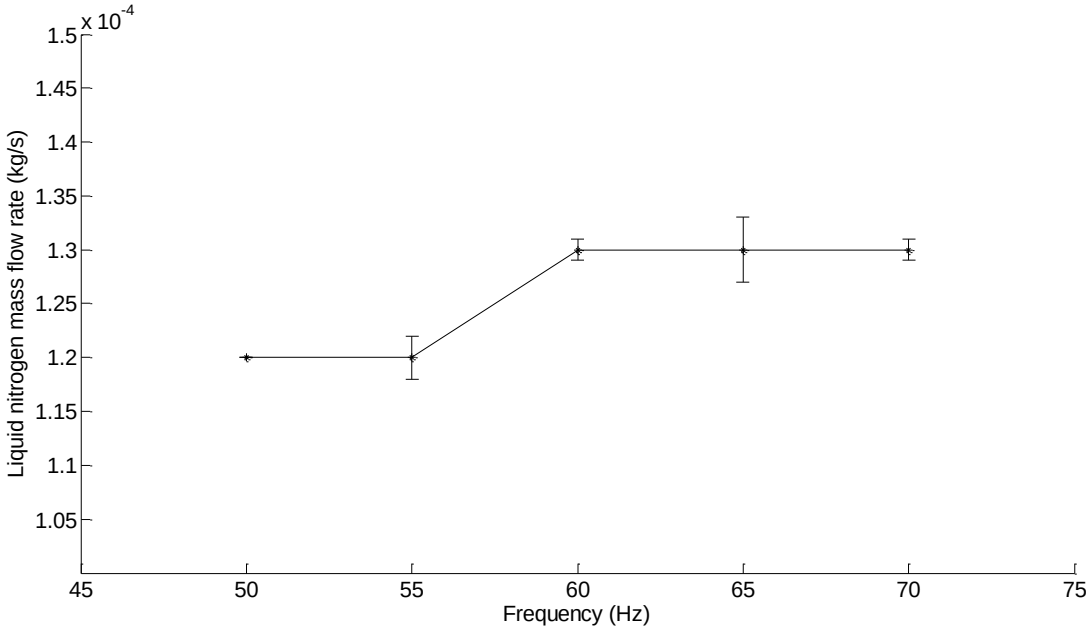

Figure 136: Average liquid nitrogen mass flow rate (kg/s) at different driving frequencies

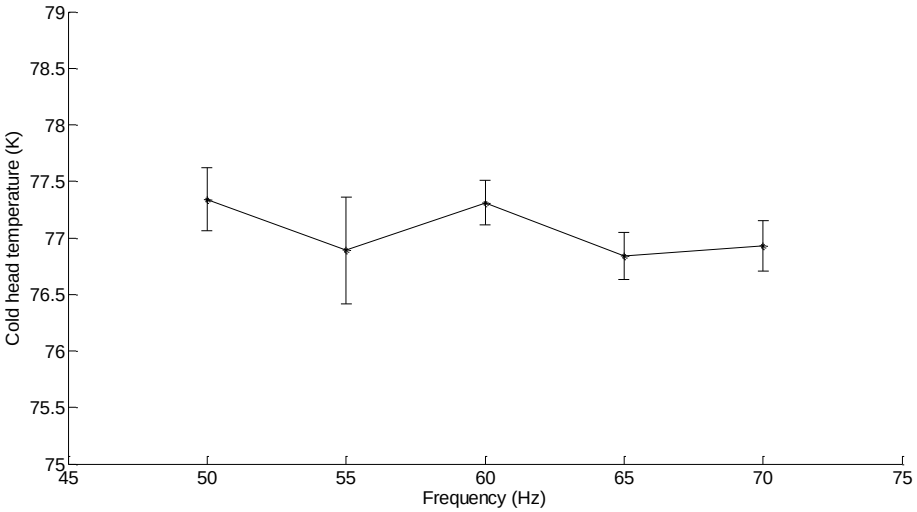

Figure 137: Average cold head temperature (K) at different driving frequencies

The range of values across the 10 hour averages thus give an indication of the repeatability of the observations. These values are also tabulated for average compressor input power, liquid nitrogen mass flow rate and cold head temperature in Table 15, Table 16, and Table 17. Other parameters such as average helium gas suction and discharge pressure, average helium gas discharge temperature, average cooling water inlet and outlet temperature, room temperature and pressure during operation at these driving frequencies are tabulated in Table 18.

Table 15: Average compressor input power (kW) at different frequencies

Frequency (Hz)	Average compressor input power (kW) from 10 hours			Average input power from 3 sets	Standard deviation	Standard error
50	1.7	1.9	2.0	1.9	0.2	0.1
55	2.1	2.0	1.7	1.9	0.2	0.1
60	2.1	2.2	2.1	2.1	0.1	0.1
65	2.4	2.3	2.4	2.4	0.0	0.0
70	2.6	2.7	2.6	2.6	0.0	0.0
75*	2.9	-	-	2.9	0.3	0.006

Note. 75*: One set of complete 10 hour data on this frequency. Standard deviation for parameters at this frequency=Deviation from mean values within 10 hour duration.

Table 16: Average liquid nitrogen mass flow rate (kg/s) at different frequencies

Frequency (Hz)	Average liquid nitrogen mass flow rate (kg/s) from 10 hours			Average mass flow rate from 3 sets	Standard deviation	Standard error
50	0.00012	0.00012	0.00012	0.00012	0.000000	0.0000002
55	0.00012	0.00012	0.00012	0.00012	0.000002	0.0000013
60	0.00012	0.00013	0.00013	0.00013	0.000001	0.0000008
65	0.00013	0.00014	0.00013	0.00013	0.000003	0.0000016
70	0.00013	0.00013	0.00014	0.00013	0.000001	0.0000004
75*	0.00015	-	-	0.00015	0.000017	0.0000066

Note. 75*: One set of complete 10 hour data on this frequency. Standard deviation for parameters at this frequency=Deviation from mean values within 10 hour duration.

Table 17: Average cold head temperature (K) at different frequencies

Frequency (Hz)	Average cold head temperature (K) from 10 hours			Average cold head temperature from 3 sets	Standard deviation	Standard error
50	77.590	77.402	77.040	77.344	0.280	0.161
55	77.390	76.830	76.450	76.890	0.473	0.273
60	77.430	77.410	77.080	77.307	0.197	0.113
65	77.070	76.660	76.800	76.843	0.208	0.120
70	77.180	76.770	76.830	76.927	0.221	0.128
75*	77.230	-	-	77.230	0.038	0.001

Note. 75*: One set of complete 10 hour data on this frequency. Standard deviation for parameters at this frequency=Deviation from mean values within 10 hour duration.

Table 18: List of average values for parameters at different frequencies

Frequency (Hz)	Helium gas			Cooling water temperature		Motor		Room	
	Suction pressure (kPaG)	Discharge pressure (kPaG)	Discharge temperature (^{0}C)	Inlet (^{0}C)	Outlet (^{0}C)	Oil temperature (^{0}C)	Current (Amp)	Temperature (^{0}C)	Pressure (kPa)
50	311.0	1630.4	66.2	15.8	19.7	27.6	5	27.4	98.718
55	286.8	1644.5	67.9	15.4	19.3	27.4	5	27.3	98.463
60	269.1	1655.6	70.7	15.2	18.9	27.5	6	27.4	98.830
65	251.3	1671.6	73.1	15.6	19.1	29.1	7	27.5	97.639
70	231.2	1680.5	76.4	14.5	18.9	29.8	7	27.1	98.730
75*	227.6	1661.1	80.8	7.9	14.7	26.2	8	24.3	98.310

Note. 75*: One set of complete 10 hour data on this frequency.

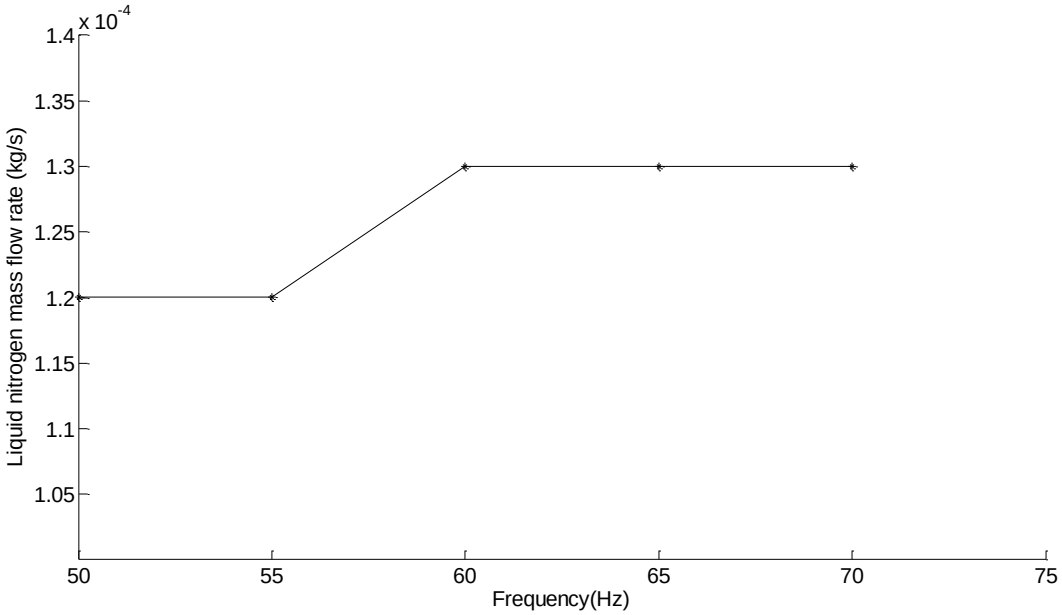

Figure 138: Motor driving frequency vs. liquid nitrogen mass flow rate (kg/s)

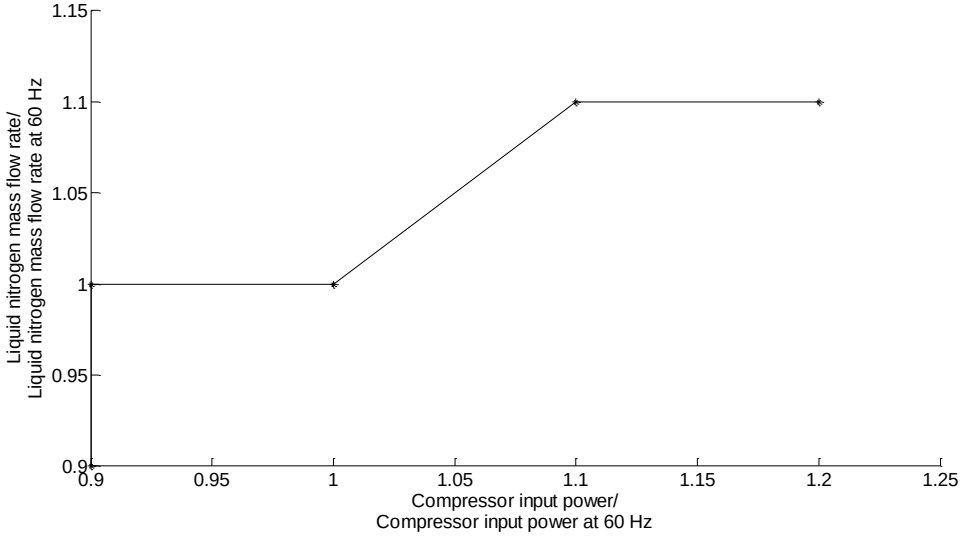

Figure 139: Compressor motor power performance vs. liquid nitrogen mass flow rate (kg/s)

Experimentally, the average compressor power and the average liquid nitrogen mass flow rate (kg/s) increased with increase in motor driving frequencies. There is slight increase in liquid nitrogen mass flow rate (kg/s) when the frequency is changed from 50 Hz to 75 Hz. The mass flow rate was 0.00012 kg/s at 50 Hz and 55 Hz. However, the average liquid nitrogen

mass flow rate (kg/s) was constant at 0.00013 kg/s when the compressor was operating at driving frequency of 60 Hz, 65 Hz and 70 Hz. Similarly, the mass flow rate increased to 0.00015 kg/s at 75 Hz. However, the compressor input power increased linearly with frequency as is shown in Figure 135. The compressor input power showed higher variances when operating at frequencies of 50 and 55 Hz. The liquid nitrogen mass flow rate (kg/s) varied from the average value most at frequency of 65 Hz and 55 Hz respectively. The cold head temperature had the maximum variation when the system was operating at a frequency of 55 Hz. This indicates that the parameters vary from their mean values when operating at other frequencies than at the standard motor operating frequency of 60 Hz most of the time.

The variances seen in Figure 135 to Figure 137 may differ depending on various other parameters such as room temperature, room pressure, the pressure inside Dewar vessel, and the amount liquid nitrogen mass in the Dewar vessel. Also, the liquid nitrogen mass flow rate (kg/s) attains its optimum value although there is increase in compressor motor frequency and thus compressor input power due to the fact that the helium compressor has a fixed volume surge tank and that the rotary valve present in the cryocooler has fixed timing set for opening and closing the valve. Therefore, the liquid nitrogen mass flow rate (kg/s) curve is approaching an optimum rate as is seen in Figure 136 and Figure 138.

8.3.3 Sinusoidal varying motor driving frequency tests

This section presents the purpose, experimental method, obtained results, discussion and conclusions on the experimental work performed. The GM cryocooler system was operated at the standard operating frequency of 60 Hz until some liquid nitrogen is collected in Dewar vessel. The parameters that were recorded using the data acquisition system were: the helium pressure at compressor inlet, helium pressure and temperature at compressor outlet, VFD

power consumption, cooling water inlet and outlet temperature, cold head temperature and cumulative liquid nitrogen produced. The purpose of carrying out this test was to determine the system performance in a multiple set of motor driving frequencies. The hypothesis set out for this experimental work was that although the system is provided with sinusoidal varying set of driving frequencies, the liquid nitrogen mass flow rate produced will be fairly constant.

A set of 14 set point changes of motor frequency to represent the complete cycle from 48Hz to 75Hz and back to 48Hz were used to generate sinusoidal frequency input as shown in Figure 91 (see Section 7.6.2). The duration between these set points were 1 minute. The experiments were run for 2 hours each, and repeated 3 times. At first the system was operated at constant frequency of 60 Hz to attain the steady state. When the cold head reached ~77.325 K and when the system started producing some liquid nitrogen, the set of sinusoidal frequency set points as presented in Figure 91 was applied to the helium VFD compressor. During the experimentation, total power consumed, total liquid nitrogen produced, helium temperature, suction and delivery helium pressures across compressor, and motor oil temperature were recorded. This set of experiment was repeated for three times and similar results were obtained. For convenience, the compressor driving frequency (Hz), the compressor input power (kW) and the liquid nitrogen mass flow rate (kg/s) are presented in Figure 140 and Figure 141 respectively and the rest of the experimental results are presented in Appendix I.

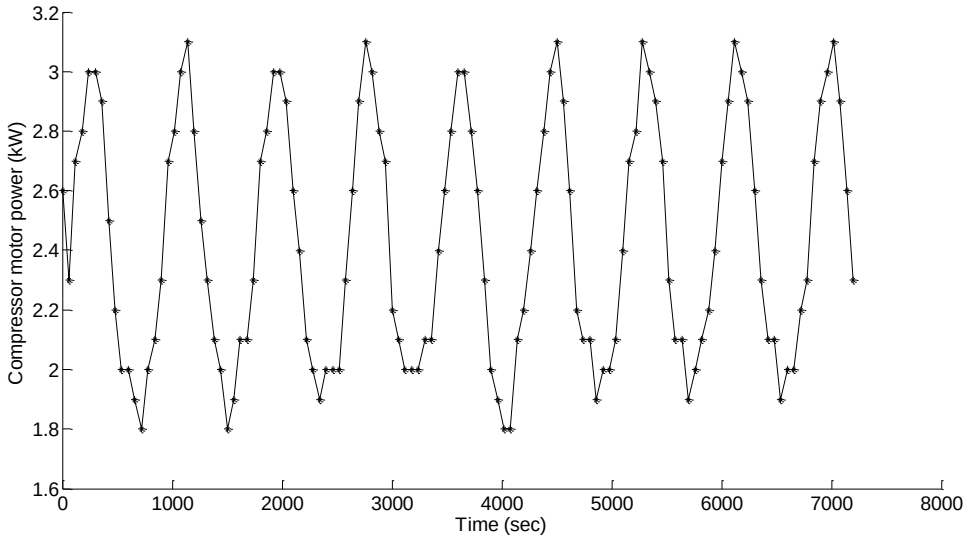

Figure 140: Corresponding compressor input power (kW) with respect to time (sec)

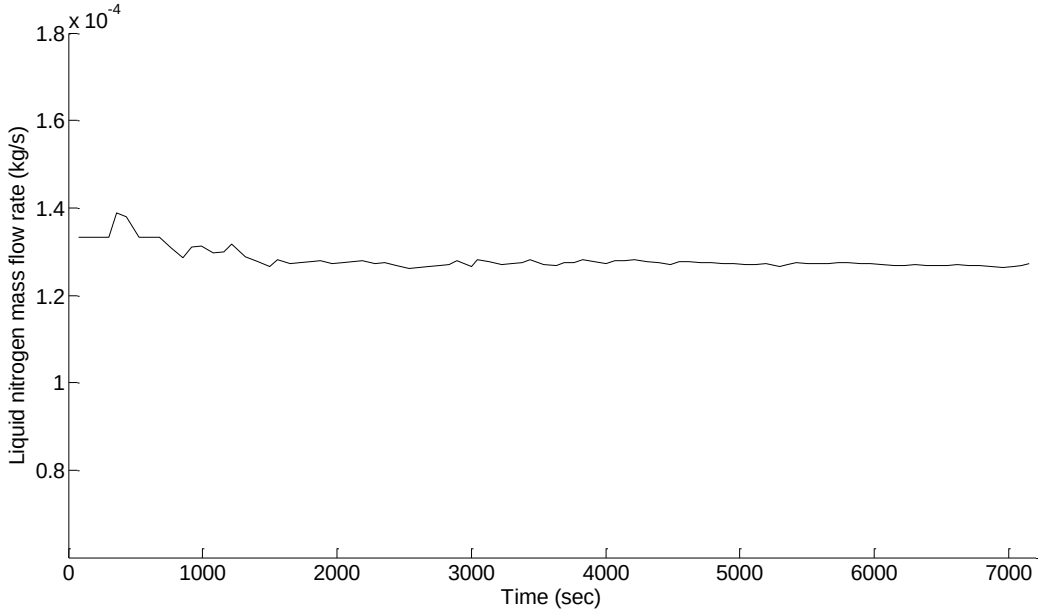

Figure 141: Liquid nitrogen mass flow rate (kg/s) with respect to time

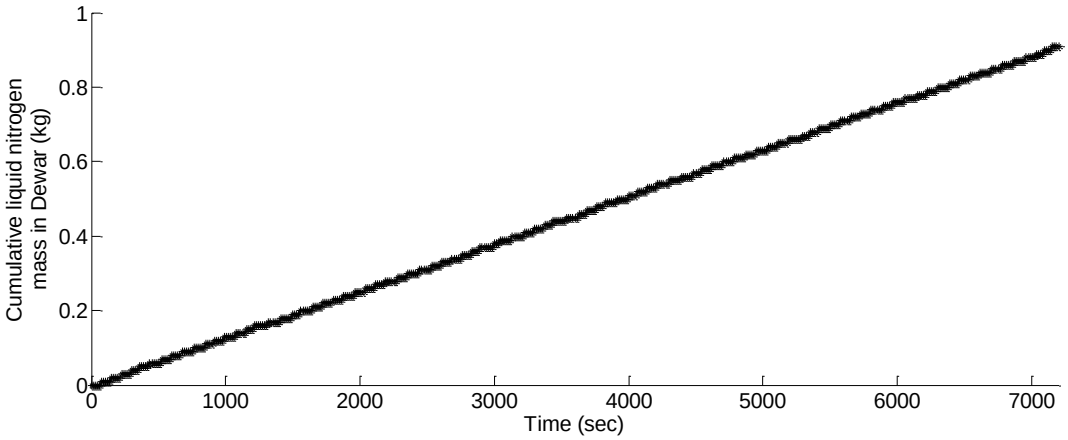

Figure 142: Cumulative liquid nitrogen collected in Dewar (kg) with respect to time

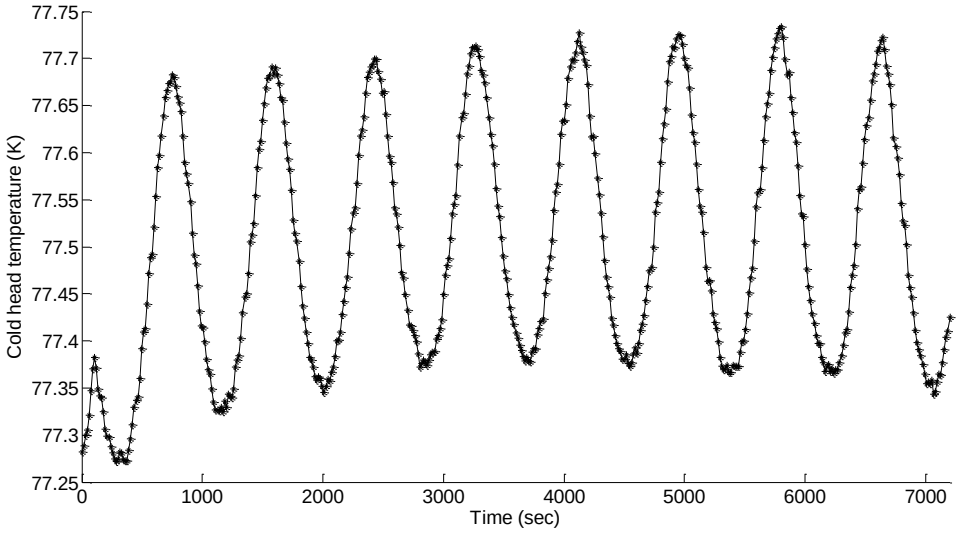

Figure 143: Cold head temperature (K) with respect to time

From the experiments, it was found that the compressor input power (kW), helium discharge temperature, suction and delivery helium pressures across compressor, motor oil temperature, motor current, cold head temperature, cooling water outlet temperature, all follow the sinusoidal trend as the compressor input frequency. However, the liquid nitrogen mass flow rate (kg/s) as shown in Figure 141 tends to follow a relatively constant line (for mass flow rate). The liquid nitrogen mass flow rate (kg/s) result obtained with the sinusoidal compressor

frequency input is very similar to that obtained with constant compressor frequency (60 Hz) input as presented in Section 8.3 (as shown in Figure 134). The average compressor input power was 2.4 kW, the average cold head temperature was 77.587 K and the average liquid nitrogen mass flow rate for this set of experiment was 0.00013 kg/s. Similarly, the average helium gas suction and discharge pressure were 262.6 kPaG, 1599.9 kPaG, the mean cooling water inlet and outlet temperature was 5.7 ^{0}C and 14.6 ^{0}C, the helium gas discharge temperature was 73.8 ^{0}C, the compressor motor oil temperature was 24.9 ^{0}C and the average motor current was 6 Amperes.

The similarity in the nature of the liquid nitrogen mass flow rate (kg/s) curve to that obtained from operating the compressor at 60 Hz may be due to the fact that there is accumulation of liquid nitrogen in Dewar vessel which increases with time. This liquid nitrogen inside the Dewar helps in cooling the incoming warm gaseous nitrogen faster. As a result, the nitrogen condensation process may attain a constant rate (higher or lower) irrespective of the frequency applied at the compressor motor or the input power consumed by the compressor.

8.3.4 Random variation of motor driving frequency

For this section, experiments were carried out on random frequency input at different time intervals: random time interval and 1 minute. The random set-point changes in the motor frequency were drawn from the range of 48 Hz and 75 Hz. For this set of experiments, the frequency was changed by manually entering the frequency (Hz) in the LabVIEW block diagram when the system was running continuously. The purpose of this experimental work was to test the transient system response.

This section presents the purpose, experimental method, obtained results, discussion and conclusions on the experimental work performed. The GM cryocooler system was operated

at an operating frequency of 60 Hz for ~2-3 hours to generate some liquid nitrogen in the Dewar vessel before starting this experiment. The parameters that were recorded using the data acquisition system were: the helium pressure at compressor inlet, helium pressure and temperature at compressor outlet, VFD power consumption, cooling water inlet and outlet temperature, cold head temperature and cumulative liquid nitrogen produced. The purpose of carrying out this test was to determine the system performance under randomly varying set of frequencies. The hypothesis set out for this experimental work was that although the compressor motor is operating at varying frequencies, liquid nitrogen is produced in a constant rate.

At first, the GM cryocooler was operated at normal operating frequency of 60 Hz until it started producing liquid nitrogen. The data collection for this phase was also started after that. The system was set to operate for 10 hours with input frequency as shown in Figure 95 (see Section 7.6.3.

The results from these experiments are presented in the graphs from Figure 144 to Figure 147. Data was recorded every 15 seconds. Detailed results for helium discharge temperature, helium suction and discharge pressures, motor oil temperature and cold head temperature are presented in Appendix J.

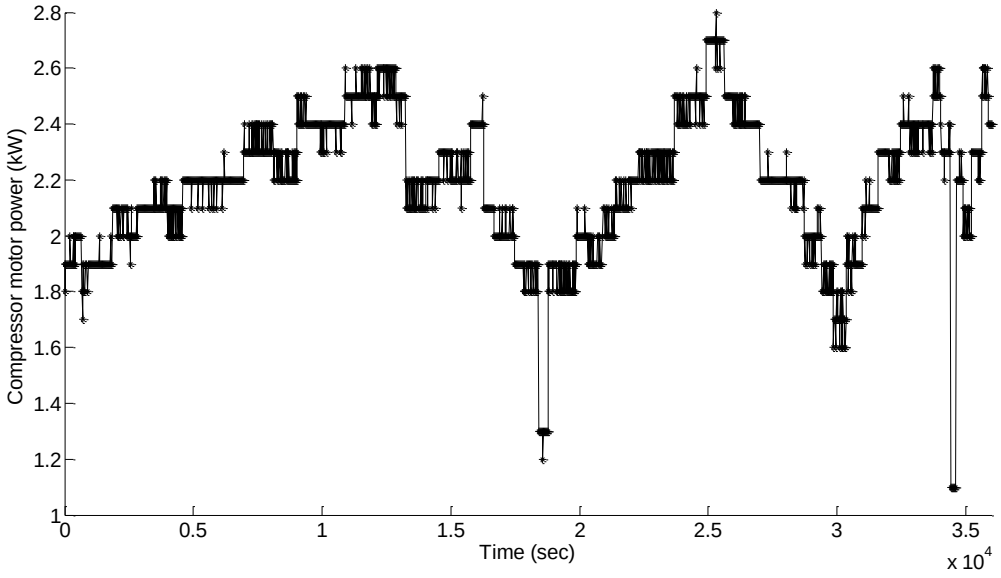

Figure 144: Power input to compressor (kW)

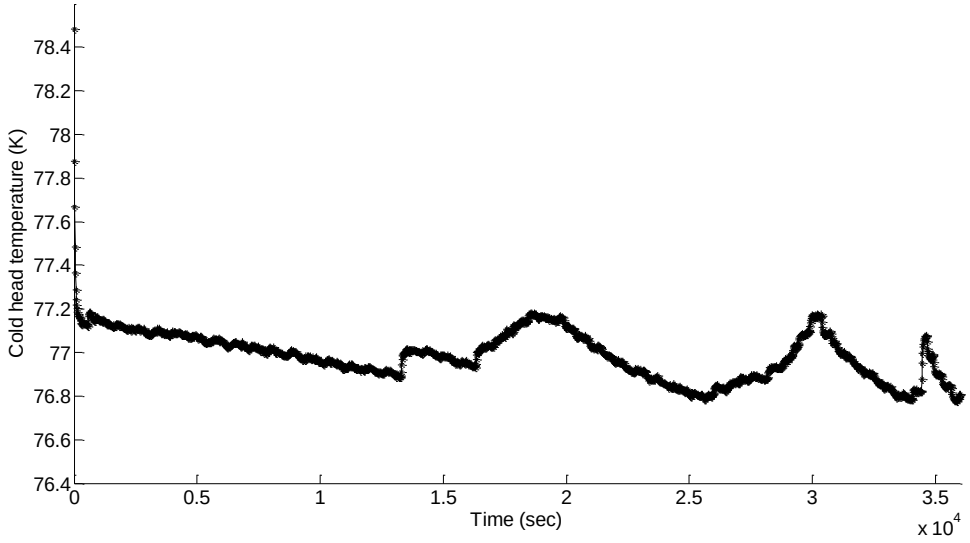

Figure 145: Cold head temperature (K)

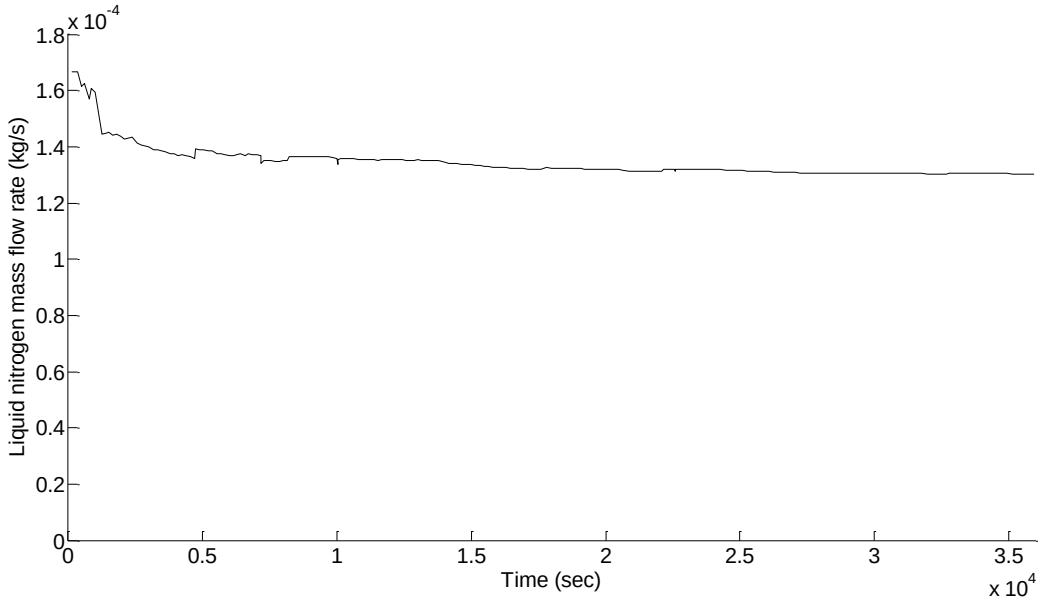

Figure 146: Liquid nitrogen mass flow rate (kg/s) with respect to time

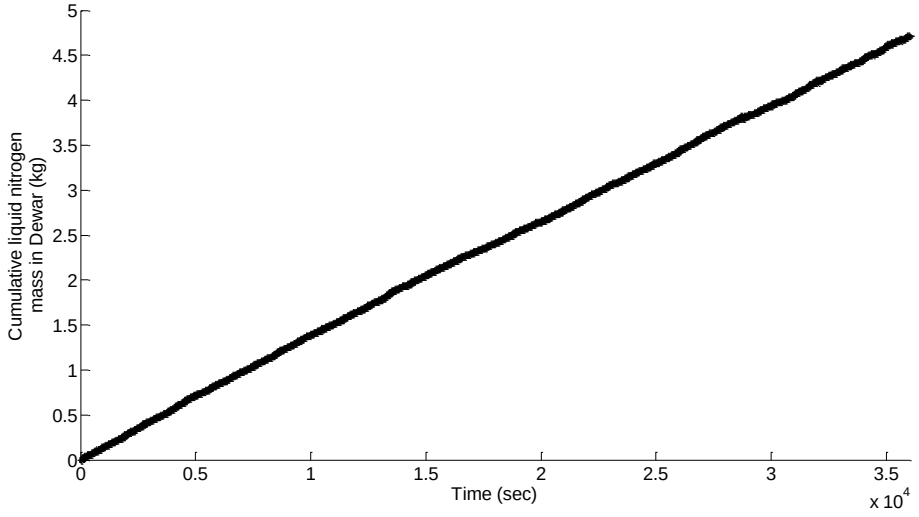

Figure 147: Cumulative liquid nitrogen mass flow rate (kg/s) with respect to time

The average compressor input power was 2200 W. The average cold head temperature was 77.037 K and the average liquid nitrogen produced for this set of experiment was 0.00013 kg/s. The average helium gas suction and discharge pressure was 272.8 kPaG and 1649.2 kPaG, the average helium discharge temperature was 70.8 ^{0}C, the average cooling inlet and

outlet temperatures were 13.9 ^{0}C and 17.8 ^{0}C , the average motor oil temperature was 27.1 ^{0}C. The average room temperature and pressure was 26.7 ^{0}C and 98.4 kPa respectively.

The results obtained from the experiments suggested that the liquid nitrogen mass flow rate (kg/s) tend to stabilize after certain time. This is because the Dewar vessel is highly insulated, therefore preserving and maintaining the temperature inside it for steady gaseous nitrogen condensation.

The next set of experiments was carried out for around 22 minutes in which the compressor driving frequency was changed randomly every minute. The set of random compressor input frequency (Hz) applied was as presented in Figure 100 in Section 7.6.3. The resulting compressor input power (kW) due to change in driving frequency is shown in Figure 148 and finally the liquid nitrogen mass flow rate (kg/s) with respect to time is presented in Figure 149.

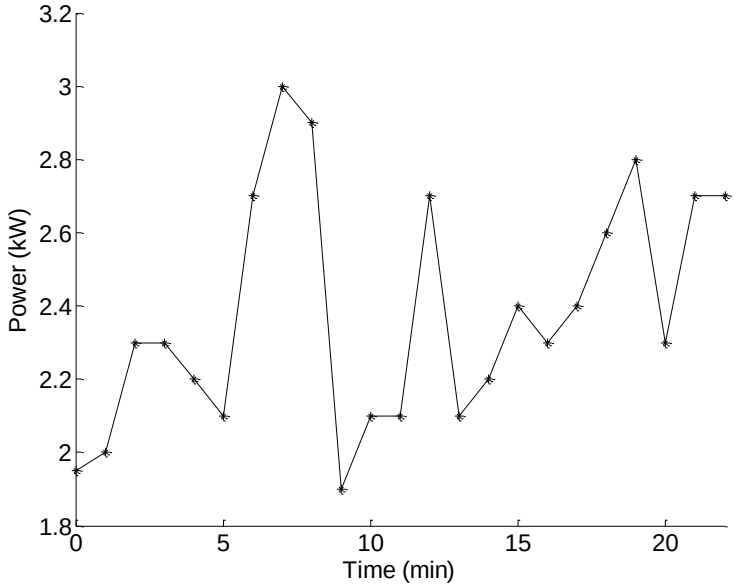

Figure 148: Compressor input power (kW)

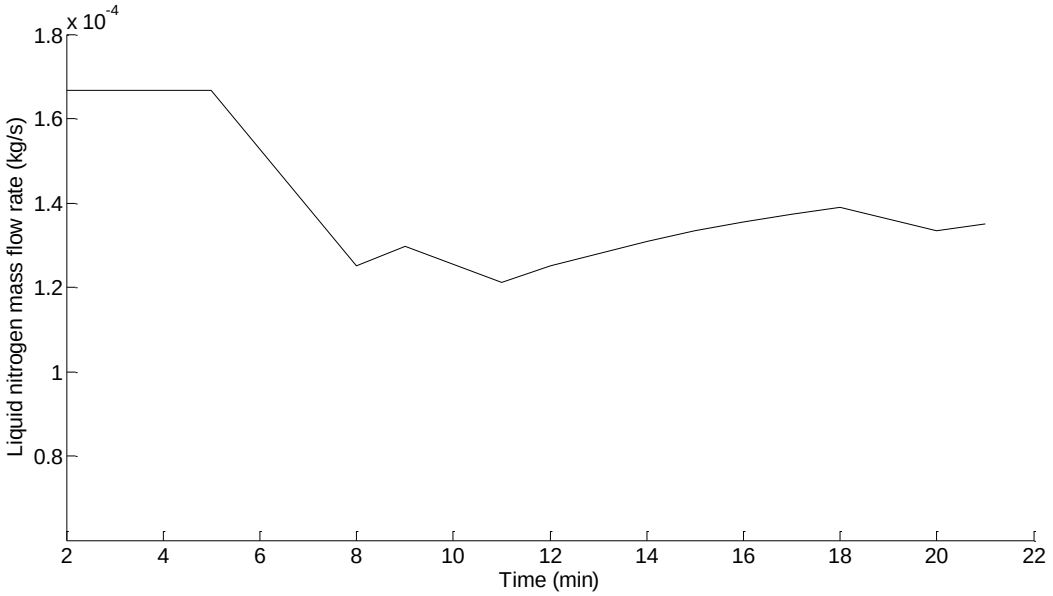

Figure 149: Liquid nitrogen mass flow rate (kg/s)

The experimental results obtained showed that the liquid nitrogen mass flow rate (kg/s) changes with the compressor driving frequency in the beginning of the experiments providing evidences for the unsteady data points in charts presented earlier such as in Figure 134, Figure 141, and Figure 146. However, after certain period of time the liquid nitrogen mass production rate attempts to stabilise due to the presence of thermal inertia inside Dewar as can be seen in the graphs mentioned earlier (Figure 134, Figure 141, and Figure 146). The average compressor input power for this set of experiment was 2400 W, the average cold head temperature was 77.330 K and the average liquid nitrogen mass flow rate was 0.00015 kg/s.

The average helium suction and discharge pressure was 278.4 kPaG and 1645.5 kPaG, the helium discharge temperature was 66.9 ^{0}C, cooling water inlet and outlet temperatures were 15.6 ^{0}C and 18.7 ^{0}C, average motor oil temperature was 27.2 ^{0}C, average motor current was 6 Amperes. The average room temperature and pressure was 25.6 ^{0}C and 100.5 kPa respectively.

The results indicate that the liquid nitrogen mass flow rate was higher in this case, however it should also be noted that the average power input consumed by compressor motor was also higher during this particular experiment which is due to the greater motor driving frequencies.

8.3.5 Wind speed time series scaled to motor driving frequency

In this section, experiments were carried out by using the set point changes of motor frequency drawn from the range from 48Hz to 75Hz scaled to mimic variable work input defined by wind speed data (m/s). The wind speed data used for this experiment are ten minute average data from Roskrow (13th Nov, 8:00 am to 6:00 pm) as shown in Figure 104 in Section 7.6.4.

This section presents the purpose, experimental method, obtained results, discussion and conclusions on the experimental work performed. The GM cryocooler system was operated at an operating frequency of 60 Hz for some hours before starting the experimentation. The parameters that were recorded using the data acquisition system were: the helium pressure at compressor inlet, helium pressure and temperature at compressor outlet, VFD power consumption, cooling water inlet and outlet temperature, cold head temperature and cumulative liquid nitrogen produced. The purpose of carrying out this test was to find out how the system would perform when the driving frequency represents the variability of wind speed. The hypothesis set out for this experimental work was that although the input compressor motor frequency is variable, the rate of liquid nitrogen produced will be fairly constant.

Ten minute average data were treated as 1 minute average while performing the experiment so the driving frequency was changed every minute. The wind speed data used and the corresponding compressor input frequency are same as were presented in Figure 104 and Figure 105 respectively (see Section 7.6.4). The compressor input power (kW) and the resulting

liquid nitrogen mass flow rate (kg/s) during the experiment period of 10 hours are shown in Figure 150 and Figure 151 respectively. Detailed results are presented in Appendix K.

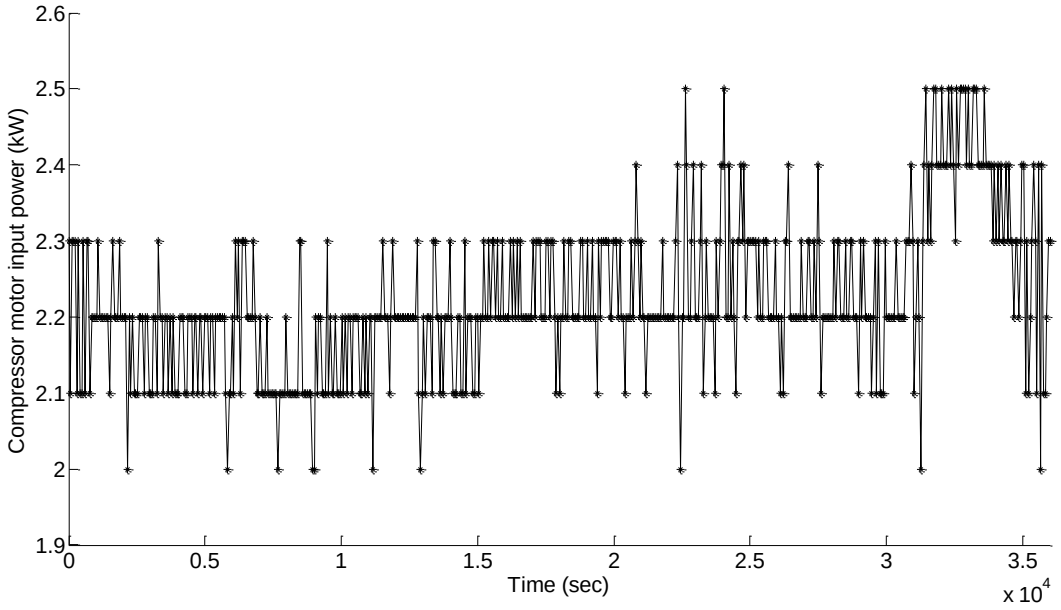

Figure 150: Compressor input power (kW) with respect to time (sec)

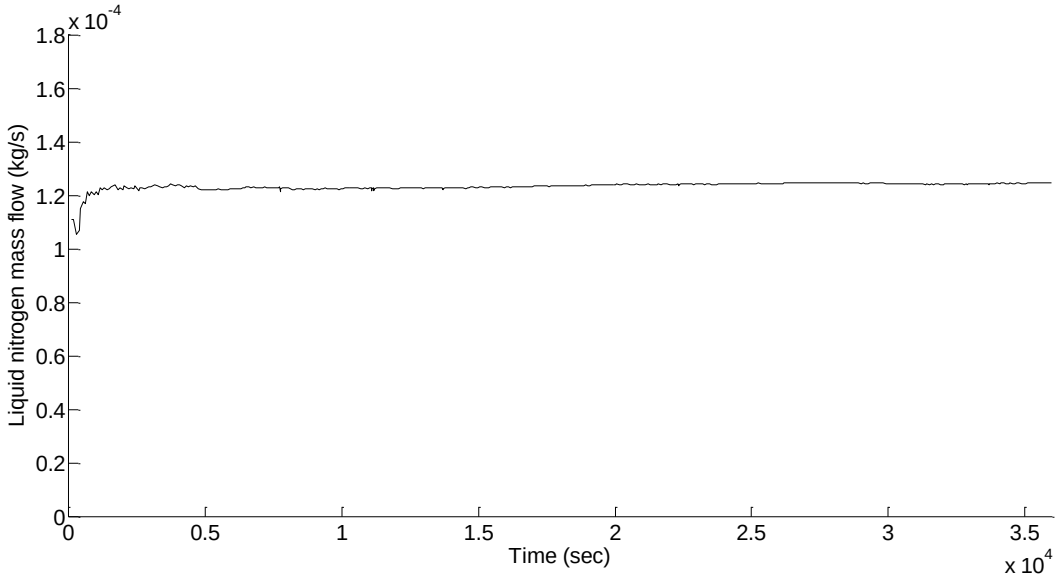

Figure 151: Liquid nitrogen mass flow rate (kg/s) with respect to time (sec)

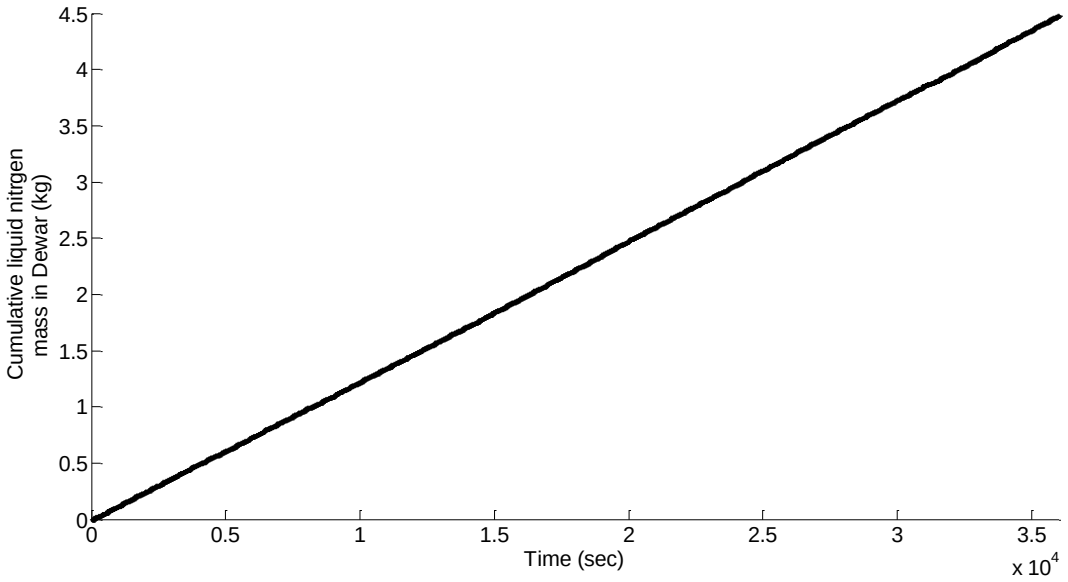

Figure 152: Cumulative liquid nitrogen mass in Dewar (kg)

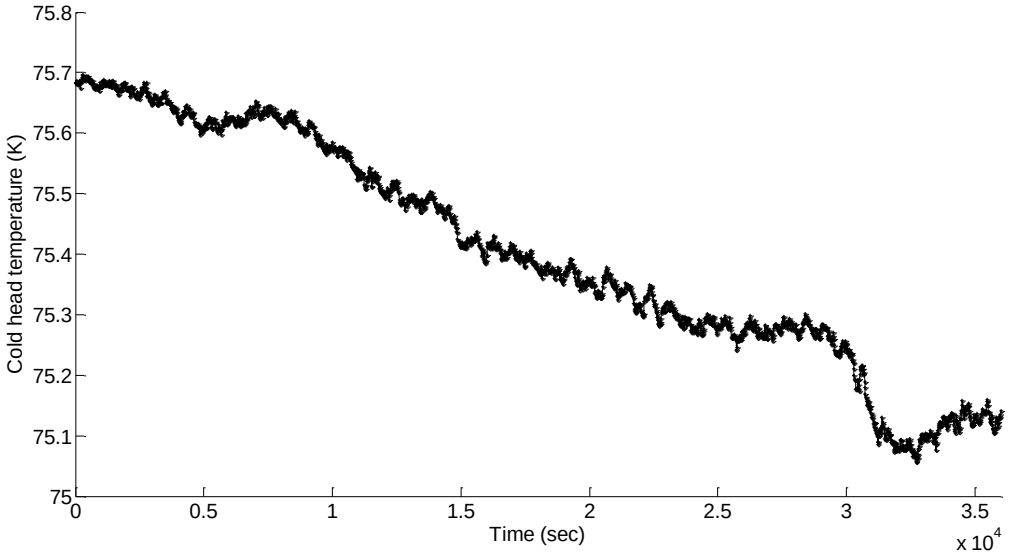

Figure 153: Cold head temperature (K) with respect to time (sec)

As can be seen from Figure 151 again that liquid nitrogen mass flow rate (kg/s) follows a constant mass flow rate procession without any effect of the random driving frequencies applied to the motor/compressor shaft. This is because of the thermal inertia of the cryogen production

processes. The constant liquid nitrogen production rate (kg/s) is demonstrated by various experimental results presented in this chapter.

8.4 Summary

This chapter presented the laboratory verification of the dynamic simulation of the GM cryocooler system that was presented in Chapter 7. For this, the experimental setup and equipment were introduced first, which was followed by the explanation on development of supervisory control and data acquisition system, and the chapter ended with the experimental programs that were performed in the laboratory under specified circumstances. The purpose of this chapter was to determine if the simulation model developed was in conformity with the experiments, and also to determine if the liquid nitrogen mass flow rate (kg/s) attained a steady trend even if the work input to drive the gas liquefaction system was varying. Therefore, experimental results at different settings of the compressor driving frequencies were required for the verification.

The experimental program was designed to test the major hypothesis of this thesis which was whether or not the cryogen production remains comparatively steady when the electric motor that drives the compressor is fed with variable work input. After completion of the commissioning checks, experimental works were performed. Initial tests included operating the GM cryocooler system at standard normal operating frequency of 60 Hz, which was then followed with experiments at other steady frequencies such as 50 Hz, 65 Hz, 70 Hz and 75 Hz. Then the system was fed with different sets of driving frequencies which included random frequency set points, sinusoidal varying set points, and set points following wind speed patterns. Each of the subsections in Section 8.3 presented each test carried out, method adopted, reduced results from raw results, discussion, conclusion and recommendations.

The experimental results obtained in each subsection are in good agreement to the simulation results earlier presented in Chapter 7. Acquired results from all the experiments also support one of our hypotheses that stated the rate of cryogen produced remains steady after an initial transient irrespective of the variable work input to the compressor. However, a detailed comparison and the range of statistics are presented in Chapter 9 that follows.

9 Comparison of simulation and experimental results

This chapter presents the comparison between the simulated results and the obtained experimental results from the laboratory. The results obtained from simulation of the GM cryocooler unit were presented in Chapter 7 and the experimental results were presented in Chapter 8. For the comparison purpose, the mean and standard deviation for all the results obtained are calculated. R squared values and standard error values are also estimated while comparing the simulated results with the experimental results.

9.1 Comparisons at different driving frequencies

The simulation and experiment were performed for 10 hours at different compressor driving frequencies. The data were recorded every 15 seconds. The average values from the results for each driving frequency were calculated for all the parameters presented. The comparison for compressor input work, cold head temperature and liquid nitrogen mass flow rate (kg/s) at different constant frequencies is shown in Figure 154 to Figure 156.

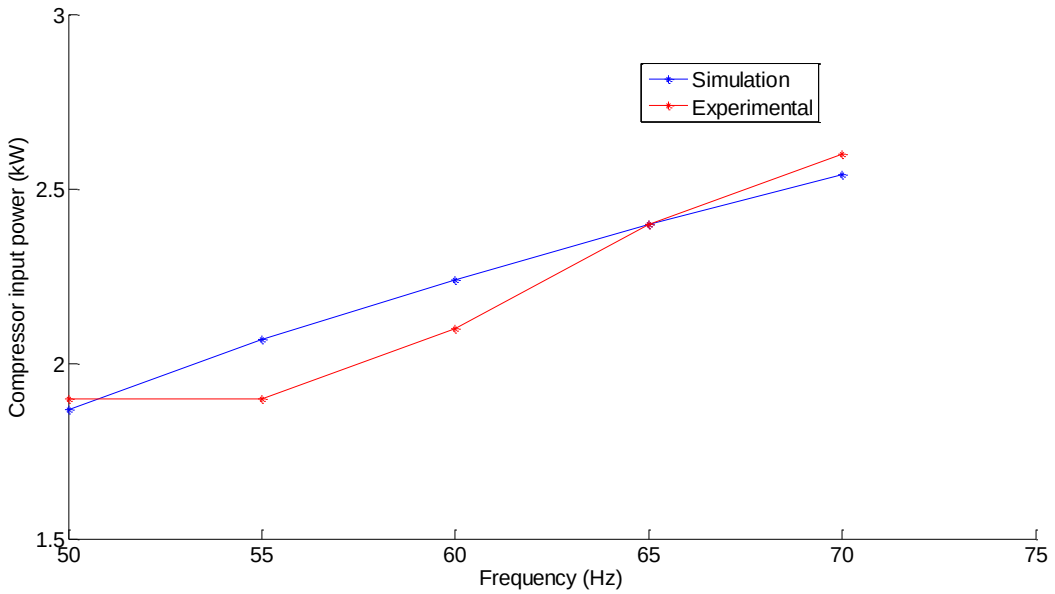

Figure 154: Average compressor input power (W) at different driving frequency (Hz)

The compressor input power corresponding to frequency input (Hz) to the compressor during simulation and experiment is presented in Figure 154. They have an R squared value of 0.90 and a standard error of 97.6. The correlation coefficient between the experimental and simulated datasets is 0.95. The difference between the compressor input power in the simulated and experimental result is due to the helium gas high and low pressures, which fluctuates even during steady state system operation. The model assumes a constant helium suction and discharge pressures for calculation of the input power required for the compressor which is not the case during experiments. The fluctuations in helium suction and discharge pressures (presented later in Figure G.3 and Figure G.4), can result due to the operating procedure of the suction and discharge valves in the helium compressor and also due to the open and close timing of the rotary valve in the cold head.

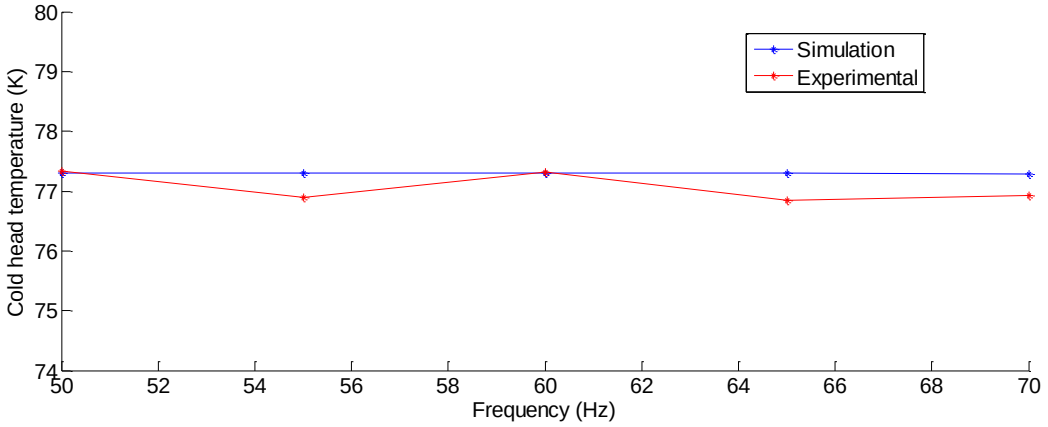

Figure 155: Cold head temperature (K) at various driving frequencies (Hz)

The cold head temperature predicted by the simulation and those obtained from the experiments while driving the compressor at various frequencies is presented in Figure 155. They have an R squared value of 0.33 and a standard error of 0.004. The correlation coefficient between the experimental and simulated datasets is 0.57. The cold head temperature (K) during experiments can have different values depending on several parameters that include the helium pressure when it expands in the expansion space within cold head, the density and mass of helium within that space (pressure and density are dependent on the compressor motor frequency setting), setting of the low pressure regulator on the Dewar vessel, the amount of liquid nitrogen inside Dewar vessel.

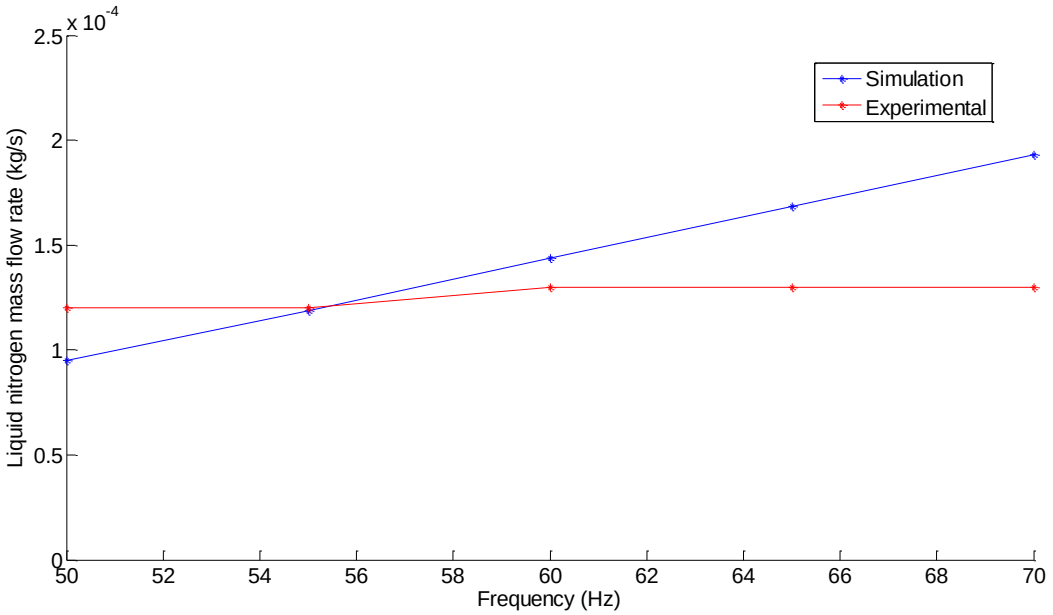

Figure 156: Average liquid nitrogen mass flow rate (kg/s) at various driving frequencies (Hz)

The liquid nitrogen mass flow rate (kg/s) obtained from the simulation and from experiments is presented in Figure 156. They have an R squared value of 0.88 and a standard error of 0.00003 respectively. The correlation coefficient between the experimental and simulated datasets is 0.87. These predictions are based on the model which assumes constant helium discharge pressure and density, which is not the case in the experiment. However, they have higher correlation coefficient and R squared values. The range of statistics for the simulation and experiments carried out at individual frequencies for 10 hours are presented in Table 19 and Table 20 respectively.

Table 19: Range of statistic for simulated results

Frequency (Hz)	Compressor power (W)		Cold head temperature (K)		Liquid nitrogen mass flow rate (kg/s)	
	Mean	Standard deviation	Mean	Standard deviation	Mean	Standard deviation
50	2167.61	4.77E-11	77.301	0.009	0.000095	2.64E-10
55	2384.37	2.59E-11	77.298	0.102	0.000119	2.86E-10
60	2601.13	4.91E-11	77.296	0.011	0.000144	3.03E-10
65	2817.90	1.17E-10	77.294	0.011	0.000168	3.17E-10
70	3034.66	7.96E-11	77.292	0.012	0.000193	3.29E-10
75	3251.42	7.37E-11	77.289	0.012	0.000218	3.38E-10

Table 20: Range of statistics for experimental results

Frequency (Hz)	Compressor power (W)		Cold head temperature (K)		Liquid nitrogen mass flow rate (kg/s)	
	Mean	Standard deviation	Mean	Standard deviation	Mean	Standard deviation
50	1900	0.2	77.344	0.280	0.00012	0.000000
55	1900	0.2	76.890	0.473	0.00012	0.000002
60	2100	0.1	77.307	0.197	0.00013	0.000001
65	2400	0.0	76.843	0.208	0.00013	0.000003
70	2600	0.0	76.927	0.221	0.00013	0.000001
75*	2900	0.1	77.230	0.038	0.00015	0.000017

Note. 75*: One set of complete 10 hour data on this frequency. Standard deviation for parameters at this frequency=Deviation from mean values within 10 hour duration.

9.2 Comparisons at sinusoidal varying frequencies

For the set of sinusoidal varying compressor driving frequencies, the simulation and experiment were performed for 2 hours. The data were recorded every 15 seconds. The sinusoidal input frequency to the compressor motor was presented in Figure 91, Section 7.6.2. The comparison for compressor input work, cold head temperature and liquid nitrogen mass flow rate (kg/s) are presented in Figure 157 to Figure 159.

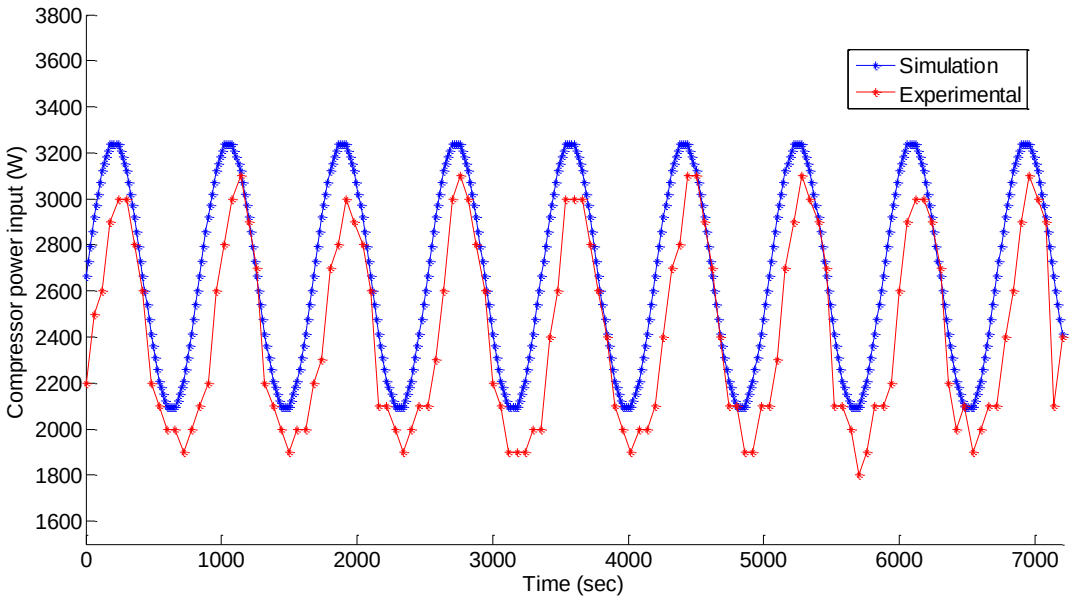

Figure 157: Compressor input power (W)

The compressor input power corresponding to sinusoidal frequency input (Hz) to the compressor during simulation and experiment is presented in Figure 157. Two datasets have an R squared value of 0.88 and a standard error of 139.92. The mean value for compressor input work for the simulation was 2686.57 W with a standard deviation of 402.2 W. Similarly, for the experimental result, the mean compressor input work was 2400 W with a standard deviation of 410 W. The correlation coefficient between two datasets is 0.75. The simulated and experimental results for the compressor input power resemble each other very well with a correlation coefficient of 0.75 and an R squared value of 0.88. The reason for the differences in them is similar to that mentioned in Section 9.1.

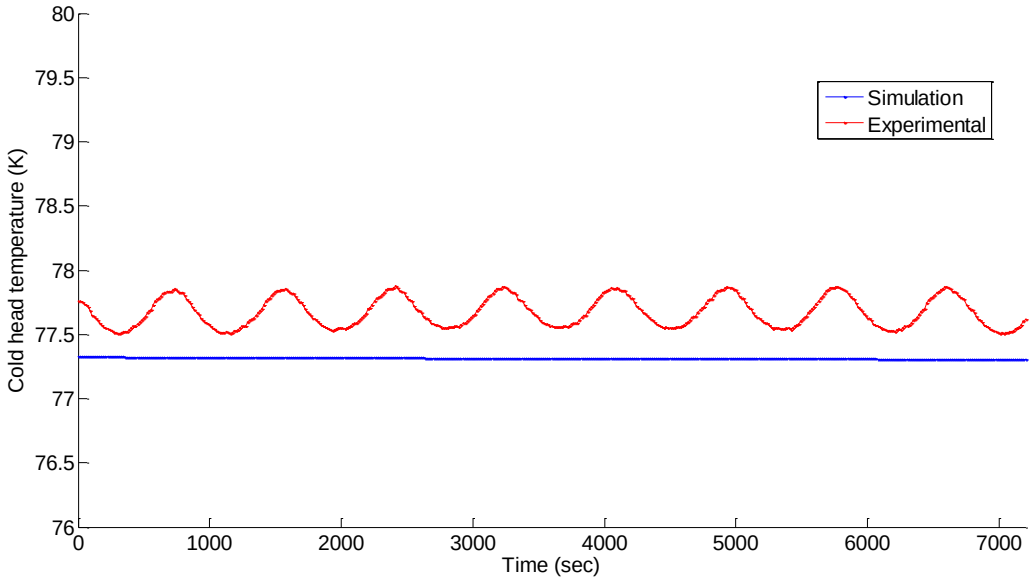

Figure 158: Cold head temperature (K)

Similarly, the cold head temperature (K) corresponding to the sinusoidal frequency input (Hz) to the compressor obtained from simulation and from experiment is presented in Figure 158. They have an R squared value of 0.001 and a standard error of 0.005. The mean cold head temperature for the simulation was 77.314 K with a standard deviation of 0.005 K. The mean cold head temperature for the experimental results was 77.674 K with a standard deviation of 0.116 K respectively. The correlation coefficient between the simulated data and experimental data was -0.038. The results showed that they have very low R squared value and a negative correlation coefficient value. The reason for the differences in two curves has been presented in Section 9.1. Although the two curves do not match each other very well, they have lower deviations from their own mean values. The cold head temperatures can vary depending on the various parameters as discussed earlier but this change in temperature makes no difference as long as it is within the range (of temperature and pressure) in which liquid nitrogen remains in liquid phase.

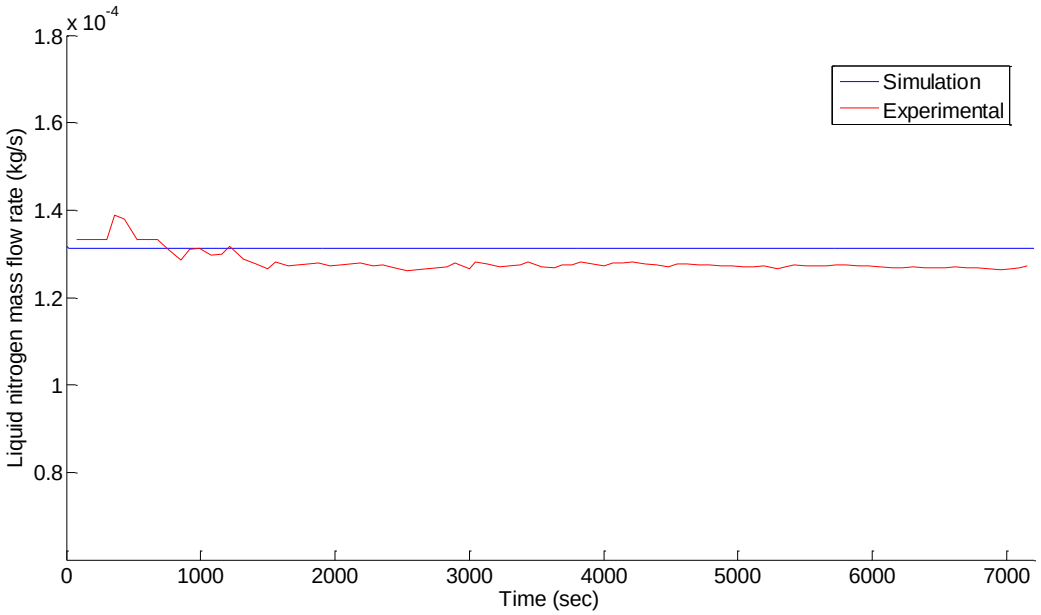

Figure 159: Liquid nitrogen mass flow rate (kg/s)

Finally, the liquid nitrogen mass flow rate (kg/s) obtained from the simulation and experiment is presented in Figure 159, which has a R squared value of 2E-15 and a standard error of 2.4E-06. The simulated average liquid nitrogen mass flow rate was 0.00013 kg/s with a standard deviation of 2.9E-08 kg/s and the experimental average liquid nitrogen mass flow rate was 0.00013 kg/s with a standard deviation of 2.4E-06 kg/s. The correlation coefficient for the liquid nitrogen mass flow rate (kg/s) for the simulated and experimental data was 7.6E-15. As seen from the figure and the statistical values, the average liquid nitrogen mass flow rate values for both the simulated and experimental results are the same, despite the lower R-squared and correlation coefficient values.

9.3 Comparisons at random varying frequencies

Random set points of frequencies were used as input driving frequencies for 10 hours, changing the motor frequency randomly, as was presented in Sections 7.6.3 and 8.3.4. The comparison

for compressor input work, cold head temperature and liquid nitrogen mass flow rate (kg/s) are presented in Figure 160 to Figure 162.

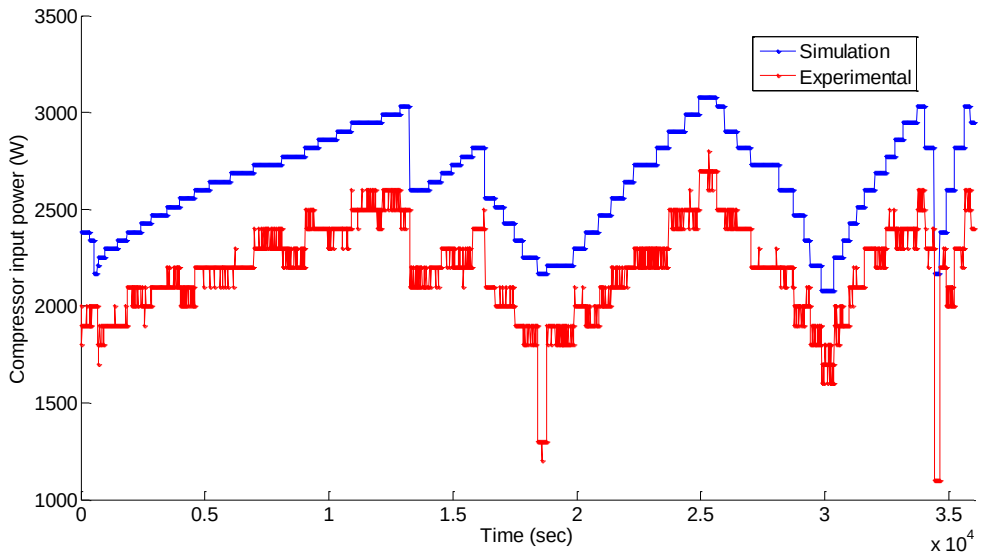

Figure 160: Compressor input power (W)

The compressor input power corresponding to random frequency input (Hz) to the compressor during simulation and experiment is presented in Figure 160. They have an R squared value of 0.83 and a standard error of 103.20. The simulated average compressor input power was 2636.88 W with a standard deviation of 251.604 W and the experimental average compressor input power was 2200 W with a standard deviation of 253 W. The correlation coefficient between the simulation and experimental data was 0.91.

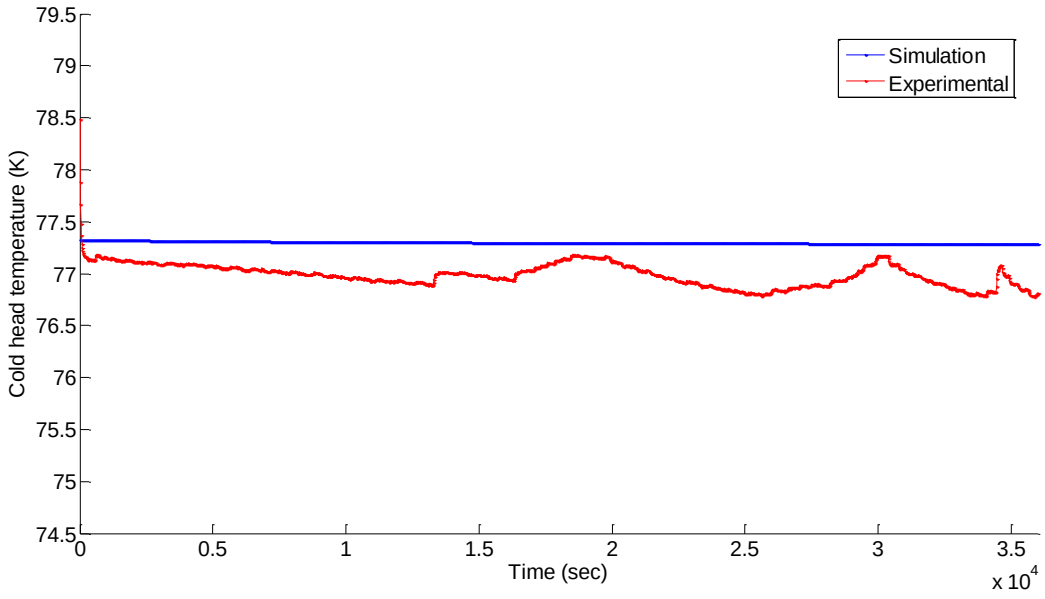

Figure 161: Cold head temperature (K)

Similarly, the cold head temperature (K) corresponding to the random frequency input (Hz) to the compressor obtained from simulation and from experiment is presented in Figure 161. It has a R squared value of 0.32 and a standard error of 0.009. The simulated average cold head temperature was 77.300 K with a standard deviation of 0.0105 K and the experimental average cold head temperature was 76.990 K with a standard deviation of 0.112 K. The correlation coefficient between the simulated and experimental data for cold head temperature was 0.57. Although the simulated and experimental results have lower to moderate R-squared and correlation coefficient values, the deviation from the mean and the standard error are less.

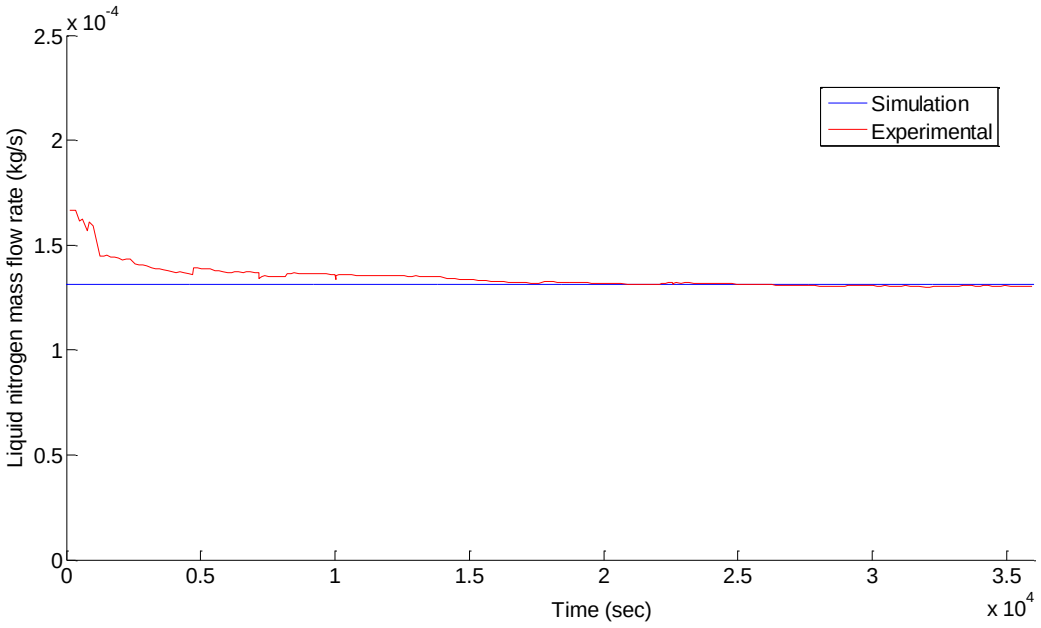

Figure 162: Liquid nitrogen mass flow rate (kg/s)

Finally, the liquid nitrogen mass flow rate (kg/s) obtained from the simulation and experiment is presented in Figure 159 which has an R squared value of -3.6E-16 and a standard error of 6.2E-06. The simulated average liquid nitrogen mass flow rate was 0.00013 kg/s with a standard deviation of 2.9E-10 kg/s and the experimental average liquid nitrogen mass flow rate was 0.00014 kg/s with a standard deviation of 6.2E-6 kg/s. The correlation coefficient between the simulated and experimental data for cold head temperature was 9.6E-15. These values suggest that the simulation and experimental results are not similar. The start-up liquid nitrogen mass flow rate could not be predicted well in the simulation, although there is very less difference in the predicted and experimental average liquid nitrogen mass flow rate values.

Second set of simulation and experiment were performed at varying frequency set points where the frequency was changed every minute. The compressor motor input frequency is presented in Section 7.6.3 and the corresponding results for compressor input power, the cold

head temperature and the liquid nitrogen mass flow rates for both cases are presented in Figure 163 to Figure 165 for comparison.

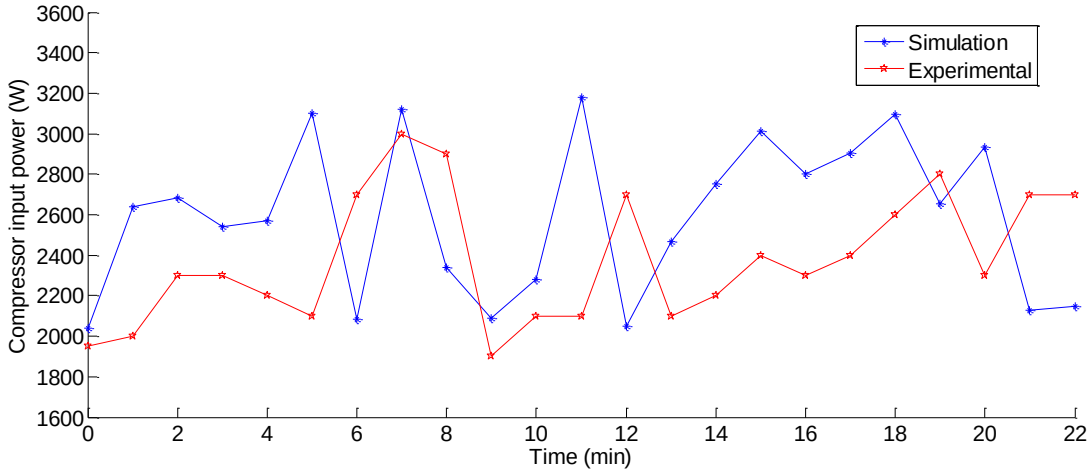

Figure 163: Compressor input power (W)

The compressor input power corresponding to random frequency input (Hz) to the compressor during simulation and experiment is presented in Figure 163. They have an R squared value of 0.0007 and a standard error of 397.0. The simulated average compressor input power was 2592.37 W with a standard deviation of 388.03 W and the average experimental compressor input work was 2400 W with a standard deviation of 320.1 W. The correlation coefficient of the two datasets was -0.0274.

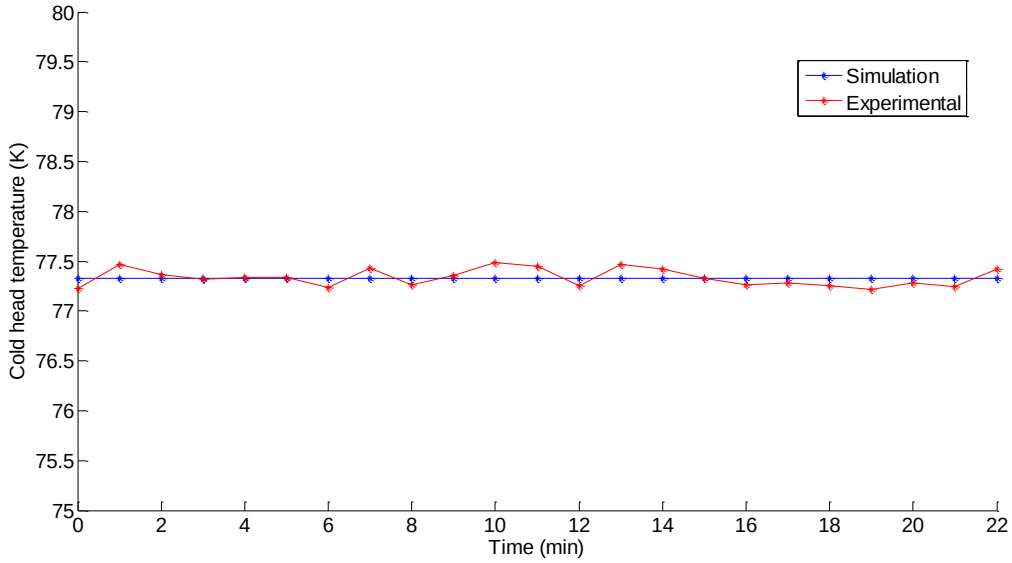

Figure 164: Cold head temperature (K)

Similarly, the cold head temperature (K) corresponding to the random frequency input (Hz) to the compressor obtained from simulation and from experiment is presented in Figure 164. They have an R squared value of 0.033 and a standard error of 0.0005. The simulated average cold head temperature was 77.320 K with a standard deviation of 0.0005 K and the average experimental cold head temperature was 77.330 K with a standard deviation of 0.09 K. The correlation coefficient of the two datasets was 0.18. The average cold head temperature for the simulation and experimental results resemble very well.

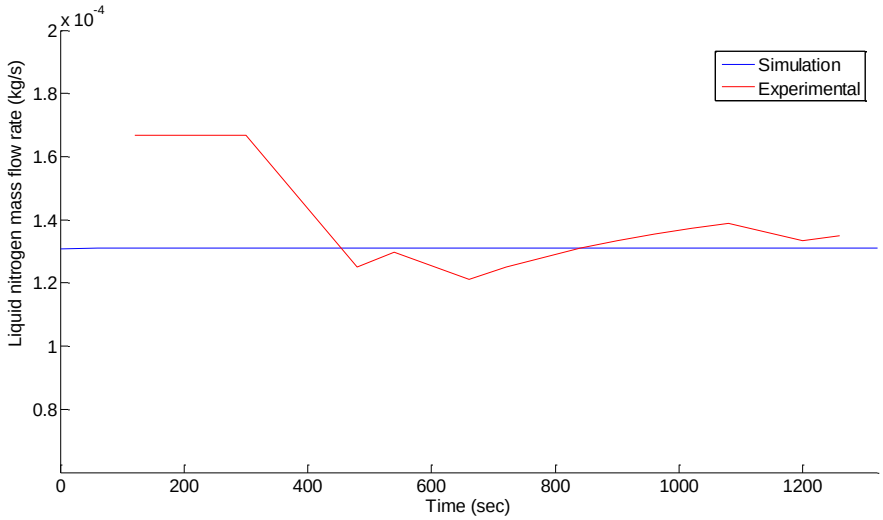

Figure 165: Liquid nitrogen mass flow rate (kg/s)

Finally, the liquid nitrogen mass flow rate (kg/s) obtained from the simulation and experiment is presented in Figure 165, which has an R squared value of 0 and a standard error of 5.8E-08. The simulated average liquid nitrogen mass flow rate was 0.00013 kg/s with a standard deviation of 7.6E-08 kg/s and the average experimental liquid nitrogen mass flow rate was 0.00015 kg/s with a standard deviation of 3.6E-05 kg/s. The correlation coefficient of the two datasets was -0.43. As seen in Figure 165, the experimental mass flow rate starts only after 120 seconds, and the flow rate before that time period was 0. However, this is not the case in simulation and liquid nitrogen is produced since the commencing of experiment.

9.4 Comparisons for motor frequency corresponding to wind speeds

The compressor driving input frequency for this test scenario comprised of motor driving frequencies correspond to the wind speed as explained earlier in Section 7.6.4 and Section 8.3.5. The comparison results are presented in Figure 166 to Figure 168.

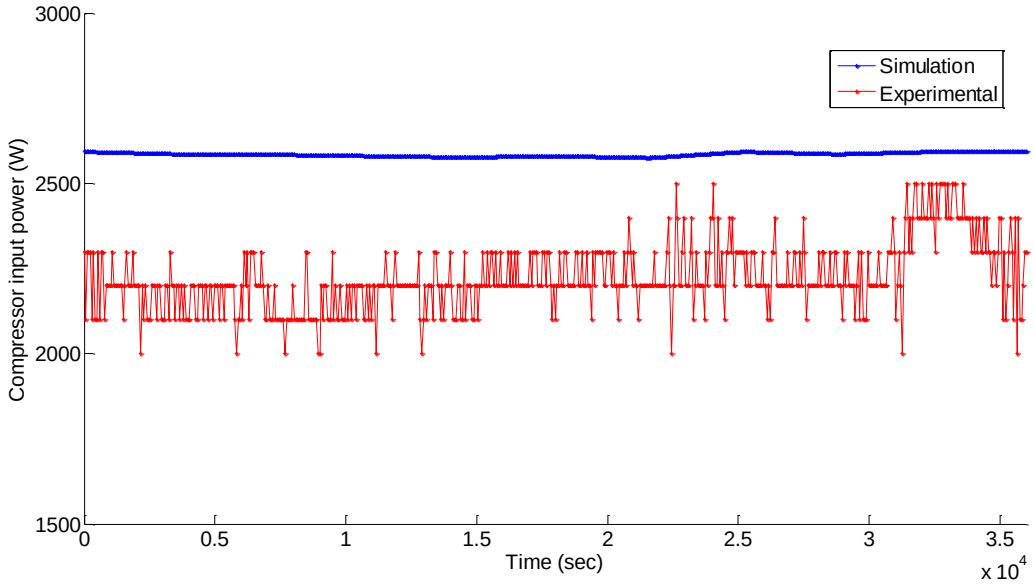

Figure 166: Compressor input power (W)

The compressor input power during simulation and experiment is presented in Figure 166. They have an R squared value of 0.10 and a standard error of 5.24. The simulated average compressor input power was 2585.71 W with a standard deviation of 5.52 and the average experimental compressor input power was 2200 W with a standard deviation of 100.0 W. The correlation coefficient between the simulated and experimental data is 0.62.

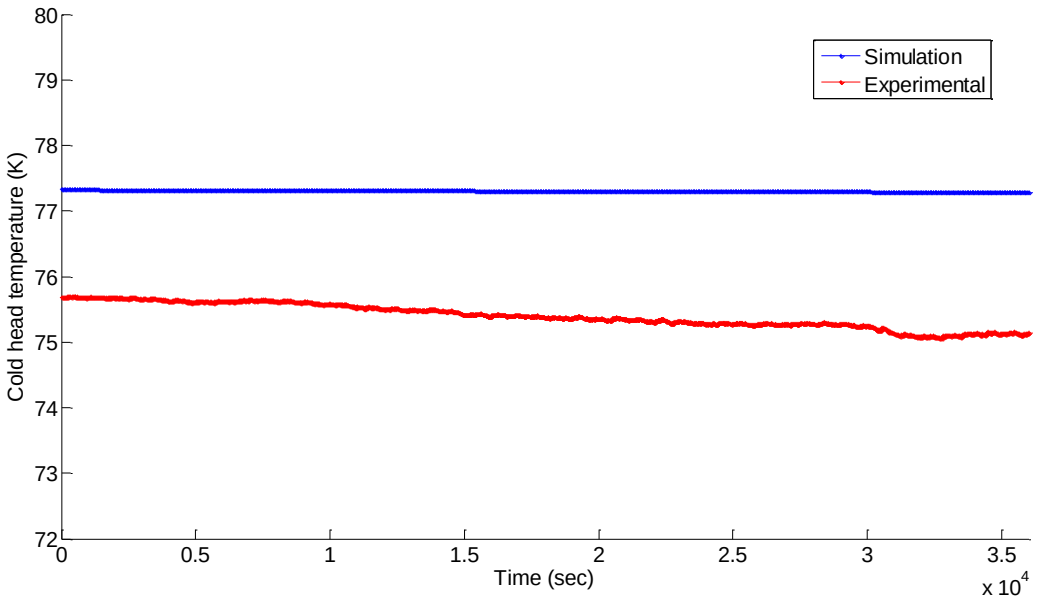

Figure 167: Cold head temperature (K) for simulated and experimental work

Similarly, the cold head temperature (K) corresponding to the frequency input (Hz) to the compressor obtained from simulation and from experiment is presented in Figure 167. They have a R squared value of 0.97 and a standard error of 0.002. The simulated average cold head temperature was 77.310 K with a standard deviation of 0.011 K and the average experimental cold head temperature was 75.400 K with a standard deviation of 0.185 K. The correlation coefficient between two datasets is 0.98.

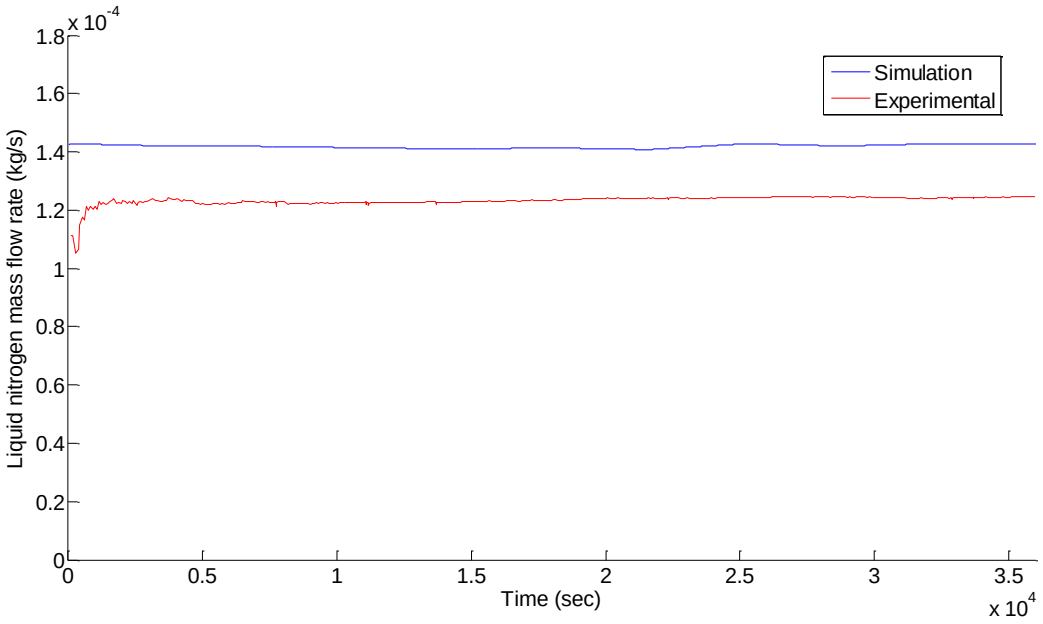

Figure 168: Liquid nitrogen mass flow rate (kg/s)

Finally, the liquid nitrogen mass flow rate (kg/s) obtained from the simulation and experiment is presented in Figure 168, which has an R squared value of 1.0E-05 and a standard error of 1.7E-06. The simulated average liquid nitrogen mass flow rate of 0.00013 kg/s with a standard deviation of 1.5E-08 and the average experimental liquid nitrogen mass flow rate were 0.00012 kg/s with a standard deviation of 1.8E-06 kg/s. The correlation coefficient between two datasets is -0.003.

9.5 Summary

A detailed comparison between the experimental and the simulation results has been presented in this chapter. The simulation results are in good agreement with the experimental results. The simulation was able to predict the average parameter values very well. The observed differences in the simulated and experimental results in some cases may be due to the presence of thermal stratification inside the Dewar vessel as shown in Figure 169, which

could not be predicted by model in absence of temperature measurements along the height of inner vessel of Dewar, helium discharge temperature (aftercooled), helium return temperature, and corresponding helium enthalpy values at different temperature and pressure. Thermal stratification causes reduction in liquid nitrogen production because of the simultaneous evaporation and condensation processes.

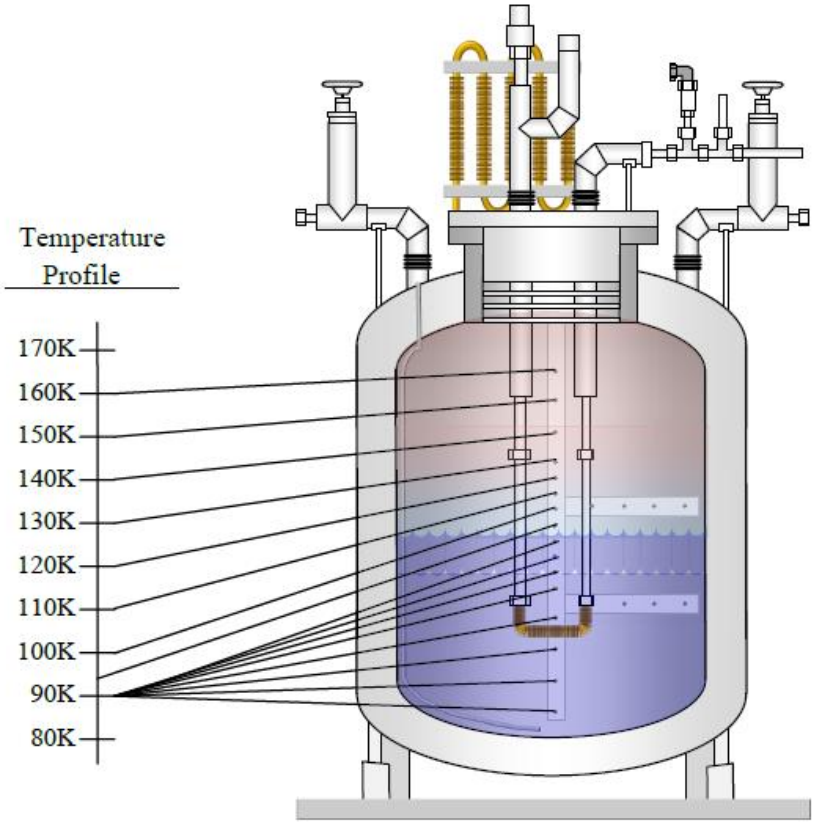

Figure 169: Dewar vessel showing thermal stratification, taken from (Partridge, 2010)

Also, the helium high and low pressure fluctuations (that resulted in cold head temperature fluctuations) may be other reasons which resulted in simulation and experimental results differences. This could not be incorporated in the model presented in this thesis. Similar type of circumstances have also been discussed by various authors including Notardonato (2006) and Partridge (2010) in detail. From the results presented, it has also been observed that

the cryocooler system produced more liquid nitrogen when driven at higher motor frequencies, in both the simulation and experiments. However, the system also consumes more input power while operating at those frequencies, resulting in higher motor temperatures, which is not desirable for the system.

10 Extended simulations of a 5MW wind energy driven liquid nitrogen production system

This chapter comprises of sets of simulations performed to test the system performance for a wind-energy driven liquid nitrogen production system model that is built in MATLAB/Simulink. The first model developed provides input power to the laboratory scale GM cryocooler and the second model provides input power to a large scale liquid nitrogen production system. The wind turbine rotor selected for the first case is a 6 kW variable speed HAWT and for the second case is a 5 MW variable speed HAWT. The parameters for the model are listed in the corresponding sections that follow. MATLAB script and Simulink model are presented in Appendix F. Most of the parameters for the 5 MW hydraulic wind turbine system are taken from Rajabhandharaks (2014).

10.1 Simulation with steady wind speeds

This section includes simulations carried out considering steady wind speeds. The wind rotor is selected such that it can provide sufficient power to drive the laboratory scale GM cryocooler unit which consumes a total of ~3.7 kW (helium compressor ~2 kW and an air compressor which consumes ~1.7 kW) of power. The wind rotor selected has a rated power of 6 kW. For the simulation work that has been performed, helium compressor is directly coupled to the hydraulic motor. The wind rotor is coupled with a hydrostatic transmission system which in turn is coupled with a helium compressor as mentioned in earlier sections, and as shown in Figure 170. This system can have a single hydraulic motor as shown in Figure 170, and/or it can have 2 motors within the hydraulic circuit as was presented in Section 6.7 (and shown in Figure 61). A single

hydraulic motor is presented in Figure 170 for simplicity but 2 hydraulic motors as discussed in Section 6.7 have been used during simulation. The parameters for the wind turbine rotor, hydrostatic transmission system and helium compressor are same as presented earlier in Section 7.1.

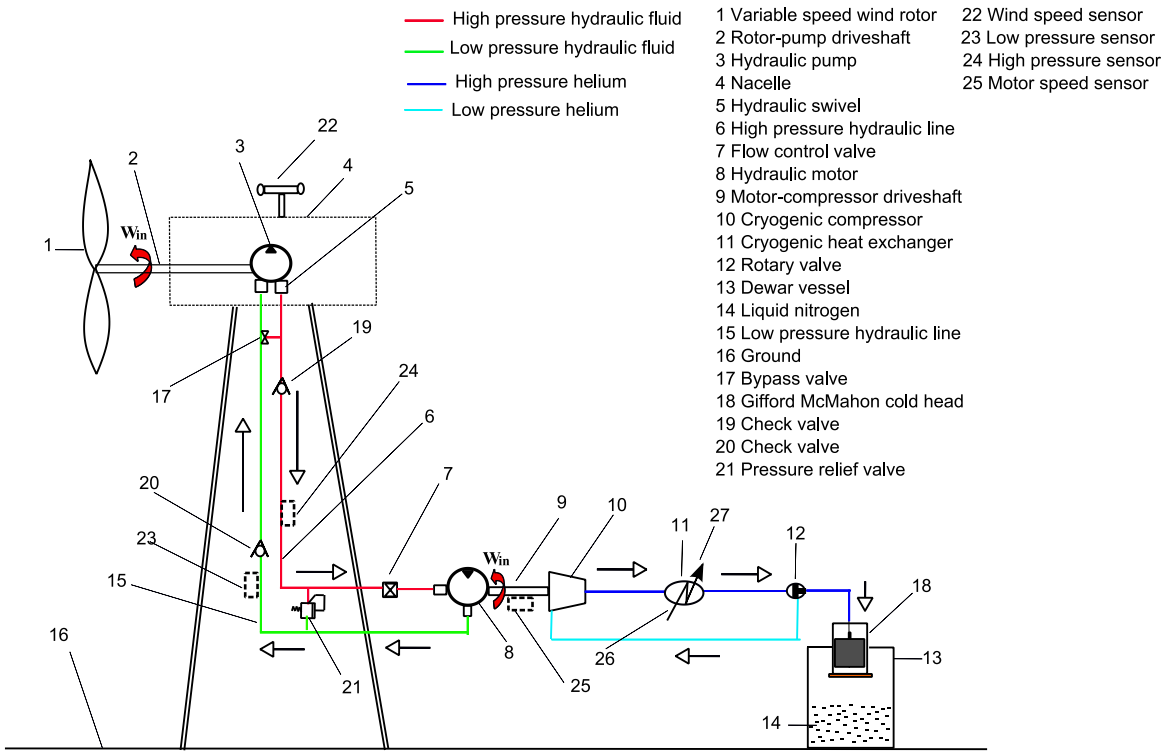

Figure 170: CryoVent schematic showing a wind energy driven GM cryocooler system for production of liquid nitrogen

The system is provided with constant wind speeds of 4m/s, 6m/s, 10m/s, 13m/s and 25 m/s for a total period of 10 minutes each. The average power from the wind, the wind turbine rotor power, power available to the hydraulic motor and the average liquid nitrogen produced during the simulation time period are reported in Figure 171, Figure 172, and Figure 173 respectively.

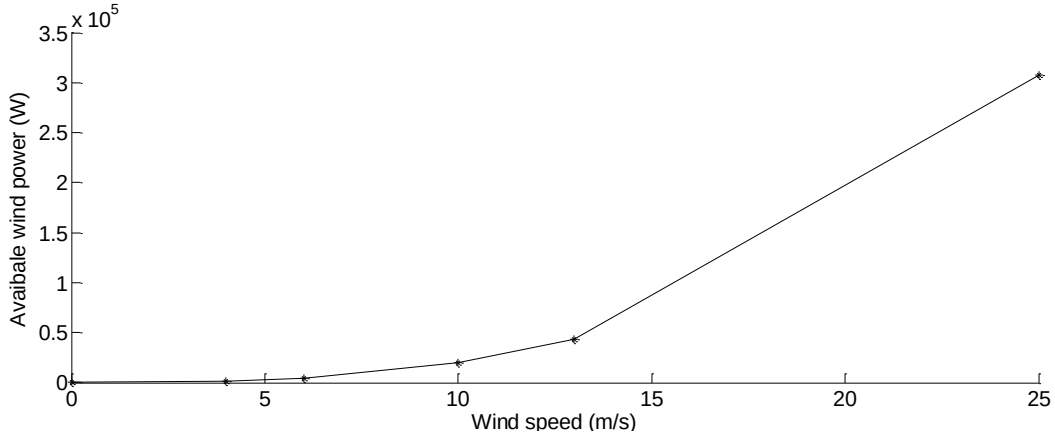

Figure 171: Average available power in wind (W) at different wind speeds (m/s)

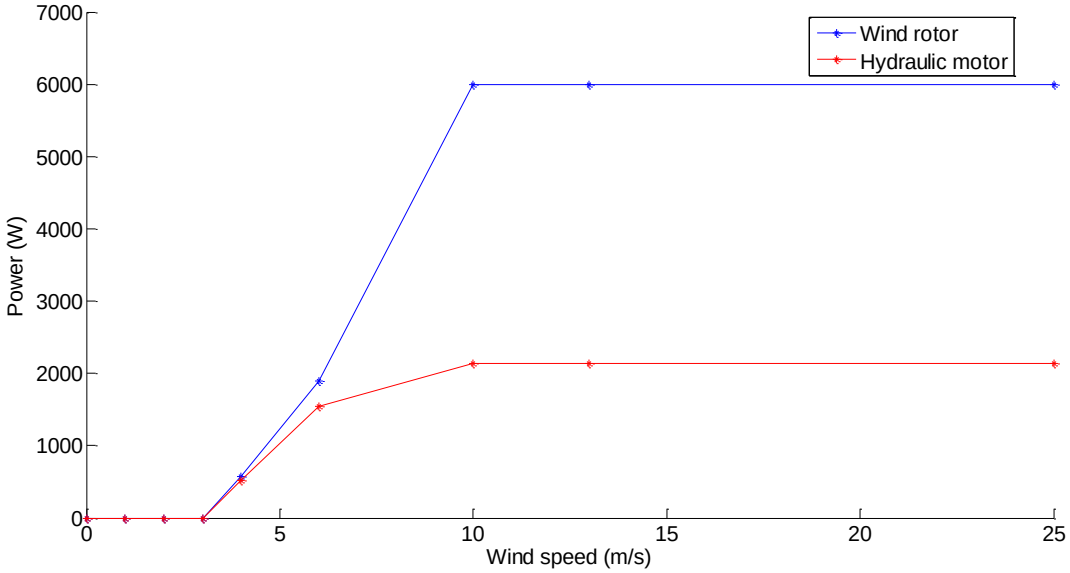

Figure 172: Average wind turbine power (W) and average hydraulic motor power (W) at different wind speeds (m/s)

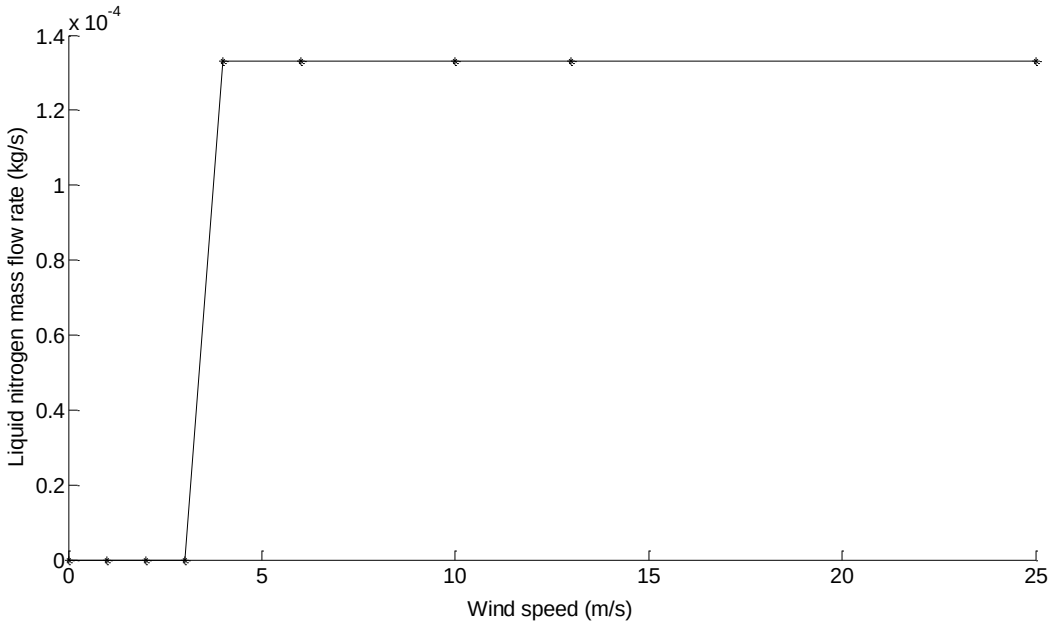

Figure 173: Average liquid nitrogen mass flow rate (kg/s) at different wind speeds (m/s)

The available power in wind (W) increases with wind speed (m/s) as shown in Figure 172. On the other hand, when the wind speed keeps on increasing and reaches a value greater than 25 m/s, the wind turbine shuts down for safety and no power is delivered from the wind turbine rotor to the hydraulic pump as shown in Figure 172. During such situations, the hydrostatic transmission and the gas liquefaction system should still be able to operate as long as there is some energy stored in the hydraulic accumulator. The liquid nitrogen produced for all the other wind speeds are nearly constant at 0.00013 kg/s as can be seen in Figure 173.

10.2 Simulation with actual wind speed time series from SWMTF 4Hz data

A series of consecutive 10 minute simulations was performed using the 4Hz wind speed data from SWMTF, Exeter, UK as input to the model. The wind turbine rotor considered is same as that in Section 10.1 that can power the laboratory GM cryocooler unit. Three different series of consecutive 10 minute wind speed data were considered as presented in Figure 174. These

particular wind speed time series from the available 4Hz data were selected because these represent the high wind condition, medium wind speed condition and low wind speed condition respectively that are ideal to supply to the model for determining the system performance.

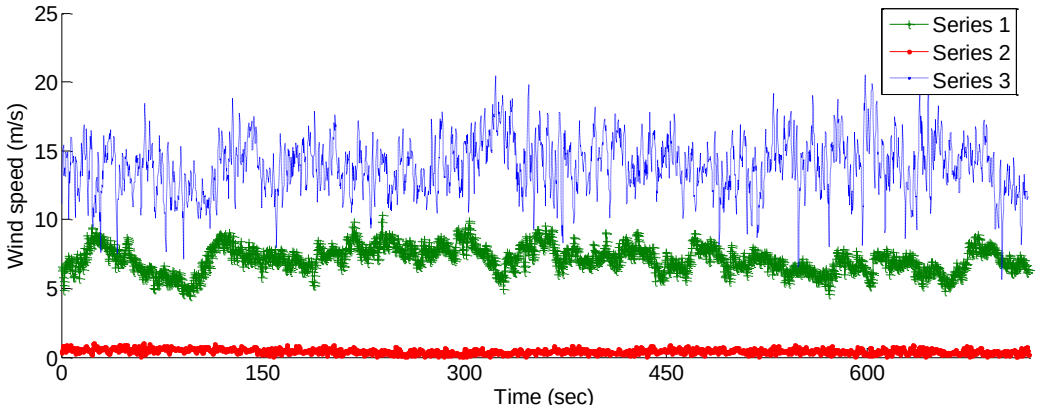

Figure 174: Series of 4Hz wind speeds (m/s) data from SWMTF used for simulation for a period of 10 minutes

The rate of cryogen production during the simulation time period is presented in Figure 175. The cryogen production rate (kg/s) for the wind speed input Series 1 and 2 are overlapping each other meaning the rate was constant for both the wind speed series, Series 1 and Series 2. However, the liquid nitrogen production rate (kg/s) started decreasing after some time of simulation for the wind speed input of Series 3 as shown in Figure 175.

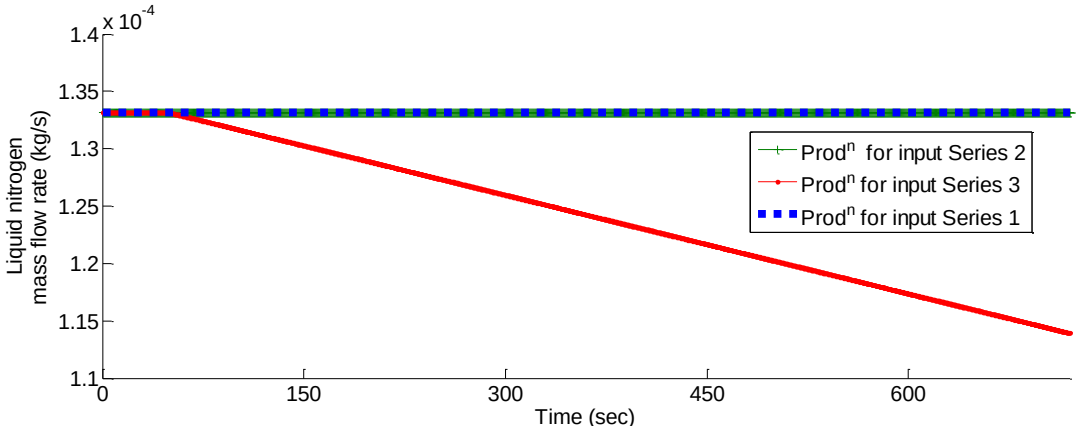

Figure 175: Liquid nitrogen mass flow rate (kg/s) during simulation

The range of statistics in terms of mean and standard deviation of the wind speed and the cryogen production rate for this simulation are presented in Table 21.

Table 21: Results summary of the simulation

	Wind speed (m/s)		Cryogen production (kg/s)	
	Average	Standard deviation	Average	Standard deviation
Series 1 (Blue line)	13.92	2.01	0.00013	1.3e-08
Series 2 (Green line)	7.12	0.93	0.00013	1.3e-08
Series 3 (Red line)	0.43	0.17	0.00012	5.8e-06

10.3 Simulation with 5MW rated wind rotor with Roskrow Barton 10 minute wind speed

The 10 minute average wind speed data for 1 year from Roskrow Barton was used for this simulation work. The mean, minimum and the maximum wind speeds were then calculated. A series of consecutive 10 minute simulations with constant speed for each 10 minute (simulation time) were performed. The hydraulic accumulator volume considered for this simulation is 50 m^3. This simulation is performed to study the system response to different wind speed cases and to determine the required volume of hydraulic accumulator for the start-up of the wind turbine rotor during low wind conditions. In this simulation it is assumed that the energy provided by the high pressure fluid in accumulator provides the minimum rotor speed (~4 rad/s) with the hydraulic pump/motor consuming a lower high pressure fluid rate of ~0.0009 m^3/s. It is also assumed that the pressure in the high pressure fluid line is maintained during the simulation time so that the hydraulic motor driving the compressor is provided with constant speed. The parameters used for this simulation are presented in Table 22.

Table 22: Parameters for wind turbine rotor and hydrostatic transmission

Symbol	Description	Value	Unit
ρ_a	Air density	1.225	kg/m^3
R	Rotor radius	63	m
J_L	Rotor shaft inertia	38759228	kg.m^2
D_p	Hydraulic pump displacement	0.3	m^3/rad
D_{mA}	Hydraulic motor displacement	8e-4	m^3/rad
ρ	Fluid density	852.8	kg/m^3
v	Fluid viscosity	18.78e-6	m^2/s
V_0	Hydraulic accumulator volume	50	m^3

The time series plots of the hydraulic storage level for three different scenarios during the simulation are presented in this section. The minimum, maximum and the average wind speed (m/s) for 1 year was calculated for the Roskrow Barton farm and was found to be 0.1, 21.5 and 6.92 m/s respectively. Therefore the simulations were carried out for these three wind speed values.

1. Simulation with constant wind speed of 0.1 m/s for 10 minutes

Simulation was performed for a time period of 10 minutes (simulation time) with a constant wind speed of 0.1 m/s. For the first set of simulation carried out, the initial volume of the high pressure fluid in hydraulic accumulator was taken as 1 m^3 and the hydraulic accumulator volume was 50 m^3. The situation considered for this simulation is a situation of low wind or close to no wind condition. The wind speed is below the cut-in wind speed for the wind turbine to function as a result of which the system has to depend on the energy stored in the hydraulic accumulator. This simulation assumes there is stored energy in the hydraulic accumulator. The results obtained during simulation regarding the high pressure fluid level in hydraulic accumulator are presented in Figure 176 and Figure 177 respectively.

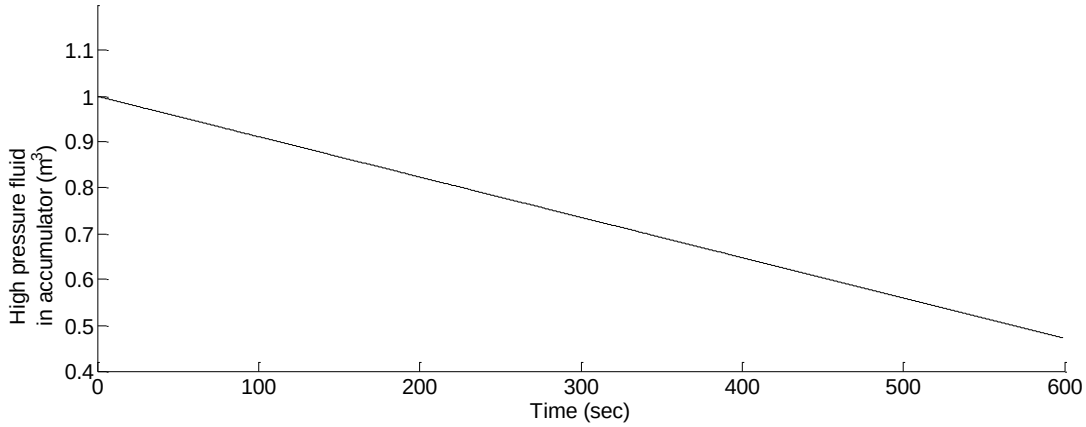

Figure 176: High pressure fluid in accumulator (m^3) with respect to time

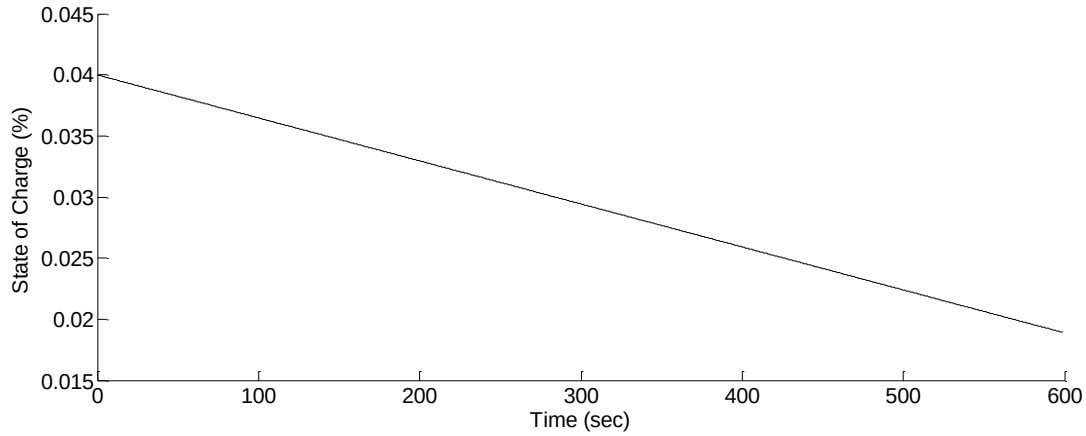

Figure 177: State of charge (%) of high pressure fluid in accumulator

A second set of simulation for the same wind speed was performed taking the initial volume of high pressure fluid in accumulator as 0.1 m^3 to determine if the hydraulic accumulator stocks out of high pressure hydraulic fluid during the simulation time.

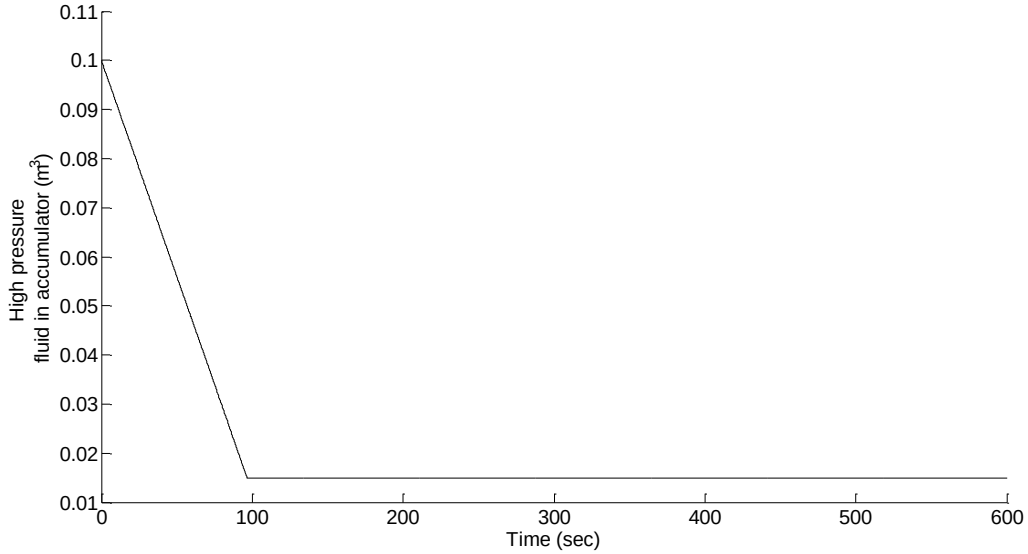

Figure 178: High pressure fluid in accumulator (m^3) with respect to time

As can be seen from the results presented in Figure 176, the hydraulic accumulator had a volume of 0.46 m^3 of high pressure hydraulic fluid in it at the end of 10 minutes. 0.54 m^3 was utilized by the hydraulic pump/motor to provide minimum rotational speed to the wind turbine rotor.. The hydraulic accumulator volume was taken as 50 m^3 and the initial high pressure fluid volume in accumulator as 1 m^3. Therefore, the high pressure fluid in the hydraulic accumulator was not completely used up until the end of simulation time.

However, taking the initial high pressure fluid volume in the accumulator as 0.1 m^3 and carrying out the simulation, the stored high pressure fluid in the accumulator stocked out to its minimum volume at around 97 seconds of simulation time. 0.1 m^3 of high pressure fluid volume was not sufficient to provide the minimum rotational speed to the wind turbine for the complete duration of 600 seconds of simulation time.

2. Simulation with mean wind speed of 6.92 m/s

For this set of simulation, the input wind speed was taken to be 6.92 m/s, the hydraulic accumulator volume was taken as 50 m^3 and the initial hydraulic fluid in accumulator was taken as 1 m^3 respectively. The results obtained from the simulation for the high pressure hydraulic fluid in the accumulator and the state of charge of the hydraulic accumulator are presented in Figure 179 and Figure 180 respectively.

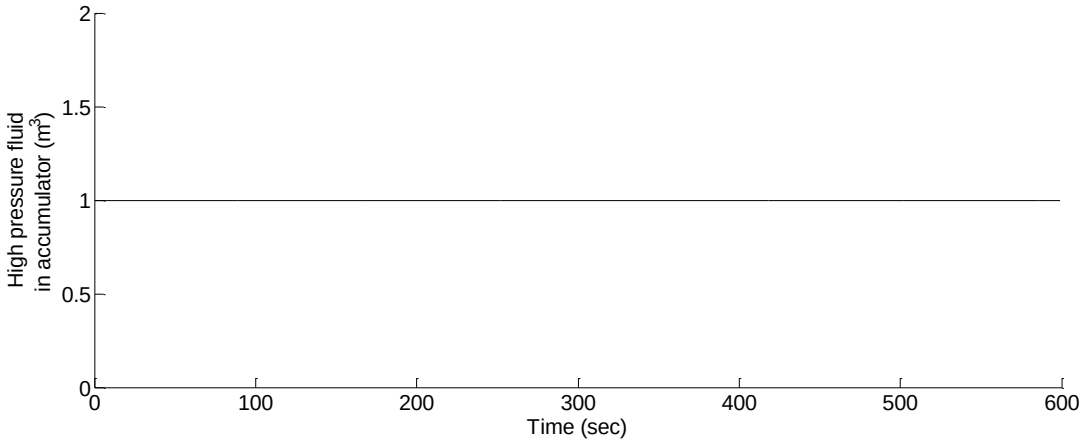

Figure 179: High pressure fluid in accumulator (m^3) with respect to time

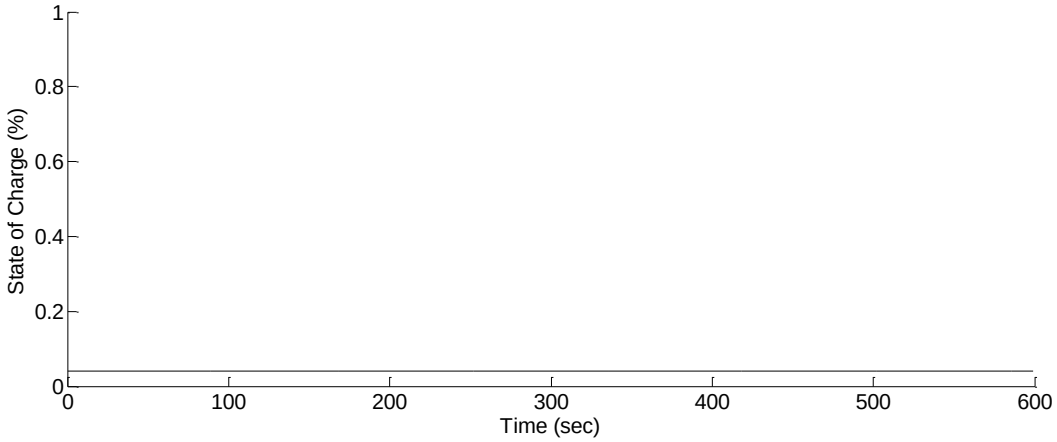

Figure 180: State of charge (%) of high pressure fluid in accumulator

From the results obtained, it was evident that there was no change in the hydraulic storage level because there was no availability of excess high pressure hydraulic fluid during the simulation time to be stored in the hydraulic accumulator.

3. Simulation with maximum wind speed of 21.5 m/s

Another set of simulation was performed with the input wind speed of 21.5 m/s for 10 minutes. This was also the maximum wind speed recorded from the Roskrow Barton data. This simulation was performed to determine if the hydraulic accumulator with a finite storage volume of 50 m^3 will be completely filled. The results obtained are presented in Figure 181 and Figure 182.

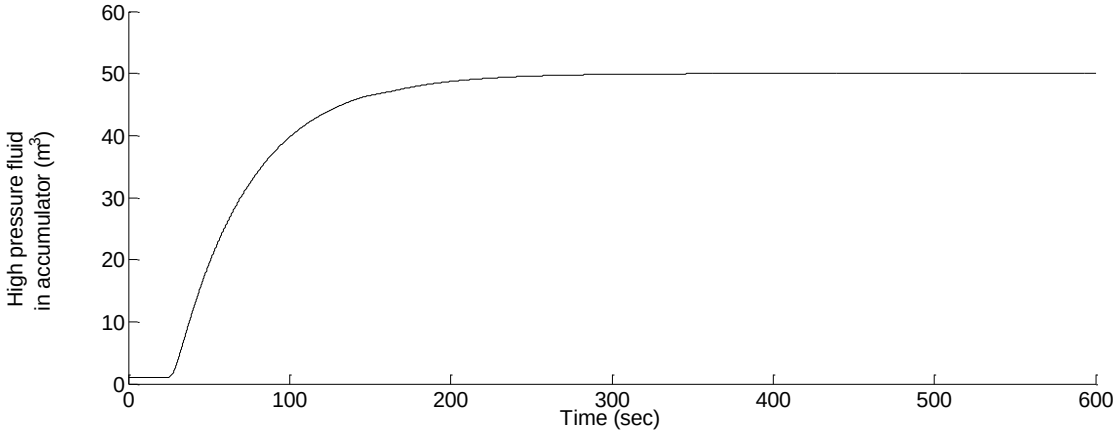

Figure 181: High pressure fluid in accumulator (m^3) with respect to time

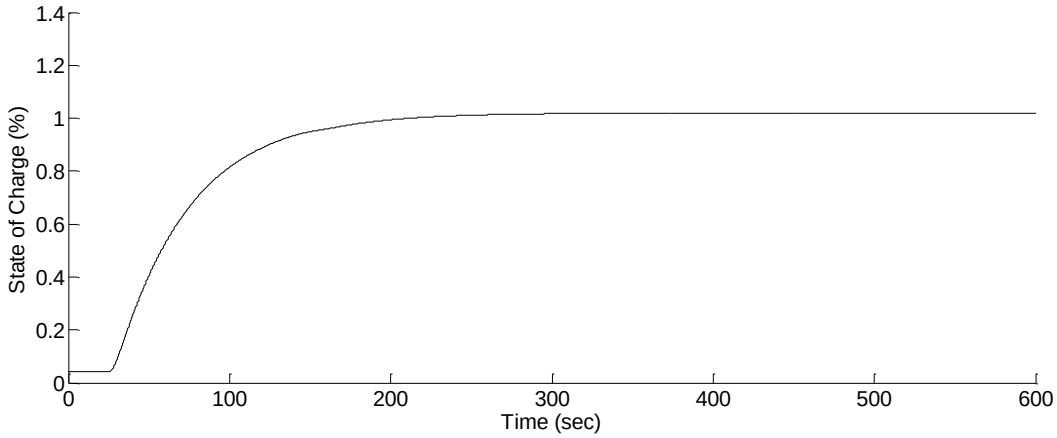

Figure 182: State of charge (%) of high pressure fluid in accumulator

As can be seen from the results, the hydraulic accumulator gets completely filled after around 300 seconds of simulation and remains constant as shown in Figure 181 and Figure 182. The wind speed was taken constant at 21.5 m/s for 600 seconds, which is not the case in practical. When the accumulator gets completely filled and the pressure inside the accumulator increases at the same time, the flow from the accumulator needs to be directed towards the low pressure reservoir. The results also showed that the hydraulic motor did not consume any high pressure hydraulic fluid from the accumulator during the simulation. This is because the power was continuously delivered by the wind turbine rotor for the system operation. The excess energy was therefore stored in the accumulator.

10.4 Hydraulic accumulator volume calculations example

The calm period was calculated for the wind speed data available from Roskrow Braton wind farm, UK. It was determined that the year 2010 the calm period was present for 18.3% of the year. If we assume that this period is evenly distributed in each hour in a year, then each hour would include 11.1 minutes of calm period. This situation would rarely happen in reality but it is assumed here for a comparison purpose. Knowing this, a $5MW_w$ rated CryoVent wind turbine would require 150 m^3 of high pressure fluid stored in the hydraulic accumulator to power the gas liquefaction system during 53.8% of the calm period (which is 5.9 minutes). If it is intended to power the gas liquefaction system for 100% of the calm period, i.e. 11.1 minutes, then a high pressure fluid of 300 m^3 would be needed. These volumes of hydraulic accumulators can be accommodated inside the wind turbine tower as has been proposed in this work. This calculation was performed assuming the hydraulic pump/motor has a volumetric displacement of 0.3 m^3/rad of high pressure fluid even during the low wind conditions, and that the hydraulic pump/motor connected to the wind turbine has a rotational speed of 1.4 rad/s, and the hydraulic

motor driving the gas liquefaction system has a speed of 188 rad/s (all other specifications for the system assumed for calculation are same as those presented for system considered in Section 10.3). If it is desirable to provide only minimal rotational speed to the wind rotor for start-up, the stored high pressure fluid could provide energy for a longer period of time.

10.5 Summary

The MATLAB/Simulink model and simulations performed for 5MW rated wind driven liquid nitrogen production system were presented in this chapter. The model was also tested against various wind speed time series data to determine expected system performance. This chapter presented sets of simulation that tested the system performance for a wind-energy driven liquid nitrogen production system, first set of simulation for the laboratory scale GM cryocooler and second set of simulation for a large scale liquid nitrogen production system. The main purpose of this chapter was to feed the MATLAB/Simulink model with the synthesised high sampling frequency (such as 4Hz or 1 sec) wind speed data of at least 1 year to determine the required volume for a hydraulic accumulator. However, the wind speed time series data synthesis in Chapter 4 needs some further work to be able to generate wind speed time series data as desired. This chapter also analyzed if energy stored in the hydraulic accumulator could be utilized to power the gas liquefaction system during low or no wind conditions.

From the simulations, it was apparent that the smaller the hydraulic accumulator volume considered, the more rapidly it would fill up during high wind conditions. Some of the high pressure fluid stored in the hydraulic accumulator was utilized by the hydraulic pump/motor during low wind conditions for smooth operation of the system. The energy stored in the accumulator was also used during start up of the hydrostatic transmission system after a calm wind period and also when there were fluctuations in the power delivered to the hydraulic motor

driving the helium compressor. Overall, the open loop hydrostatic transmission operated as desired.

11Conclusions, Contributions and Future Works

The major motivation for the development of this research work approached from the need for high volumes of cold ventilating air for deep mines. Therefore one of the major applications of the proposed concepts is in the cooling of deep mines. Liquefied air mixed with ambient bulk mine ventilation air (auto-compressed and geothermally heated) would cause the liquid air to evaporate and the ventilation air to cool and both components to result in the same state, with unchanged chemistry. The 'coolant' is non-toxic, and direct contact evaporative heat exchange, with no need for component separation post contact is the most effective method of heat transfer.

The intent is that substantial volumes of liquefied air can be delivered by means of a completed bore-hole from surface to the sub-surface to at least provide cooling of underground workings but also could represent the main air flow volume into the mine itself and may also eliminate the need for huge ventilation shafts just to get air underground for mines producing 100,000 tonnes per day. The applications of this CryoVent project could be numerous, such as application in cryogen production with close to zero marginal cost, in utility scale energy storage and transportation, as has been presented in detail in Chapter 1. This chapter outlines the results and conclusions from all the chapters. It also presents the contributions of this research work, and suggested future works.

11.1 Conclusions

The time series analysis executed in Chapter 4 suggested that wind time series data is multifractal (trifractal) for the wind speed data obtained from Roskrow Barton wind farm for the year 2010. Further analysis with the same wind speed data source (for different years) and also

with different wind speed data sources is required to depict a conclusion if all the wind speed time series data hold similar multifractal behavior within the same range of lags considered. This Chapter also suggested that the power spectrum of wind speed time series data contains the information about the frequencies on which the power of the signal is distributed which is helpful in determining the major cycles for the signal (such as daily, monthly, yearly cycles) and their occurrences. A relation between the power spectrum components of lower sampling frequency data and higher sampling frequency data has also been established in this chapter, which is the first step towards the synthesis of time series data. A novel method for the synthesis of wind speed time series is developed in this chapter but further investigation is required. The result of this investigation will be published in a journal article when fully completed.

The modeling and simulation on the closed and open loop hydrostatic transmission presented in Chapter 6 has provided positive agreement with that of Hamzehlouia et al. (2013), which motivated on developing the link of wind turbine rotor to hydrostatic transmission to gas liquefaction system. The slight differences in the results obtained may be due to the PI controller present in the system. A wind driven gas liquefaction model was however developed in MATLAB/Simulink and found to produce results satisfactory for the objectives and purposes of this thesis.

The dynamic simulation of a wind energy driven GM cryocooler was performed in Chapter 7 and the results obtained from the simulation were discussed. The average liquid nitrogen mass flow rate remained steady with only modest fluctuations, irrespective of the simulated random driving frequencies applied to the simulated motor/compressor shaft. These simulation results are thus consistent with the principal hypothesis of the thesis: CryoVent systems can be designed so that cryogen production rates are steady, in the face of variable

and intermittent wind rotor work input. Most importantly, the experimental results of Chapter 8 exhibited good correspondence to the simulated results of Chapter 7. The review of the degree of agreement between simulated and experimental results in Chapter 9 thus lends further support to the primary hypothesis of this thesis being true.

Despite these general trends being apparent, there are nevertheless some observations of the experimental set up and method that weaken the firmness with which such a conclusion can be made. Both relate to quantization of signals from instrumentation. Firstly electric motor power curves showing power consumed at different driving frequencies over the various tests completed have a stepped appearance. This is caused by the precision with which the power is reported by the variable frequency drive (VFD) controller. Despite detailed investigations to see if this could be improved through alteration of the control scheme of the VFD, or independent monitoring of current and voltage reported by the VFD, no improvement was obtained, or obtainable, with the equipment available. In contrast, improvements were made to overcome the second instrumentation problem relevant to observation precision in the experiments. A more detailed interface to the electronic system of the mass balance led to higher reportable precision, and this was achieved through the writing of a custom firmware driver for the SCADA program, LabVIEW with the help from the manufacturer.

To definitively overcome the apparent experimental deficiencies, more expensive sensors would be required. A mass balance providing observations with a precision of a tenth of a gram or better in 100 kilograms was prohibitively expensive for this work. Similarly, to improve the precision of input power reporting from the VFD would have required a much more expensive controller unit. However, these cautions being applied, and albeit, 'on the averages', the experimental program has nevertheless confirmed the major hypothesis of the thesis: that

the rate of cryogen production is robustly independent of, or uncorrelated with, the variability and intermittency of input work. Most importantly, the fact that the CryoVent system simulations of Chapter 7 corresponded to the experimental work of Chapter 8 clearly shows that the key understandings of CryoVent system design and operation, intrinsic to the CryoVent model formulation tested, have been reliably won. Consequently, for a stage of further work extending the research reported in this thesis, a higher level of expenditure on equipment and instrumentation appears well justified.

Although both the condensation and evaporation models for Dewar heat transfer mechanism in Chapter 7 have shown to be in good agreement with the experimental results, the confidence in the model can be increased further. The main challenge for this model and simulation was the unavailability of individual component dimensions. The laboratory GM cryocooler unit was a modified unit from the standard liquid nitrogen generator LNP10 unit from Cryomech Inc. Cryomech Inc., assembled the unit as per our requirement. The detailed inner dimensions were not available as Cryomech was not the manufacturer of the Dewar and when the manufacturer were contacted regarding the dimensions, they refused to provide the information as we were not their customers, and that the information they provide was confidential. The availability of all the required information for input to the model would increase its reliability further. This would also assist in the model verification process.

The model on Dewar heat transfer mechanism and the GM cryocooler model could also be improved by using improved and more instrumentation such as temperature sensors along the height of Dewar (inner) vessel, a Wattmeter on compressor/motor shaft, a mass flow meter on helium delivery line, and temperature sensors along the height of cold head. It is also useful to know the helium mass flow rate in the compression and expansion volume of the cold head.

The inclusion of gas properties in simulation such that they are updated in each time step is also essential.

Chapter 10 presented the simulation results performed for 6 kW (field demonstrator prototype scale) and 5 MW (full production scale) rated wind driven liquid nitrogen production system. The state of charge of hydraulic accumulator at different wind speed situations was also determined in this chapter. The simulation results suggested that smaller the hydraulic accumulator volume considered sooner it would fill up during high wind conditions. The stored fluid in the hydraulic accumulator could provide power to drive the cryocooler compressor even during the low and/or no wind conditions. It could also provide energy to the wind rotor for start-up following calm period.

11.2 Contributions

The main contributions of this research work are in the development of a technique to produce cryogens using wind energy in a safe approach and progress towards development of a novel method to synthesize wind speed time series. The cryogens produced could be used for deep mine cooling and ventilation. The contributions of this work are comprehensively listed in the following:

- Development of a technique to safely produce cryogens using wind energy.
- MATLAB/Simulink model developed for linking wind turbine rotor to hydrostatic transmission system to gas liquefaction system to Dewar vessel.
- Whole body development of experimental work, including LabVIEW program, VFD interfacing, temperature monitor, improved logging mass balance.

- An experimentally validated thermo-mechanical dynamic model and process simulation of the GM cryocooler.
- Identified a procedure to analyse wind speed time series for multi-fractal behaviour and also identified that the phase spectrum of the wind speed time series is a curve well characterized as white noise.
- Developed a new technique to generate high frequency wind speed time series data with available low frequency data. Synthesis of time series data using the technique developed is in progress.
- Provided a simulation model to buffer the variable nature of wind energy by means of cryogen production.
- Provided comparative figures on the conventional and the Cryovent method of providing cooling in terms of costs and efficiency.

11.3 Future works

This research work presented the basic linkage that was necessary to couple the wind turbine rotor to hydrostatic transmission to gas liquefaction system. There are some suggestions and recommendations on some potential future works. Additional works in Chapter 4 are required. For drawing conclusion on the presence of multifractal behaviour in all wind speed time series data, further analysis would be beneficial that may be performed on the same wind speed data source for different years and also on wind speed data from several other sources/locations. Additional attempts are also required on the wind speed time series data synthesis model, which will also be the final outcome of Chapter 4. This could not be covered in this thesis but is a part of further work. The new model developed can then be applied for the generation of high sampling frequency wind speed time series from available low sampling

frequency wind speed time series data. This part of further work will be presented in a peer-reviewed journal article when completed.

The reason behind the slight differences present in the simulation results obtained when compared with those of Hamzehlouia et al. (2013) in Chapter 6 needs further investigation to determine if it was actually due to the PI controller.

Although the mathematical linkage necessary for coupling the three major systems has been set forth in this research work and has been subject to laboratory experimental verification, it requires that it is tested and verified practically. The experimental verification of the proposed concept on a prototype field demonstrator and at full scale is necessary in a path to commercialization of the CryoVent concept. Experimentation on the full scale demonstrator with proper instrumentation would help in resolving the technical risks associated with commercialization, and provide definitive statements on the economics.

The gas liquefaction system to be used in the CryoVent concept could be any established recuperative liquefier or regenerative cryocooler. The efficiency of conversion of wind energy to cryogen was not a primary objective of this thesis as it was always known that practically establishing maximum efficiency would be a design optimization process. However, at least, there is now a model on which such optimization exercises could be applied - at least for Gifford McMahon cryocoolers.

Studies on determination of most suitable and commercial locations for the development of demonstrator and also for the application of the concept generally are required to amplify the case for commercialization, especially given the ease with which this model for renewable wind energy capture may be integrated with existing energy production, distribution and consumption networks and systems.

Therefore to summarize, the principal future works for this research work are to:

- incorporate the known issues such as the helium high and low pressure fluctuations and possibly the Dewar (inside) vessel thermal stratification in the GM cryocooler simulation model,
- conduct reliability long term tests for the GM cryocooler system,
- expand on the method of extrapolating wind speed time series data while preserving the multifractal character of the wind, and
- to develop a CryoVent demonstrator equipped with enhanced instrumentation as was presented in Figure 170.

References

Acuña, E. I., & Soto, G. (2014). Theoretical determination of the number of adits and cross-sectional area for the airflow requirements of the New Level Mine Project Theoretical determination of the number of adits and cross-sectional area for the airflow requirements of the New Level Mi. In M. Huydma & Y. Potvin (Eds.), *Deep Mining 2014*.

Agrawal, R., & Ayres, C. L. (1991). *U.S. Patent No. 5139547*. Washington, DC: U.S. Patent and Trademark Office. Retrieved from http://www.google.ca/patents/US5139547

Air products. (2017). Typical Bulk Liquid Storage Systems. Retrieved January 11, 2017, from http://www.airproducts.com/products/Gases/supply-options/bulk-deliveries-and-storage-systems/typical-bulk-liquid-storage-systems.aspx

Air Products and Chemicals, I. (2013). Cryogenic liquid containers. Retrieved from http://www.airproducts.com/~/media/files/pdf/company/safetygram-27.pdf

Ameel, B., T'Joen, C., De Kerpel, K., De Jaeger, P., Huisseune, H., Van Belleghem, M., & De Paepe, M. (2013). Thermodynamic analysis of energy storage with a liquid air Rankine cycle. *Applied Thermal Engineering*, *52*(1), 130–140. http://doi.org/10.1016/j.applthermaleng.2012.11.037

Amos, W. A. (1998). *Costs of Storing and Transporting Hydrogen*. National Renewable Energy Laboratory. https://www.nrel.gov/docs/fy99osti/25106.pdf

ANSI. (2017). Wind Turbine Standards. Retrieved May 5, 2017, from http://webstore.ansi.org/energy/wind-turbine/default.aspx?source=blog

Artemis Intelligent Power. (2016). Technology - Artemis IP. Retrieved February 1, 2017, from http://www.artemisip.com/technology/

Bai, J., Xie, A., Yu, X., & Zhou, L. (2010). Simulation Model of Hydraulic Speed Control System and Its Parameters Identification Based on Resilient Adaptive Particle Swarm Optimization Algorithm. *Power and Energy Engineering Conference (APPEEX), Asia-Pacific*, 1–4.

Barron, R. F. (1985). *Cryogenic Systems*. (R. G. (Universit. of S. Scurlock, Ed.) (Second). Oxford University Press Inc., 200 Madison Avenue, New York, New York 10016.

Bellasio, R. (2014). Analysis of wind data for airport runway design. *Journal of Airline and Airport Managment*, *4*(2), 97–116. http://doi.org/10.3926/jairm.26

Brøndsted, P., Lilholt, H., & Lystrup, A. (2005). COMPOSITE MATERIALS FOR WIND POWER TURBINE BLADES. *Annu. Rev. Mater. Res*, *35*, 505–38. http://doi.org/10.1146/annurev.matsci.35.100303.110641

Brown, B. G., Katz, R. W., & Murphy, A. H. (1984). Time Series Models to Simulate and Forecast Wind Speeds and Power. *Journal of Climate and Applied Meteorology*. http://doi.org/10.1175/1520-0450(1984)023<1184:TSMTSA>2.0.CO;2

Burton, T., Sharpe, D., Jenkins, N., & Bossanyi, E. (2001). *Wind energy Handbook. Uma ética para quantos?* England: John Wiley and Sons Ltd.

Butterfield, C. ., & Muljadi, E. (2000). Pitch-Controlled Variable-Speed Wind Turbine Generation, (February). Retrieved from http://www.nrel.gov/docs/fy00osti/27143.pdf

Canadian Standards Association. (2008). CSA Guide to Canadian wind turbine codes and standards. Retrieved from http://www.csagroup.org/documents/codes-and-standards/standards/energy/CSAGuidetoCanadianWindTurbineCodes.pdf

Carlin, P. W., Laxson, A. S., & Muljadi, E. B. (2001). The History and State of the Art of Variable-Speed Wind Turbine Technology The History and State of the Art of Variable-Speed Wind Turbine Technology, (February). Retrieved from http://www.nrel.gov/docs/fy01osti/28607.Pdf

Carrillo, C., Cidrás, J., Díaz-Dorado, E., & Obando-Montaño, A. F. (2014). An approach to determine the weibull parameters for wind energy analysis: The case of Galicia (Spain). *Energies*, *7*(4), 2676–2700. http://doi.org/10.3390/en7042676

Castle, W. F. (2002). Air separation and liquefaction: recent developments and prospects for the beginning of the new millennium. *International Journal of Refrigeration*, *25*(1), 158–172. http://doi.org/http://dx.doi.org/10.1016/S0140-7007(01)00003-2

Chang, T.-P., Ko, H.-H., Liu, F.-J., Chen, P.-H., Chang, Y.-P., Liang, Y.-H., … Chen, Y.-H. (2012). Fractal dimension of wind speed time series. *Applied Energy*, *93*, 742–749. http://doi.org/10.1016/j.apenergy.2011.08.014

Claude, G. (1909). *U.S. Patent No. 981748*. Washington, DC: U.S. Patent and Trademark Office. Retrieved from https://www.google.com/patents/US981748

Cryofab. (2017). Dewar Flasks. Retrieved January 23, 2017, from http://www.cryofab.com/products/Cryogenic-Dewar-Flasks

Cryomech. (2014). *LNP10 liquid nitrogen generator manual*.

Cryomech. (2017). *Cryogenic Refrigerator*. Syracuse, New York.

D'Amico, G., Petroni, F., & Prattico, F. (2014). Wind speed and energy forecasting at different time scales: A nonparametric approach. *Physica A: Statistical Mechanics and Its Applications*, *406*, 59–66. http://doi.org/10.1016/j.physa.2014.03.034

Dasgupta, K., Mandal, S. K., & Pan, S. (2012). Dynamic analysis of a low speed high torque hydrostatic drive using steady-state characteristics. *Mechanism and Machine Theory*, *52*(0), 1–17. http://doi.org/http://dx.doi.org/10.1016/j.mechmachtheory.2011.12.004

De Waele, A. T. A. M. (2000). Pulse-tube refrigerators: principle, recent developments, and prospects. *Physica B: Condensed Matter*, *280*(1–4), 479–482. http://doi.org/http://dx.doi.org/10.1016/S0921-4526(99)01840-2

Design Aerospace LLC. (2013). Check Valve, Hydraulic - Description. Retrieved May 3, 2017, from http://www.daerospace.com/HydraulicSystems/CheckValveHydraulicDesc.php

Diepeveen, N. F. B. (2004). Seawater-Based Hydraulics for Offshore Wind Turbines. *We-At-Sea.Org*. Retrieved from http://www.we-at-sea.org/leden/docs/reports/RL1-4 2004-012C Delft Offshore Turbine.pdf

Diepeveen, N. F. B. (2013). *On the Application of Fluid Power Transmission in Offshore Wind Turbines*. Delft University of Technology.

Dincer, I., & Kanoglu, M. (2010). *Refrigeration Systems and Applications* (Second). The Atrium, Southern Gate, Chichester, West Sussex: John Wiley and Sons Ltd.

Djemai, N., & Bouktir, T. (2008). Impact of Wind Power on the Angular Stability of a Power System. *Leonardo Electronic Journal of Practices and Technologies*. Retrieved from

https://www.researchgate.net/publication/259526605_Impact_of_Wind_Power_on_the_Angular_Stability_of_a_Power_System
Douglas, J. (2006). A Virtual Field Trip of Physical Geography in Ventura County. Retrieved March 30, 2017, from http://geographyventuracounty.info/index.htm
DTU Wind Energy. (2017). Wind energy industry-standard software - WAsP. Retrieved January 10, 2017, from http://www.wasp.dk/
Eastop, T. D., & McConkey, A. (1993). *Applied Thermodynamics for Engineering Technologists*. Edinburgh Gate, Harlow, Essex CM20 2JE: Pearson Education.
eCompressedair. (2017). Deltech HGE-75 Non-Cycling Compressed Air Dryer. Retrieved January 23, 2017, from http://www.ecompressedair.com/air-dryers/refrigerated/non-cycling/deltech-hge-75.aspx
Enercon GmbH. (2016). WEC components. Retrieved April 18, 2017, from http://www.enercon.de/en/technology/wec-components/
Esposito, A. (2009). *Fluid power with applications* (7th Editio). Upper Saddle River, New Jersey.
Fairbanks Scales. (2017). Ultegra MAX Flat Top. Retrieved January 16, 2017, from https://www.fairbanks.com/products/?pid=31081C
Finotek. (2006). A Pressure Relief Valve - Finotek. Retrieved April 7, 2017, from http://www.finotek.com/what-is-a-pressure-relief-valve/
Gasch, R., & Twele, J. (Eds.). (2012). *Wind power plants- Fundamentals, Design, Construction and Operation* (Second Edi, Vol. 1). Berlin: Springer. http://doi.org/10.1017/CBO9781107415324.004
Gifford, W. ., & Longsworth, R. . (1963). Pulse Tube Refrigeration Progress. In *Advances in Cryogenic Engineering* (pp. 69–79). Syracuse, New York. Retrieved from http://www.cryomech.com/pdfs/WilliamGiffordPulseTube.pdf
Gifford, W. E., & McMahon, H. O. (1957). *U.S. Patent No. 2906101*. Washington, DC: U.S. Patent and Trademark Office. Retrieved from https://www.google.com/patents/US2906101
Gomes, P., & Castro, R. (2012). Wind Speed and Wind Power Forecasting using Statistical Models : AutoRegressive Moving Average (ARMA) and Artificial Neural Networks (ANN). *International Journal of Sustainable Energy Development (IJSED), 1*(1), 36–45. Retrieved from http://infonomics-society.org/wp-content/uploads/ijsed/published-papers/volume-1-2012/Wind-Speed-and-Wind-Power-Forecasting-using-Statistical-Models-AutoRegressive-Moving-Average-ARMA-and-Artificial-Neural-Networks-ANN.pdf
Hamzehlouia, S., Izadian, A., & Anwar, S. (2013). An Energy Storage Technique for Gearless Wind Power Systems. In *IEEE International Conference on Electro/Information Technology (EIT)* (pp. 1–6). http://doi.org/10.1109/EIT.2013.6632699
Hamzehlouia, S., Izadian, A., Pusha, A., & Anwar, S. (2011). Controls of hydraulic wind power transfer. *IECON Proceedings (Industrial Electronics Conference)*, 2475–2480. http://doi.org/10.1109/IECON.2011.6119698
Heylandt, P., & Wilhel, C. (1927). *U.S. Patent No. 1777040*. Washington, DC: U.S. Patent and Trademark Office. Retrieved from http://www.google.com/patents/US1777040

Highview Power Storage. (2014). Liquid Air Energy Storage (LAES). Retrieved January 11, 2017, from http://www.highview-power.com/wp-content/uploads/Highview-Brochure-2014.pdf

Higuchi, T. (1988). Approach to an irregular time series on the basis of the fractal theory. *Physica D*, *31*, 277–283.

Hitachi. (2014). *Hitachi inverter SJ700D-3 SERIES instruction manual*.

Hitachi America Ltd. (2015). Helium refrigerating scroll compressor. Retrieved February 2, 2017, from https://www.hitachi-america.us/ice/pdf/HR-E594P.PDF

Homola, M. C. (2005). *Wind Energy in the BSR: Impacts and Causes of Icing on Wind Turbines*. Narvik University College.

Huston, E. L. (1984). Liquid and Solid storage of Hydrogen. In *Proceedings of the 5th World Hydrogen Energy Conference*. Toronto, Canada.

Hydraulics & Pneumatics. (2012). Fundamentals of Hydraulic Reservoirs | Reservoirs & Accessories content from Hydraulics & Pneumatics. Retrieved January 12, 2017, from http://hydraulicspneumatics.com/200/TechZone/ReservoirsAcces/Article/False/6448/TechZone-ReservoirsAcces

Ibrahim, H., Ghandour, M., Dimitrova, M., Ilinca, A., & Perron, J. (2011). Integration of Wind Energy into Electricity Systems: Technical Challenges and Actual Solutions. *Impact of Integrated Clean Energy on the Future of the Mediterranean Environment?*, *6*(0), 815–824. http://doi.org/http://dx.doi.org/10.1016/j.egypro.2011.05.092

IEC. (1997). *Wind turbine generator systems – Part 1 Safety Requirements* (1997th ed.).

IEC. (1998). *WIND TURBINE GENERATOR SYSTEMS – PART 1: Safety requirements*. Retrieved from http://faculty.mu.edu.sa/public/uploads/1337948377.8659IEC.pdf

International Energy Agency. (2013). *Technology Roadmap: Wind Energy - 2013 edition*. Retrieved from http://www.iea.org/publications/freepublications/publication/technology-roadmap-wind-energy---2013-edition.html

Isaaks, E. H., & Srivastava, M. R. (1989). *An Introduction to Applied Geostatistics*. New York, NY: Oxford University Press Inc., 200 Madison Avenue, New York, New York 10016.

Izadian, A., Hamzehlouia, S., Deldar, M., & Anwar, S. (2014). A Hydraulic Wind Power Transfer System: Operation and Modeling. *IEEE Transactions on Sustainable Energy*, *5*(2), 457–465. http://doi.org/10.1109/TSTE.2013.2291835

Jiang, Y. (2010). Wind turbine cooling technologies. In U. W. TONG, Kollmorgen Corporation (Ed.), *Wind power generation and wind turbine design* (Vol. 44, pp. 613–640). WITpress. http://doi.org/10.2495/978-1-84564

Johnson, J. (2014). Hydraulic-Electric Analogies: Capacitors and Accumulators, Part 1 | Accumulators content from Hydraulics & Pneumatics. Retrieved April 7, 2017, from http://hydraulicspneumatics.com/accumulators/hydraulic-electric-analogies-capacitors-and-accumulators-part-1

Johnson, K. E. (2008). *Adaptive Torque Control of Variable Speed Wind Turbines*. Golden.

Johnson, K. E., Pao, L. Y., Balas, M. J., & Fingersh, L. E. E. J. (2006, June). Control of Variable-Speed Wind Turbines: Standard and Adaptive Techniques for maximizing energy capture. *IEEE Control Systems Magazine*, 70–81.

Joselin Herbert, G. M., Iniyan, S., Sreevalsan, E., & Rajapandian, S. (2007). A review of wind energy technologies. *Renewable and Sustainable Energy Reviews*, *11*(6), 1117–1145. http://doi.org/http://dx.doi.org/10.1016/j.rser.2005.08.004

Kanoglu, M., Dincer, I., & Rosen, M. A. (2007). Performance analysis of gas liquefaction cycles. *International Journal of Energy Research*, *32*, 35–43. http://doi.org/10.1002/er

Kanoglu, M., Dincer, I., & Rosen, M. A. (2008). Performance analysis of gas liquefaction cycles. *International Journal of Energy Research*, *32*(1), 35–43. http://doi.org/10.1002/er.1333

Kopeliovich, D. (2017). Nitrogen membrane generator [SubsTech]. Retrieved January 20, 2017, from http://www.substech.com/dokuwiki/doku.php?id=nitrogen_membrane_generator

Krajači, G., Martins, R., Busuttil, A., Dui, N., Da, M., & Carvalho, G.-A. (2008). Hydrogen as an energy vector in the islands' energy supply. *International Journal of Hydrogen Energy*, *33*, 1091–1103. http://doi.org/10.1016/j.ijhydene.2007.12.025

Krasae-in, S., Stang, J. H., & Neksa, P. (2010). Development of large-scale hydrogen liquefaction processes from 1898 to 2009. *Novel Hydrogen Production Technologies and Applications Novel Hydrogen Production Technologies and Applications*, *35*(10), 4524–4533. http://doi.org/http://dx.doi.org/10.1016/j.ijhydene.2010.02.109

KSH. (2015). Engineering Services at KSH Solutions Inc. Retrieved June 4, 2017, from http://www.kshsolutions.ca/?page_id=3973

Kunwar, S., & Millar, D. L. (2014). Using wind energy to produce cryogens for use in deep mine cooling and ventilation. In *5th World Renewable Energy Technology Congress*. New Delhi, India. Retrieved from http://wretc.in/downloads/abstracts/2014/full-abstract/S_Kunwar.pdf

La Torre, F. C.-D., González-Trejo, J. I., Real-Ramírez, C. a, & Hoyos-Reyes, L. F. (2013). Fractal dimension algorithms and their application to time series associated with natural phenomena. *Journal of Physics: Conference Series*, *475*, 012002. http://doi.org/10.1088/1742-6596/475/1/012002

Lachenal, X., Daynes, S., & Weaver, P. M. (2012). Review of morphing concepts and materials for wind turbine applications. *Wind Energy*, *17*(April 2013), 657–669. http://doi.org/10.1002/we

Lawan, S. M., Abidin, W. a W. Z., Chai, W. Y., Baharun, A., & Masri, T. (2014). Some methodologies of wind speed prediction : A critical review. *International Journal of Renewable Energy*, *9*(1). Retrieved from http://www.sert.nu.ac.th/IIRE/login/FP_V9N1(5).pdf

Lemmon, E. W., Huber, M. ., & McLinden, M. O. (2013). NIST Standard Reference Database 23: Reference Fluid Thermodynamic and Transport Properties-REFPROP, Version 9.1, National Institute of Standards and Technology. http://doi.org/http://dx.doi.org/10.18434/T4JS3C

Li, R., Onishi, A., Satoh, T., & Kanazawa, Y. (1997). Optimization of intake and exhaust valves for 4 K Gifford-McMahon cryocooler. In *Proceedings of 16th International Cryogenic Engineering Conference and International Cryogenic Materials Conference* (Vol. 1, pp. 339–342). RD Centre, Sumitomo Heavy Ind. Ltd., Kanagawa, Japan: Elsevier.

Li, Y., Chen, H., Zhang, X., Tan, C., & Ding, Y. (2010). Renewable energy carriers: Hydrogen or liquid air/nitrogen? *Applied Thermal Engineering*, *30*(14–15), 1985–1990. http://doi.org/http://dx.doi.org/10.1016/j.applthermaleng.2010.04.033

Liu, J., Ren, G., Wan, J., Guo, Y., & Yu, D. (2016). Variogram time-series analysis of wind speed. *Renewable Energy*, *99*, 483–491. http://doi.org/10.1016/j.renene.2016.07.013

Manwell, J. F., McGowan, J. G., & Rogers, A. L. (2010). *Wind energy explained, theory, design and application*. *Statewide Agricultural Land Use Baseline 2015* (Second Edi, Vol. 1). UK: John Wiley & Sons, Ltd. http://doi.org/10.1017/CBO9781107415324.004

Masuyama, S., Fukuda, Y., Imazu, T., & Numazawa, T. (2011). Characteristics of a 4 K Gifford-McMahon cryocooler using the Gd 2O2S regenerator material (Vol. 51, pp. 337–340). Oshima National College of Maritime Technology, Suo-oshima, Yamaguchi 742-2193, JapanNational Institute for Materials Science, Tsukuba, Ibaraki 305-0003, Japan: Elsevier Ltd. http://doi.org/10.1016/j.cryogenics.2010.06.008

Masuyama, S., Matsui, K., Tamura, K., & Numazawa, T. (2012). Attractive performance of a Gifford–McMahon cryocooler by co-axial layout of regenerator materials. *Special Issue: ACASC 2011*, *52*(12), 695–698. http://doi.org/http://dx.doi.org/10.1016/j.cryogenics.2012.04.018

McPherson, M. J. (2000). Subsurface Ventilation Engineering (pp. 18– 1–18– 78). 1625 Shaw Ave #103, Clovis, CA 93611: Mine Ventilation Services Inc. Retrieved from https://www.mvsengineering.com/files/Subsurface-Book/MVS-SVE_Chapter00.pdf

Melikoglu, M. (2017). Pumped hydroelectric energy storage: Analysing global development and assessing potential applications in Turkey based on Vision 2023 hydroelectricity wind and solar energy targets. *Renewable and Sustainable Energy Reviews*, *72*, 146–153. http://doi.org/10.1016/j.rser.2017.01.060

Millar, D. L., & Parish, D. . (2010). Electricity generating apparatus. United Kingdom.

Mohammad, R. S., & S. E., S. (2000). On the Nonlinear Control of Hydraulic Servo-Systems. In *Proceedings of the 2000 IEEE International Conference on Robotics & Automation* (pp. 1276–1282). San Francisco, CA.

Muyeen, S. M. (2012). Calculation Method of Losses and Efficiency of Wind Generators. In S. M. Muyeen (Ed.), *Wind energy conversion systems: Technology and Trends*. New York: Springer-Verlag London Limited. Retrieved from http://books2.scholarsportal.info/viewdoc.html?id=/ebooks/ebooks2/springer/2012-05-29/1/9781447122012

National Instruments. (2009). *The Fundamentals of FFT-Based Signal Analysis and Measurement in LabVIEW and LabWindows/CVI - National Instruments*. Retrieved from http://www.ni.com/white-paper/4278/en/

National Instruments. (2017). *Understanding FFTs and Windowing*. Retrieved from http://download.ni.com/evaluation/pxi/Understanding FFTs and Windowing.pdf

Nishikata, S., & Tatsuta, F. (2013). Studies on a Wind Turbine Generating System that Employs a Thyristor Inverter. *Electrical Engineering in Japan*, *185*(3), 57–66. http://doi.org/10.1002/eej.21262

Nissen, P. D. (2010). Closed cycle refrigerators -Pulse tube coolers. Retrieved from http://www.nbi.dk/~nygard/PDN-Pulsetubecoolers_low2010.pdf

NIST/SEMATECH. (2003). Process or Product Monitoring and Control. In *NIST/SEMATECH e-Handbook of Statistical Methods*. Retrieved from http://www.itl.nist.gov/div898/handbook/toolaids/pff/index.htm

Notardonato, W. U. (2006). *ANALYSIS AND TESTING OF AN INTEGRATED REFRIGERATION AND STORAGE SYSTEM FOR LIQUID HYDROGEN ZERO BOIL-OFF, LIQUEFACTION, AND DENSIFICATION*. University of Florida.

NREL. (2016). Energy Analysis - Energy Technology Cost and Performance Data. Retrieved February 15, 2017, from http://www.nrel.gov/analysis/tech_lcoe_re_cost_est.html

Orecchini, F. (2006). The era of energy vectors. *International Journal of Hydrogen Energy*, *31*(14), 1951–1954. http://doi.org/10.1016/j.ijhydene.2006.01.015

Oy, N. (1992). *New Hydrogen Technologies Project Report: Evaluation of Techniques*.

Partridge, J. K. (2010). *EXPERIMENTAL STUDIES OF LIQUEFACTION AND DENSIFICATION OF LIQUID OXYGEN*. University of Central Florida. Retrieved from https://ntrs.nasa.gov/archive/nasa/casi.ntrs.nasa.gov/20100036659.pdf

Pereira, D. (Mathworks). (2015). Wind Rose - File Exchange - MATLAB Central. Retrieved January 10, 2017, from https://www.mathworks.com/matlabcentral/fileexchange/47248-wind-rose

Philippopoulos, K., & Deligiorgi, D. (2005). Stochastic Modeling of Hourly Average Wind Speed Sequences in National Observatory of Athens , Greece, (September), 1–3. Retrieved from http://www.srcosmos.gr/srcosmos/showpub.aspx?aa=6770

Qiu, L. M., Wang, C., Gan, Z. H., & Dong, W. Q. (2012). Study on G-M type pulse tube cryocooler with a novel active gas distribution system. In *AIP Conference Proceedings*. http://doi.org/10.1063/1.4706921

Queneau, P. E., & Marcuson, S. W. (1996). Oxygen pyrometallurgy at copper cliff - a half century of progress. *JOM*, *48*(1), 14–21.

Radebaugh, R. (1999). Development of the Pulse Tube Refrigerator as an Efficient and Reliable Cryocooler * * * *.

Radebaugh, R. (2007). Historical Summary of Cryogenic Activity Prior to 1950. In R. P. Timmerhaus, Klaus D, Reed (Ed.), *Cryogenic Engineering Fifty Years of Progress* (pp. 3–27). New York, NY. Retrieved from https://books.google.ca/books?id=YGsbU1XVmG8C&pg=PA5&lpg=PA5&dq=Cryogenics+development+from+1850+to+1950&source=bl&ots=QTzlGjpXOr&sig=QZXbQdaMlIi0xYbmTaDCyEH0Esk&hl=en&sa=X&ved=0ahUKEwjquNrwyt_NAhUCOz4KHWA3AUYQ6AEIHjAA#v=onepage&q=Cryogenics development f

Radebaugh, R. (2009). Cryocoolers: the state of the art and developments*. *J. Phys.: Condens. Matter*, *21*(21), 164219–9. http://doi.org/10.1088/0953-8984/21/16/164219

Ragheb, A., & Ragheb, M. (2010). WIND TURBINE GEARBOX TECHNOLOGIES. In *Proceedings of the 1st International Nuclear and Renewable Energy Conference (INREC10)*. Amman, Jordan. Retrieved from http://www.ragheb.co/Wind Power Gearbox Technologies.pdf

Ragheb, M. (2017). WIND SHEAR, ROUGHNESS CLASSES AND TURBINE ENERGY PRODUCTION. Retrieved from http://mragheb.com/NPRE 475 Wind Power Systems/Wind Shear Roughness Classes and Turbine Energy Production.pdf

Ragheb, M., & Ragheb, A. M. (2011). Wind Turbines Theory-The Betz Equation and Optimal Rotor Tip Speed Ratio. In R. Carriveau (Ed.), *Fundamentals and Advanced Topics in Wind Power* (pp. 19–38). InTech. Retrieved from http://cdn.intechopen.com/pdfs-wm/16242.pdf

Rajabhandharaks, D. (2014). *Control of Hydrostatic Transmission Wind Turbine*. San Jose State University. Retrieved from http://scholarworks.sjsu.edu/cgi/viewcontent.cgi?article=8060&context=etd_theses

Rapp, J. (2015). *Hydrostatic Transmission in Wind Turbines Development of Test Platform*. Linkoping University Institute of Technology. Retrieved from https://www.diva-portal.org/smash/get/diva2:851478/FULLTEXT01.pdf

Rastler, D. (2010). *Electricity Energy Storage Technology Options*. Retrieved from www.epri.com

Reif-Acherman, S. (2009). Several motivations, improved procedures, and different contexts: The first liquefactions of helium around the world. *International Journal of Refrigeration*, *32*(5), 738–762. http://doi.org/http://dx.doi.org/10.1016/j.ijrefrig.2009.02.019

Research hubs. (2015). Pitch-regulated and Stall-regulated Wind Turbine. Retrieved April 8, 2017, from http://researchhubs.com/post/engineering/wind-energy/pitch-regulated-and-stall-regulated-wind-turbine.html

Roy, P. C., Das, P. K., & Sarangi, S. K. (2006). SOME EXPERIMENTAL STUDIES ON PULSE TUBE REFRIGERATION. In *Proceedings of the 3rd BSME-ASME International Conference on Thermal Engineering*. Dhaka, Bangladesh. Retrieved from http://bsmeicte2012.iutoic-dhaka.edu/proceedings/3rd-bsme-asme-icte-2006/Final Papers/Paper_BA-097.pdf

Safaei, H., & Keith, D. W. (2014). Compressed air energy storage with waste heat export: An Alberta case study. *Energy Conversion and Management*, *78*(0), 114–124. http://doi.org/http://dx.doi.org/10.1016/j.enconman.2013.10.043

Sasaki, M., Yuge, A., Hayashi, T., Nishino, H., & Uchida, M. (2014). Large Capacity Hydrostatic Transmission with Variable Displacement. *The 9th International Fluid Power Conference*. Retrieved from http://www.artemisip.com/wp-content/uploads/2016/03/2014-03-24to26-9th-IFK-Aaacehn-MHI-DDT.pdf

Shaw, D., Cai, J.-Y., & Liu, C.-T. (2012). Efficiency analysis and controller design of a continuous variable planetary transmission for a CAES wind energy system. *Applied Energy*, *100*, 118–126. http://doi.org/10.1016/j.apenergy.2012.06.024

Sheer, J., Burton, R., & Bluhm, S. (1984). RECENT DEVELOPMENTS IN THE COOLING OF DEEP MINES. *South African Mechanical Engineer*, *34*(1), 12–18.

Shu, Z. R., Li, Q. S., & Chan, P. W. (2015). Investigation of offshore wind energy potential in Hong Kong based on Weibull distribution function. *Applied Energy*, *156*, 362–373. http://doi.org/10.1016/j.apenergy.2015.07.027

Smith, S. W. (1997). The discrete Fourier transform. In *The Scientist and Engineer's Guide to Digital Signal Processing*. Retrieved from http://www.dspguide.com/ch8/3.htm

Taylor, D. (2004). Wind Energy. In G. Boyle (Ed.), *Renewable Energy* (Second). United Kingdom: Oxford University Press, Oxford in association with the Open University, Milton, Keynes.

Tchernev, D. I. (1993). *U.S. Patent No. 5251458*. Washington, DC: U.S. Patent and Trademark Office. Retrieved from https://www.google.com/patents/US5251458

Tetsuya, S. (2002). STATISTICAL AND GEOSTATISTICAL ANALYSIS OF WIND : A CASE STUDY OF DIRECTION STATISTICS. In *Symposium on Geospatial Theory,*

Processing and Applications. Ottawa. Retrieved from http://www.sciencedirect.com/science/article/pii/S0098300406000276
Thomas, R. J., Ghosh, P., & Chowdhury, K. (2012). Role of heat exchangers in helium liquefaction cycles: Simulation studies using Collins cycle. *Fusion Engineering and Design*, *87*(1), 39–46. http://doi.org/10.1016/j.fusengdes.2011.08.009
Thombare, D. G., & Verma, S. K. (2008). Technological development in the Stirling cycle engines. *Renewable and Sustainable Energy Reviews*, *12*(1), 1–38. http://doi.org/http://dx.doi.org/10.1016/j.rser.2006.07.001
Timmerhaus, C., & Flynn, T. M. (1989). *Cryogenic Engineering*. New York: Plenum Press.
Tomaru, T., Suzuki, T., Haruyama, T., Shintomi, T., Yamamoto, A., Koyama, T., & Li, R. (2004). Vibration analysis of cryocoolers. *Cryogenics*, *44*(5), 309–317. http://doi.org/http://dx.doi.org/10.1016/j.cryogenics.2004.02.003
University of Exeter. (2017). Renewable Energy Research. Retrieved from http://emps.exeter.ac.uk/renewable-energy/research/research-interests/offshore/reliability/facilities/southwestmooringtestfacilityswmtf/
Urieli, I. (2010). Engineering Thermodynamics-A Graphical Approach. Retrieved May 3, 2017, from https://www.ohio.edu/mechanical/thermo/
Vaezi, M., & Izadian, A. (2014). Control of a Hydraulic Wind Power Transfer System under Wind Disturbance. In *3rd International Conference on Renewable Energy Research and Applications*. Milwakuee, USA. Retrieved from http://doi.org/10.1109/ICRERA.2014.7016512
Vaisala. (2017). Energy Measurement, Assessment and Forecasting. Retrieved May 5, 2017, from http://www.vaisala.com/en/energy/Pages/default.aspx?utm_medium=direct&utm_source=alias&utm_content=energy
Van der Hoven, I. (1956). Van der Hoven-Power spectrum.pdf. *Journal of Meteorology*, *14*, 160–164. Retrieved from http://rsandt.com/media/Van der Hoven.pdf
Van Sciver, S. W. (2012). *Helium cryogenics*. (S. W. Van Sciver., Ed.) (Vol. 2nd ed.). New York : Springer, c2012. Retrieved from http://books.scholarsportal.info/viewdoc.html?id=/ebooks/ebooks2/springer/2012-05-29/3/9781441999795
Varpe, S. A. (2008). *Control System on a Wind Turbine*. Norwegian University of Science and Technology.
Venkatarathnam, G. (2008). *Cryogenic mixed refrigerant processes*. (K. D. Timmerhaus & C. Rizzuto, Eds.). Springer Science+Business Media, LLC.
Venkatarathnam, G. (2010). *Cryogenic Mixed Refrigerant Processes*. (K. D. Timmerhaus & C. Rizzuto, Eds.)*International Journal of Refrigeration* (Vol. 33). Springer Science+Business Media, LLC. http://doi.org/10.1016/j.ijrefrig.2009.11.013
Wan, Y. H. (2012). Long-Term Wind Power Variability Long-Term Wind Power Variability, (January). Retrieved from http://www.nrel.gov/docs/fy12osti/53637.pdf
Wang, C. (2005). Efficient helium recondensing using a 4K pulse tube cryocooler. *Cryogenics*, *45*(12), 719–724. http://doi.org/10.1016/j.cryogenics.2005.06.010

Wikimapia. (2016). Roskrow Barton Wind Turbines | wind farm. Retrieved March 31, 2017, from http://wikimapia.org/24958130/Roskrow-Barton-Wind-Turbines
Wind Energy The Facts. (2017). Wind atlases. Retrieved January 10, 2017, from https://www.wind-energy-the-facts.org/wind-atlases.html
Woodbank Communications Ltd. (2005). Aerodynamic Lift and Drag and the Theory of Flight. Retrieved April 8, 2017, from http://www.mpoweruk.com/figs/flight_theory.htm
Wu, B., Lang, Y., Zargari, N., & Kouro, S. (2011). Fundamentals of Wind Evergy Conversion System Control. In *Power CoWind Energy Systems* (pp. 25–47). http://doi.org/10.1002/9781118029008.ch2

Appendices

Appendix A. **Conference paper**

Using wind energy to produce cryogens for use in deep mine cooling and ventilation

S. Kunwar, D.L. Millar
Bharti School of Engineering, Laurentian University
935 Ramsey Lake Road
Sudbury, ON, P3E 2C6
Canada
(Corresponding author: skunwar@mirarco.org)

This paper sets out a technical case for the buffering of wind energy variability and intermittency through the direct use of horizontal axis wind turbine work to drive compressor components in air liquefaction cycles. Open loop hydrostatic transmissions and standard torque converters are key system components that provide the necessary conversion between the low speed-high torque characteristics of the wind rotors, and lower torque and high speed characteristics required for compressors used in cryogenic plant. These, together with the other principal components for such a wind-to-cryogen device, are reviewed and compared with the components of conventional systems. The comparison extends to an economic analysis based on i) a wind turbine electricity generation model, ii) a grid-electricity-to-air compression process and iii) a compressed air to cryogen process. The process of wind rotor work-to-cryogen is compared alongside these more conventional options to reveal differences in cryogen production cost, life-cycle energy consumed and carbon savings, which motivate the investigations. The work also discusses novel options for i) integration of wind energy into energy supply systems via cryogen production, ii) wind energy storage in the form of cryogens, iii) wind energy produced cryogens as energy vectors, and iv) the novel application of a wind-to-cryogen process to provide a source of coolth to cool the ventilating air in deep mines.

I. Introduction and Motivation - Deep Mine Cooling

The development of the alternative means of provision of cooling is motivated by the exhaustion of world class surface mineral ore bodies and the consequent need to exploit deeper ore bodies using underground mining methods. Also, ore bodies that are already exploited using underground mining methods are extending workings deeper and so that the working environment for both workers and machinery is becoming hotter. At 3,000 metres depth, the temperature of air entering ore producing areas may be 20°C to 30°C higher than the surface air temperature due to (mostly) adiabatic autocompression alone in the confined enmvironment of an air shaft. Ventilation air mass flow rates are of order 1 tonne/s in medium to large scale producing underground mines. At these depths where the virgin rock temperatures exceed 50°C in most mining areas, geothermal heat transfers will further increase the air temperature. The current methods of cooling the air centre on vapour compression refrigeration cycles, with large scale cooling towers to eject condenser heat and bulk air cooling chambers (both direct contact heat exchangers with high factors of merit as high as 0.7 to 0.8 for industrial packed towers (McPherson, 2000). The ratings of the largest plants used in mines can exceed 60MW_r. Refigeration plants can also be installed in the sub-surface to simplify cooling distribution, but these operate with much lower coefficients of performance due to high condenser heat reject temperatures. The cumulative effect of these circumstances is a dramatic increase in energy consumption and the cost of production of raw materials due to the introduction of these large scale refrigeration loads as mining moves deeper.

The principal desired characteristic of an alternative cooling method is thus that it should deliver cooling cheaply. Load factors of current refrigerating plants are approaching unity, or will do so, with the greater depths, so the cooling needs to be provided continuously. This means that the capital costs of cooling plant (conventional or alternative) are less important than the operating and energy input costs. This suggests the use of a renewable energy source to provide cooling because the input energy costs are close to zero. However renewable energy resources arise from natural geo-processes that are subject to natural variability and intermittency and so, whatever alternative cooling method is devised must be able to store the coolth produced while the renewable energy resource is active and used at 'on-demand' rates. The

locations where the renewable energy resources are most abundant may be coincident with the locations of mineral deposits, but it must be assumed that, for the general case, they will not. Consequently, the alternative cooling method must allow for means of transportation and distribution of the cooling produced between producing areas and the consumer centres. In summary the desired characteristics are that the cooling should: be produced cheaply, be storable and be transportable and distributable.

We propose that the production of liquefied air using wind energy may be a suitable solution to the problem of providing cooling to deep mines. Wind turbines are the most mature, and largest scale technology that harnesses renewable energy. If configured for the production of liquefied air, rather than electricity, the traditional difficulties of integrating wind energy into electricity distribution grids are avoided altogther, the cooling is stored in the form of the condensed liquid, and the storage, distribution and transportation of cryogens at bulk scales also use established, mature technologies. What we discuss in the remainder of this paper is a possible configuration of a wind turbine for the production of liquefied air, rather than electricity.

II. The Simple Linde Hampson Cycle

Carl Von Linde and William Hampson independently developed the air liquefaction cycle called the Linde-Hampson cycle in 1895 (Venkatarantham, 2008). Atmospheric air is first compressed (pressure ratio typically 200) and then passed through heat exchangers to cool it down (typically lower than -150°C) after which it is allowed to expand, either through an expansion valve or an expansion turbine. In the latter instance some work can be extracted from the fluid. In either case, a proportion of the air condenses and is collected in a Dewar vessel. The remaining non-condensed air is sent to the cold side of the heat exchanger to cool the compressor delivery air and then is returned to the compressor, completing the cycle as shown in the (the Linde Group, 2004 & Wankat et al., 2010).

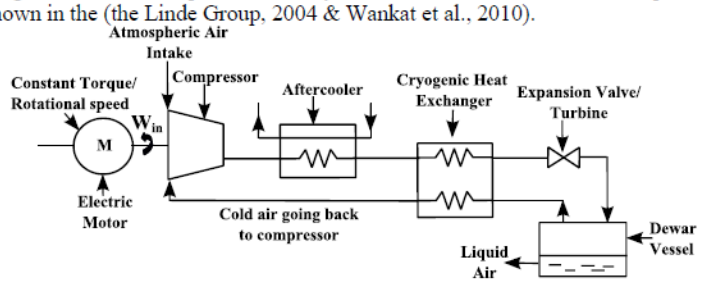

Figure 1: Schematic of the Linde-Hampson liquefaction system

III. Simple air liquefaction system integrated with wind turbine:

With a steady rate of work input as depicted in Figure 1, such a system may be reliably expected to produce cryogens as the Linde Hampson cycle has been used commercially for decades. The proposed concept is to integrate wind energy capture with a cryogen production system (a cryogen is a gas/air which has a boiling point at atmospheric pressure below -150^{0}C). This is illustrated in Figure 2. Rotational speed and torque developed by a wind turbine rotor can be highly variable and so the key question that arises is whether liquefed air would be as efficiently produced. In order to buffer the intermittency and variability of the wind energy in the very short term, an open loop hydrostatic transmission could be deployed as in Figure 2. Such a system would consist of a positive displacement hydraulic pump, a hydraulic motor, required control valves, pipes, pressurized and non-pressurized reservoirs and fittings. The motor is driven by pressurized fluid drawn from an accumulating reservoir, replenished by the pump. Thus the hydrostatic transmission can also be used to adjust and regulate wind rotor speed as described by Esposito (2009), and the rotor blade tip speed ratio can be regulated to maximise efficiency over varying wind speeds. The fluid coupling of the wind rotor to the compressor is a form of torque converter equipped with energy storage.

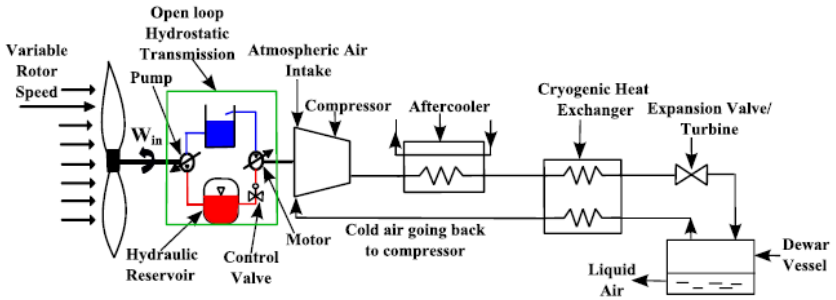

Figure 2: Schematic diagram of the proposed concept, considered installed within a wind turbine nacelle

The whole liquefaction system depends on the effectiveness of the heat exchangers. Compact indirect heat exchangers such as the plate and fin heat exchangers, have proven to be the most suitable for cryogenic purposes because they separate the fluid streams and high surface area available for heat transfer (Gupta & Atrey, 2000).

There are examples of reciprocating and rotary compressors that are of positive displacement type which work by mechanically changing the volume of the working fluid. Dynamic displacement machines compress gases by mechanically changing the velocity of the working fluid and can sustain high flow rates (Eastop, 1993). However these compressors are open and thus there is a total loss of pressure when rotation ceases. This must be a consideration if intermittent wind energy is to drive the system, and leads directly to the adoption of a positive displacement compressor. The compression process can be considered isentropic while an experimentally determined isentropic efficiency characterises the deviation from this ideality to permit the characterisation of the state of the air after the real compression process. For multi-stage compression with intercooling and aftercooling, the compression process moves closer to an isothermal compression process, reducing the required input work.

An expansion valve, expansion engine or expansion turbine can be used to expand the air and lower its temperature and pressure, so that a fraction of it condenses. For the latter two options, isentropic processes and isentropic efficiencies can be established for analysis as for the compressors. For the expansion valve an irreversible isenthalpic process applies, with no heat or work transfer (Eastop, 1993). The liquefied air may be collected and stored in an insulated vessel called a Dewar flask.

IV. Advances in air liquefaction and separation plants:

The compressor, heat exchanger and expander components used in the modern air separation and liquefaction plants have been subjected to improvements in efficiency, product recovery and feed air purification over years to gain higher effectivenesse than Linde-Hampson's original systems (Castle, 2000). More recently, there have been changes in the air distillation column to utilize low-pressure, high efficiency structured packing instead of the sieve trays. Control improvements ensure maximum stability, greater liquid production with higher purity both for the dynamic and steady state conditions, and they also allow for remote control of the plants. For adsorption and air separation processes another recent innovation is the use of molecular sieve adsorbents (Castle, 2000).

The major power consuming machines in the air separation and liquefaction system are the compressors. Therefore significant effort has been expended in improve their effectiveness and the efficiency of the expanders, and to reduce the overall specific power consumption (kWh/kg cryogen). The use of computational fluid dynamics (CFD) to enhance geometry and to assess effects of stator wheels and guide vanes has led to some improvement. Active magnetic bearings have also been introduced in the expansion turbines to decrease the friction losses (Castle, 2000). Air purification with the improved, cheaper,

adsorbents has reduced the overall capital and operating costs (Castle, 2000). Large vacuum-brazed heat exchangers have enhanced heat transfer, have conserved refrigeration effect and have permitted multi-stream configurations (Castle, 2000). In separation plants, the conventional arrangement of the condenser/reboiler in the low pressure liquid oxygen sump can be replaced with the downflow arrangement with no hydraulic head following effective removal of hydrocarbons in the process stream and lead to 3-4% reduction of the overall power consumption (Castle, 2000). Refrigeration circuits integrated with air liquefaction systems are the current features of the air liquefaction systems that have increased productivity and lowered the overall capital and operating costs. The larger plants usually have complex process schemes to reduce the costs (Castle, 2000).

The table and the paragraph below present specific power consumption for various cycles for different fluids.

Table: Specific power consumption for various fluids using Linde-Hampson cycle (Kanoglu et al., 2007)

	Air	Nitrogen	Oxygen	Argon	Methane	Fluorine
Liquefaction temperature (^{0}C)	-194.2	-195.8	-183.0	-185.8	-161.5	-188.1
Fraction of gas liquefied	0.0823	0.0756	0.107	0.122	0.199	0.076
Cooling effect (kWh/kg liquid)	0.117	0.120	0.112	0.075	0.253	0.095
Work input (kWh/kg liquid)	1.522	1.720	1.043	0.736	1.080	1.239

Similarly, the specific power consumption for hydrogen liquefaction using pre-cooled Claude cycle is 12.5-15 kWh/kg_{LH2}[4], by theoretical pre-cooled Linde-Hampson system is 64.5-71.7 kWh/kg_{LH2} and by theoretical helium-refrigerated system is 29.3-49.5 kWh/kg_{LH2}. The specific power consumed by large scale Praxair, Air products and Air Linde plant system are also ~12-15 kWh/kg_{LH2}, by WE-NET (with Nitrogen pre-cooled large-scale Claude plant) is ~8.5 kWh/kg_{LH2} and that by four helium Joule-Brayton cascade cycle is 5.04 kWh/kg_{LH2} (Krasae et al, 2010).

V. Cost comparisons for various power generating systems using wind energy:

-Wind turbine installation costs:

For electricity generation from wind turbines the largest constituents of the total installed development cost are the wind turbine rotor, gear box and tower which together account for 50-60%. The generator, transformer and/or power electronics and auxiliaries can account for 13%. Overall, the turbine cost is in the range of 64-84% of the development cost. Items such as grid connection, civil works, and other development costs account for the balance (Blanco, 2009 and EWEA 2009). However, installation and power generation costs can vary appreciably depending on the regulatory regime, installation site, and local costs for materials and services, as is illustrated in Table 1. According to the International Energy Agency (IEA) Wind Energy Roadmap 2011, capital cost reductions in land-based wind turbine developments will be 23% as the sector matures and scales to 2050. The corresponding estimate for offshore installation is 35%.

Table 1: Cost of different power generation technology (Source: Renewable Energy Network Policy for the 21st Century, 2012)

Power Generation Technology	Typical Characteristics	Capital Costs (USD/kW)	Typical costs (US cents/kWh)
Wind: Onshore	Turbine size: 1.5-3.5 MW Capacity factor: 20-40%	1,750-1,770 (General) 925-1,470 (China & India)	5-6 (OECD) 4-16(non-OECD)
Wind: Offshore	Turbine size: 1.5-7.5 MW Capacity factor: 35-45%	3, 000-4,500	15-23
Wind: Small-scale	Turbine size: Upto 100 kW	3,000-6,000 (USA) 1, 580 (China)	15-20 (USA)

OECD = Organization for Economic Co-operation and Development

-Costs of various energy generating systems using wind power:

The electricity generated by wind energy can be used for general purposes if the turbine is connected to an electricity distribution system. If, in the same place as the wind energy is harnessed, the design intent is to compress air for cryogen production, the generation of electricity may be an unnecessary intermediate energy conversion step (Shaw et. al, 2012). The following diagrams clearly present various integration methods for energy generation using wind power. Differences in the annuitized costs along with the efficiency of each system are also presented.

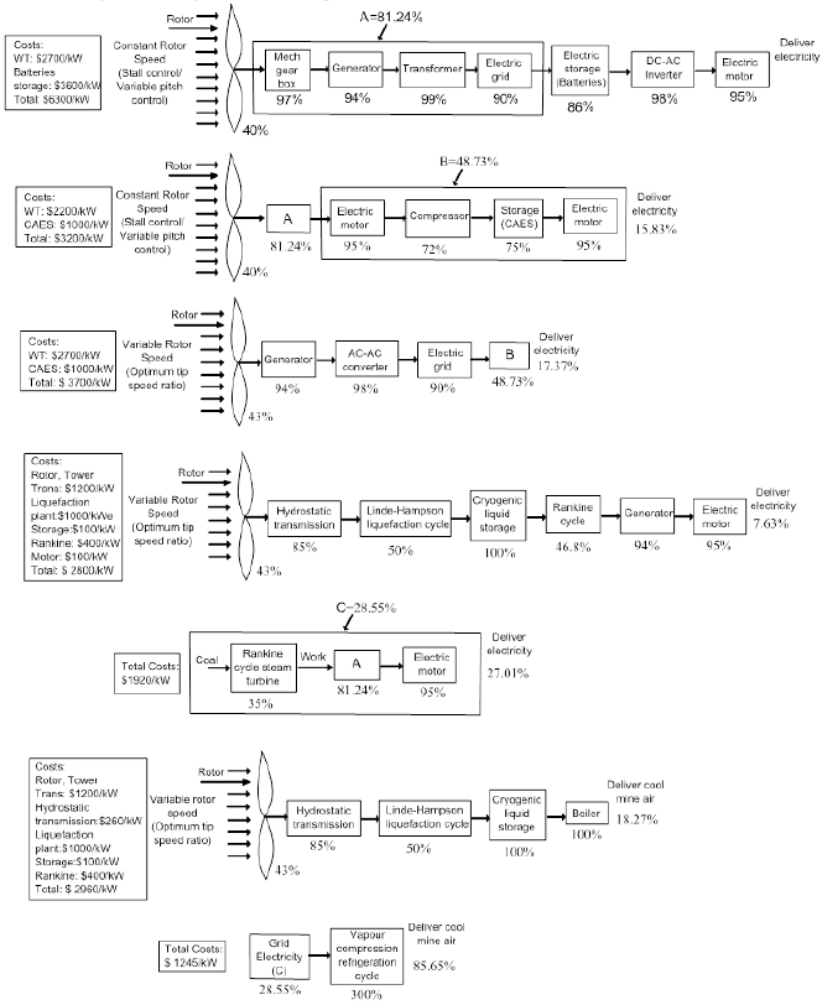

Figure 3: Schematic showing various energy generating systems using wind power with their respective costs and overall efficiencies. WT=Wind Turbine

The efficiency diagrams are presented above for comparison of different integration technologies for electricity and cooling effect generation using wind energy. All these options are compared with each other and also with the proposed Cryovent concept. Capital cost comparison is done. The annuitized costs are also calculated with some assumptions and the references available. The overall efficiencies of each system are shown on the right, while the capital costs are given on the left side of the respective integration diagrams.

Assumptions:

The vapour compression cycle is assumed to be 300% efficient (COP=3) and the Rankine cycle boiler is assumed to be 100% efficient. The cryogenic liquid storage is assumed to be 100% efficient (Li et al, 2010). The Rankine cycle steam turbine efficiency is assumed to be 37%. The cost of liquefaction plant is calculated based on KSH Dick engg, 2014. The average cost of a Rankine cycle generator is taken as $400/kW and that of an electric motor to be $100/kW. The maximum efficiency of a constant rotor speed wind turbine is taken to be 40% and that of the variable rotor speed to be 43%. The wind turbine installation costs are taken from GL Garrad Hassan report.

Generating electricity:

1. In first power generation method, with constant rotor speed using the conventional power generation system (system with gear box, generator and transformers), and storing electricity in batteries, the system will be 26.01% efficient whereas the cost of such an integration will be ~$2450/kW of power generated.
2. In the second power generation method, again with the constant rotor speed of the wind turbine, generating power, compressing air and storing the electricity in the form of compressed air, and generating electricity on demand will be 15.83% efficient with a cost of ~$2125/kW.
3. The third power generation method with variable rotor speed (with optimum tip speed ratio) and the gearless generator with AC-AC converter will be 17.3% efficient whereas the cost of such integration will be ~$2325/kW of power generated.
4. The proposed cryovent concept (fourth diagram) with a hydrostatic transmission, Linde-Hampson liquefaction system, with the storage in Dewar vessel, the power generation will be 7.63% efficient with the total costs of ~$2800/kW.
5. The conventional coal-fired power plant (fifth diagram) will be 28.5% efficient for electricity production.

Delivering cool mine air:

6. The proposed Cryovent concept for delivering cool mine air (sixth diagram) is assumed to be 18.27% efficient with total cost of ~$2700/kW but providing some amount of cooling. The annuitized cost for this system would be $7,900k/year with zero input energy costs. The same concept would cost $6,958k/year if it uses electricity to run the system with $2, 499k/year input energy costs.
7. The conventional vapor compression refrigeration plant run by the electric grid would be 85.8% efficient with ~$900/kW total costs providing the same amount of cooling as cryovent but the annuitized cost for this system would be $6, 963k/year with $3,796k/year input energy costs. (The refrigeration plant costs are calculated assuming 20MW_r, with COP=3, interest rate=10%, 15 years life time, and the installation cost of $65/MWh).

VI. Wind energy power generation and storage issues:

The major issue with exploitation of wind energy is its variability. It can be a barrier for some processes where a continuous source of power supply is needed. Studies have been done on the storage of the variable wind energy which can offset its variability and unpredictability. Wind energy can be transformed into compressed air which can then be stored in a tank (for a small-scale), in underground (abandoned) mines like paste-fills or in the salt caverns (for large-scale purposes), and also in above ground reservoirs- pressure vessels (Safaei & Keith, 2014) which can later be used to generate electricity on demand. The underground storage capacity can be affected by the geological constraints (Ameel et al., 2013). Wind energy can also be stored using batteries but storing wind energy in batteries is expensive. As discussed by Shaw et al. in their article, according to Electric Power Research Institute (EPRI, 2010),

the total installed cost for storing wind energy using Compressed Air Energy Storage (CAES) is around USD 125/kW/h for 8 hour duration and USD 450/kW/h for lead acid storage for 4 hour duration.

Liquefied air can store wind energy compactly. 1 kg of liquefied air at atmospheric temperature stores around 440 kJ of cooling (at ~ -200°C) that would be recovered through reboiling using the heat within ambient (mine ventilation) air (at ~30°C). 1 m^3 of liquefied air effectively stores 400 MJ (111 kWh) of cooling for the same conditions. Once the cryogens are produced, they can be stored in an insulated vessel at atmospheric pressure and then transported easily. If they are produced offshore and need to be stored onshore for electricity generation later, they can be delivered onshore with no extra cost except the pumping costs (Li et al., 2010). The energy density of cryogens is around 20 times higher than that of the CAES. Cooling loss with cryogens stored in a Dewar vessel is principally by heat dissipation which is ~1%/day (Li et al., 2010).

For the production of work from the stored cooling, the recovery efficiency of cryogens is as low as 36.8% with the Rankine cycle using waste heat and around 43% with combined cycle (combined Rankine and Linde cycle) at 300K. This can be compared to CAES in which the recovery efficiency is around 75%. If the compression and expansion processes are not isothermal, the recovery efficiency of the stored cryogens decreases further up to 22%. The efficiency increases to 70% when using high grade heat at 800K (Ameel et al., 2013). These figures may present a negative picture of the use of cryogens as a form of energy storage, but they are for the recovery of work from the stored heat, not the recovery of cooling capacity for which the efficiency will depend on the factor of merit of the heat exchangers.

VII. Comparison of Greenhouse Gas Emissions from various energy sources:

The life-cycle Green House Gases (GHG) emission intensity (mean values) from various electricity generation technologies in tonnes CO_2e/GWh, according to WNA (2011), is 1, 054 from lignite, 888 from coal, 733 from oil, 499 from natural gas, 85 from Solar PV, 45 from biomass, 29 from nuclear and the hydroelectric and wind power being the least carbon emitters emitting only around 26 tonnes CO_2e/GWh (WNA Report, 2011). The carbon emissions associated with wind energy account for the carbon emitted during the manufacture of different components of wind turbine and its site installation.

VIII. Conclusion:

Integrating wind power with cryogen production process is one of the low-carbon and comparatively most economic method to generate and store energy.

Application of the energy vector produced by integrating wind energy to the liquefaction system mechanically as explained in this paper would be for several purposes. But the motivation for the development of this concept comes from the need of high-volume of ventilating air in the deep-mines. With the available natural resources being depleted in the surface, the global mining industries are acquiring the underground concept to increase the mine-operation life by some additional years. The fact that the auto-compression and geothermal gradient only add heat to the prevailing hot temperature in the underground mine working area is putting the mining industries in a constraint of having an efficient and cost-effective way for deep mine cooling and ventilation.

Use of cryogens that can be delivered by a bore-hole from surface to the sub-surface will eliminate the need of huge ventilation shafts. The cryogens also provide bulk cooling to the ventilating air during expansion. Though liquefying air is costly, the initial installment costs of such plant is offset with the two major benefits of using cryogens as compared to the conventional ventilation method for the deep mines, which are the low-cost electricity and the additional benefit of cooling. Therefore on the long run, the proposed concept of producing cryogens with the use of wind energy, storing the surplus production and using them on demand for the deep mine cooling and ventilation can be a promising way to minimize the energy costs in the mine operations.

References:

1. McPherson, M. J. (2000). *Subsurface Ventilation and Environmental Engineering* .1625 Shaw Ave #103, Clovis, CA 93611: Mine Ventilation Services, Inc.
2. Venkarathnam, G. (2008). Cryogenic mixed refrigerant processes. International Cryogenic Monograph Series.
3. The Linde Group, (1879). http://www.linde-engineering.com/internet.global.lindeengineering.global/en/images/chronicle_e%5B1%5D19_9855.pdf (Accessed on 6/25/2014)
4. Wankat, Phillip C., & Kostroski, Kyle P. (2010). Hybrid air separation processes for production of oxygen and nitrogen. Separation Science and Technology, *45*(9), 1171-1185.
5. Esposito, A. (2009). *Fluid power with applications-7th edition*. Upper Saddle River, New Jersey 07458: Pearson Education, Inc.
6. Gupta, P., & Atrey, M. D. (2000). Performance evaluation of counter flow heat exchangers considering the effect of heat in leak and longitudinal conduction for low-temperature applications.40(7), 469-74.
7. Eastop, T. D. (1993). *Applied Thermodynamics for Engineering Technologists*. Edinburgh Gate, Harlow, Essex CM20 2JE, England: Pearson Education.
8. Castle, W. F. (2002). Air separation and liquefaction: Recent developments and prospects for the beginning of the new millennium. *International Journal of Refrigeration, 25*(1), 158-172. doi:http://dx.doi.org/10.1016/S0140-7007(01)00003-2
9. Kanoglu, M., Dincer, I., & Rosen, M. A. (2008). Performance analysis of gas liquefaction cycles. *International Journal of Energy Research, 32*(1), 35-43. doi:10.1002/er.1333
10. Krasae-in, S., Stang, J. H., & Neksa, P. (2010). Development of large-scale hydrogen liquefaction processes from 1898 to 2009. *International Journal of Hydrogen Energy, 35*(10), 4524-4533. doi:http://dx.doi.org/10.1016/j.ijhydene.2010.02.109
11. McCourt, I. (1983). Hydrostatic variable speed/torque transmissions: A basic introduction. Paper presented at the Proceedings of the Conference on Drives/Motors/Controls *83,* 192-5.
12. Casadei, D., Serra, G., Tani, A., & Zarri, L. (2013). Direct torque control for induction machines: A technology status review.
13. Bartos, J. (2006). Understand compressor types to make the right selection. Plant Engineering, 60(1), 42-5.
14. Eastop, T. D. (1993). *Applied Thermodynamics for Engineering Technologists*. Edinburgh Gate, Harlow, Essex CM20 2JE, England: Pearson Education.
15. Yeter, P., Guler, O., & Akdag, S. A. (2012). The impact of wind speed variability on wind power potential and estimated generation cost. Energy Sources, Part B (Economics, Planning and Policy), 7(4), 339-47.
16. Gibescu, M., Brand, A. J., & Kling, W. L. (2009). Estimation of variability and predictability of large-scale wind energy in the Netherlands. Wind Energy, 12(3), 241-260.
17. Izadian, A., Hamzehlouia, S., Deldar, M., & Anwar, S. (2014). A hydraulic wind power transfer system: Operation and modeling. IEEE Transactions on Sustainable Energy, 5(2), 457-65.
18. Mason, J. E., & Archer, C. L. (2012). Baseload electricity from wind via compressed air energy storage (CAES).*16*(2), 1099-109.
19. Nishikata S., & Tatsuta F. (2013). Studies on a Wind Turbine Generating System that Employs a Thyristor Inverter. Electrical Engineering in Japan (English Translation of Denki Gakkai Ronbunshi), 130(4), pp. 407-414.
20. Yukita, K., Washizu, S., Nakano, H., Torii, A., Ueda, A., Goto, Y., & Ichiyanagi, K. (2012). A study of AC link and DC link method for wind power generation connected to electric power system. Electrical Engineering in Japan (English Translation of Denki Gakkai Ronbunshi), 178(3), pp. 21-30.
21. Joselin Herbert, G. M., Iniyan, S., Sreevalsan, E., & Rajapandian, S. (2007). A review of wind energy technologies. Renewable and Sustainable Energy Reviews, 11(6), 1117-1145. doi:http://dx.doi.org/10.1016/j.rser.2005.08.004
22. Milligan, M., Ela, E., Lew, D., Corbus, D., Yih-huei Wan, Hodge, B., & Kirby, B. (2012). Operational analysis and methods for wind integration studies *3*(4), 612-19.
23. Queneau, P. E., & Marcuson, S. W. (1996). Oxygen pyrometallurgy at copper cliff - a half century of progress. Jom, *48*(1), 14-21.

24. Shaw, D., Jyun-Yu Cai, & Chien-Ting Liu. (2012). Efficiency analysis and controller design of a continuous variable planetary transmission for a CAES wind energy system. Applied Energy, 100, 118-26. doi:10.1016/j.apenergy.2012.06.024.
25. Dindorf, R. (2012). Estimating potential energy savings in compressed air systems. Procedia Engineering, *39*(0), 204-211. doi:http://dx.doi.org/10.1016/j.proeng.2012.07.026
26. Li, Y., Chen, H., Zhang, X., Tan, C., & Ding, Y. (2010). Renewable energy carriers: Hydrogen or cryogens/nitrogen? Applied Thermal Engineering, 30(14–15), 1985-1990. doi:http://dx.doi.org/10.1016/j.applthermaleng.2010.04.033
27. Ameel, B., T'Joen, C., De Kerpel, K., De Jaeger, P., Huisseune, H., Van Belleghem, M., & De Paepe, M. (2013). Thermodynamic analysis of energy storage with a cryogens rankine cycle. Applied Thermal Engineering, 52(1), 130-140. doi:http://dx.doi.org/10.1016/j.applthermaleng.2012.11.037
28. Safaei, H., & Keith, D. W. (2014). Compressed air energy storage with waste heat export: An alberta case study. Energy Conversion and Management, 78(0), 114-124. doi:http://dx.doi.org/10.1016/j.enconman.2013.10.043
29. Deep mine cooling study, MIRARCO (2014).
30. World Nuclear Association, WNA (2011) http://www.worldnuclear.org/uploadedFiles/org/WNA/Publications/Working_Group_Reports/comparison_of_lifecycle.pdf (Accessed on 6/4/2014)
31. Renewable Energy Network 21, 2013 http://www.ren21.net/portals/0/documents/resources/gsr/2013/gsr2)013_lowres.pdf (Accessed on 6/4/2014)
32. International Energy Agency (IEA) 2011, Wind Energy Roadmap. Retrieved from https://www.iea.org/media/workshops/2011/oao/Chandler_wind_roadmap.pdf (Accessed on 6/4/2014)
33. KSH Dick Engineering, (2010). High Purity Oxygen Line: Vale Canada Limited. http://www.dickeng.com/projects/minerals-and-metals/high-purity-oxygen-line/ (Accessed on 7/6/2014)
34. GL Garrad Hassan, (2012). Assessment of the estimated costs of wind energy in British Columbia. http://www.canwea.ca/pdf/Assessment_Est-Cost-of-Wind-Energy_BC.pdf (Accessed on 6/23/2014)
35. The liquid air energy network. http://liquidair.org.uk/full-report/report-chapter-six/ (Accessed on 4/26/2014)
36. World nuclear organization, (2001). http://www.world-nuclear.org/ (Accessed on 6/5/2014)
37. The Diavik Diamond Mine, (2012). http://www.diavik.ca/ENG/ouroperations/565_wind_farm.asp (Accessed on 6/23/2014)
38. Enercon wind turbines, http://www.wind-power-program.com/Library/Turbine%20leaflets/Enercon/ENERCON_Product_Overview_Eng.pdf (Accessed 7/14/2014)
39. Gear Technology Magazine, www.geartechnology.com, July 2011 (Accessed on 7/9/2014)
40. Grauers, A. (1996). Efficiency of three wind generator systems. http://faculty.mu.edu.sa/public/uploads/1337956177.4188loss_mech_elec..pdf (Accessed on 7/6/2014)
41. Virginia transformer Corp, http://www.vatransformer.com/Transformer-Products.aspx (Accessed on 7/9/2014)
42. Brown, M. A. (2014). Enhancing efficiency and renewables with smart grid technologies and policies. *Futures, 58*(0), 21-33. doi:http://dx.doi.org/10.1016/j.futures.2014.01.001
43. Boyle, G. (1996). Renewable Energy: Power for a Sustainable Future. Walton Street, Oxford OX2 6DP, UK: Oxford University Press.
44. Cuevas, C., Lebrun, J., Lemort, V., & Winandy, E. (2010). Characterization of a scroll compressor under extended operating conditions. *Applied Thermal Engineering, 30*(6–7), 605-615. doi:http://dx.doi.org/10.1016/j.applthermaleng.2009.11.005
45. Power electronics Europe (2011) http://www.power-mag.com/ (Accessed on 7/5/2014)
46. Poullikkas, A. (2013). A comparative overview of large-scale battery systems for electricity storage. *Renewable and Sustainable Energy Reviews, 27*(0), 778-788. doi:http://dx.doi.org/10.1016/j.rser.2013.07.017
47. Hydraulics & Pneumatics, http://hydraulicspneumatics.com/hydraulic-pumps-amp-motors/hydrostatic-transmissions-power-play-wind-turbine-design (Accessed on 7/6/2014)

Appendix B. Script for Higuchi algorithm

```
kmax = 20000;
kinc = 1;
NumInAve=300;

NumK = fix(kmax/kinc);

K=zeros(1,NumK);
MyLk=zeros(1,NumK);


K(1) = 1;
for i = 2:NumK
    K(i)=K(i-1)+kinc;
end


for i = 1:NumK
  MyLk(i)=Lk(y,NumInAve,K(i));
end

PlotHiguchi(K,MyLk)
```

Appendix C. Parameter list and script written by candidate for comparison of the hydraulic wind turbine model with that of Hamzehlouia et al. (2013)

```
% wind turbine parameter
rho_air = 1.225;         % Air density in kg/m^3
R = 16;                  % wind blade radius in m
Area = pi()*R^2;         % Blade swept area in m^2
pitch= 0;                % Pitch angle in degree
c1=0.5176;               % Parameter for power coefficient
c2=116;                  %Parameter for power coefficient
c3=0.4;                  %Parameter for power coefficient
c4=5;                    %Parameter for power coefficient
c5=21;                   %Parameter for power coefficient
c6=0.0068;               %Parameter for power coefficient
Cp_opt=0.48;             %Optimal power coeffcient
lamda_opt=8.1;           %Optimal tip-speed ratio
Tip_rd = 2*pi*R;         %Tip rotation distance
% Pump
Dp = 0.0226;     %Pump_displacement (m^3/rev)
PVeff=0.95;     %Pump_vol_eff
PTeff=0.90;      %Pump_total_eff
PPnom=30000;      %Pump_nominal_pressure (kPa)
Pwnom=1800;      %Pump_nominal_angular_velocity
Pvisc_nom=5;     %Pump_nominal_viscosity
w_p=560;         %Pump_ref_speed
Rho=850;         %Fluid density (kg/m3)
visc=0.00000712;     %fluid_viscosity (m2/s)
KP_Leakage=Dp*Pwnom*(1-PVeff)*Pvisc_nom*Rho/(PPnom*visc*Rho);  %Pump leakage
coeff
%Motors
DmA = 0.00013;  %(m3/rev)Motor_displacement
DmB = 0.00013;   %(m3/rev) %Motor_disp
MVeff=0.95;     %Motor_volumetric_eff
MTeff=0.90;     %Motor_total_eff
MPnom=30000;     %(kPa)Motor_nominal_pressure
Mwnom=1800;     %(rpm) %Motor_nominal_angular_velocity
Mvisc_nom=5;     %Motor_nominal_kinemotoric_visc
I_mA=0.0005;    %(kg/m2) %Motor_inertia
B_mA=0.0026;    %(Nm/(rad/s)) %damping coefficient
I_mB=0.0005;    %(kg/m2) %Motor_inertia
B_mB=0.0022;    %(Nm/(rad/s)) %damping coefficient
KMA_Leakage=DmA*Mwnom*(1-MVeff)*Mvisc_nom*Rho/(MPnom*visc*Rho); %Pump Leakage
coeff
KMB_Leakage=DmB*Mwnom*(1-MVeff)*Mvisc_nom*Rho/(MPnom*visc*Rho); %Pump Leakage
coeff
TL=0            %Nm
```

```
%Compressebility
SG = 0.94;
Gamma=62.4*0.88;
Rho=850;             %(kg/m3)
Visc=0.00000712;     %(m2/s)
B=1266394;          %Fluid bulk modulus (kPa)
L=10;               %(m)%Pipe length
D=(3/8);            %Pipe diameter
A=pi*(D/2)^2;       %Area of pipe
g=9.81;             %(m/s^2) Acc due to gravity
V=2;                %(m^3)
%Check valve
P_0 = 15341;          %(kPa) Cracking pressure
C=0.2;                %flow coeff
A_disc=0.000452;      %(m^2) Area of valve
I_b = (sqrt(A_disc/pi)*2*pi);  %valve perimeter
k_s=10;         %spring stiffness
%PRV
Kzb=2.2;
P_b = 30000;    %PRV set pressure
```

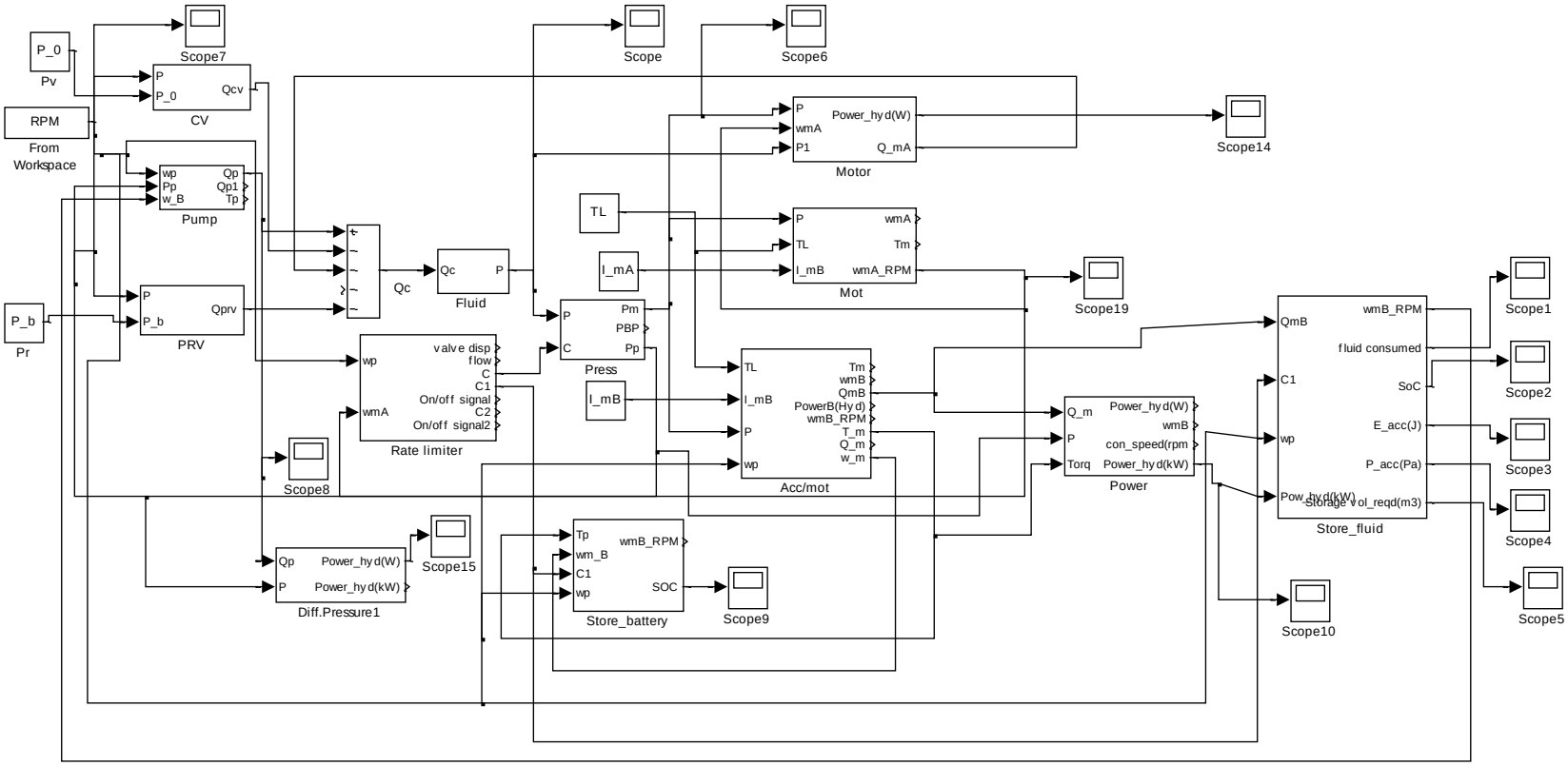

Figure C.1: Simulink model for a hydraulic wind turbine

Appendix D. Parameter list and script written by candidate for the GM cryocooler unit

```
%Compressor
V0=0.0000013;          %Dead volume (m3)
Vs=0.0000375;         %swept volume (m3/rev)
Vol_flow = 0.00217;   % (m3/s)
%Regenerator
Length_reg = 0.10;    %length (m)
Diam_reg = 0.02;      %diameter (m)
Porosity=0.4;         %Porosity
Hyd_diam=0.00001;     %Hydraulic diam (m)
%Displacer
Lt=0.141;              %length (m)
dt=0.046;             %diameter (m)
%cold end block
Vdcx=0.00005;      %dead volume (m3)
%hot end
Vdhx=0.00005;      %dead volume (m3)
Vdrg=0.00005;      %Voild vol reg (m3)
Vdac=0.00005;      %Void volume aftercooler (m3)
Vd=0.00022;        %Disp vol (m3)
Vcomp=0.0022;      %compressor cylinder vol (m3)
%Valve
Diam=0.0005;      %valve diam (m)
P0=16000000;      %average pressure (Pa)
f=2.4;             %frequency (Hz)
Tc=77.325;           %cold end temp (K)
Th=297.15;          %hot end temp (K)
%He-gas properties (@p2 & 300K)
rho=2.64;            %He density (kg/m3)
C_p=5192.0;           %sp heat cap (J/kgK)
R=2074.6;             %Gas constant for He (J/kgK)
G=1.67;               %Gamma for He
Dyn_visc=19.81e-6;    %Dynamic viscosity (Ns/m2)
Vh=0.00009;           %hot end volume(m3)
Vc=0.00009;           %cold end volume(m3)
Xd=Vc/Vd;
%For Dewar heat transfer
Dn = 0.1016;        %outer diameter Dewar neck (m)
De = 0.03175;       % outer diameter extraction valve (m)
D_prv = 0.03175;    % outer diameter prv and burst disc valve (m)
D_li = 0.0127;      % outer diameter level indicator (m)
D_vac = 0.0381;     % outer diameter vacuum release port (m)
Area_neck = pi*(Dn)^2;        %Dewar neck area (m2)
Area_ext_vlv = pi*(De)^2;     %Extraction valve area (m2)
Area_prv = pi*(D_prv)^2;      %Pressure relief valve area (m2)
Area_li= pi*(D_li)^2;         %Level indicator area (m2)
Area_vac = pi*(D_vac)^2;      %Vacuum port area (m2)
%Surface area for radiation heat transfer
```

```
SA_neck = Area_neck/4;          %surface area neck (m2)
SA_ext_vlv = Area_ext_vlv/4;    %surface area ext valve (m2)
SA_prv = Area_prv/4;            %surface area prv(m2)
SA_li = Area_li/4;              %surface area level ind(m2)
SA_vac = Area_vac/4;            %surface area vac port (m2)
%For radiative heat transfer
%Acc to ASME Boiler & Pressure vessel code section VIII
Fe = 0.04215;                     % Emmisivity factor
F_1_2= 1;                         %configuration factor
sigma = 5.67e-08;                  %Stefan-Boltzman constant (W/m^2-K^4)
dt_rad=((296.15^4)-(77.325^4));  %temp diff
inner_sa = pi*(0.28^2);          % cylinder inner surface area (m2)
L_n = 0.53;           %Length Dewar neck (m)
L_e = 0.53;           %Length extraction valve (m)
L_li = 0.3280;        %Length level indicator (m)
Thick_n = 0.0005;         %thickness Dewar neck (m)
Thick_e = 0.0002;         % thickness extraction valve (m)
Thick_prv = 0.0002;       % thickness prv and burst disc valve (m)
Thick_li = 0.0002;        % thickness level indicator (m)
%Cross section area for conductive heat transfer
CS_neck = pi*(Dn-Thick_n)*Thick_n;           %cross section neck (m2)
CS_ext_vlv = pi*(De-Thick_e)*Thick_e;        %cross section ext vlv (m2)
CS_prv = pi*(D_prv-Thick_prv)*Thick_prv;     %cross section prv (m2)
CS_li = pi*(D_li-Thick_li)*Thick_li;         %cross seciton level indicator
(m2)
k_avg = 12.3;        %Avg thermal conductivity for 304 SS (W/mK)
Cp_liq_nit = 2.04;   %Sp heat cap of liq nitrogen (kJ/kgK)
Cp_SS = 0.51;        %sp heat cap of SS 304 (kJ/kgK)
Mass_inn_vessel = 2.074;    %inner vessel mass (kg)
%Liq nitrogen
liq_volume = 0.035;   %total liq nitrogen vol (m3)
liq_density = 807;    %liq nitrogen density (kg/m3)
liq_mass = liq_volume*liq_density;    %liq nitrogen mass (kg)
%Gas nitrogen
gas_volume = 0.035;   %total gas nitrogen vol (m3)
gas_density = 1.225;    %gas nitrogen density (kg/m3)
gas_mass = gas_volume*gas_density;    %gas nitrogen mass (kg)
h_1 = refpropm('H','T',293.15,'P',260.325,'air.ppf')/1000; %Enthalpy(kJ/kg)
h_2 = refpropm('H','T',293.15,'P',260.325*6.4,'air.ppf')/1000;
hg = refpropm('H','T',77.325,'Q',1,'air.ppf')/1000;
hf = refpropm('H','T',77.325,'Q',0,'air.ppf')/1000;
s_1 = refpropm('S','T',293.15,'P',260.325,'helium')/1000;
s_2 = refpropm('S','T',293.15,'P',260.325*6.4,'helium')/1000;
%Aftercooler for compressor
rho_a = refpropm('D','T',294.15,'P',260.325*6.4,'helium');
s_a = refpropm('S','T',294.15,'P',260.325*6.4,'helium')/1000;
h_a = refpropm('H','T',294.15,'P',260.325*6.4,'helium')/1000;
T_2 = refpropm('T','P',260.325*6.4,'S',s_1,'helium');
%Delivery temp. changes acc to compression ratio (K)
T2_= 72+273.15;                                              %Temp (K)
Act_h = refpropm('H','T',T2_,'P',260.325*6.4,'helium')/1000;
Press_water = 300;                        %cooling water pressure (kPa)
```

```
Feed_temp = 12+273.15;
%cooling water inlet temp(K)
Outlet_temp = 19+273.15;              %cooling water outlet temp(K)
Cp_w = refpropm('C','T',Feed_temp,'P',Press_water,'water')/1000;     %water
specific heat (kJ/kgK)
%Aftercooler for compressor
rho_aa = refpropm('D','T',294.15,'P',260.325*6.4,'helium');
s_aa = refpropm('S','T',294.15,'P',260.325*6.4,'helium')/1000;
h_aa = refpropm('H','T',294.15,'P',260.325*6.4,'helium')/1000;
T_2a = refpropm('T','P',260.325*6.4,'S',s_1,'helium');
%Delivery temp. changes acc to compression ratio (K)
T2_a= 72+273.15;                                        %Temp (K)
Act_ha = refpropm('H','T',T2_a,'P',260.325*6.4,'helium')/1000;
Press_air = 101.325;                    %cooling air pressure (kPa)
In_temp = 20+273.15;                   %cooling water inlet temp(K)
Out_temp = 28+273.15;                        %cooling water outlet temp(K)
Cp_a = refpropm('C','T',Feed_temp,'P',Press_air,'air.ppf')/1000;
%water specific heat (kJ/kgK)
rho_1 = refpropm('D','T',293.15,'P',260,'helium');
rho_2 = refpropm('D','P',1666,'S',s_1*1000,'helium');
%additional prop for Claude system
h_3 = refpropm('H','T',270,'P',260.325*6.4,'air.ppf')/1000;
s_3 = refpropm('S','T',270,'P',260.325*6.4,'air.ppf')/1000;
s_e = s_3;
h_e = refpropm('H','T',86.1,'P', 260.325,'air.ppf')/1000;
%Prop for GM cooler
h_3G = refpropm('H','T',67.99,'P',1735.20,'helium')/1000;
rho_3 = refpropm('D','T',67.99,'P',1735.20,'helium');
s_3G = refpropm('S','T',67.99,'P',1735.20,'helium')/1000;        %(J/kgK) to
get right h_4G
s_4G = s_3G;
h_4G = refpropm('H','P',370.19,'S',s_4G*1000,'helium')/1000;
h_5G = refpropm('H','T',67.99,'P',370.19,'helium')/1000;
h_4_ = h_4G+((1-0.80)*(h_3G-h_4G));   %Actual enthalpy at end of expansion
rho_4_ = refpropm('D','P',370.19,'H',h_4_*1000,'helium');
Mass_ratio = rho_4_/rho_3;                                  % mass ratio
```

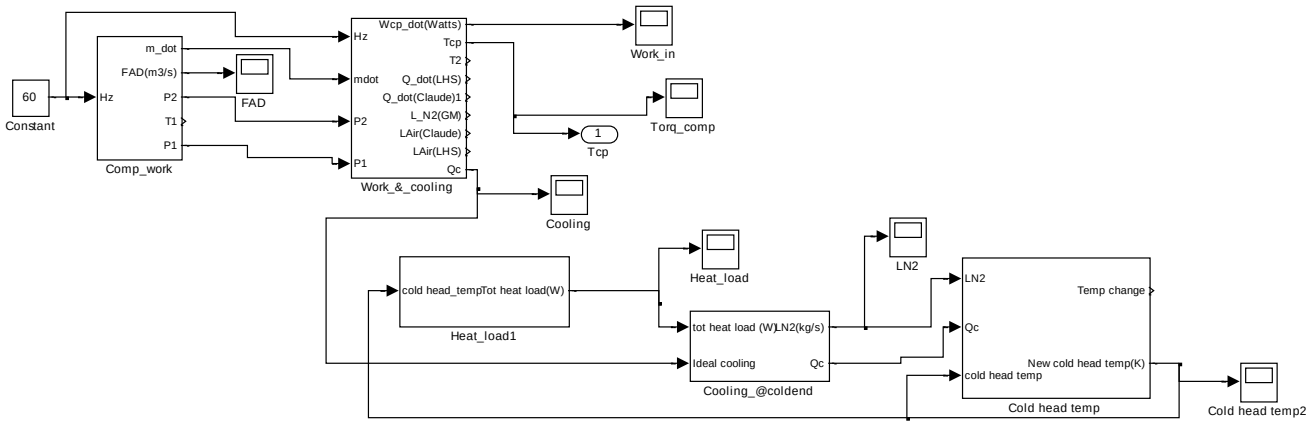

Figure D.1: Simulink model for GM cryocooler unit

Appendix E. Script for wind-driven GM cryocooler

```
% wind turbine parameter
rho_air = 1.225;          % Air density in kg/m^3
Radius = 3.2;             % Blade radius in m
Area = pi()*Radius^2;    % Blade swept area in m^2
pitch= 0;                 % Pitch angle in degree
c1=0.5176;                % Parameter for power coefficient
c2=116;                   %Parameter for power coefficient
c3=0.4;                   %Parameter for power coefficient
c4=5;                     %Parameter for power coefficient
c5=21;                    %Parameter for power coefficient
c6=0.0068;                 %Parameter for power coefficient
Cp_opt=0.48;              %Optimal power coeffcient
lamda_opt=7.2;            %Optimal tip-speed ratio
Tip_rd = 2*pi*Radius;     %Tip rotation distance
J_Lss = 890;              %Shaft inertia (kgm2)
Dp =0.0000149;     %Pump_displacement (m^3/rad)
PVeff=0.95;     %Pump_vol_eff
PTeff=0.95;      %Pump_total_eff
PPnom=2.2e7;      %Pump_nominal_pressure (Pa)
Pwnom=31.4;      %Pump_nominal_angular_velocity (rad/s)
Pvisc_nom=18.78e-6;    %(m2/s) %Pump_nominal_viscosity
w_p=560;                %Pump_ref_speed (rpm)
Rho=852.8;              %Fluid density (kg/m3)
visc=18.78e-6;               %fluid_viscosity (m2/s)
KP_Leakage=Dp*Pwnom*(1-PVeff)*Pvisc_nom*Rho/(PPnom*visc*Rho);  %Pump leakage
coeff
%Motors
DmA = 9.9e-7;  %(m3/rad)Motor_displacement
DmB = 9.9e-7;    %(m3/rad) %Motor_disp
MVeff=0.95;     %Motor_volumetric_eff
MTeff=0.95;     %Motor_total_eff
MPnom=2.2e7;     %(Pa)Motor_nominal_pressure
Mwnom=125.6637;     %(rpm) %Motor_nominal_angular_velocity
Mvisc_nom=18.78e-6;    %(m2/s) %Motor_nominal_kinemotoric_visc
I_mA=134.116;    %(kgm2) %Motor_inertia
B_mA=0.0026;    %(Nm/(rad/s)) %damping coefficient
I_mB=134.116;    %(kgm2) %Motor_inertia
B_mB=0.0022;    %(Nm/(rad/s)) %damping coefficient
KMA_Leakage=DmA*Mwnom*(1-MVeff)*Mvisc_nom*Rho/(MPnom*visc*Rho); %Pump Leakage
coeff
KMB_Leakage=DmB*Mwnom*(1-MVeff)*Mvisc_nom*Rho/(MPnom*visc*Rho); %Pump Leakage
coeff
Ks=2.67e5;                  %Nm/rad torq coeff
Kd_1=1.07e4;               %(Nm/(rad/s) damping torq coeff
Kp=500*I_mA;               %Motor angle controller
Kd=20*I_mA;                %Motor speed controller
w_motor_sync=125.6637;     %motor sync speed
Rated_disp = 1.16*10^-6;  %Rated displacement
```

```
%Compressebility
Rho=852.8;              %Density (kg/m3)
Visc=18.78e-6;          %(m2/s)
Beta=1.40403e9;      %(Pa)%Fluid bulk modulus
L=60;                %(m)%Pipe length
D=3;               %Pipe diameter
A=pi*(D/2)^2;        %Area of pipe
g=9.81;              %(m/s^2) Acc due to gravity
%change dia of the pipe to fix volume of the fluid (to get reqd fluid vol)
Vol=10000000;             %(m^3)Fluid volume subjected to the pressure effect
rh=1.5e-5;            %pipe roughness
Init_gas=5;           %Initial vol of gas (m3)
P_rated=11*10^6;  %Rated pressure (Pa)
Init_hp = 10000;         % initial high pressure volume in acc (m3)
w_rated = 11;          %rated wind speed (m/s)
%Check valve
P_0 = 10*10^6;    % Cracking pressure (Pa)
C=0.2;            %flow coeff
A_disc=0.001;     %(m^2) Area of valve
I_b = (sqrt(A_disc/pi)*2*pi);  %valve perimeter
k_s=10;                       %spring stiffness
%PRV
Kzb=2.2;
P_b = 10*10^6;    %PRV set pressure (Pa)
%compressor
V0=0.000013;          %Dead volume (m3)
Vs=0.0000375;         %swept volume (m3/rev)
%Air properties for simple Linde Hampson system
C_p_air=1009.875;           %sp heat cap (J/kgK)
R_air=286.9;              %Gas constant for He (J/kgK)
G_air=1.4;                 %Gamma for Air
Dyn_visc_air=19.81e-6;     %Dynamic viscosity (Ns/m2)
Th = 296.388;           %Room temperature (K)
h_1 = refpropm('H','T',293.15,'P',260.325,'air.ppf')/1000; %Enthalpy(kJ/kg)
h_2 = refpropm('H','T',293.15,'P',260.325*6.4,'air.ppf')/1000;
hg = refpropm('H','T',77.325,'Q',1,'air.ppf')/1000;
hf = refpropm('H','T',77.325,'Q',0,'air.ppf')/1000;
s_1 = refpropm('S','T',293.15,'P',260.325,'helium')/1000;
s_2 = refpropm('S','T',293.15,'P',260.325*6.4,'helium')/1000;
%Aftercooler for compressor
rho_a = refpropm('D','T',294.15,'P',260.325*6.4,'helium');
s_a = refpropm('S','T',294.15,'P',260.325*6.4,'helium')/1000;
h_a = refpropm('H','T',294.15,'P',260.325*6.4,'helium')/1000;
T_2 = refpropm('T','P',260.325*6.4,'S',s_1,'helium');
%Delivery temp. changes acc to compression ratio (K)
T2_= 72+273.15;                                                    %Temp (K)
Act_h = refpropm('H','T',T2_,'P',260.325*6.4,'helium')/1000;
Press_water = 300;          %cooling water pressure (kPa)
Feed_temp = 12+273.15;                      %cooling water inlet temp(K)
Outlet_temp = 19+273.15;                 %cooling water outlet temp(K)
Cp_w = refpropm('C','T',Feed_temp,'P',Press_water,'water')/1000;     %water
specific heat (kJ/kgK)
%Aftercooler for compressor
```

```
rho_aa = refpropm('D','T',294.15,'P',260.325*6.4,'helium');
s_aa = refpropm('S','T',294.15,'P',260.325*6.4,'helium')/1000;
h_aa = refpropm('H','T',294.15,'P',260.325*6.4,'helium')/1000;
T_2a = refpropm('T','P',260.325*6.4,'S',s_1,'helium');
%Delivery temp. changes acc to compression ratio (K)
T2_a= 72+273.15;
%Temp (K)
Act_ha = refpropm('H','T',T2_a,'P',260.325*6.4,'helium')/1000;
Press_air = 101.325;
%cooling water pressure (kPa)
In_temp = 20+273.15;                  %cooling water inlet temp(K)
Out_temp = 28+273.15;                %cooling water outlet temp(K)
Cp_a = refpropm('C','T',Feed_temp,'P',Press_air,'air.ppf')/1000;
%water specific heat (kJ/kgK)
rho_1 = refpropm('D','T',293.15,'P',260,'helium');
rho_2 = refpropm('D','P',260.325*6.4,'S',s_1*1000,'helium');
%additional prop for Claude system
h_3 = refpropm('H','T',270,'P',260.325*6.4,'air.ppf')/1000;
s_3 = refpropm('S','T',270,'P',260.325*6.4,'air.ppf')/1000;
s_e = s_3;
h_e = refpropm('H','T',86.1,'P', 260.325,'air.ppf')/1000;
%Prop for GM cooler
h_3G = refpropm('H','T',77.325,'P',260.325*6.4,'helium')/1000;
rho_3 = refpropm('D','T',77.325,'P',260.325*6.4,'helium');
s_3G = refpropm('S','T',77.325,'P',260.325*6.4,'helium'); %(J/kgK) to get
right h_4G
s_4G = s_3G;
h_4G = refpropm('H','P',260.325,'S',s_4G,'helium')/1000;
h_5G = refpropm('H','T',78,'P',101.325,'helium')/1000;
h_4_ = h_4G+((1-0.95)*(h_3G-h_4G));    Actual enthalpy at end of expansion
rho_4_ = refpropm('D','P',260.325,'H',(h_4_*1000),'helium');
Mass_ratio = rho_4_/rho_3;                % mass ratio
%Regenerator
Length_reg = 0.10;    %length (m)
Diam_reg = 0.02;      %diameter (m)
Porosity=0.4;         %Porosity
Hyd_diam=0.00001;     %Hydraulic diam (m)
%Displacer
Lt=0.12;              %length (m)
dt=0.0508;            %diameter (m)
%cold end block
Vdcx=0.00002;      %dead volume (m3)
%hot end
Vdhx=0.00002;      %dead volume (m3)
Vdrg=0.00002;      %Void vol reg (m3)
Vdac=0.00002;      %Void volume aftercooler (m3)
Vd=0.000044;        %Disp vol (m3)
Vcomp=0.0022;      %compressor cylinder vol (m3)
%Valve
Diam=0.0005;      %valve diam (m)
P0=16000000;      %average pressure (Pa)
f=2.4;             %frequency (Hz)
Tc=77.325;           %cold end temp (K)
```

```
%He-gas properties (@16.34 bar & 300K)
rho=2.64;             %He density (kg/m3)
C_p=5192.0;            %sp heat cap (J/kgK)
R=2074.6;              %Gas constant for He (J/kgK)
G=1.67;                %Gamma for He
Dyn_visc=19.81e-6;     %Dynamic viscosity (Ns/m2)
%For Dewar heat transfer
Dn = 0.1016;                   %outer diameter Dewar neck (m)
De = 0.03175;                  %outer diameter extraction valve (m)
D_prv = 0.03175;               %outer diameter prv and burst disc valve (m)
D_li = 0.0127;                 %outer diameter level indicator (m)
D_vac = 0.0381;                %outer diameter vacuum release port (m)
Area_neck = pi*(Dn)^2;         %Dewar neck area (m2)
Area_ext_vlv = pi*(De)^2;      %Extraction valve area (m2)
Area_prv = pi*(D_prv)^2;       %Pressure relief valve area (m2)
Area_li= pi*(D_li)^2;          %Level indicator area (m2)
Area_vac = pi*(D_vac)^2;       %Vacuum port area (m2)
%Surface area for radiation heat transfer
SA_neck = Area_neck/4;          %surface area neck (m2)
SA_ext_vlv = Area_ext_vlv/4;    %surface area ext valve (m2)
SA_prv = Area_prv/4;            %surface area prv(m2)
SA_li = Area_li/4;              %surface area level ind(m2)
SA_vac = Area_vac/4;            %surface area vac port (m2)
%For radiative heat transfer
%Acc to ASME Boiler & Pressure vessel code section VIII
Fe = 0.04215;                      %Emmisivity factor
F_1_2= 1;                          %configuration factor
sigma = 5.67e-08;                  %Stefan-Boltzman constant (W/m^2-K^4)
dt_rad=((296.15^4)-(77.325^4));    %temp diff
inner_sa = pi*(0.28^2);            %cylinder inner surface area (m2)
L_n = 0.53;           %Length Dewar neck (m)
L_e = 0.53;           %Length extraction valve (m)
L_li = 0.3280;        %Length level indicator (m)
Thick_n = 0.0005;         %thickness Dewar neck (m)
Thick_e = 0.0002;         % thickness extraction valve (m)
Thick_prv = 0.0002;       % thickness prv and burst disc valve (m)
Thick_li = 0.0002;        % thickness level indicator (m)
%Cross section area for conductive heat transfer
CS_neck = pi*(Dn-Thick_n)*Thick_n;           %cross section neck (m2)
CS_ext_vlv = pi*(De-Thick_e)*Thick_e;        %cross section ext vlv (m2)
CS_prv = pi*(D_prv-Thick_prv)*Thick_prv;     %cross section prv (m2)
CS_li = pi*(D_li-Thick_li)*Thick_li;         %cross seciton level indicator
(m2)
k_avg = 12.3;                  %Avg thermal conductivity for 304 SS (W/mK)
Cp_liq_nit = 2.04;             %Sp heat cap of liq nitrogen (kJ/kgK)
Cp_SS = 0.51;                  %sp heat cap of SS 304 (kJ/kgK)
Mass_inn_vessel = 2.074;       %inner vessel mass (kg)
%Liq nitrogen
liq_volume = 0.035;           %total liq nitrogen vol (m3)
liq_density = 807;            %liq nitrogen density (kg/m3)
liq_mass = liq_volume*liq_density;   %liq nitrogen mass (kg)
%Gas nitrogen
gas_volume = 0.035;    %total gas nitrogen vol (m3)
```

```
gas_density = 1.225;    %gas nitrogen density (kg/m3)
gas_mass = gas_volume*gas_density;    %gas nitrogen mass (kg)
```

Appendix F. Script for Chapter 10 simulation

```
% wind turbine parameter
rho_air = 1.225;          % Air density in kg/m^3
Radius = 63;             % Blade radius in m
Area = pi()*Radius^2;    % Blade swept area in m^2
pitch= 0;                % Pitch angle in degree
c1=0.5176;               % Parameter for power coefficient
c2=116;                  %Parameter for power coefficient
c3=0.4;                  %Parameter for power coefficient
c4=5;                    %Parameter for power coefficient
c5=21;                   %Parameter for power coefficient
c6=0.0068;                %Parameter for power coefficient
Cp_opt=0.48;             %Optimal power coeffcient
lamda_opt=8.1;           %Optimal tip-speed ratio
Tip_rd = 2*pi*Radius;    %Tip rotation distance
J_Lss = 38759228;             %Shaft inertia (kg/m2)
Dp =0.3 ;    %Pump_displacement (m^3/rad)
PVeff=0.95;     %Pump_vol_eff
PTeff=0.95;      %Pump_total_eff
PPnom=2e7;      %Pump_nominal_pressure (Pa)
Pwnom=1;      %Pump_nominal_angular_velocity (rad/s)
Pvisc_nom=18.78e-6;    %(m2/s) %Pump_nominal_viscosity
w_p=560;                %Pump_ref_speed (rpm)
Rho=852.8;              %Fluid density (kg/m3)
visc=18.78e-6;               %fluid_viscosity (m2/s)
KP_Leakage=Dp*Pwnom*(1-PVeff)*Pvisc_nom*Rho/(PPnom*visc*Rho);  %Pump leakage
coeff
%Motor
DmA = 8e-4;  %(m3/rad)Motor_displacement
DmB = 8e-4;   %(m3/rad) %Motor_disp
MVeff=0.95;     %Motor_volumetric_eff
MTeff=0.95;     %Motor_total_eff
MPnom=2e7;     %(Pa)Motor_nominal_pressure
Mwnom=125.6637;     %(rpm) %Motor_nominal_angular_velocity
Mvisc_nom=18.78e-6;    %(m2/s) %Motor_nominal_kinemotoric_visc
I_mA=534.116;    %(kg/m2) %Motor_inertia
B_mA=0.0026;    %(Nm/(rad/s)) %damping coefficient
I_mB=534.116;    %(kgm2) %Motor_inertia
B_mB=0.0022;    %(Nm/(rad/s)) %damping coefficient
KMA_Leakage=DmA*Mwnom*(1-MVeff)*Mvisc_nom*Rho/(MPnom*visc*Rho); %Pump Leakage
coeff
KMB_Leakage=DmB*Mwnom*(1-MVeff)*Mvisc_nom*Rho/(MPnom*visc*Rho); %Pump Leakage
coeff
Ks=2.67e5;      %Nm/rad torq coeff
Kd_1=1.07e4;     %(Nm/(rad/s) damping torq coeff
Kp=500*I_mA;     %Motor angle controller
Kd=20*I_mA;       %Motor speed controller
w_motor_sync=125.6637;    %motor sync speed
%Compressebility
Rho=852.8;            %Fluid density (kg/m3)
```

```
Visc=18.78e-6;       %(m2/s)
Beta=1.40403e9;     %(Pa)%Fluid bulk modulus
L=60;               %(m)%Pipe length
D=1.5;              %Pipe diameter
A=pi*(D/2)^2;       %Area of pipe
g=9.81;             %(m/s^2) Acc due to gravity
%Vol=A*L;           %(m^3)Fluid volume subjected to the pressure effect
Vol= A*L*2;
rh=1.5e-5;          %pipe roughness
Init_gas=10;        %Initial vol of gas (m3)
P_rated=11.3*10^6;  %Rated pressure (Pa)
w_rated=11;         %Rated wind speed (m/s)
Init_hp = 0.1;      %initial hydraulic fluid vol (m3)
%Check valve
P_0 = 20*10^6;                  %Cracking pressure (Pa)
C=0.2;                          %flow coeff
A_disc=0.001;                   %(m^2) Area of valve
I_b = (sqrt(A_disc/pi)*2*pi);  %valve perimeter
k_s=10;                        %spring stiffness (10)
%PRV
Kzb=2.2;
P_b = 40*10^7;   %PRV set pressure (Pa)
%Air properties for simple Linde Hampson system
rho=1.225;          %Air density (kg/m3)
C_p=1009.875;       %sp heat cap (J/kgK)
R=286.9;            %Gas constant for He (J/kgK)
G=1.4;              %Gamma for Air
Dyn_visc=19.81e-6;  %Dynamic viscosity (Ns/m2)
Th = 293.15;        %Room temperature (K)
T2_= 74+273.15;     % Temp (K)
h_1 = refpropm('H','T',293.15,'P',101.325,'air.ppf')/1000; %Enthalpy(kJ/kg)
h_2 = refpropm('H','T',293.15,'P',101.325*50,'air.ppf')/1000;
hg = refpropm('H','T',78.8,'Q',1,'air.ppf')/1000;
hf = refpropm('H','T',78.8,'Q',0,'air.ppf')/1000;
s_1 = refpropm('S','T',293.15,'P',101.325,'air.ppf')/1000;
s_2 = refpropm('S','T',293,'P',101.325*50,'air.ppf')/1000;
%Aftercooler for compressor
rho_a = refpropm('D','T',282.15,'P',101.325*50,'air.ppf');
s_a = refpropm('S','T',282.15,'P',101.325*50,'air.ppf')/1000;
h_a = refpropm('H','T',282.15,'P',101.325*50,'air.ppf')/1000;
T_2 = refpropm('T','P',101.325*50,'S',s_1,'air.ppf'); %Delivery temp. changes
acc to compression ratio (K)                                    %temp
(K)
Act_h = refpropm('H','T',T2_,'P',101.325*50,'air.ppf')/1000;
Press_water = 300;                          %cooling water pressure (kPa)
Feed_temp = 7+273.15;                       %cooling water inlet temp(K)
Outlet_temp = 22+273.15;                    %cooling water outlet temp(K)
Cp_w = refpropm('C','T',Feed_temp,'P',Press_water,'water')/1000;     %water
specific heat (kJ/kgK)
%additional prop for Claude system
h_3 = refpropm('H','T',270,'P',101.325*50,'air.ppf')/1000;
s_3 = refpropm('S','T',270,'P',101.325*50,'air.ppf')/1000;
s_e = s_3;
```

```
h_e = refpropm('H','T',86.1,'P',101.325,'air.ppf')/1000;
%Prop for GM cooler
h_3G = refpropm('H','T',78.8,'P',101.325*50,'air.ppf')/1000;
rho_3 = refpropm('H','T',78.8,'P',101.325*50,'air.ppf');
s_3G = refpropm('S','T',78.8,'P',101.325*50,'air.ppf')/1000;
%(J/kgK) to get right h_4G
s_4G = s_3G;
h_4G = refpropm('H','P',101.325*50,'S',s_4G*1000,'air.ppf')/1000;
h_5G = refpropm('H','T',78.8,'P',101.325,'air.ppf')/1000;
h_4_ = h_4G+((1-0.85)*(h_3G-h_4G));   %Actual enthalpy at end of expansion
rho_4_ = refpropm('D','P',101.325,'H',(h_4_*1000),'air.ppf');
Mass_ratio = rho_4_/rho_3;   % mass ratio
%For Dewar heat transfer
Dn = 1.516;         %outer diameter Dewar neck (m)
De = 0.03175;        % outer diameter extraction valve (m)
D_prv = 0.03175;     % outer diameter prv and burst disc valve (m)
D_li = 0.0127;       % outer diameter level indicator (m)
D_vac = 0.0381;      % outer diameter vacuum release port (m)
Area_neck = pi*(Dn)^2;         %Dewar neck area (m2)
Area_ext_vlv = pi*(De)^2;      %Extraction valve area (m2)
Area_prv = pi*(D_prv)^2;       %Pressure relief valve area (m2)
Area_li= pi*(D_li)^2;          %Level indicator area (m2)
Area_vac = pi*(D_vac)^2;       %Vacuum port area (m2)
%Surface area for radiation heat transfer
SA_neck = Area_neck/4;          %surface area neck (m2)
SA_ext_vlv = Area_ext_vlv/4;    %surface area ext valve (m2)
SA_prv = Area_prv/4;            %surface area prv(m2)
SA_li = Area_li/4;              %surface area level ind(m2)
SA_vac = Area_vac/4;            %surface area vac port (m2)
%For radiative heat transfer
%Acc to ASME Boiler & Pressure vessel code section VIII
Fe = 0.04215;                     % Emmisivity factor
F_1_2= 1;                         %configuration factor
sigma = 5.67e-08;                  %Stefan-Boltzman constant (W/m^2-K^4)
dt_rad=((296.15^4)-(77.325^4));  %temp diff
inner_sa = pi*(0.28^2);          % cylinder inner surface area (m2)
L_n = 0.53;           %Length Dewar neck (m)
L_e = 1.53;           %Length extraction valve (m)
L_li = 1.3280;        %Length level indicator (m)
Thick_n = 0.0005;         %thickness Dewar neck (m)
Thick_e = 0.0002;         % thickness extraction valve (m)
Thick_prv = 0.0002;       % thickness prv and burst disc valve (m)
Thick_li = 0.0002;        % thickness level indicator (m)
%Cross section area for conductive heat transfer
CS_neck = pi*(Dn-Thick_n)*Thick_n;            %cross section neck (m2)
CS_ext_vlv = pi*(De-Thick_e)*Thick_e;         %cross section ext vlv (m2)
CS_prv = pi*(D_prv-Thick_prv)*Thick_prv;      %cross section prv (m2)
CS_li = pi*(D_li-Thick_li)*Thick_li;          %cross seciton level indicator
(m2)
k_avg = 12.3;        %Avg thermal conductivity for 304 SS (W/mK)
Cp_liq_nit = 2.04;   %Sp heat cap of liq nitrogen (kJ/kgK)
Cp_SS = 0.51;        %sp heat cap of SS 304 (kJ/kgK)
Vessel_vol = 35;     % Dewar volume (m3)
```

```
SS_Density = 8000;  %Stainless steel density (kg/m3)
Mass_inn_vessel = Vessel_vol*SS_Density;   %inner vessel mass (kg)
%Liq nitrogen
liq_volume = 35;                          %total liq nitrogen vol (m3)
liq_density = 807;                        %liq nitrogen density (kg/m3)
liq_mass = liq_volume*liq_density;        %liq nitrogen mass (kg)
%Gas nitrogen
gas_volume = 35;                      %total gas nitrogen vol (m3)
gas_density = 1.225;                  %gas nitrogen density (kg/m3)
gas_mass = gas_volume*gas_density;    %gas nitrogen mass (kg)
```

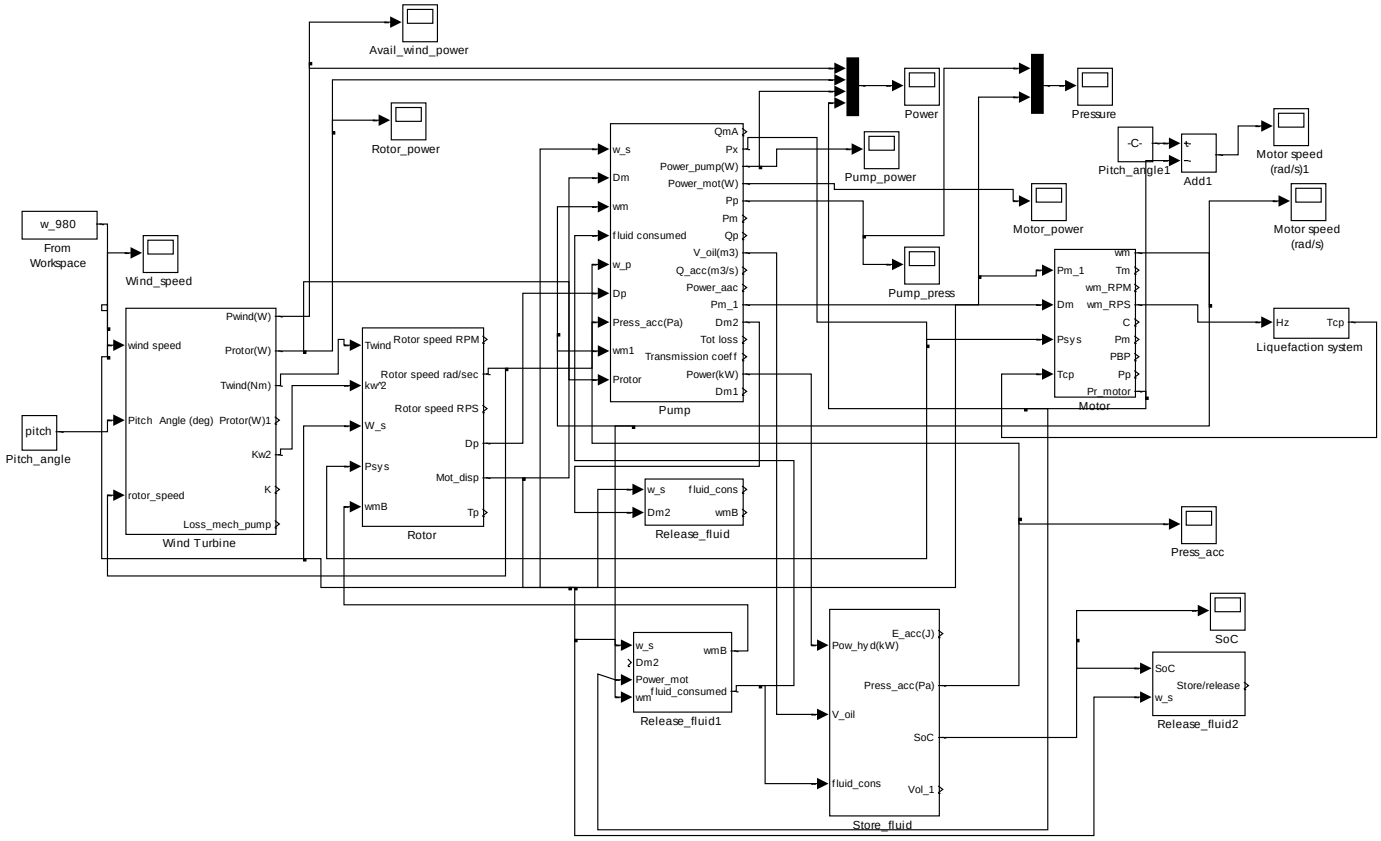

Figure F.1: Simulink model for Chapter 10 simulation

Appendix G. Experimental results from 60 Hz operation

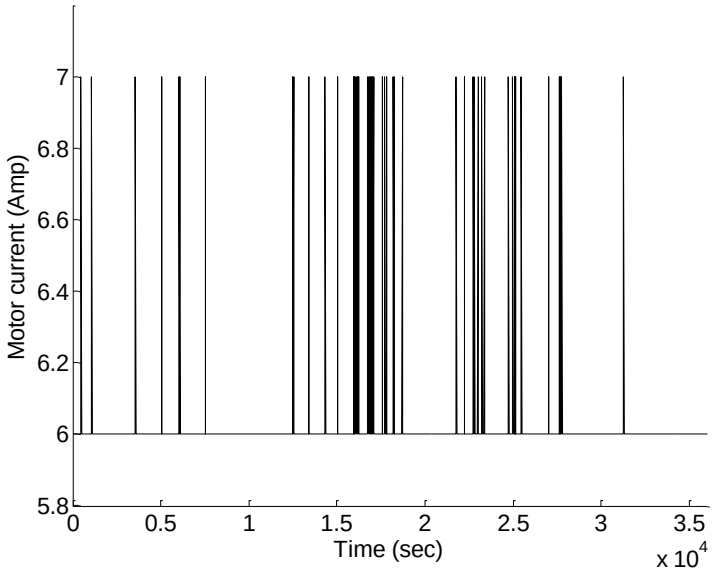

Figure G.1: Motor current (A) with time

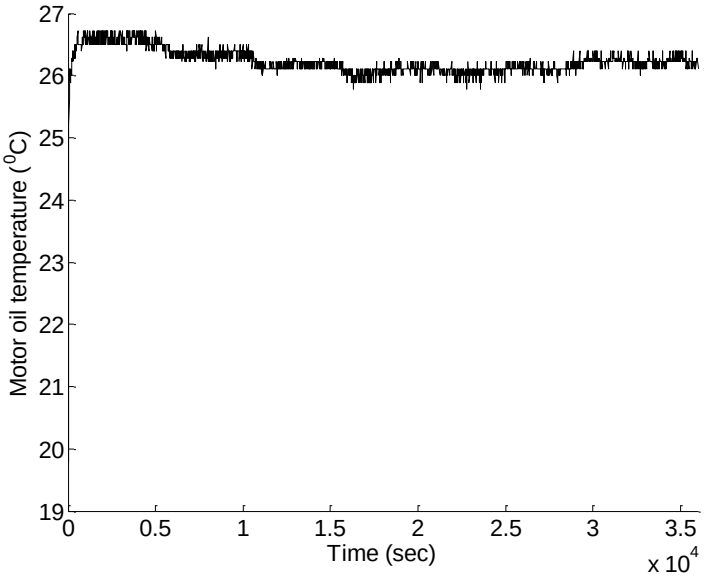

Figure G.2: Motor oil temperature (^{0}C) during 60 Hz operation

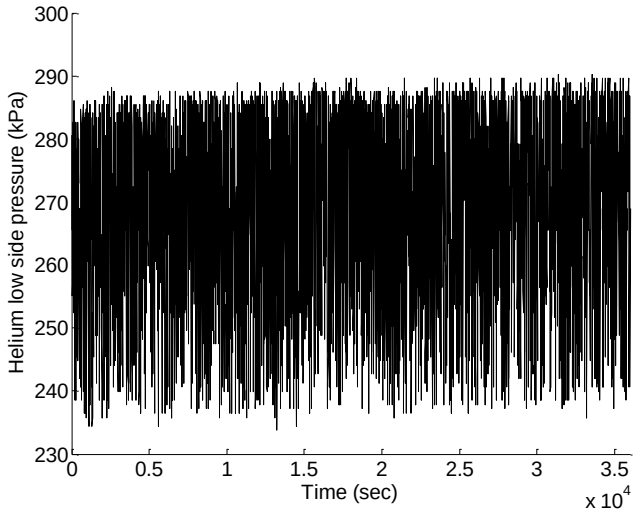

Figure G.3: Helium gas low side pressure (kPaG) with respect to time

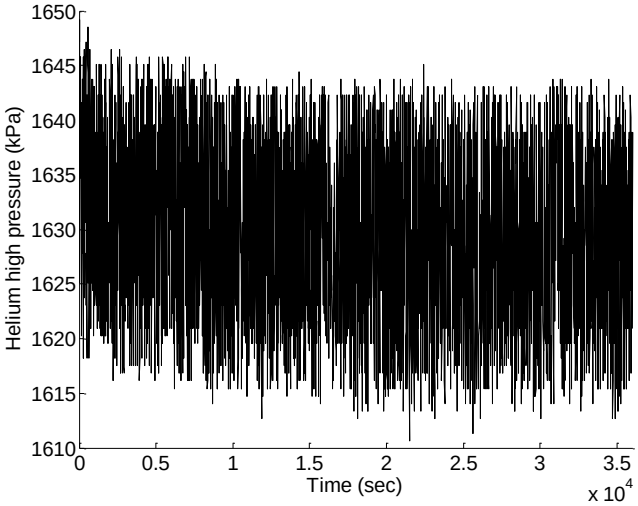

Figure G.4: Helium high side pressure (kPaG) with respect to time

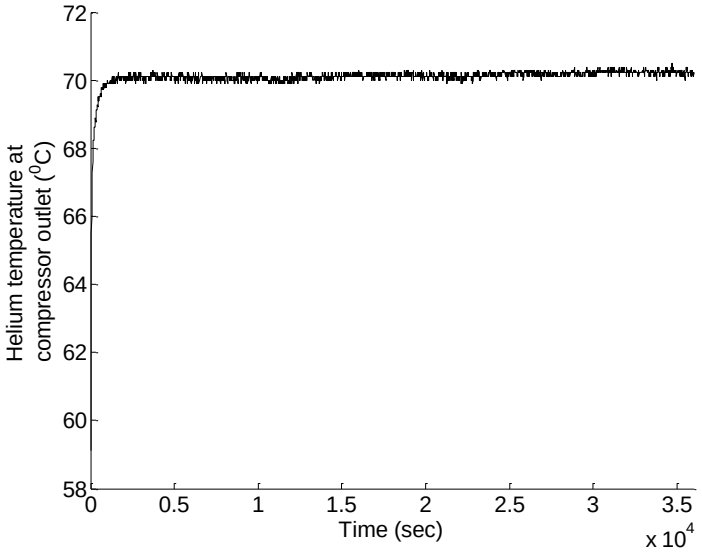

Figure G.5: Helium gas discharge temperature (^{0}C) during 60 Hz operation

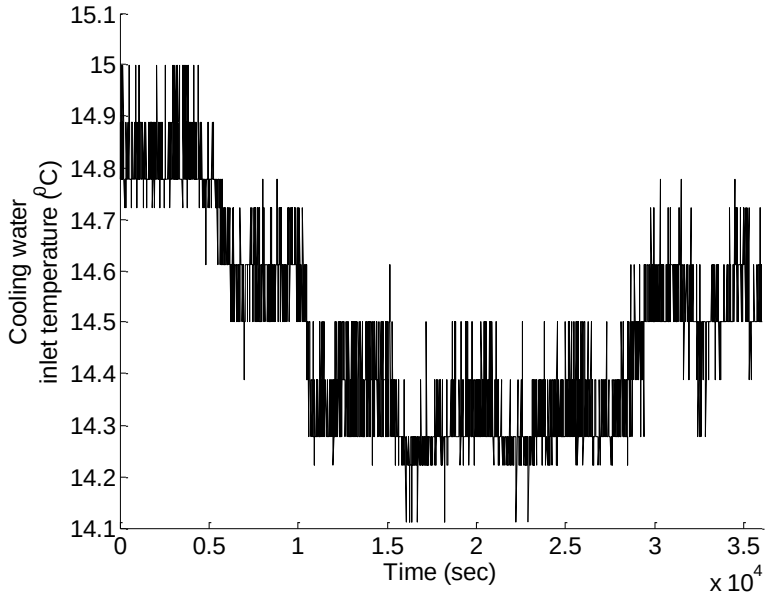

Figure G.6: Cooling water inlet temperature (^{0}C) during 60 Hz operation

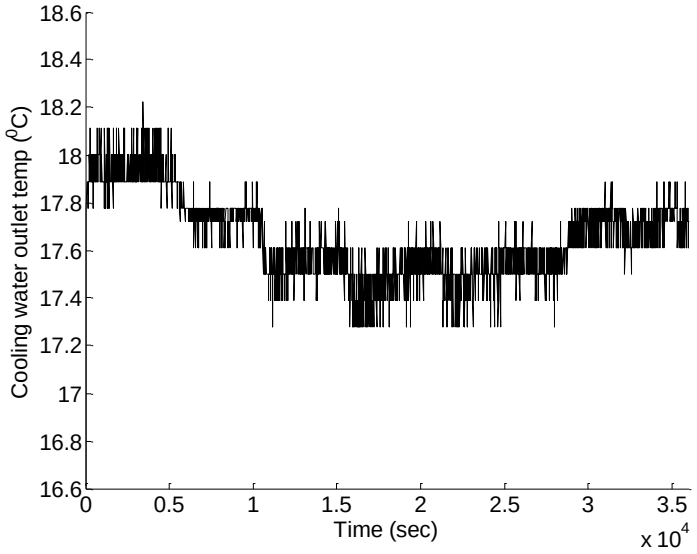

Figure G.7: Cooling water outlet temperature (^{0}C) during 60 Hz operation

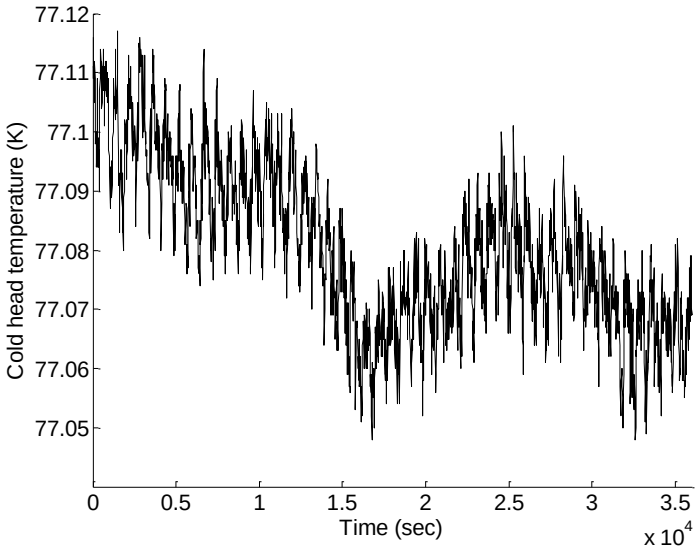

Figure G.8: Cold head temperature (K) during 60 Hz operation

Appendix H. Experimental results from operating compressor at different frequencies

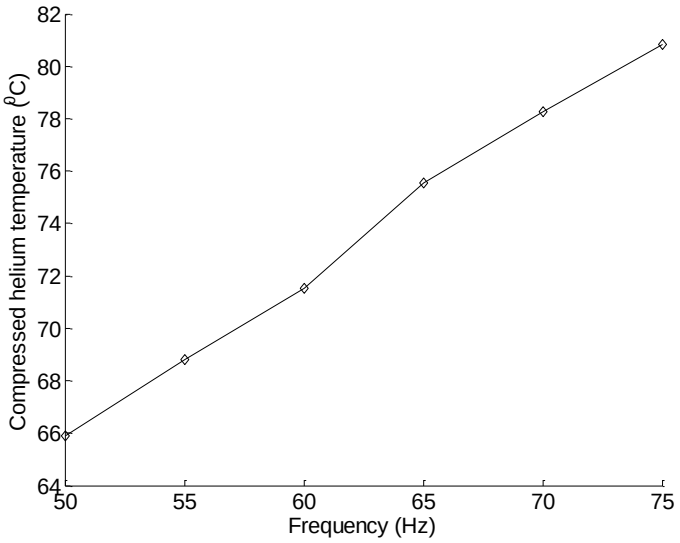

Figure H.1: Average helium gas discharge temperature (^{0}C)

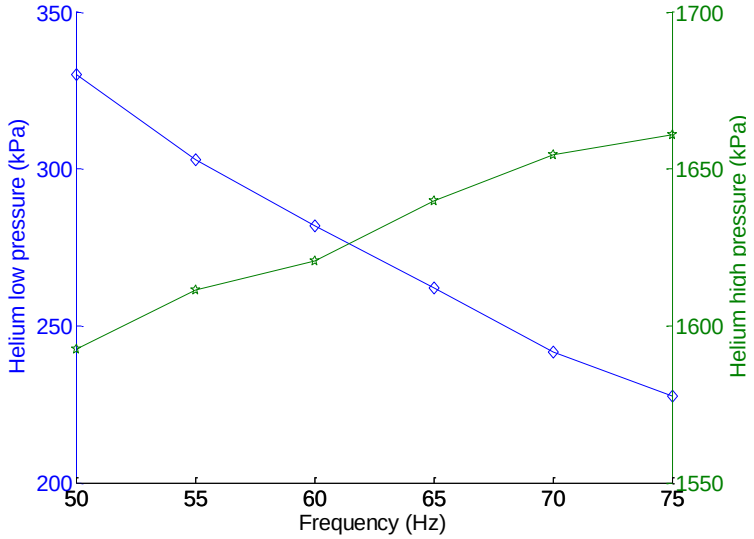

Figure H.2: Average helium gas low and high pressure (kPaG)

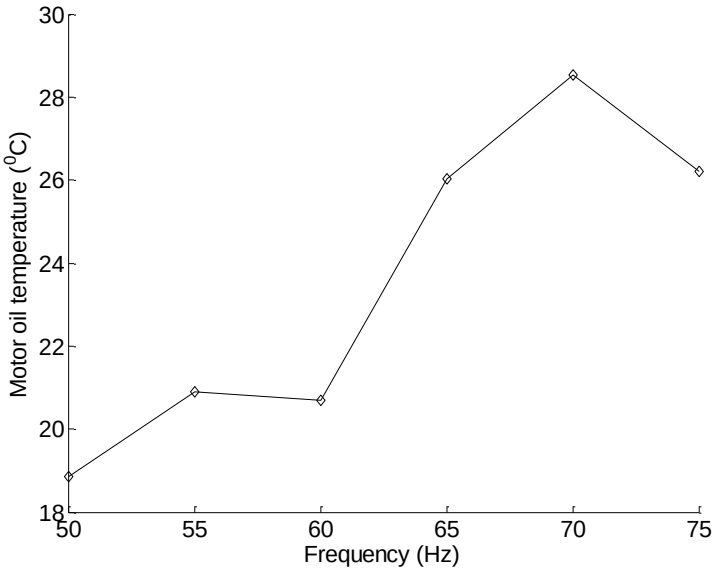

Figure H.3: Average motor oil temperature (^{0}C)

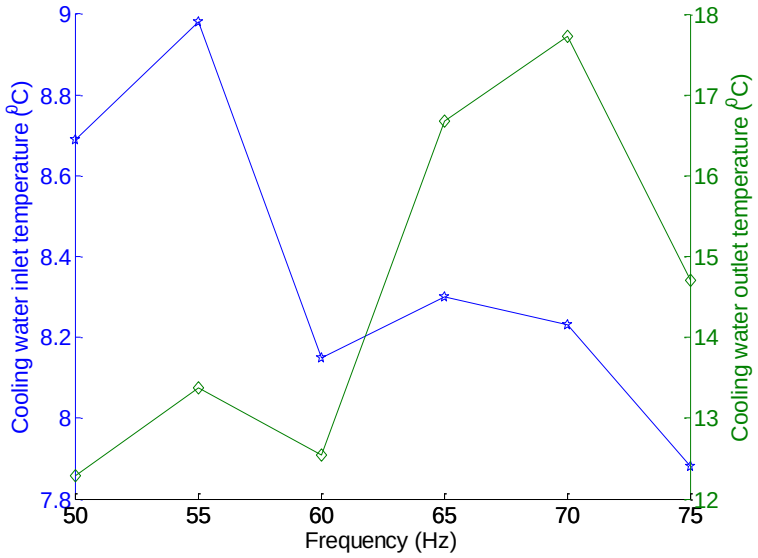

Figure H.4: Average cooling water inlet and outlet temperatures (^{0}C)

Appendix I. Experimental results from operating compressor at sinusoidal frequency input to compressor

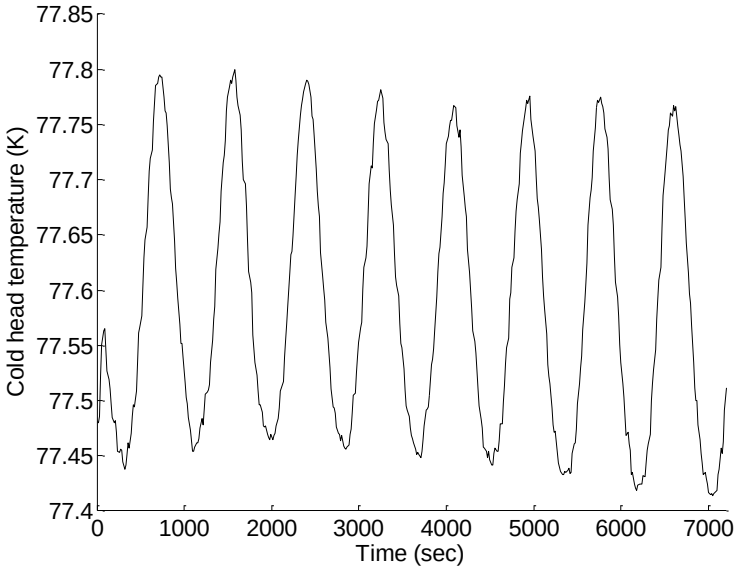

Figure I.1: Cold head temperature (K) for Sinusoidal frequency input to compressor motor

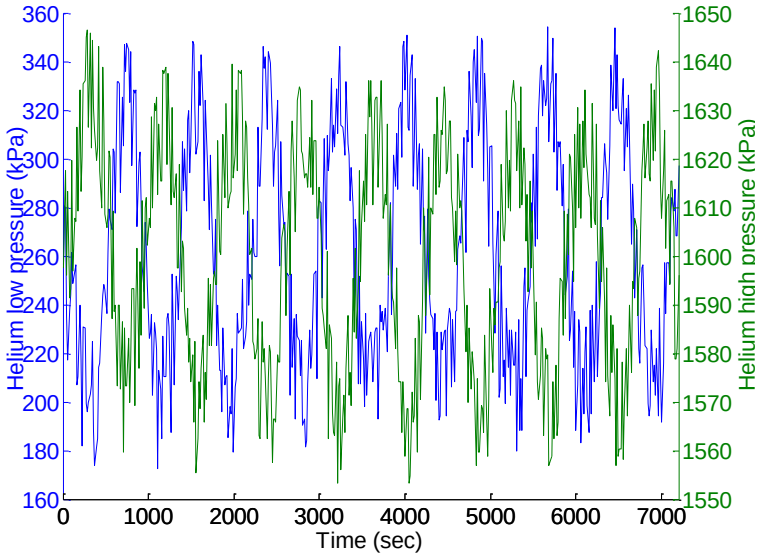

Figure I.2: Helium low and high pressure (kPaG)

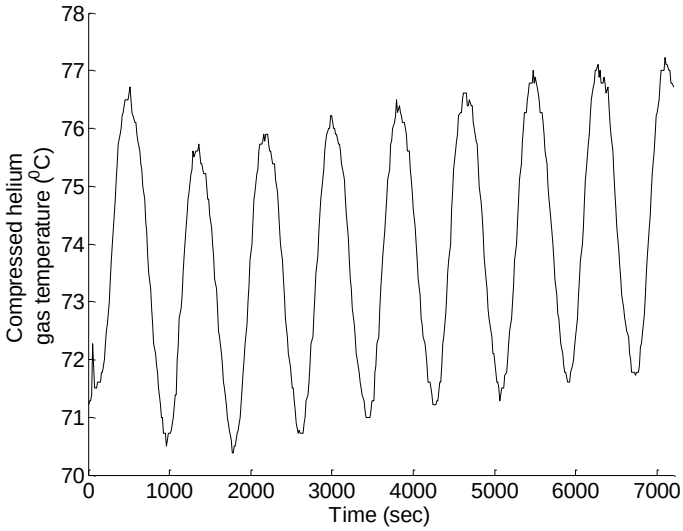

Figure I.3: Helium gas discharge temperature (^{0}C)

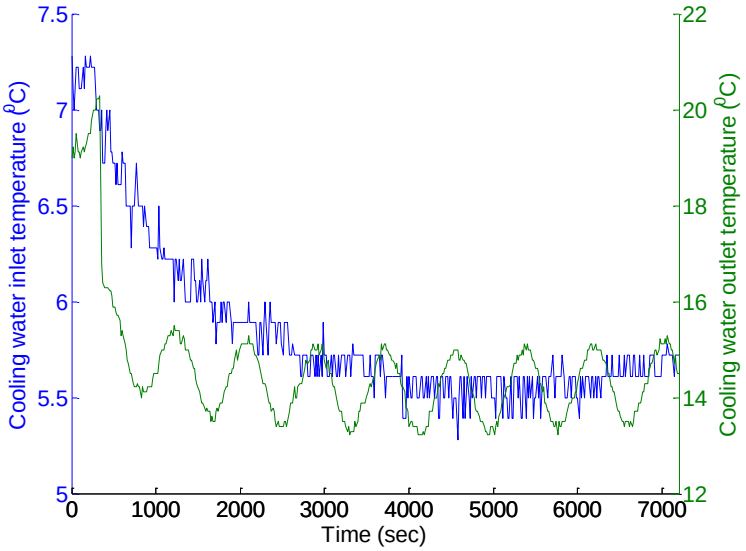

Figure I.4: Cooling water inlet and outlet temperature (^{0}C)

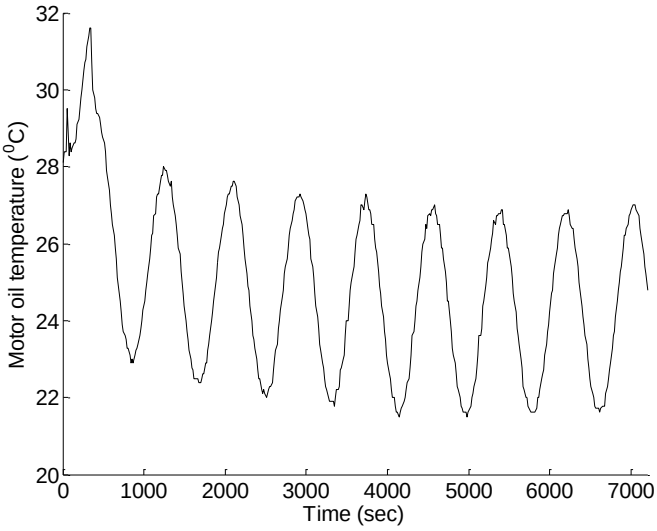

Figure I.5: Compressor motor oil temperature (^{0}C)

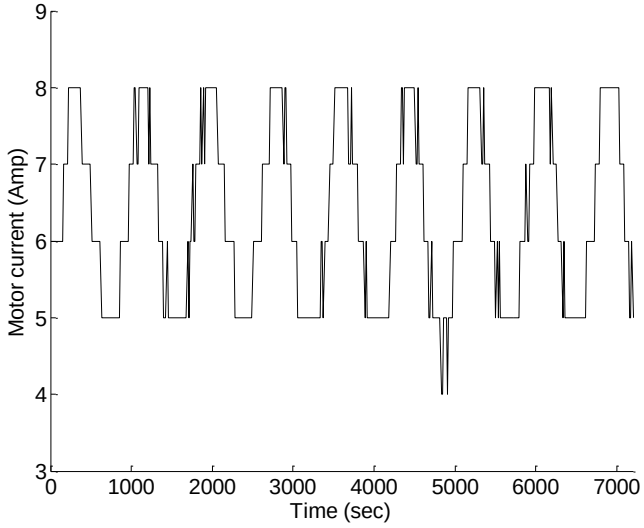

Figure I.6: Compressor motor current (Amp)

Appendix J. Experimental results from operating compressor at random frequency input

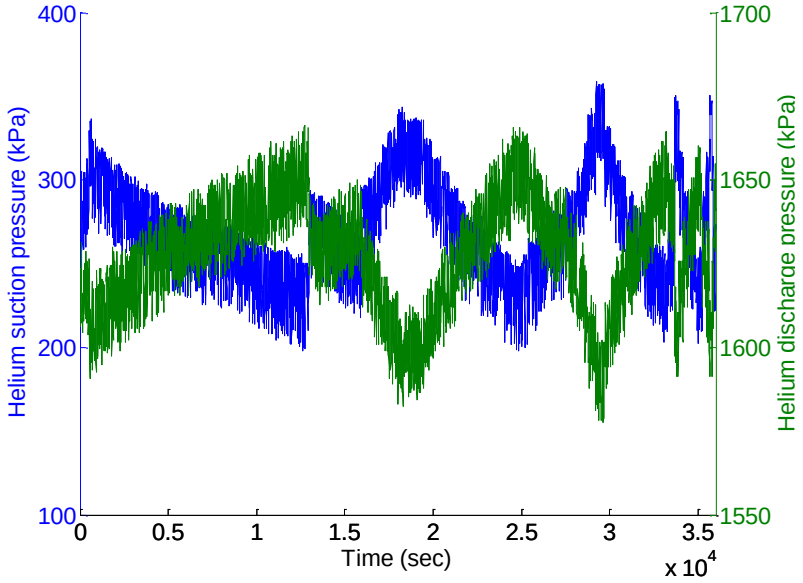

Figure J.1: Helium low and high pressure (kPaG)

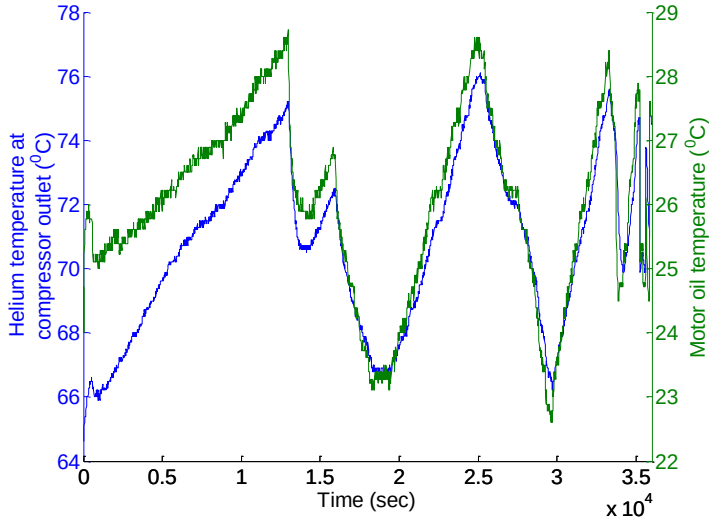

Figure J.2: Helium discharge temperature (^{0}C) and compressor motor oil temperature (^{0}C)

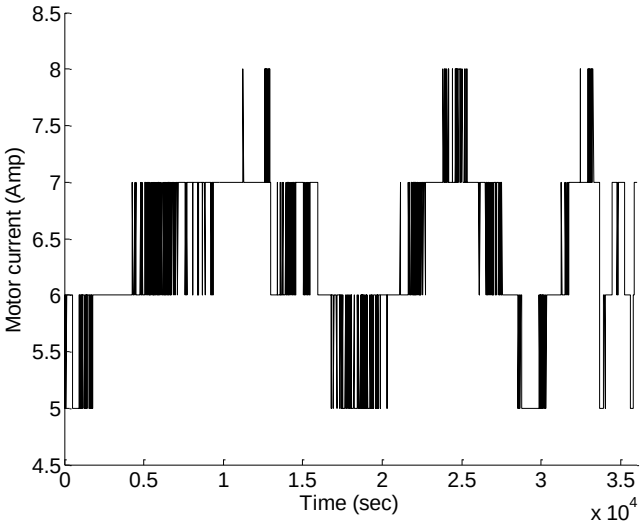

Figure J.3: Compressor motor current (Amp)

Appendix K. Experimental results when operating compressor with frequency scaled down from actual wind speed data

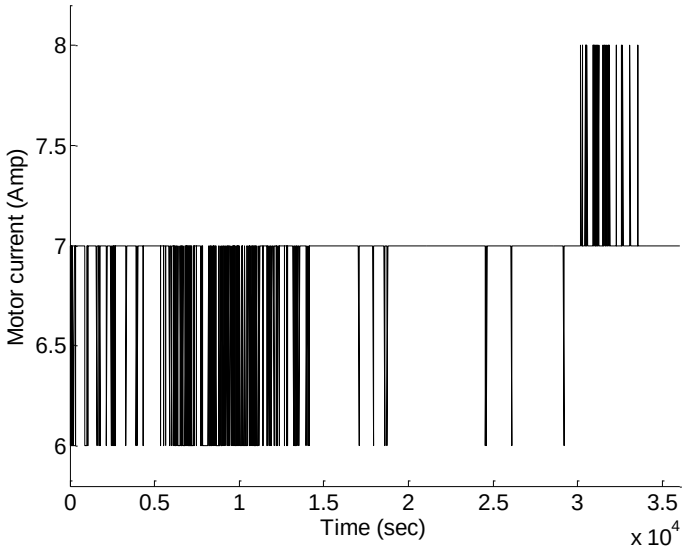

Figure K.1: Motor current (Amp)

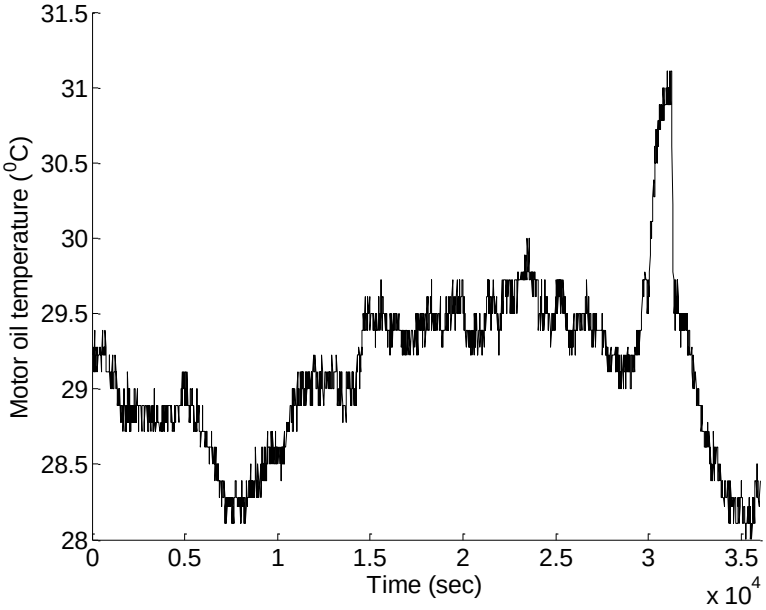

Figure K.2: Motor oil temperature (^0C)

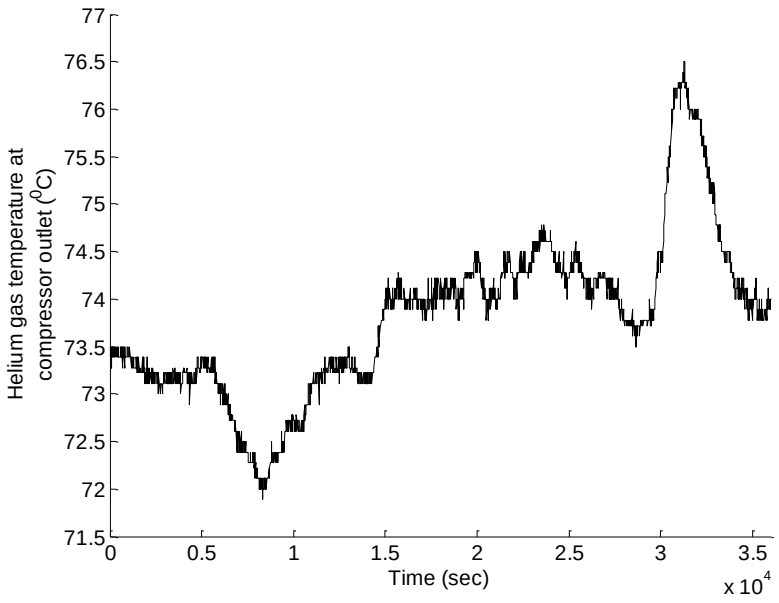

Figure K.3: Helium gas discharge temperature (^{0}C)

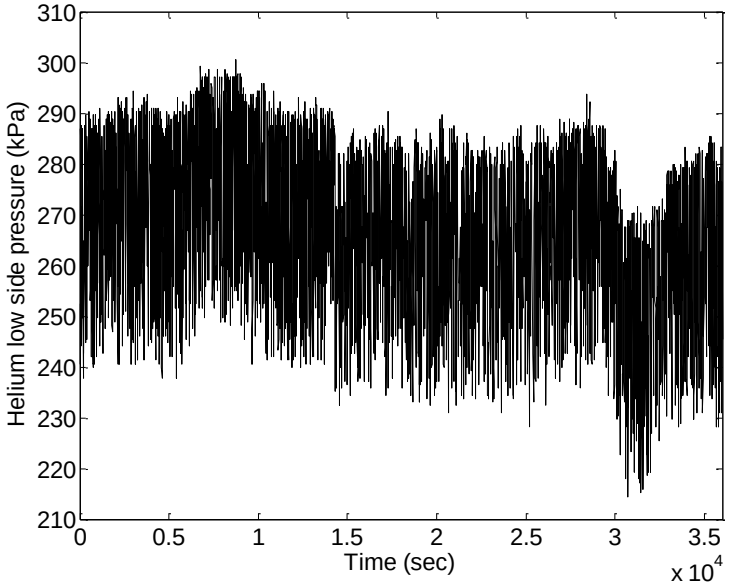

Figure K.4: Helium gas low pressure (kPaG)

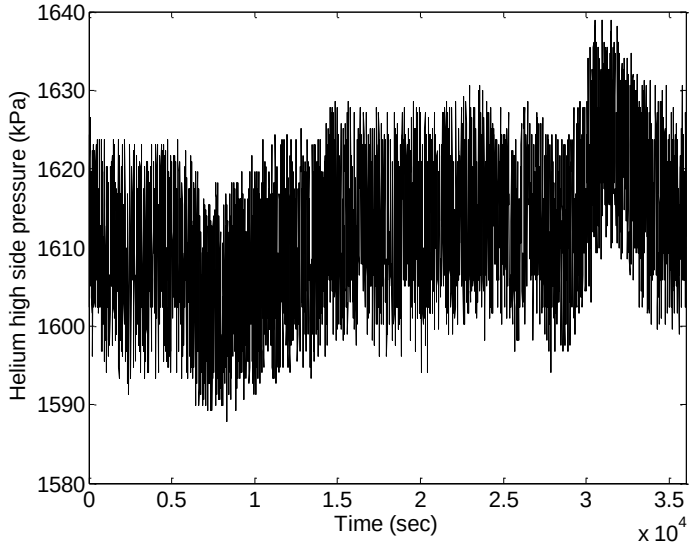

Figure K.5: Helium gas discharge pressure (kPaG)

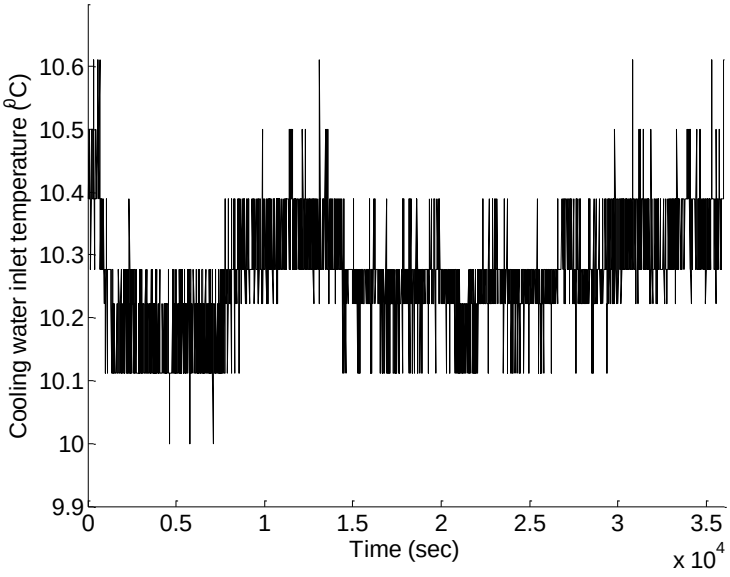

Figure K.6: Cooling water inlet temperature (^{0}C)

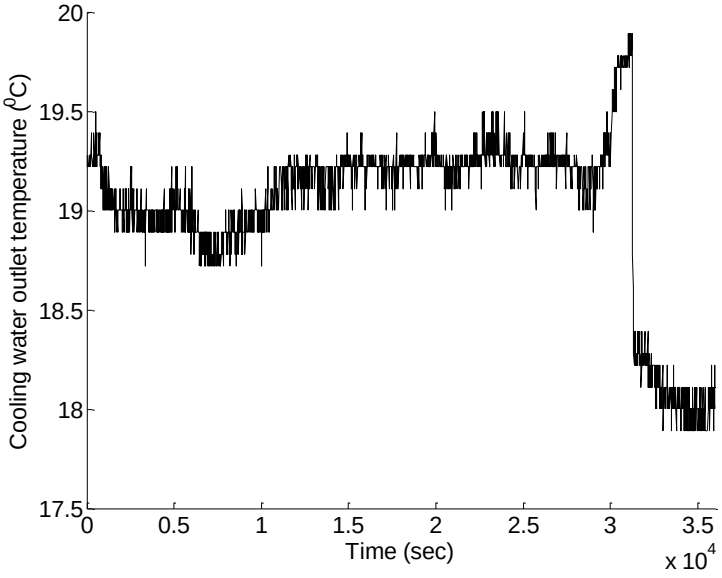

Figure K.7: Cooling water outlet temperature

Appendix L. Laboratory equipment

Figure L.1: Air compressor for delivery of pressurized air to nitrogen generator

Figure L.2: Dewar vessel front and rear views with GM cold head on its top and the fittings

Figure L.3: Front view of helium compressor panel showing Hitachi VFD and helium high and low pressure lines

Figure L.4: Helium compressor and Dewar vessel